Fundamentals of Ship Physics

Mechanics, Hydrodynamics, and Propulsion

Vahit ÇALIŞIR, PhD

EĞİTİM
yayınevi

Fundamentals of Ship Physics Mechanics, Hydrodynamics, and Propulsion
Vahit Çalışır

Chairman of the Publishing House Group: Yusuf Ziya Aydoğan (yza@egitimyayinevi.com)
Editor in Chief: Yusuf Yavuz (yusufyavuz@egitimyayinevi.com)
Interior Designer: Kübra Konca Nam
Cover Designer: Egitim Publishing House Design Department

Turkish Republic Ministry of Tourism and Culture
Publisher Certificate No: 76780

E-ISBN: 978-625-385-818-6
1. Edition, March 2026

Library Information Card
Fundamentals of Ship Physics Mechanics, Hydrodynamics, and Propulsion
Vahit Çalışır
219 s., 150x220 mm
Includes references, no index.
E-ISBN: 978-625-385-818-6

EĞİTİM yayınevi

Publisher Türkiye Office: İstanbul: Eğitim Yayınevi Tic. Ltd. Şti., Atakent mah. Yasemen sok. No: 4/B, Ümraniye, İstanbul, Türkiye

Konya: Eğitim Yayınevi Tic. Ltd. Şti., Fevzi Çakmak Mah. 10721 Sok. B Blok, No: 16/B, Safakent, Karatay, Konya, Türkiye +90 332 351 92 85, +90 533 151 50 42
bilgi@egitimyayinevi.com

Publisher USA Office: New York: Egitim Publishing Group, Inc.
P.O. Box 768/Armonk, New York, 10504-0768, United States of America
americaoffice@egitimyayinevi.com

Logistics and Shipping Center: Kitapmatik Lojistik ve Sevkiyat Merkezi, Fevzi Çakmak Mah. 10721 Sok. B Blok, No: 16/B, Safakent, Karatay, Konya, Türkiye
sevkiyat@egitimyayinevi.com

Bookstore Branch: Eğitim Kitabevi, Şükran mah. Rampalı 121, Meram, Konya, Türkiye
+90 332 499 90 00
bilgi@egitimkitabevi.com
Internet Sales: www.kitapmatik.com.tr
bilgi@kitapmatik.com.tr

EĞİTİM YAYINEVİ GRUBU

Contents

Preface

This book provides a unified, first-principles treatment of the physics that governs the design, behaviour, and operation of ships. It is intended for senior undergraduate and early postgraduate students in naval architecture, marine engineering, and ocean science, and assumes familiarity with single-variable calculus, introductory mechanics, and basic thermodynamics.

A ship is simultaneously a floating body governed by hydrostatics, a structure under load, a vehicle moving through a viscous fluid that generates waves, a platform responding to those waves, and a thermodynamic system that converts fuel into thrust. No single branch of physics suffices; the naval architect must draw on classical mechanics, fluid dynamics, thermodynamics, and their couplings—often within the same design decision. This text treats each domain in turn and, wherever possible, exposes the connections between them.

The organisation progresses from the mechanics of rigid and floating bodies (Chapters 1–4), through fluid dynamics and seakeeping (Chapters 5–6), to thermodynamics and propulsion (Chapters 7–8). Each chapter develops the physics from first principles, derives the key equations, and connects them to maritime practice through worked applications.

Vahit ÇALIŞIR
March 2026

Chapter 1

Introduction to Physics in Maritime Science

1.1 Introduction

The physics of buoyancy was understood by Archimedes around 220 BC, yet nearly two thousand years elapsed before it was systematically applied to the design of ships (Ferreiro, 2006). That delay was not for want of ships: throughout those centuries vessels were built, lost, and rebuilt by the thousand. What was missing was the institutional will and the analytical tools to translate physical law into engineering practice—a theme that runs through every chapter of this book.

Five physical domains govern the marine environment—mechanics, the physical and chemical properties of seawater, thermodynamics, electromagnetic radiation, and acoustics—each bearing directly on vessel design, operation, and safety (Dera, 1992). Decades of global casualty data confirm the practical stakes: physics-related failure modes, from structural collapse to hydrodynamic instability, dominate maritime losses (Guedes Soares & Santos, 2015).

This chapter surveys the physical principles that underpin maritime engineering, traces their historical development from Archimedes to Froude, and establishes the analytical framework and notation used in the subsequent chapters.

1.2 Scientific Background

1.2.1 The Role of Physics in Maritime Engineering

The physics relevant to maritime engineering spans the full breadth of the discipline. The thermodynamic equation of state for seawater links temperature, salinity, and pressure to density—a quantity that directly determines a vessel's displacement and freeboard. Electromagnetic radiation governs both remote

sensing of the ocean surface and the penetration of solar light into the water column, driving primary productivity and heat storage. Sound propagation in seawater provides the only practical means of long-range underwater communication and detection (Dera, 1992).

Classical mechanics governs the motion and stability of the vessel itself: Newton's laws determine speed and acceleration, hydrostatics determines floating position, and the balance of restoring and heeling moments determines whether a vessel rights itself or capsizes (Chapters 2–4). Fluid dynamics governs hull resistance, wave generation, and propeller performance (Chapters 5–8). Structural mechanics determines whether the hull girder can withstand the bending moments imposed by waves (see the *Structural Mechanics of Ships* chapter of the companion volume). No single branch of physics suffices; the maritime engineer must draw on mechanics, thermodynamics, electromagnetism, and acoustics simultaneously.

These domains are coupled rather than independent. The thermodynamic state of seawater determines its density, which governs both the vessel's floating position and the speed of sound used for underwater detection; wave loading drives structural stress, which accumulates as fatigue damage over the vessel's service life (Faltinsen, 1990); and hull resistance sets fuel consumption, linking fluid dynamics to thermodynamic efficiency. The resulting web of interactions, rather than any single physical principle, is what distinguishes maritime engineering as a multidisciplinary field (Dera, 1992; Newman, 1977).

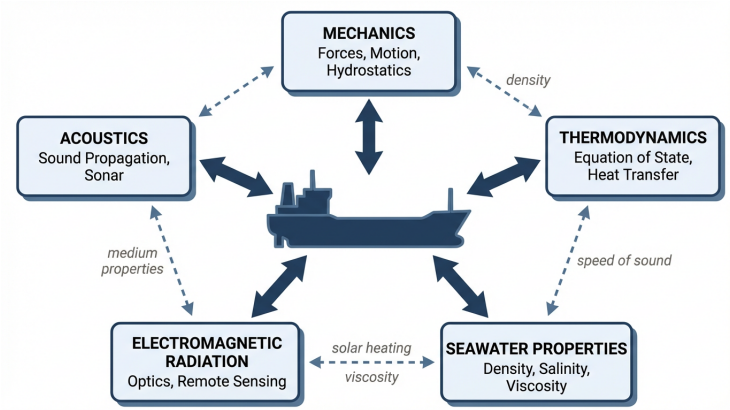

Figure 1.1: The five physical domains of the marine environment and their coupling. Each domain interacts with the others through shared state variables: density links thermodynamics to hydrostatics; wave loading connects fluid dynamics to structural mechanics; and the speed of sound depends on the thermodynamic state of seawater.

1.2.2 Historical Development of Maritime Physics

The theoretical foundations of maritime physics were remarkably slow to develop. Ferreiro (2006) documented a striking paradox: Archimedes' principle of hydrostatics—that the weight of a floating body equals the weight of the displaced liquid—was established around 220 BC, yet it was not systematically applied to ships for nearly two thousand years. For most of that period, Aristotle's qualitative notion that floating and sinking depended on the shape or relative weight of a body dominated scientific thought, particularly in the Jesuit schools that educated most of Europe's scientists. As late as 1611, Galileo found it necessary to defend Archimedes' principle in a public three-day debate against proponents of Aristotle's "shape theory." Even the laws of hydrostatic pressure developed by Simon Stevin and Blaise Pascal "found no real use in ship theory until the nineteenth century" (Ferreiro, 2006). The French Jesuit naval instructor Georges Fournier declared in 1643 that it was "morally impossible" to determine a vessel's displacement precisely (Ferreiro, 2006). The first practical demonstration that displacement *could* be calculated systematically was provided by Anthony Deane in his 1670 *Doctrine of Naval Architecture*, in which he divided the hull into frame sections and computed the displaced volume numerically (Ferreiro, 2006).

The effort to place ship design on a scientific footing began in earnest during the Scientific Revolution, driven not by academic curiosity but by military necessity. The pivotal figure was Jean-Baptiste Colbert, France's minister of the navy from 1669 to 1683. In a letter dated 10 September 1678, Colbert wrote that his intention was "to work to establish a theory on the subject of the construction of vessels" so that each ship would be "assured ... of carrying sail well, that the batteries will be well-established, that it will fight well ... in a word, that it will be perfect." Colbert believed that such a theory would serve as a force multiplier, improving the fighting effectiveness of individual French warships to compensate for France's numerical inferiority against the British and Dutch fleets (Ferreiro, 2006). To this end, he had already founded the French Academy of Sciences in 1666 and created hydrography schools under Jesuit control in 1681. The Jesuit Paul Hoste, who occupied the mathematics chair at the Brest Academy of Navy Guards, produced the first attempt at a synthesis of naval architecture with his *Théorie de la construction des vaisseaux* in 1697 (Ferreiro, 2006).

Isaac Newton's *Principia* (1687) introduced what would become the dominant model of hydrodynamic resistance for over a century. Newton visualised fluids as collections of hard particles that struck a moving body's surface, imparting an impulse proportional to $\rho v^2 \sin^2\theta$, where ρ is the fluid density, v is the velocity, and θ is the angle of incidence (Ferreiro, 2006). This "shock" or impulsion theory, and the related problem of the "solid of least resistance," shaped ship hydrodynamics throughout the eighteenth century (see Chapter 5). Newton's theory built upon earlier experimental work: Christiaan Huygens had demonstrated in 1668–1669 that fluid resistance is proportional

to the square of velocity, and Edmé Mariotte confirmed experimentally in 1681 that resistance is proportional to surface area, fluid density, and v^2—the first systematic use of the term "shock" for the action of fluids on solid bodies (Ferreiro, 2006).

The most consequential theoretical advance of this era was the invention of the **metacenter**—the initial measure of a ship's transverse stability (see Chapter 4). Pierre Bouguer (1698–1766), justly called the "father of naval architecture," conceived this concept while serving on the ten-year Geodesic Mission to Peru, where the French Academy of Sciences was measuring the shape of the Earth. Bouguer's *Traité du navire* (1746) was unprecedented: it was "the first work to provide a complete set of principles that governed scientific naval architecture—hydrostatics, hydrodynamics, stability—and it was the first to provide useful mathematical tools for the ship constructor" (Ferreiro, 2006). The metacenter became "the most important development of early naval architecture" and remains "the only theory surviving to the present day" (Ferreiro, 2006).

Leonhard Euler's 1727 entry to the French Royal Academy's competition addressed the optimal placement of masts on a vessel. Euler went far beyond this early work: his monumental *Scientia Navalis* (1749) developed general equations for idealised fluid motion based on Newton's laws, providing the mathematical framework from which virtually all subsequent fluid models descend. Euler's career spanned fifty years, and his collected works fill over one hundred volumes (Ferreiro, 2006). Together, Bouguer's *Traité du navire* and Euler's *Scientia Navalis* constituted the twin pillars of rational naval architecture.

Since Euler's time, Daniel Bernoulli clarified the relationship between the conservation of momentum (mv) and the conservation of *vis viva* (mv^2), established fundamental rules of vector analysis for forces, and modelled ship oscillation using the second moment of inertia (Ferreiro, 2006).

The historical record of catastrophic stability failures illustrates the practical consequences of these theoretical developments. The Swedish warship *Vasa* capsized in Stockholm harbour on 10 August 1628, less than thirty minutes after leaving the wharf, when a gust of wind heeled her to port and open gun ports admitted water. The English *Mary Rose* had capsized in nearly identical circumstances off Portsmouth on 19 July 1545, with the loss of over five hundred men. Yet stability accidents were, paradoxically, relatively rare: between 50 and 60 per cent of British warship losses during this period resulted from navigational accidents rather than capsizing (Ferreiro, 2006). It was ultimately the perception that French theoretical superiority in ship design gave their constructors a decided advantage that spurred the formation of the Society for the Improvement of Naval Architecture in Britain in 1791, "instigating an important series of experiments that would eventually lead to William Froude's work in the 1870s" (Ferreiro, 2006).

William Froude's experimental work in the 1870s established the foundations of modern ship hydrodynamics. Froude resolved the total resistance of

a ship into frictional and residuary (wave-making) components and demonstrated that geometrically similar hulls, tested at the same Froude number $V/\sqrt{gL}$, produce the same non-dimensional wave resistance (Rawson & Tupper, 2001). This principle, known as Froude's law of comparison, enabled the tank-testing methodology that is still the standard for predicting full-scale ship resistance from model experiments. Froude also investigated the rolling of ships at sea, formulating the equation of unresisted rolling (see Chapter 6, Section 6.3.1) and identifying the condition of synchronism between wave encounter period and natural roll period as the primary cause of dangerous rolling (Attwood, 1899).

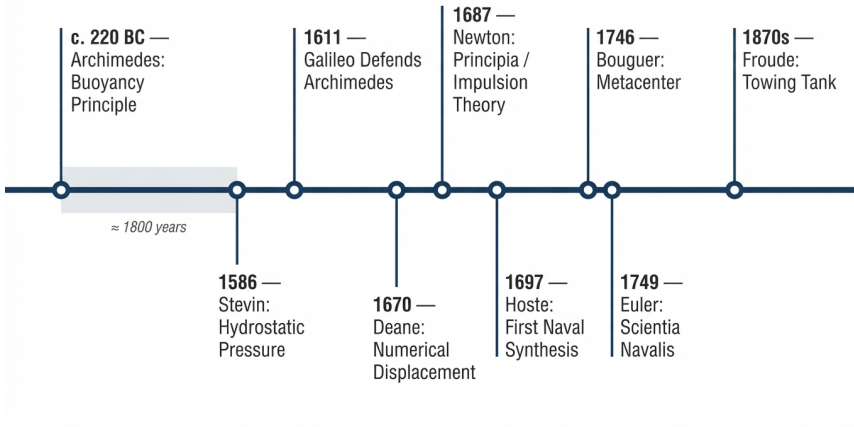

Figure 1.2: Key milestones in the development of maritime physics, from Archimedes' buoyancy principle (c. 220 BC) through the Scientific Revolution to Froude's towing-tank methodology (1870s). The two-thousand-year gap between theoretical knowledge and systematic engineering application is a recurring theme of this history.

1.2.3 Interdisciplinary Nature of Maritime Science

Maritime science draws on virtually every branch of physics. The physics of the marine environment can be organised into five broad domains (Dera, 1992): (i) the physical processes governing ocean dynamics (forces, motion, rotation), (ii) the physical and chemical properties of seawater as a medium, (iii) the thermodynamics of seawater (equation of state, heat transfer, compressibility), (iv) the interaction of electromagnetic radiation with the ocean (optics), and (v) the propagation of sound in seawater (acoustics). Each of these domains intersects with practical maritime operations: the equation of state governs ship draft in waters of varying salinity (Chapter 3), ocean acoustics underpins echo sounding and sonar (see the *Acoustics and Underwater Sound* chapter of the companion volume), and the Coriolis effect shapes both

weather systems (see the *Marine Meteorology and Atmospheric Physics* chapter of the companion volume) and ocean currents (see the *Physical Oceanography* chapter of the companion volume).

The present text is organised to reflect this interdisciplinary structure, following a progression established in the standard references on naval architecture (Lewis, 1988; Tupper, 2013). Chapters 2–4 develop the core solid-body and hydrostatic mechanics: Newton's laws applied to ship motion, the statics of floating bodies, and the stability criteria that determine whether a vessel rights itself or capsizes. Chapters 5–6 treat the vessel's hydrodynamic environment: resistance and propulsion in calm water, the generation and propagation of ocean waves, and the response of the hull to those waves at sea. Chapter 7 addresses the thermodynamics of marine power plants and seawater properties, while Chapter 8 develops the physics of converting engine power into thrust. The companion volume turns to the broader physical environment—electromagnetic navigation, atmospheric dynamics, and the large-scale physics of the ocean—and examines structural loading, underwater acoustics, safety and risk, and the environmental physics of maritime operations. Together, the two volumes cover the full range of physics constituting the marine physical environment (Dera, 1992).

1.3 Theoretical Framework

1.3.1 Fundamental Physical Laws and Maritime Relevance

The physical laws governing maritime systems operate at multiple levels simultaneously. Four principles recur throughout the chapters that follow (for a comprehensive introduction to these foundational concepts, see (Hewitt et al., 2012)):

- **Newton's second law and force balance:** At steady state the driving force on a vessel must equal the total resistance of the water. This equilibrium condition determines speed; in non-equilibrium conditions the net force governs acceleration (Chapter 2) (Campbell, 2025).

- **Conservation of momentum:** The thrust delivered by a propeller or sail equals the rate of momentum change imparted to the surrounding fluid. The same principle governs collision dynamics and jet propulsion (Campbell, 2025).

- **Structural equilibrium:** Every structural member—hull girder, frames, rudder stock—must satisfy rotational equilibrium under the applied loads. The balance between the bending moment and the material's allowable stress determines the required scantlings (see the *Structural Mechanics of Ships* chapter of the companion volume) (Campbell, 2025).

- **Dimensional similarity:** The Buckingham π-theorem guarantees that the governing physics can be expressed in terms of a small number of dimensionless parameters (Reynolds, Froude, and Euler numbers), establishing the scaling laws that connect model tests to full-scale performance (Birk, 2019).

These four principles—force balance, momentum exchange, structural equilibrium, and dimensional similarity—form the analytical framework applied throughout this text.

1.3.2 Mathematical Tools and Notation

The quantitative treatment of maritime systems begins with the language of kinematics—the mathematical description of motion. The fundamental kinematic quantities are successive time derivatives of position (Campbell, 2025).

The *instantaneous velocity* of an object is the time derivative of its position:

Equation 1.1 — Velocity as time derivative of position:

$$v(t) = \frac{\mathrm{d}}{\mathrm{d}t}\, x(t) \tag{1.1}$$

and the *instantaneous acceleration* is the time derivative of velocity (i.e. the second derivative of position) (Campbell, 2025); for a concise treatment, see (Fischer-Cripps, 2014). These kinematic definitions recur in every dynamical analysis that follows—from vessel acceleration and wave propagation to propeller shaft dynamics.

Throughout this book, vector quantities (displacement, velocity, force) are set in boldface (**v**, **F**) and scalar quantities (temperature, pressure, energy) in italic (T, p, E). For marine vehicle dynamics, two coordinate frames are used: an Earth-fixed frame whose z-axis points toward the centre of the Earth, and a body-fixed frame whose x-axis points toward the bow. The six degrees of freedom are labelled surge, sway, heave (translational) and roll, pitch, yaw (rotational), following the convention established by the Society of Naval Architects and Marine Engineers. These coordinate conventions are developed formally in Chapter 2.

The SI unit system is used consistently; key derived units include the newton ($\mathrm{N} = \mathrm{kg\,m\,s^{-2}}$), the pascal ($\mathrm{Pa} = \mathrm{N\,m^{-2}}$), and the watt ($\mathrm{W} = \mathrm{J\,s^{-1}}$).

1.3.3 Dimensional Analysis and Scaling in Maritime Systems

Dimensional analysis is one of the most powerful tools in maritime physics. It allows engineers to identify the key non-dimensional parameters that govern physical phenomena and to establish scaling laws between models and full-scale vessels.

Applying the Buckingham π-theorem to the ship resistance problem illustrates the method (Birk, 2019): if the total resistance R_T depends on $n = 6$

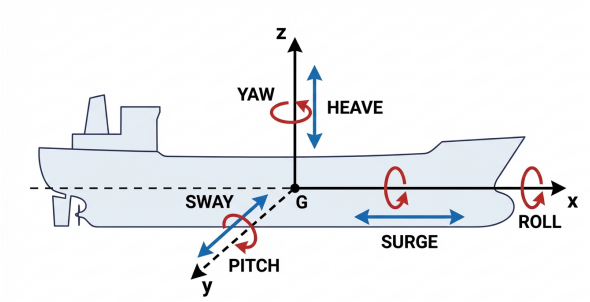

Figure 1.3: The six degrees of freedom of a floating vessel. Translational motions (surge, sway, heave) and rotational motions (roll, pitch, yaw) are defined relative to a body-fixed coordinate frame with origin at the centre of gravity, x-axis toward the bow, y-axis to port, and z-axis upward.

physical variables (density ρ, speed v, length L, viscosity μ, gravitational acceleration g, and pressure p) expressible in $k = 3$ fundamental dimensions (mass, length, time—or equivalently force, length, time in the FLT system used by Birk (2019)), then $m = n - k = 3$ independent dimensionless parameters govern the problem.

The three characteristic numbers that result are:

- **Reynolds number** $Re = vL/\nu$, where $\nu = \mu/\rho$ is the kinematic viscosity. The Reynolds number characterises the ratio of inertia forces to viscous (friction) forces and governs the frictional resistance component (Birk, 2019).
- **Froude number** $Fr = v/\sqrt{gL}$, characterising the ratio of inertia forces to gravity forces. The Froude number governs wave-making resistance and is the basis for the law of corresponding speeds used in model testing (Birk, 2019).
- **Euler number** $Eu = p/(\frac{1}{2}\rho v^2)$, characterising the ratio of pressure forces to inertia forces. In the context of propellers, the Euler number relates to cavitation (Birk, 2019).

The total resistance coefficient is thus a function of all three parameters: $C_T = f(Re,\, Fr,\, Eu)$ (Birk, 2019). Since it is physically impossible to match both Re and Fr simultaneously at model scale (unless the model is the same size as the ship), the standard towing tank procedure tests at the correct Froude number and corrects for the Reynolds number mismatch using the ITTC-57 friction line (Chapter 5) (Birk, 2019).

The power of dimensional analysis extends beyond resistance prediction. An analysis of 96 sailboat models spanning displacements from hundreds to tens of thousands of kilograms shows that key geometric ratios—beam to draft,

length to beam, and mast height to hull length—are independent of absolute vessel size (Bejan et al., 2020). The most intuitive of these is the beam-to-draft ratio:

Equation 1.2 — Beam-to-draft ratio:

$$\frac{D_x}{D_y} \sim 2 \tag{1.2}$$

Here $D_x \equiv B$ (beam) and $D_y \equiv T$ (draft) in the notation of Bejan et al. (2020). This value follows from the balance between frontal (pressure) drag and frictional (wetted-surface) drag; the same force balance constrains the hull slenderness ratio L/B and the mast-height-to-hull-length ratio H/L (Bejan et al., 2020). The scale-independence of these proportions is itself a consequence of the dimensionless character of the governing parameters—a direct parallel to the $Re/Fr/Eu$ analysis above.

1.4 Applications in Maritime Systems

1.4.1 Ship Design

Ship design proceeds not as a linear sequence but as an iterative cycle—the so-called design spiral—in which each physical discipline is revisited as the design matures (Birk, 2019; Papanikolaou, 2014). An early choice of hull length sets the operating Froude number and thereby the wave-making resistance; that resistance estimate feeds into the propulsion calculation, which determines engine size and fuel capacity; the added weight alters displacement, which shifts the floating position and the stability margins; and revised stability may in turn demand a different beam-to-draft ratio, sending the designer back to the resistance estimate (Birk, 2019). Structural loads set the scantlings of frames and plating at each iteration (see the *Structural Mechanics of Ships* chapter of the companion volume). The physics of each discipline thus enters the design not once but repeatedly, and an error in any one loop propagates through all subsequent iterations.

The physics of propulsion determines how efficiently a vessel converts engine power into forward motion. The propulsive coefficient—the ratio of effective horsepower to indicated horsepower—decomposes into hull efficiency, propeller efficiency, and mechanical efficiency; Froude's *Greyhound* experiments measured a best-case value of only 42%, confirming that over half of the prime-mover energy is dissipated before producing useful thrust (Attwood, 1899). The towing-tank methodology that connects these model-scale measurements to full-scale predictions is developed in Chapters 5 and 8.

1.4.2 Navigation and Communication

Underwater navigation and communication rely almost exclusively on acoustics, because electromagnetic radiation is strongly attenuated in seawater.

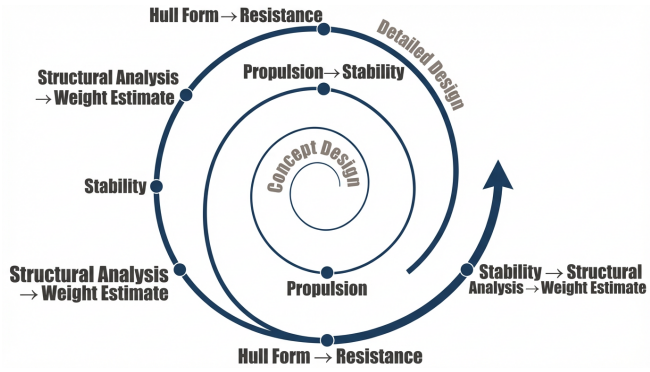

Figure 1.4: The ship design spiral. Each revolution revisits hull form, resistance, propulsion, stability, and structural analysis with increasing precision. The physics of each discipline enters the design repeatedly; an error in any one loop propagates through all subsequent iterations.

Sound propagates at approximately $1500\ \mathrm{m\,s^{-1}}$ in seawater—roughly 4.4 times the speed in air ($\approx 343\ \mathrm{m\,s^{-1}}$)—and can travel hundreds of kilometres within the deep sound channel (SOFAR channel) (Urick, 1983). This property is exploited in echo sounding, side-scan sonar, and acoustic Doppler current profilers.

Surface navigation, by contrast, exploits electromagnetic radiation. Radar operates in the microwave band precisely because these wavelengths propagate well through the atmosphere and are reflected by solid and liquid surfaces. Satellite positioning (GNSS) uses L-band signals that traverse the atmosphere with minimal absorption. The choice of frequency band for each maritime communication or sensing system is dictated by the physics of wave propagation in the relevant medium (Dera, 1992).

1.4.3 Safety and Environmental Protection

Global casualty statistics confirm the practical importance of physics in maritime safety. A comprehensive global analysis of 10,841 serious shipping casualties during 1990–2012, covering 602,998 cumulative ship-years of exposure across 13 ship types, revealed that hull and machinery damage constitutes approximately 37% of all incidents, followed by wrecked/stranded events (21%) and collisions (20%) (Guedes Soares & Santos, 2015). The total losses amounted to 940 vessels and 6,569 lives, with general cargo ships accounting for 52.3% of total losses. These statistics demonstrate that the physics of structural failure, flooding, wave loading, and collision mechanics—developed in Chapter 4 and in the *Structural Mechanics of Ships* and *Maritime Safety and Risk Physics* chapters of the companion volume—are of immediate practical consequence.

Physics contributes directly to maritime safety and environmental monitoring. The optical properties of seawater determine how quickly oil slicks, suspended sediments, and algal blooms can be detected from satellites. Ocean waters are classified into Jerlov types based on their spectral transmittance, a framework now used routinely in remote sensing algorithms (Dera, 1992).

The vertical density structure of the ocean, governed by the equation of state (see Chapter 7), controls the stability of the water column. A stable density stratification inhibits vertical mixing, trapping pollutants near the surface; an unstable profile promotes overturning and dispersal. Predicting the fate of contaminants discharged into the marine environment therefore requires a quantitative grasp of these processes (Dera, 1992).

1.5 Discussion

The historical narrative developed in Section 1.2.2 reveals a recurring theme in applied physics: fundamental knowledge, once available, is not automatically or rapidly translated into engineering practice. The Scientific Revolution transformed ship design from an empirical craft into a physics-based discipline over the period 1600–1800, yet Archimedes' principle had been available for nearly two thousand years before it was systematically applied to ships (Ferreiro, 2006). The critical catalysts were institutional—Colbert's academies, the Jesuit educational network, the prize systems of learned societies—rather than purely intellectual. The metacenter, invented by Bouguer in 1746, remains the foundational stability calculation in naval architecture to this day, demonstrating that when theory and practice do converge, the result can be extraordinarily durable (Ferreiro, 2006).

The five physical domains of the marine environment—mechanics, seawater properties, thermodynamics, electromagnetic optics, and acoustics (Dera, 1992). The casualty statistics cited in Section 1.1 (Guedes Soares & Santos, 2015) confirm that deficiencies in any one domain—structural, hydrodynamic, or navigational—carry severe consequences. The organisation of the present text into four chapter groups (Section 1.2.3) mirrors this breadth, progressing from solid-body mechanics through fluid dynamics, the wider physical environment, and finally structural integrity and safety.

The integrated engineering curriculum at the United States Naval Academy provides contemporary validation of this physics-centred organisation (United States Naval Academy, 2021). By structuring an entire naval architecture programme around the successive application of hydrostatics, resistance, propulsion, seakeeping, and structural analysis to the same hull form, the USNA course demonstrates that a single physics framework suffices to address the full range of ship performance problems. The laboratory exercises accompanying each topic close the loop between theory and measurement, reinforcing the connection between analytical prediction and physical observation that has been the hallmark of the post-Scientific-

Revolution era (Ferreiro, 2006; United States Naval Academy, 2021).

The historical record and the modern casualty statistics converge on a single conclusion: the gap between available physics and its effective application to ships has narrowed dramatically since the eighteenth century, but it has not closed. The failure modes that dominate global casualty analyses—structural collapse, flooding, grounding—are precisely the phenomena for which the underlying physics is well understood and presented in the chapters that follow (Guedes Soares & Santos, 2015). That such failures continue to occur at scale suggests that the challenge today is less one of fundamental knowledge than of its consistent, rigorous application across the fleet.

1.6 Conclusion

Maritime engineering is applied physics. The marine environment demands simultaneous attention to mechanics, thermodynamics, electromagnetism, and acoustics—five coupled domains whose interactions determine whether a vessel floats safely, moves efficiently, and survives the loads imposed upon it (Dera, 1992). History teaches that the availability of relevant physics is necessary but not sufficient: Archimedes' buoyancy principle waited nearly two millennia before Bouguer's metacenter (1746) and Euler's fluid equations (1749) finally placed ship design on a rational footing (Ferreiro, 2006). When the translation from theory to practice did occur, the results proved remarkably durable—the metacenter remains the standard measure of initial stability to this day.

The analytical framework that emerged from this long evolution rests on a small number of powerful ideas. Dimensional analysis reduces the ship resistance problem to three governing parameters—Reynolds, Froude, and Euler numbers—whose ratios encode the competition between viscous, gravitational, and pressure forces (Birk, 2019). The same dimensionless reasoning explains why vessel proportions are scale-independent (Bejan et al., 2020). These scaling laws underpin the towing-tank methodology that still connects model experiments to full-scale predictions, and they recur in every quantitative chapter that follows.

The chapters ahead develop this physics in sequence: solid-body mechanics and hydrostatics first, then fluid dynamics and waves, followed by thermodynamics and propulsion, and finally the broader physical environment, structural integrity, and safety. Each topic builds on its predecessors, so that the reader builds, chapter by chapter, the physical framework that modern maritime engineering demands (United States Naval Academy, 2021).

References

Attwood, E. L. (1899). *A text-book of theoretical naval architecture*. Longmans, Green; Co.

Bejan, A., Ferber, L., & Lorente, S. (2020). Convergent evolution of boats with sails. *Scientific Reports*, *10*, Article 2703. https://doi.org/10.1038/s41598-020-58940-5

Birk, L. (2019). *Fundamentals of ship hydrodynamics: Fluid mechanics, ship resistance and propulsion*. John Wiley & Sons. https://doi.org/10.1002/9781119191575

Campbell, C. (2025). *Physics: A focused introduction*. CRC Press. https://doi.org/10.1201/9781003571568

Dera, J. (1992). *Marine physics* (P. Senn, Trans.) [Translated from Polish. Original: *Fizyka morza*, 1983]. Elsevier.

Faltinsen, O. M. (1990). *Sea loads on ships and offshore structures*. Cambridge University Press.

Ferreiro, L. D. (2006). *Ships and science: The birth of naval architecture in the Scientific Revolution, 1600–1800*. The MIT Press. https://doi.org/10.7551/mitpress/9780262062596.001.0001

Fischer-Cripps, A. C. (2014). *The physics companion* (2nd ed.). CRC Press. https://doi.org/10.1201/b17356

Guedes Soares, C., & Santos, T. A. (Eds.). (2015). *Maritime technology and engineering: Proceedings of MARTECH 2014*. CRC Press.

Hewitt, P. G., Suchocki, J. A., & Hewitt, L. A. (2012). *Conceptual physical science* (5th ed.). Pearson.

Lewis, E. V. (Ed.). (1988). *Principles of naval architecture* (2nd ed.) [Three volumes]. The Society of Naval Architects; Marine Engineers.

Newman, J. N. (1977). *Marine hydrodynamics*. The MIT Press.

Papanikolaou, A. (2014). *Ship design: Methodologies of preliminary design*. Springer. https://doi.org/10.1007/978-94-017-8751-2

Rawson, K. J., & Tupper, E. C. (2001). *Basic ship theory* (5th ed.). Butterworth-Heinemann.

Tupper, E. C. (2013). *Introduction to naval architecture* (5th ed.). Butterworth-Heinemann.

United States Naval Academy. (2021). En400: Principles of ship performance [Course notes, Fall AY2021].

Urick, R. J. (1983). *Principles of underwater sound* (3rd ed.). McGraw-Hill.

Chapter 2

Classical Mechanics and Ship Motion

2.1 Introduction

Classical mechanics—the study of forces, motion, and equilibrium—underpins the quantitative analysis of maritime systems. Ship motion through water, mooring loads, collision forces, and cargo handling all reduce to applications of Newton's laws.

The steady-state speed of a sailing vessel follows from the equilibrium between the aerodynamic force on the sail and the hydrodynamic drag on the hull (Bejan et al., 2020). This application of Newton's second law (at equilibrium, net force equals zero) yields quantitative predictions of optimal vessel geometry.

2.2 Scientific Background

2.2.1 Newton's Laws of Motion in Maritime Context

Newton's second law states that the net force on a body equals the product of its mass and acceleration (Hewitt et al., 2012). For a vessel in steady-state motion (constant velocity), the acceleration is zero, and the law reduces to a force balance: the sum of all forces must equal zero.

Applying this principle to a sailing vessel yields a particularly transparent example (Bejan et al., 2020):

- **Driving force:** The wind exerts an aerodynamic drag force F_a on the sail, which acts as the propulsive force.
- **Resisting force:** The water exerts a hydrodynamic drag force F_w on the hull, opposing the motion.

At steady state:

Equation 2.1 — Force balance (Newton's second law at equilibrium):

$$F_a = F_w \tag{2.1}$$

This balance determines the steady-state speed V_w of the vessel for a given wind speed V_a and vessel geometry (Bejan et al., 2020). Newton's third law is also evident: the sail pushes the air backward (reaction), while the air pushes the sail forward (action).

In the general (non-equilibrium) case, the net external force produces an acceleration proportional to the body's mass:

Equation 2.2 — Newton's second law (general form):

$$\mathbf{F}_{\text{NET}} = m\,\mathbf{a} \tag{2.2}$$

For a vessel accelerating from rest or decelerating during an emergency stop, Equation 2.2 governs the time history of velocity. When the mass of the system changes—as in a rocket-propelled lifeboat or a vessel burning fuel—the more fundamental form $\mathbf{F} = d\mathbf{p}/dt$ must be used, where $\mathbf{p}$ is the momentum (Section 2.3.3).

2.2.2 Kinematics of Ship Motion

Kinematics describes motion without reference to its causes. Under constant acceleration $\mathbf{a}$, the velocity and position of a body evolve according to three fundamental kinematic equations (Campbell, 2025):

Equation 2.3 — Kinematic equations for constant acceleration:

$$\begin{aligned} \mathbf{v}_f &= \mathbf{v}_i + \mathbf{a}\,\Delta t \\ \mathbf{x}_f &= \mathbf{x}_i + \mathbf{v}_i\,\Delta t + \tfrac{1}{2}\,\mathbf{a}\,(\Delta t)^2 \\ v_f^2 &= v_i^2 + 2\,\mathbf{a}\cdot\Delta\mathbf{x} \end{aligned} \tag{2.3}$$

The first equation relates velocity to elapsed time; the second gives position as a function of time; the third eliminates time and links velocity directly to displacement (Campbell, 2025).

In the maritime domain, these relations are essential for estimating *stopping distance*. Consider a vessel of mass m travelling at speed v_i that applies full astern thrust producing a constant deceleration a. The distance to a complete stop ($v_f = 0$) follows from the third kinematic equation:

$$d_{\text{stop}} = \frac{v_i^2}{2\,|a|}$$

For a laden tanker with $v_i = 8\ \text{m s}^{-1}$ (approximately 15.5 knots) and $|a| \approx 0.01\ \text{m s}^{-2}$, the stopping distance is roughly $d_{\text{stop}} \approx 3200\ \text{m}$, illustrating why collision avoidance must begin well in advance. Similarly, the second kinematic equation governs the approach trajectory during berthing, where the pilot targets a specific contact speed at the fender line.

2.2.3 Reference Frames and Coordinate Systems

Maritime dynamics must account for the fact that the Earth is a rotating reference frame. An observer fixed to the Earth's surface is in a non-inertial frame rotating with angular velocity $\omega = 7.292 \times 10^{-5}$ rad s^{-1}. This rotation introduces two pseudo-forces into the equations of motion: the centripetal acceleration and the Coriolis acceleration (Dera, 1992).

The centripetal acceleration for a body at latitude φ on a sphere of radius R is directed toward the rotation axis and has magnitude:

Equation 2.4 — Centripetal acceleration:

$$a_c = \omega^2 R \cos\varphi \tag{2.4}$$

This acceleration is small (maximum ≈ 0.034 m s^{-2} at the equator) and is absorbed into the effective gravitational field. The Coriolis acceleration, by contrast, acts on moving bodies and is perpendicular to the velocity vector:

Equation 2.5 — Coriolis force:

$$\mathbf{F}_C = -2m\,(\boldsymbol{\omega} \times \mathbf{v}) \tag{2.5}$$

where m is the mass of the body and $\mathbf{v}$ is its velocity relative to the Earth (Dera, 1992). In the horizontal plane, the Coriolis force deflects moving objects to the right in the Northern Hemisphere and to the left in the Southern Hemisphere. Although negligible for ship manoeuvring at harbour scales, the Coriolis effect governs ocean currents, atmospheric wind patterns, and the large-scale trajectory of projectiles—all of which are relevant to maritime operations (see Chapter 5 and the *Marine Meteorology and Atmospheric Physics* and *Physical Oceanography* chapters of the companion volume).

2.2.4 Rotational Dynamics and Angular Momentum

Many maritime phenomena—propeller torque reaction, rudder-induced yaw, roll oscillation—involve rotation rather than translation. The rotational analog of Newton's second law connects the net *torque* on a body to its angular acceleration. The torque (or moment) produced by a force $\mathbf{F}$ applied at position $\mathbf{r}$ from the axis of rotation is:

$$\boldsymbol{\tau} = \mathbf{r} \times \mathbf{F}, \qquad |\boldsymbol{\tau}| = rF\sin\alpha,$$

where α is the angle between $\mathbf{r}$ and $\mathbf{F}$. The *moment of inertia* of a rigid body about a given axis measures its resistance to angular acceleration, just as mass measures resistance to linear acceleration:

$$I = \sum_i m_i\, r_i^2 \quad \text{(discrete)}, \qquad I = \int r^2\, dm \quad \text{(continuous)},$$

where r_i is the perpendicular distance of each mass element from the rotation axis. For a ship, the moments of inertia I_x, I_y, I_z about the body-fixed axes

determine the vessel's resistance to roll, pitch, and yaw respectively. These are commonly expressed through the *radius of gyration* k as $I = mk^2$; typical values for merchant ships are $k_{xx} \approx 0.35$–$0.45\,B$ for roll and $k_{yy} \approx 0.24$–$0.26\,L$ for pitch (Attwood, 1899; Lewis, 1988).

Newton's second law for rotation then takes the compact form:

Equation 2.6 — Newton's second law for rotation:

$$\sum \boldsymbol{\tau} = I\,\boldsymbol{\alpha} \tag{2.6}$$

where $\boldsymbol{\alpha} = d\boldsymbol{\omega}/dt$ is the angular acceleration; for a concise treatment, see (Fischer-Cripps, 2014). This is the rotational foundation upon which the six-DOF equations of motion (Section 2.3.2) are built.

The *angular momentum* of a rigid body rotating with angular velocity $\boldsymbol{\omega}$ is:

Equation 2.7 — Angular momentum and its conservation:

$$\mathbf{L} = I\,\boldsymbol{\omega}, \qquad \text{and} \qquad \frac{d\mathbf{L}}{dt} = \sum \boldsymbol{\tau}_{\text{ext}} \tag{2.7}$$

When no external torque acts ($\sum \boldsymbol{\tau}_{\text{ext}} = \mathbf{0}$), angular momentum is conserved. This principle has immediate maritime applications. A spinning propeller carries angular momentum $L_p = I_p\,\omega_p$; by Newton's third law, the engine torque that spins the propeller exerts an equal and opposite reaction torque on the hull, causing a single-screw vessel to heel slightly toward the torque-reaction side (Russell et al., 2015). Gyroscopic precession, which couples pitch and yaw in vessels with large rotating machinery, also follows from the vector form of Equation (2.7).

2.3 Theoretical Framework

2.3.1 Rigid Body Dynamics at Sea

A vessel can be modelled as a rigid body with six degrees of freedom: three translational (surge, sway, heave) and three rotational (roll, pitch, yaw). While a full six-DOF treatment requires the formalism developed in Section 2.3.2, the simplest case—forward motion (surge) under force balance—is instructive.

For a sailing vessel in steady forward motion, the surge equation reduces to the balance between the sail force F_a and the hull drag F_w. Equating the aerodynamic drag on the sail, $F_a \sim C_D(HL/2)\,\frac{1}{2}\rho_a V_a^2$, to the dominant skin-friction drag on the hull, $F_w \sim C_f(2D_y + D_x)L\,\frac{1}{2}\rho_w V_w^2$, and noting that the geometric ratios D_x/D_y, H/L, and the density ratio ρ_a/ρ_w are scale-independent constants, the boat-speed-to-wind-speed ratio reduces to (Bejan et al., 2020):

Equation 2.8 — Speed ratio from force balance:

$$\frac{V_w}{V_a} \sim \left(\frac{H}{L}\right)^{1/2} \tag{2.8}$$

where H is the mast height and L is the hull length. This result shows that the speed of the vessel is directly linked to its geometric proportions—a purely mechanical relationship.

For the horizontal-plane manoeuvring problem, the three-DOF equations of motion coupling surge, sway, and yaw take the form (Guedes Soares & Santos, 2015):

Equation 2.9 — Three-DOF ship manoeuvring equations:

$$\begin{aligned}(m+\mu_{11})\,\dot{u} - (m+\mu_{22})\,v\,r &= X_H + X_P \\ (m+\mu_{22})\,\dot{v} + (m+\mu_{11})\,u\,r &= Y_H + Y_P + Y_S \\ (I_{66}+\mu_{66})\,\dot{r} &= N_H + N_P + N_S\end{aligned} \tag{2.9}$$

where m is the ship mass, μ_{11}, μ_{22}, μ_{66} are the added masses in surge, sway, and yaw respectively, u, v, r are the surge velocity, sway velocity, and yaw rate, I_{66} is the yaw moment of inertia, and the right-hand side terms represent the hull hydrodynamic forces (X_H, Y_H, N_H), propulsor forces (X_P, Y_P, N_P), and skeg/appendage forces (Y_S, N_S) (Guedes Soares & Santos, 2015).

These equations are coupled with the kinematic relations transforming body-fixed velocities to the Earth-fixed frame (Guedes Soares & Santos, 2015):

Equation 2.10 — Kinematic equations:

$$\begin{aligned}\dot{\xi} &= u\cos\psi - v\sin\psi \\ \dot{\eta} &= u\sin\psi + v\cos\psi \\ \dot{\psi} &= r\end{aligned} \tag{2.10}$$

where $(\xi,\,\eta)$ are the ship coordinates in the Earth-fixed frame and ψ is the heading angle.

The added masses are estimated from the ship's principal dimensions using ellipsoidal approximations (Guedes Soares & Santos, 2015):

$$\mu_{11} = \left(\frac{T}{L}\right)^{2} m, \qquad \mu_{22} = 2\left(\frac{T}{B}\right)^{1/2} m, \qquad \mu_{66} = 2\left(\frac{T}{B}\right)^{1/2} I_{66}$$

where L, B, T are the ship length, breadth, and draught. This formulation extends the one-dimensional force balance of Equation 2.8 to the full horizontal-plane dynamics required for manoeuvring analysis.

The three-DOF equations above govern horizontal-plane motion. In the general case, a marine vehicle simultaneously experiences forces and moments in all six degrees of freedom—surge, sway, heave (translational) and roll, pitch, yaw (rotational). The complete six-DOF formulation, which accounts for all coupling terms between translational and rotational motions, is developed in Section 2.3.2 using the standard notation established by the Society of Naval Architects and Marine Engineers (Al Makdah et al., 2019).

2.3.2 Six Degrees of Freedom of Ship Motion

The general motion of a marine vehicle in three-dimensional space involves six independent modes: three translational—*surge* (fore-and-aft), *sway* (lateral), and *heave* (vertical)—and three rotational—*roll* (about the longitudinal axis), *pitch* (about the transverse axis), and *yaw* (about the vertical axis). Following the SNAME notation convention, the state of the vehicle is described by three vectors (Al Makdah et al., 2019):

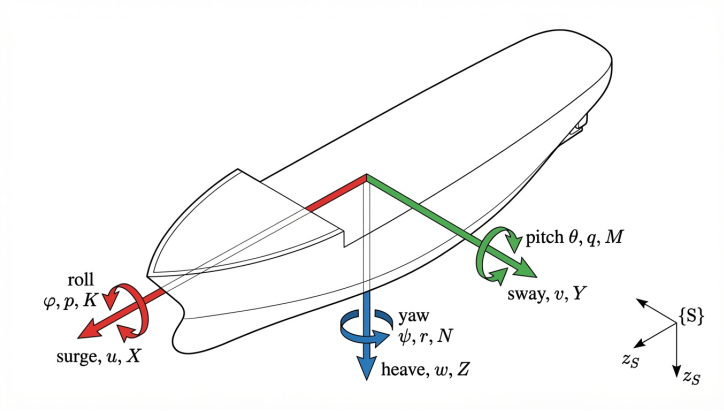

Figure 2.1: SNAME body-fixed coordinate system and the six degrees of freedom of a marine vehicle. Translational modes: surge (x), sway (y), heave (z). Rotational modes: roll (ϕ), pitch (θ), yaw (ψ). Forces and moments are resolved along the body-fixed axes.

Equation 2.11 — SNAME state vectors for six-DOF motion:

$$\begin{aligned} \boldsymbol{\eta} &= \begin{bmatrix} x & y & z & \phi & \theta & \psi \end{bmatrix}^T, \\ \boldsymbol{\nu} &= \begin{bmatrix} u & v & w & p & q & r \end{bmatrix}^T, \\ \boldsymbol{\tau} &= \begin{bmatrix} X & Y & Z & K & M & N \end{bmatrix}^T, \end{aligned} \tag{2.11}$$

where $\boldsymbol{\eta}$ contains the position (x, y, z) and orientation (ϕ, θ, ψ) relative to the Earth-fixed frame, $\boldsymbol{\nu}$ contains the linear velocities (u, v, w) and angular velocities (p, q, r) expressed in the body-fixed frame, and $\boldsymbol{\tau}$ contains the external forces (X, Y, Z) and moments (K, M, N) acting on the body in the body-fixed frame. Two reference frames are employed: an Earth-fixed frame $\{S\}$ with the z_S-axis pointing toward the centre of the Earth, and a body-fixed frame $\{B\}$ with the x_B-axis pointing toward the bow (Al Makdah et al., 2019).

The velocity transformation from the body-fixed frame to the Earth-fixed frame is given by the kinematic relation (Al Makdah et al., 2019):

Equation 2.12 — Six-DOF kinematic transformation:

$$\dot{\boldsymbol{\eta}} = \mathbf{J}(\boldsymbol{\eta}_2)\, \boldsymbol{\nu}, \tag{2.12}$$

where $\mathbf{J}$ is a 6×6 block-diagonal transformation matrix composed of the linear velocity transformation $\mathbf{J}_1$ and the angular velocity transformation $\mathbf{J}_2$:

$$\mathbf{J}_1 = \begin{bmatrix} c\psi\, c\theta & -s\psi\, c\phi + c\psi\, s\theta\, s\phi & s\psi\, s\phi + c\psi\, c\phi\, s\theta \\ s\psi\, c\theta & c\psi\, c\phi + s\phi\, s\theta\, s\psi & -c\psi\, s\phi + s\theta\, s\psi\, c\phi \\ -s\theta & c\theta\, s\phi & c\theta\, c\phi \end{bmatrix},$$

$$\mathbf{J}_2 = \begin{bmatrix} 1 & s\phi\, t\theta & c\phi\, t\theta \\ 0 & c\phi & -s\phi \\ 0 & s\phi/c\theta & c\phi/c\theta \end{bmatrix},$$

where s, c, and t denote sin, cos, and tan, respectively. Note that $\mathbf{J}_2$ is singular when $\theta = \pm 90°$, a condition rarely encountered for surface ships but relevant for deeply pitching underwater vehicles. Equation (2.12) generalises the three-DOF kinematic relations in Equation (2.10) to include heave, roll, and pitch motions.

The six-DOF dynamic equations of rigid body motion, derived from Newton's second law applied to a body with its centre of gravity at (x_G, y_G, z_G) relative to the body-fixed origin, are (Al Makdah et al., 2019):

Equation 2.13 — Six-DOF equations of motion:

$$\begin{aligned} m\big[\dot{u} - vr + wq - x_G(q^2+r^2) + y_G(pq-\dot{r}) + z_G(pr+\dot{q})\big] &= X, \\ m\big[\dot{v} - wp + ur - y_G(r^2+p^2) + z_G(qr-\dot{p}) + x_G(qp+\dot{r})\big] &= Y, \\ m\big[\dot{w} - uq + vp - z_G(p^2+q^2) + x_G(rp-\dot{q}) + y_G(rq+\dot{p})\big] &= Z, \\ I_x\dot{p} + (I_z - I_y)qr + m\big[y_G(\dot{w} - uq + vp) - z_G(\dot{v} - wp + ur)\big] &= K, \\ I_y\dot{q} + (I_x - I_z)rp + m\big[z_G(\dot{u} - vr + wq) - x_G(\dot{w} - uq + vp)\big] &= M, \\ I_z\dot{r} + (I_y - I_x)pq + m\big[x_G(\dot{v} - wp + ur) - y_G(\dot{u} - vr + wq)\big] &= N, \end{aligned} \tag{2.13}$$

where m is the vessel mass, I_x, I_y, I_z are the moments of inertia about the body-fixed axes, and the right-hand side terms (X, Y, Z, K, M, N) represent the total external forces and moments. The coupling terms (e.g., $-vr + wq$ in the surge equation) arise from the Coriolis and centripetal effects inherent in the body-fixed frame description; the terms involving x_G, y_G, z_G account for the offset between the body-fixed origin and the centre of gravity (Al Makdah et al., 2019).

These equations can be written compactly in vectorial form (Al Makdah et al., 2019):

Equation 2.14 — Vectorial form of the equations of motion:

$$\mathbf{M}_{RB}\,\dot{\boldsymbol{\nu}} + \mathbf{C}_{RB}(\boldsymbol{\nu})\,\boldsymbol{\nu} = \boldsymbol{\tau}_{RB}, \tag{2.14}$$

where $\mathbf{M}_{RB}$ is the 6×6 rigid body inertia matrix containing m, I_x, I_y, I_z and the centre-of-gravity offsets, $\mathbf{C}_{RB}(\boldsymbol{\nu})$ is the matrix of Coriolis and centripetal terms, and $\boldsymbol{\tau}_{RB}$ is the total external force and moment vector.

The total external force acting on a marine vehicle can be decomposed into distinct physical contributions (Al Makdah et al., 2019; Newman, 1977):

Equation 2.15 — Decomposition of external forces:

$$\boldsymbol{\tau}_{RB} = \boldsymbol{\tau}_{\text{hydrostatic}} + \boldsymbol{\tau}_{\text{added mass}} + \boldsymbol{\tau}_{\text{drag}} + \boldsymbol{\tau}_{\text{lift}} + \boldsymbol{\tau}_{\text{propeller}}, \tag{2.15}$$

where $\boldsymbol{\tau}_{\text{hydrostatic}}$ comprises the weight and buoyancy forces, $\boldsymbol{\tau}_{\text{added mass}}$ accounts for the inertia of the surrounding fluid displaced by the accelerating body, $\boldsymbol{\tau}_{\text{drag}}$ represents the skin friction and form drag, $\boldsymbol{\tau}_{\text{lift}}$ includes the lift forces generated by appendages (fins, rudder, wings), and $\boldsymbol{\tau}_{\text{propeller}}$ is the thrust force and torque from the propulsor. The hydrostatic forces and moments, expressed in the body-fixed frame, are (Al Makdah et al., 2019):

$$\begin{aligned} X_{\text{hs}} &= -(W - B)\sin\theta, \\ Y_{\text{hs}} &= (W - B)\cos\theta\ \sin\phi, \\ Z_{\text{hs}} &= (W - B)\cos\theta\ \cos\phi, \end{aligned}$$

where W is the weight force and B is the buoyancy force. For a surface vessel in static equilibrium ($W = B$), all translational hydrostatic forces vanish. Restoring moments nevertheless arise because, when the vessel heels by an angle ϕ, the centre of buoyancy shifts laterally, creating a righting couple $\Delta\,\text{GM}\,\sin\phi$ that opposes the heel (see Chapter 4).

This six-DOF framework provides the mathematical basis for analysing the complete motion of a marine vehicle, including the heave, roll, and pitch coupling terms that are absent in the three-DOF horizontal-plane model of Equation (2.9). The added mass, drag, and lift terms in Equation (2.15) are further developed in Chapters 5 and 6.

2.3.3 Momentum, Impulse, and Collision Mechanics

Momentum transfer governs both propulsion and collision dynamics. In the context of sail propulsion, the wind transfers momentum to the sail, which propels the vessel. The rate of momentum transfer defines the driving force (Bejan et al., 2020):

$$F_a \sim C_D \cdot \frac{HL}{2} \cdot \frac{1}{2}\,\rho_a\,V_a^2$$

This is fundamentally a momentum-change formulation: the force equals the rate of change of momentum of the air deflected by the sail.

More formally, the *momentum* of a body of mass m moving with velocity $\mathbf{v}$ is:

Equation 2.16 — Linear momentum:

$$\mathbf{p} = m\,\mathbf{v} \tag{2.16}$$

When a force acts over a time interval Δt, the resulting change in momentum is called the *impulse*:

Equation 2.17 — Impulse–momentum theorem:

$$\mathbf{J} = \mathbf{F}_{\text{avg}}\,\Delta t = \Delta \mathbf{p} \tag{2.17}$$

This result is directly applicable to ship collision analysis: when two vessels make contact, the impact force multiplied by the contact duration equals the change in momentum of each vessel. A longer contact time (as provided by energy-absorbing fenders) reduces the peak force for a given impulse, protecting both the hull structure and the berth.

For a closed system—one with no net external force—Newton's third law guarantees that the total momentum is conserved (Campbell, 2025):

Equation 2.18 — Conservation of momentum:

$$\sum \mathbf{p}_i = \sum \mathbf{p}_f \tag{2.18}$$

In a head-on collision between two vessels of masses m_1 and m_2 with initial velocities $\mathbf{v}_{1i}$ and $\mathbf{v}_{2i}$, the post-collision velocities must satisfy $m_1\mathbf{v}_{1i} + m_2\mathbf{v}_{2i} = m_1\mathbf{v}_{1f} + m_2\mathbf{v}_{2f}$. Coupled with energy considerations (perfectly inelastic collisions absorb the maximum kinetic energy), this framework provides the basis for collision damage assessment.

In real ship collisions, however, the effective mass of each vessel exceeds its displacement because the surrounding water is also set in motion. This *added mass* effect is captured by hydrodynamic coefficients μ_x (surge) and μ_y (sway), so the effective mass becomes $m(1+\mu)$ (Zhang, 1999). For a general oblique collision at striking angle φ, the kinetic energy lost to structural deformation can be written in closed form:

Equation 2.19 — Collision energy loss:

$$\Delta E_{\text{collision}} = E_0\left(1 - \frac{D_\xi}{D_\xi + D_\eta}\right) \tag{2.19}$$

where E_0 is the initial kinetic energy of the striking ship in the collision-normal direction, and D_ξ, D_η are generalised mass terms that incorporate the ship masses, added masses, moments of inertia, and the geometry of the contact point (Zhang, 1999). This analytical framework—known as the *external dynamics* of ship collisions—makes no restrictions on ship size, impact velocity, or striking angle, and it yields the energy budget that the ship structures must absorb. The complementary *internal mechanics* determines how that energy is distributed among structural failure modes such as plate cutting, frame crushing, and membrane tension (see the *Structural Mechanics of Ships* chapter of the companion volume).

The nature of the collision is characterised by the *coefficient of restitution* e, defined for a one-dimensional collision as:

$$e = -\frac{v_{1f} - v_{2f}}{v_{1i} - v_{2i}},$$

where v_{1i}, v_{2i} are the initial velocities and v_{1f}, v_{2f} the final velocities. Three regimes exist: *perfectly elastic* ($e = 1$, kinetic energy conserved), *partially inelastic* ($0 < e < 1$), and *perfectly inelastic* ($e = 0$, bodies move together after impact). Introducing the *reduced mass* $\mu_r = m_1 m_2/(m_1+m_2)$, the kinetic energy dissipated in a one-dimensional collision takes the compact form (Campbell, 2025):

Equation 2.20 — Energy dissipated in a collision:

$$\Delta E = \tfrac{1}{2}\,\mu_r\, v_{\text{rel}}^2\,(1 - e^2) \tag{2.20}$$

where $v_{\text{rel}} = v_{1i} - v_{2i}$ is the relative approach velocity. Ship collisions are nearly perfectly inelastic ($e \approx 0$): the vessels typically remain in contact and virtually all relative kinetic energy is absorbed by structural deformation. For a $10\,000$-ton vessel striking a $50\,000$-ton vessel at 5 m s^{-1} (both initially stationary in the transverse direction), the reduced mass is $\mu_r \approx 8333$ tonnes and the energy absorbed is $\Delta E \approx 104$ MJ—equivalent to the detonation energy of roughly 25 kg of TNT, which explains the severe structural damage observed in even moderate-speed collisions.

2.3.4 Friction and Drag Forces

Friction and drag are the primary forces opposing the motion of a vessel through water. Two distinct contributions can be identified (Bejan et al., 2020):

1. **Form drag (pressure drag):** The frontal cross-section of the submerged hull ($D_x \times D_y$, where $D_x \equiv B$ is the beam and $D_y \equiv T$ is the draft in standard naval-architecture notation) experiences a blunt-body drag proportional to $C_D \sim 1$.

2. **Skin friction:** The wetted surface along the hull sides and bottom experiences tangential shear stress proportional to $C_f \sim 10^{-2}$ for turbulent flow.

The total drag force combines both:

$$F_w \sim \left[C_D\, D_x\, D_y + C_f\,(D_x + 2D_y)\,L\right] \frac{1}{2}\,\rho_w\, V_w^2$$

The two-order-of-magnitude difference between C_D and C_f explains why hulls are slender: reducing the frontal area (which has $100\times$ more drag per unit area) is more effective than reducing side area (Bejan et al., 2020).

Friction also governs several critical machine elements in the propulsion chain. The coefficient of friction μ governs the behaviour of journal bearings, thrust blocks, and clutch plates that are essential to the ship's propulsion system. For a marine thrust block, the friction force $F_f = \mu N$ between the collar and the bearing surface must be overcome by the engine, and the power lost to friction is $P_f = \mu N v$, where v is the sliding velocity and N is the axial

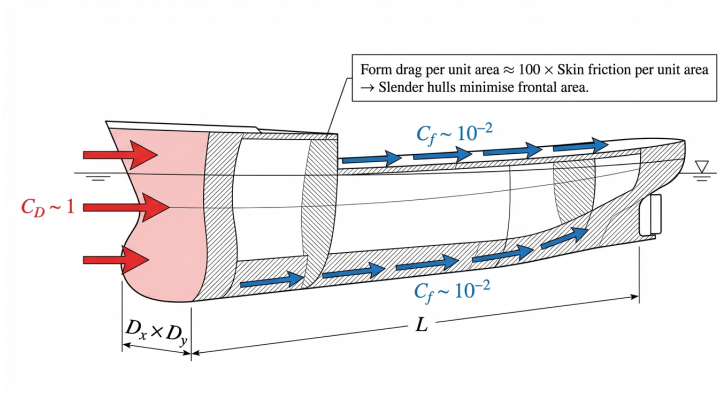

Figure 2.2: Drag decomposition for a submerged hull. Form drag acts on the frontal cross-section ($D_x \times D_y$, $C_D \sim 1$) while skin friction acts along the wetted surface ($C_f \sim 10^{-2}$). The two-order-of-magnitude difference between the coefficients drives hull slenderness.

thrust load (Russell et al., 2015). This frictional loss is one component of the mechanical efficiency e_m that appears in the propulsive coefficient (Chapter 8, Equation 8.29).

2.3.5 Work, Energy, and Power in Marine Systems

The work–energy theorem states that the net work done on a body equals its change in kinetic energy. In the context of a vessel operating in the Earth's gravitational field, potential energy plays a central role. The concept of *geopotential* accounts for the variation of gravitational acceleration with both latitude and depth (Dera, 1992):

Equation 2.21 — Effective gravitational acceleration:

$$g(\varphi) = 9.780\,318\big(1 + 5.302 \times 10^{-3} \sin^2\varphi - 5.9 \times 10^{-6} \sin^2 2\varphi\big) \quad [\mathrm{m\,s^{-2}}] \tag{2.21}$$

where φ is the geographic latitude (Dera, 1992). This expression includes the combined effect of gravitational attraction and centripetal acceleration due to Earth's rotation. The value of g ranges from $9.780\ \mathrm{m\,s^{-2}}$ at the equator to $9.832\ \mathrm{m\,s^{-2}}$ at the poles.

The *kinetic energy* of a body is:

Equation 2.22 — Kinetic energy:

$$K = \tfrac{1}{2}\, m\, v^2 \tag{2.22}$$

The *work–energy theorem* states that the total work done on a body by all forces equals the change in its kinetic energy (Campbell, 2025):

Equation 2.23 — Work–energy theorem:

$$W_{\text{TOT}} = \sum W = \Delta K \tag{2.23}$$

For a vessel of mass m at height z above the geoid, the gravitational potential energy is $E_p = m\, g(\varphi)\, z$, and the *power*—the rate at which work is done—is given by (Campbell, 2025):

Equation 2.24 — Mechanical power:

$$P = \mathbf{F} \cdot \mathbf{v} \tag{2.24}$$

Thus the power required to maintain a speed V_w against a drag force F_w is $P = F_w \cdot V_w$, and the effective horsepower (EHP) of a vessel is precisely this quantity. When computing hydrostatic pressures in the deep ocean, the latitude-dependent value of g must be used to obtain accurate results (Dera, 1992).

A force is *conservative* if the work it does depends only on the initial and final positions, not on the path taken. Gravity is conservative: raising a cargo container of mass m through a height h stores a gravitational potential energy $U = mgh$ regardless of the crane's trajectory. The total *mechanical energy* of a system is defined as:

Equation 2.25 — Conservation of mechanical energy:

$$E_{\text{mech}} = K + U, \qquad \Delta E_{\text{mech}} = W_{\text{nc}} \tag{2.25}$$

where W_{nc} is the work done by non-conservative forces (drag, friction, structural deformation). When only conservative forces act, $W_{\text{nc}} = 0$ and mechanical energy is conserved: $K_i + U_i = K_f + U_f$. In practice, maritime systems always involve non-conservative forces. The energy dissipated by hull drag during a voyage, the energy absorbed by fenders during berthing, and the collision energy loss of Equation (2.19) are all manifestations of $W_{\text{nc}} < 0$: mechanical energy is converted irreversibly into heat and structural deformation. Equation (2.25) thus unifies the work–energy theorem with potential energy and provides the bookkeeping framework for all energy analyses in later chapters.

2.3.6 Simple Harmonic Motion and Ship Oscillations

Whenever a restoring force is proportional to displacement, the resulting motion is *simple harmonic*. This condition arises throughout marine engineering: the righting moment of a ship in roll, the elastic deflection of a propeller shaft, and the oscillation of a moored vessel at its berth all produce restoring forces that, for small displacements, vary linearly with the displacement.

Consider a body of mass m subject to a restoring force $F = -kx$, where k is the stiffness (restoring-force constant) and x is the displacement from equilibrium. Newton's second law gives:

Equation 2.26 — Simple harmonic oscillator:

$$m\,\ddot{x} + k\,x = 0 \qquad \Longrightarrow \qquad \ddot{x} + \omega_n^2\,x = 0 \tag{2.26}$$

where $\omega_n = \sqrt{k/m}$ is the *natural frequency* (rad s^{-1}). The general solution is:

Equation 2.27 — SHM general solution:

$$x(t) = A\cos(\omega_n\,t + \varphi_0), \qquad T = \frac{2\pi}{\omega_n} = 2\pi\sqrt{\frac{m}{k}} \tag{2.27}$$

where A is the amplitude, φ_0 is the initial phase, and T is the *natural period* (Campbell, 2025). The total energy of the oscillator is constant and exchanges periodically between kinetic and potential forms: $E = \tfrac{1}{2}kA^2 = \tfrac{1}{2}m\omega_n^2 A^2$.

The most important maritime application of SHM is ship rolling. For small heel angles ϕ, the righting moment is $M_R = \Delta\,\mathrm{GM}\,\sin\phi \approx \Delta\,\mathrm{GM}\,\phi$, where Δ is the displacement and GM is the metacentric height. The roll equation of motion becomes (Attwood, 1899):

Equation 2.28 — Undamped roll equation:

$$I_{xx}\,\ddot{\phi} + \Delta\,\mathrm{GM}\,\phi = 0 \qquad \Longrightarrow \qquad T_{\text{roll}} = \frac{2\pi\,k_{xx}}{\sqrt{g\,\mathrm{GM}}} \tag{2.28}$$

where $I_{xx} = m\,k_{xx}^2$ is the roll moment of inertia and k_{xx} is the transverse radius of gyration (see Section 2.2.4). The roll period T_{roll} is inversely proportional to $\sqrt{\mathrm{GM}}$: a vessel with large GM rolls quickly (short period, "stiff"), while one with small GM rolls slowly (long period, "tender")—a critical indicator of stability discussed fully in Chapter 4.

In reality, ship rolling is always *damped*: viscous friction from bilge keels, skin friction, and vortex shedding dissipate energy from the roll motion. The damped oscillator equation is:

$$I_{xx}\,\ddot{\phi} + b\,\dot{\phi} + \Delta\,\mathrm{GM}\,\phi = 0,$$

where b is the damping coefficient. Defining the *damping ratio* $\zeta = b/(2\sqrt{I_{xx}\,\Delta\,\mathrm{GM}})$, three regimes appear: underdamped ($\zeta < 1$, oscillatory decay), critically damped ($\zeta = 1$, fastest return without oscillation), and overdamped ($\zeta > 1$, sluggish return). Actual ships are always underdamped ($\zeta \approx 0.01$–0.10 for most hull forms), so the roll decays exponentially with each cycle. Bilge keels increase ζ by a factor of 2–5 and are the simplest passive anti-roll device (Russell et al., 2015). The forced-oscillation extension of this equation, where the driving force comes from waves, is developed in Chapter 6 (Faltinsen, 1990).

2.4 Applications in Maritime Systems

2.4.1 Manoeuvring and Course-Keeping

The fastest sailing boats achieve maximum speed when sailing "upwind" with sails pulled close to the hull centreline. As boat speed increases, the apparent wind velocity (the vector sum of true wind and boat velocity) increases and the apparent wind angle decreases. The sail is trimmed to align with the apparent wind direction, generating lift. This interaction between boat speed, apparent wind angle, and sail trim is a direct application of vector mechanics (Bejan et al., 2020).

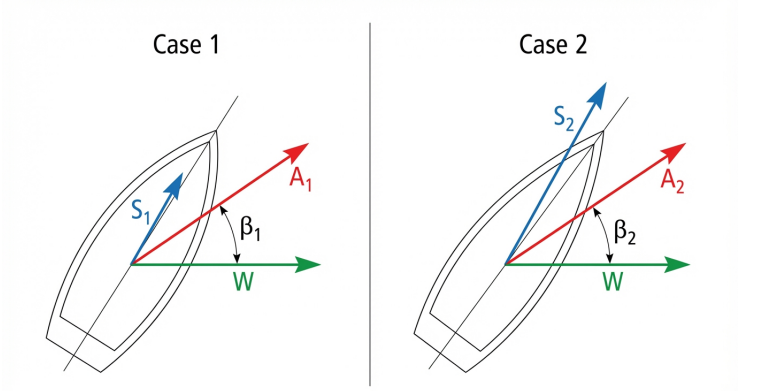

Figure 2.3: Apparent wind construction for a sailing vessel. Case 1: lower boat speed S_1 yields a larger apparent wind angle β_1. Case 2: higher boat speed S_2 shifts the apparent wind forward, reducing β_2 and requiring the sail to be trimmed closer to the centreline.

Rudder Force and Turning

When a rudder is placed at an angle θ to the ship's centreline, the deflected water stream exerts a normal pressure P on the rudder face. Attwood (1899) gave the classical expression for this force:

Equation 2.29 — Rudder normal pressure:

$$P = k\, A_r\, v^2\, \sin\theta \tag{2.29}$$

where A_r is the rudder area (m^2), v is the speed of water past the rudder (m s^{-1}), θ is the helm angle, and $k \approx 577$ N m^{-2} s^2 (converted from the original imperial value $k = 1.12$ with A_r in ft^2 and v in ft s^{-1}) (Attwood, 1899).[1] The rudder

[1] Modern hydrodynamic practice replaces this empirical pressure formula with lift and drag coefficients obtained from NACA-section data: $F_L = \tfrac{1}{2}\rho v^2 A_r C_L(\alpha)$, where α is the angle of attack and C_L is determined from foil theory or CFD. The classical formulation is retained here for its historical and pedagogical value.

area is typically expressed as a fraction of the longitudinal profile area: $A_r = LD/m$, where L is the ship length, D the mean draught, and m ranges from 33 (where exceptional manoeuvring power is desired) to 60 (large liners) (Attwood, 1899).

This force, applied at the rudder, produces a turning couple $P \times d_G \cos\theta$ about the centre of gravity, where d_G is the longitudinal distance from the centre of gravity to the rudder (Attwood, 1899). Since the couple varies as $\sin\theta\cos\theta = \tfrac{1}{2}\sin 2\theta$, the sine law would predict a maximum at $\theta = 45^\circ$; in practice, the usual maximum angle of 35° gives the best turning results because the sine law overestimates the pressure at large angles (Attwood, 1899).

Once the rudder is set, the ship traces a spiral path that soon becomes approximately circular. Attwood (1899) defined two key parameters: the *advance* (distance from helm-over to the point where the heading has changed by 90°) and the *tactical diameter* (the perpendicular offset when the heading has changed by 180°). In comparative trials of cruisers of similar dimensions (110×12 m (360×40 ft), approximately 3000 tonnes), a triple-screw ship with a propeller operating immediately ahead of the rudder achieved a tactical diameter of 503 m (≈ 550 yards, or $4.6L$), compared with 796 m (≈ 870 yards, or $7.25L$) for a twin-screw ship without this arrangement—demonstrating the decisive influence of the water velocity past the rudder (Attwood, 1899).

The three factors that most influence turning are (a) the rudder pressure, (b) the moment of resistance of the underwater body, and (c) the moment of inertia of the vessel about a vertical axis through her centre of gravity (Attwood, 1899; Rawson & Tupper, 2001). Cutting away the deadwood aft greatly reduces the moment of resistance at the stern (which is far from the pivoting point), and the ship HMS *Arrogant*, with two rudders and extensive deadwood removal, achieved a remarkably small turning circle despite being 98 m (≈ 320 ft) long (Attwood, 1899).

A ship in a steady turn heels outward due to centrifugal action. Attwood (1899) gave the resulting heel angle as:

Equation 2.30 — Heel angle when turning:

$$\sin\phi = 0.088\,\frac{V^2\,d}{R\,\mathrm{GM}} \tag{2.30}$$

where, in the original imperial formulation, V is speed in knots, d and R are in feet, and GM is in feet; the constant 0.088 absorbs the conversion factors (Attwood, 1899). In SI units (m and m s^{-1}) the dimensionally transparent form is:

$$\sin\phi = \frac{V_{\mathrm{SI}}^2\,d_{\mathrm{SI}}}{g\,R_{\mathrm{SI}}\,\mathrm{GM}_{\mathrm{SI}}}$$

where $g = 9.81$ m s^{-2}; this follows directly from the centripetal-acceleration-to-restoring-moment balance. A fast ship with a small turning circle and a small metacentric height will therefore heel considerably when turning at full speed.

Free Body Diagram of a Turning Ship

Fuss (2023) developed a rigorous free body diagram (FBD) analysis of a ship executing a steady circular turn, resolving the complete set of forces acting on the hull. In a steady turn, the ship's velocity vector **V** is tangent to the circular path, but the ship's centreline is offset from the velocity vector by the *drift angle* β. This drift angle causes the hull to move obliquely through the water, generating a hydrodynamic side force that—together with the rudder force—provides the centripetal acceleration required for curved motion (Fuss, 2023).

The FBD includes four principal categories of forces (Fuss, 2023): (i) the propeller thrust T along the ship's centreline; (ii) the hydrodynamic drag D opposing the velocity vector, further decomposed into hull drag and rudder drag; (iii) the hydrodynamic side (lift) force Y perpendicular to the velocity vector, generated by the hull and rudder operating at the drift angle; and (iv) the centripetal force $F_c = mV^2/R$ directed toward the centre of the turn. The equilibrium conditions for a steady circular turn require that the sum of forces along the velocity vector vanishes (thrust balances drag) and the sum of forces perpendicular to the velocity vector equals the centripetal force (hydrodynamic side force plus rudder lateral force provides the centripetal acceleration) (Fuss, 2023).

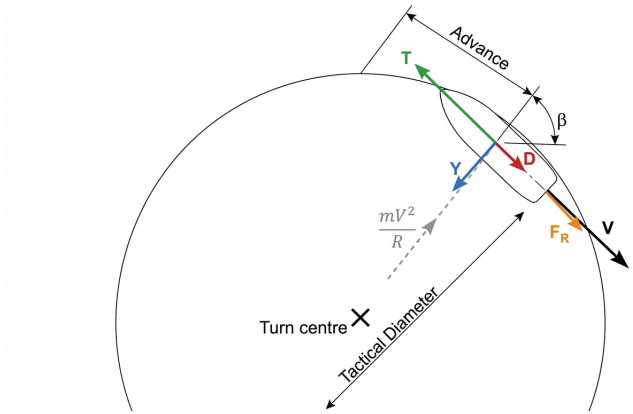

Figure 2.4: Free body diagram of a ship in a steady circular turn. The velocity vector **V** is tangent to the circular path, offset from the centreline by the drift angle β. Forces shown: propeller thrust T, hull drag D, hydrodynamic side force Y, rudder lateral force, and centripetal force mV^2/R directed toward the turn centre.

Fuss (2023) proposed a dimensionless *pleometric index*:

$$PI = \frac{V^2}{g\,R}$$

which compares the centripetal acceleration of the turning vessel to gravitational acceleration. This index provides a single scalar measure of turn sever-

ity: high values of PI correspond to tight, high-speed turns that impose large lateral forces on the hull and cargo. The pleometric index thus connects the kinematics of the turn (speed and radius) to the dynamics (force magnitudes) through the same V^2/R dependence that appears in Equation (2.30) for the heel angle (Fuss, 2023).

2.4.2 Cargo Loading and Weight Distribution

The total weight of the vessel determines its displacement, which in turn fixes the displaced volume of water $D_x\, D_y\, L$ (Bejan et al., 2020). Any change in cargo loading changes the displacement and therefore the draft D_y, with direct implications for resistance (a deeper draft increases the wetted surface and thus the skin-friction drag of Section 2.3.4), stability (the metacentric height GM that appeared in Equation 2.30 depends on the waterplane area and the vertical position of the centre of gravity), and freeboard. The beam-to-draft ratio ($D_x/D_y \sim 2$) and length-to-beam ratio ($L/D_x \gg 1$) remain as physical optima regardless of the loading condition (Bejan et al., 2020). The quantitative treatment of static stability and the effect of weight distribution on the righting-moment curve is developed in Chapter 4.

2.5 Discussion

The classical mechanics framework developed in this chapter—force balance, momentum transfer, rotational dynamics, drag decomposition, and energy methods—connects the governing equations to measurable vessel performance. Even a simplified one-dimensional force balance (sail thrust vs. hull drag) yields predictions confirmed by data from 96 sailboat models (Bejan et al., 2020). The agreement between theory and data persists even before more complex effects (wave-induced motions, unsteady flows, multi-DOF coupling) are introduced.

The extension from translational to rotational dynamics (Equations 2.6–2.7) is required for any vessel analysis beyond straight-line motion. The radius of gyration $k_{xx} \approx 0.35$–$0.45B$ for roll governs both the natural roll period and the inertial resistance to wave-induced moments; this single parameter connects the mass distribution determined by the naval architect to the seakeeping performance experienced at sea.

The kinematic equations (Equation 2.3) and the impulse–momentum theorem (Equation 2.17) extend this foundation to non-equilibrium scenarios. Stopping distances, collision impulses, and energy absorption all follow from the same Newtonian principles applied here to the maritime domain (Campbell, 2025). The coefficient of restitution framework (Equation 2.20) quantifies the energy partitioning in ship collisions: a 10,000 t vessel striking a 50,000 t vessel at 5 m/s dissipates approximately 104 MJ—energy equivalent to roughly 25 kg of TNT (Zhang, 1999). The work–energy

theorem (Equation 2.23), the power relation (Equation 2.24), and the conservation of mechanical energy (Equation 2.25) bridge the gap between force analysis and the energetic demands of propulsion, which is developed further in Chapter 8.

The rudder force analysis (Equation 2.29) illustrates how the sine law for pressure, combined with the geometric relationship between the rudder and the centre of gravity, governs the turning couple (Attwood, 1899). The heel angle during turning (Equation 2.30) shows that course changes at high speed carry stability implications—a direct coupling between translational mechanics and rotational equilibrium. The comparative trial data ($4.6L$ vs. $7.25L$ tactical diameters) further demonstrates that the velocity of water past the rudder, not merely the ship speed, determines manoeuvring performance. Fuss (2023) extended this turning analysis by constructing a complete free body diagram of a ship in a steady circular turn, resolving the force equilibrium into tangential (thrust vs. drag) and centripetal (hydrodynamic side force provides mV^2/R) components. The drift angle β and the pleometric index $PI = V^2/(gR)$ that emerge from this analysis provide a rigorous kinematic–dynamic framework that unifies the classical rudder-force approach with modern manoeuvring theory.

The simple harmonic motion analysis (Equations 2.26–2.28) reveals that a ship's natural roll period is fully determined by two quantities: the transverse radius of gyration and the metacentric height. The undamped roll equation $T_{\text{roll}} = 2\pi\, k_{xx}/\sqrt{g \cdot GM}$ provides an immediate, measurable diagnostic—a vessel with an observed roll period of 12 s and known GM can have its k_{xx} inferred without a formal inclining experiment. Damping, primarily from bilge keels, increases the damping ratio ζ by a factor of 2–5 and is essential for preventing resonance in beam seas.

The marine engineering applications of friction and these oscillatory principles complement the force-balance and drag decomposition framework by connecting the same fundamental physics—Newton's laws, energy conservation, and oscillatory motion—to the mechanical systems (thrust blocks, bearings, shafting) that transmit propulsive power from engine to propeller (Bejan et al., 2020; Russell et al., 2015).

2.6 Conclusion

Classical mechanics provides the foundational framework for understanding ship motion. At the simplest level, a one-dimensional force balance between sail thrust and hull drag determines steady-state speed, and the two-order-of-magnitude gap between form-drag ($C_D \sim 1$) and skin-friction ($C_f \sim 10^{-2}$) coefficients explains why all efficient hulls are slender (Bejan et al., 2020). When the vessel departs from steady state, Newton's second law—in both its translational and rotational forms—governs acceleration and deceleration: the kinematic equations predict stopping distances, the

impulse–momentum theorem quantifies collision forces, and the work–energy theorem connects drag to propulsive power (Campbell, 2025). The rotational analogue, $\sum \tau = I\alpha$, and the conservation of angular momentum explain why single-screw vessels heel under propeller torque reaction and why gyroscopic effects couple pitch and yaw in high-speed craft. At the most general level, the SNAME six-DOF formulation captures the coupled translational and rotational dynamics of a marine vehicle in a single compact equation, $\mathbf{M}_{RB}\dot{\boldsymbol{\nu}} + \mathbf{C}_{RB}\boldsymbol{\nu} = \boldsymbol{\tau}_{RB}$, from which all simpler models can be recovered as special cases (Al Makdah et al., 2019).

The collision mechanics developed in this chapter—from Newtonian impulse through the coefficient of restitution to closed-form collision energy loss expressions (Zhang, 1999)—quantify the enormous energies involved when ships collide. Energy methods, codified in the conservation law $\Delta E_{\text{mech}} = W_{\text{nc}}$, provide the bridge between the force-based and energy-based descriptions of ship performance, and the simple harmonic motion framework connects the same principles to the oscillatory behaviour of roll, pitch, and heave that dominates seakeeping (Russell et al., 2015).

Manoeuvring analysis extends these principles to curved motion. The classical rudder-force expression and the resulting heel angle during a turn demonstrate that course changes at speed carry direct stability implications (Attwood, 1899). The free-body-diagram approach and the pleometric index proposed by Fuss (2023) provide a modern, dimensionless framework for quantifying turn severity. Throughout, the same small set of mechanical principles—force balance, momentum conservation, energy conservation, rotational dynamics, and simple harmonic motion—reappears in contexts ranging from sail propulsion to collision energy absorption to ship rolling (Russell et al., 2015).

Two limitations apply. First, all drag and resistance expressions in this chapter assume calm water and steady flow; the modifications required for waves, currents, and unsteady motion are developed in Chapters 5 and 6. Second, the added-mass terms that appear in the manoeuvring equations (Equation 2.9) and the six-DOF formulation (Equation 2.15) are treated here as given coefficients; their physical origin in the acceleration of surrounding fluid is addressed in Chapter 5. With these caveats, the Newtonian mechanics of this chapter provides the foundation for the hydrodynamic, structural, and propulsive analyses that follow.

References

Al Makdah, A. A. R., Daher, N., Asmar, D., & Shammas, E. (2019). Three-dimensional trajectory tracking of a hybrid autonomous underwater vehicle in the presence of underwater current. *Ocean Engineering*, *185*, 115–132. https://doi.org/10.1016/j.oceaneng.2019.05.030

Attwood, E. L. (1899). *A text-book of theoretical naval architecture*. Longmans, Green; Co.

Bejan, A., Ferber, L., & Lorente, S. (2020). Convergent evolution of boats with sails. *Scientific Reports*, *10*, Article 2703. https://doi.org/10.1038/s41598-020-58940-5

Campbell, C. (2025). *Physics: A focused introduction*. CRC Press. https://doi.org/10.1201/9781003571568

Dera, J. (1992). *Marine physics* (P. Senn, Trans.) [Translated from Polish. Original: *Fizyka morza*, 1983]. Elsevier.

Faltinsen, O. M. (1990). *Sea loads on ships and offshore structures*. Cambridge University Press.

Fischer-Cripps, A. C. (2014). *The physics companion* (2nd ed.). CRC Press. https://doi.org/10.1201/b17356

Fuss, F. K. (2023). The dynamics of a turning ship: Mathematical analysis and simulation based on free body diagrams and the proposal of a pleometric index. *Dynamics*, *3*(3), 379–404. https://doi.org/10.3390/dynamics3030021

Guedes Soares, C., & Santos, T. A. (Eds.). (2015). *Maritime technology and engineering: Proceedings of MARTECH 2014*. CRC Press.

Hewitt, P. G., Suchocki, J. A., & Hewitt, L. A. (2012). *Conceptual physical science* (5th ed.). Pearson.

Lewis, E. V. (Ed.). (1988). *Principles of naval architecture* (2nd ed.) [Three volumes]. The Society of Naval Architects; Marine Engineers.

Newman, J. N. (1977). *Marine hydrodynamics*. The MIT Press.

Rawson, K. J., & Tupper, E. C. (2001). *Basic ship theory* (5th ed.). Butterworth-Heinemann.

Russell, P. A., Jackson, L., & Embleton, W. (2015). *Applied mechanics for marine engineers* (6th ed., Vol. 2). Thomas Reed.

Zhang, S. (1999). *The mechanics of ship collisions* [Doctoral dissertation]. Technical University of Denmark.

Chapter 3

Fluid Statics and Buoyancy

3.1 Introduction

Fluid statics—the study of fluids at rest and the forces they exert on immersed and floating bodies—is the oldest branch of maritime physics. The ability of a vessel to float is the most basic requirement of any ship, and it is governed entirely by the principles of hydrostatics.

Attwood (1899) opens his treatment of displacement with the foundational statement of Archimedes' principle applied to ships: "If a vessel is floating in equilibrium in still water, the weight of water she displaces must exactly equal the weight of the vessel herself with everything she has on board." This principle, established more than two thousand years ago, remains the basis of all hydrostatic calculations (Hewitt et al., 2012; Tupper, 2013).

3.2 Scientific Background

3.2.1 Properties of Fluids

The density of seawater is the single most important fluid property for ship hydrostatics. Unlike fresh water, seawater density depends on three independent state variables: temperature T, salinity S, and pressure p. The general differential equation of state (Chapter 7, Equation 7.1) expresses the fractional change in specific volume as a linear combination of changes in these three variables, governed by the thermal expansion coefficient k_T, the saline contraction coefficient k_S, and the isothermal compressibility k_p (Dera, 1992).

For practical calculations, the UNESCO International Equation of State (EOS-80) provides the operational polynomial (Chapter 7, Equation 7.9):

$$\rho(S, T, p) = \frac{\rho(S, T, 0)}{1 - p \,/\, K(S, T, p)}$$

Since 2010 the Thermodynamic Equation of Seawater (TEOS-10), based on a

Gibbs potential formulation, has replaced EOS-80 as the international standard (Dera, 1992); nonetheless, the numerical values relevant to ship hydrostatics change by less than 0.01%, so the traditional density values remain valid for naval-architectural calculations.

Typical surface seawater ($S \approx 35\,‰$, $T \approx 15\,^{\circ}\mathrm{C}$) has a density of approximately $1025\ \mathrm{kg\,m^{-3}}$, while fresh water at $4\,^{\circ}\mathrm{C}$ reaches its maximum density of $999.97\ \mathrm{kg\,m^{-3}}$ (Dera, 1992). This density difference of approximately 2.5% has direct implications for ship draft and freeboard when a vessel transits between seawater and fresh water.

3.2.2 Hydrostatic Pressure Distribution

In a fluid at rest, pressure increases with depth due to the weight of the overlying fluid. The hydrostatic pressure at depth z below the free surface is governed by the relation (Dera, 1992, Eq. 1.2.15):

Equation 3.1 — Hydrostatic pressure:

$$p(z) = p_0 + \int_0^{z} \rho(z')\, g \, \mathrm{d}z' \tag{3.1}$$

where p_0 is the atmospheric pressure at the surface, $\rho(z')$ is the in situ density, and g is the gravitational acceleration. For a layer of constant density, this reduces to $p = p_0 + \rho\, g\, z$; for a concise treatment, see (Fischer-Cripps, 2014).

In the deep ocean, the in situ density increases with depth due to compressibility—even if temperature and salinity are constant—so the integral in Equation 3.1 must account for $\rho = \rho(S, T, p(z'))$. At $1000\,\mathrm{m}$ depth, the hydrostatic pressure is approximately $100\,\mathrm{bar}$ ($10^7\,\mathrm{Pa}$), and compressibility raises the density by roughly $5\ \mathrm{kg\,m^{-3}}$ compared with the surface value (Dera, 1992).

The gravitational acceleration g itself varies with latitude and altitude. The apparent gravitational acceleration, including the centrifugal effect, is (Dera, 1992, Eq. 1.2.7):

Equation 3.2 — Apparent gravitational acceleration:

$$g_a = g - \omega^2 R \cos^2\varphi \tag{3.2}$$

where $\omega = 7.292 \times 10^{-5}\ \mathrm{rad\,s^{-1}}$ is the Earth's angular velocity, R is the Earth's radius, and φ is the geographic latitude. The variation from $g \approx 9.78\ \mathrm{m\,s^{-2}}$ at the equator to $g \approx 9.83\ \mathrm{m\,s^{-2}}$ at the poles produces a corresponding variation in hydrostatic pressure (Dera, 1992, Eq. 1.2.7).

3.2.3 Pressure on Submerged Surfaces

Pressure is formally defined as the force per unit area (Campbell, 2025):

Equation 3.3 — Pressure definition:

$$P = \frac{F}{A} \tag{3.3}$$

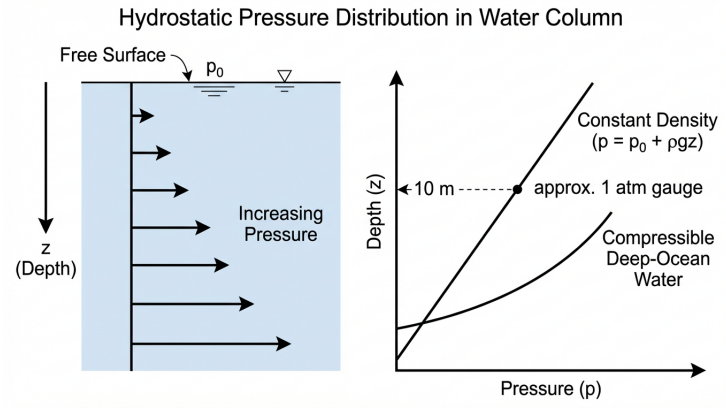

Figure 3.1: Hydrostatic pressure distribution in a water column. The gauge pressure increases linearly with depth in constant-density water ($p = p_0 + \rho g z$) and follows a gently curving profile in compressible deep-ocean water where density increases with depth. At 10 m depth in seawater the gauge pressure is approximately 1 atm.

The SI unit of pressure is the Pascal ($1\ \text{Pa} = 1\ \text{N/m}^2$). For an object submerged in a fluid of constant density ρ, the total pressure at depth d below the free surface is the sum of the atmospheric pressure and the weight of the overlying fluid column (Campbell, 2025):

Equation 3.4 — Pressure at constant-density depth:

$$P_d = P_0 + \rho\, g\, d \tag{3.4}$$

where $P_0 = 1.01 \times 10^5$ Pa is the standard atmospheric pressure.

Equation 3.4 is the constant-density simplification of the more general integral form (Equation 3.1) (Dera, 1992). At moderate depths where density variations are negligible, the linear relation is adequate: at $d = 10$ m in seawater ($\rho \approx 1025\ \text{kg m}^{-3}$), the gauge pressure is approximately 1.005×10^5 Pa ≈ 1 atm.

For a submarine window of area A at depth d, the net inward force is $F_{\text{NET}} = \rho\, g\, d\, A$, since the interior is maintained at atmospheric pressure (Campbell, 2025). At $d = 8000$ m with a circular window of 30 cm diameter, this force reaches 5.7×10^6 N—a value that dictates the minimum thickness of viewport glass and hull plating.

For a vessel's hull, the pressure acts normal to each element of the wetted surface. For the complex curved surfaces of a ship hull, the net vertical component of the hydrostatic pressure distribution integrates exactly to the buoyant force (Equation 3.5), regardless of the hull shape—a consequence that follows directly from the divergence theorem applied to a closed surface (Attwood, 1899; Newman, 1977). All horizontal pressure components cancel by symmetry for the upright vessel.

3.3 Theoretical Framework

3.3.1 Archimedes' Principle and Buoyancy

The fundamental principle of buoyancy states that a body immersed in a fluid experiences an upward force equal to the weight of the fluid displaced (Campbell, 2025; Çengel & Boles, 2019). Introducing the density $\rho = m/V$, the buoyant force on a fully submerged body of volume V is:

Equation 3.5 — Buoyant force (Archimedes' principle):

$$F_B = \rho_w \, V_{\text{disp}} \, g \tag{3.5}$$

where ρ_w is the fluid density and V_{disp} is the displaced volume (Campbell, 2025). For a floating body, $F_B = W$ and therefore only a fraction of the total volume is submerged. The fraction submerged equals the ratio of the object's average density to the fluid density: $V_{\text{disp}}/V_{\text{total}} = \rho_{\text{obj}}/\rho_w$ (Campbell, 2025). A steel vessel floats because its enclosed air spaces reduce the average density well below that of seawater.

For a floating vessel, this means the weight of the vessel equals the weight of the water displaced by the submerged portion of the hull.

Bejan et al. (2020) applied this principle as a constraint in their optimisation analysis: the displaced volume of water $D_x \, D_y \, L$ is fixed because it is dictated by the total weight of the boat. Specifically:

Equation 3.6 — Buoyancy equilibrium:

$$W = \rho_w \, g \cdot D_x \, D_y \, L \tag{3.6}$$

where W is the total weight of the vessel, ρ_w is the water density, g is gravitational acceleration, $D_x \equiv B$ is the beam, $D_y \equiv T$ is the submerged depth (draft), and L is the hull length (Bejan et al., 2020).

This constraint means that the three hull dimensions (D_x, D_y, L) cannot be chosen independently. Fixing the displacement (and hence the displaced volume) means that specifying two of the three dimensions determines the third. The optimisation of hull shape for minimum drag therefore operates under this buoyancy constraint.

3.3.2 Displacement and Draft

The relationship between displacement and draft is fundamental to naval architecture. From the buoyancy equilibrium (Equation 3.6), the submerged depth D_y is:

$$D_y = \frac{W}{\rho_w \, g \cdot D_x \, L}$$

Bejan et al. (2020) showed that for sailing vessels spanning displacements from approximately 500 kg to over $51\,000$ kg, the beam-to-draft ratio D_x/D_y

remains approximately constant at $D_x/D_y \sim 2$. This means that as displacement increases, both beam and draft increase proportionally, maintaining a nearly round submerged cross-section.

The empirical data from 96 sailboat models confirmed this prediction: the ratio D_x/D_y showed no systematic dependence on displacement (Bejan et al., 2020, Figure 5). This scale-independence is a direct consequence of the physics of drag minimisation under the buoyancy constraint. For powered commercial vessels, by contrast, beam-to-draft ratios are typically 2.5–4 and vary with ship type, reflecting different operational requirements and resistance characteristics.

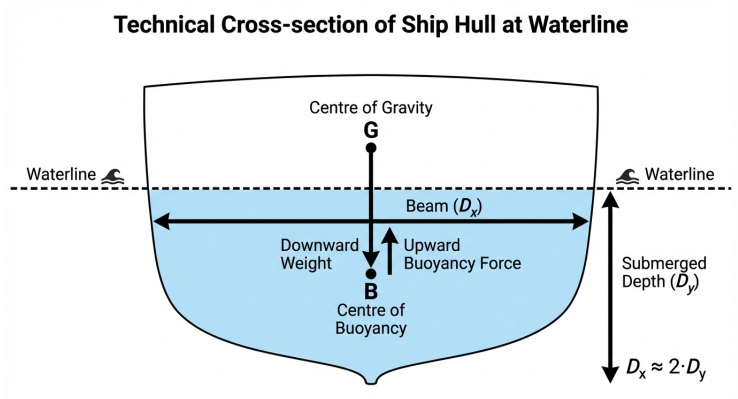

Figure 3.2: Cross-section of a ship hull at the waterline showing the beam D_x and submerged depth D_y ($D_x \approx 2D_y$ for sailing vessels). The centre of gravity G and centre of buoyancy B are marked with their respective weight and buoyancy force vectors.

3.3.3 Centre of Buoyancy and Centre of Gravity

The *centre of buoyancy* B is the centroid of the underwater volume of the hull; the resultant buoyant force acts vertically upward through this point. The vertical and longitudinal positions of B are computed by integrating the sectional areas of the hull using Simpson's rules (Attwood, 1899). For numerical integration of hull offsets at equally spaced stations, *Simpson's first rule* (three-ordinate parabolic approximation) gives the area as (Attwood, 1899; Lewis, 1988):

Equation 3.7 — Simpson's first rule:

$$A = \frac{h}{3}\left(y_1 + 4y_2 + 2y_3 + 4y_4 + \cdots + y_n\right) \tag{3.7}$$

where h is the common spacing between ordinates and $y_1, y_2, \ldots, y_n$ are the ordinate values (requiring an odd number of ordinates). This rule, which assumes a parabola of the second order through each group of three ordinates,

is the standard method for computing waterplane areas, sectional areas, and displacement volumes from the ship's lines drawing (Attwood, 1899).

The vertical position of the centre of buoyancy above the keel is found by taking moments of the waterplane areas about the keel and dividing by the total displacement volume. An approximate rule attributed to Morrish gives the height of the centre of buoyancy above the keel as (Attwood, 1899):

$$KB \approx \frac{1}{3}\left(\frac{5T}{2} - \frac{\nabla}{A_w}\right)$$

where T is the mean draught, ∇ is the displacement volume, and A_w is the waterplane area (Attwood, 1899).

Biran (2003) provides a systematic comparison of analytical approximations for the vertical centre of buoyancy. In addition to the Morrish formula above, the *Normand approximation* expresses the KB position as a function of the block and waterplane area coefficients:

$$\frac{KB}{T} \approx \frac{1}{1 + C_B/C_W}$$

where C_B is the block coefficient and C_W the waterplane area coefficient (Biran, 2003). For wall-sided vessels ($C_W = 1$, $C_B = 1$), this yields $KB/T = 0.5$, recovering the exact result for a rectangular cross-section. For a prismatic hull with V-shaped cross-section ($C_B = 0.5$, $C_W = 1$), the formula gives $KB/T = 2/3$, coinciding with the exact centroid position of the triangular section at $2T/3$ above the keel. For extreme hull forms with very fine waterplanes ($C_W \ll 1$), the approximation loses accuracy and the full numerical integration of hull offsets must be used (Biran, 2003). The practical value of these formulae lies in rapid preliminary estimation of KB before the full numerical integration of the hull offsets is carried out.

The *centre of gravity* G is determined from the weight distribution, using the same centre-of-mass formula (Equation 4.17 in Chapter 4). Both B and G must lie on the same vertical line for the vessel to float upright without heel or trim.

3.3.4 Tonnes per Centimetre Immersion (TPC)

The *tonnes per centimetre immersion* (TPC) quantifies how much the displacement changes for a unit change in mean draught (Attwood, 1899):

Equation 3.8 — Tonnes per centimetre immersion:

$$\text{TPC} = \frac{\rho_w \, A_w}{100} \tag{3.8}$$

where A_w is the waterplane area (in m^2) and ρ_w is the water density in tonnes per cubic metre (1.025 for salt water). Equivalently, in salt water, TPC $\approx A_w/97.56$ (Attwood, 1899). This coefficient is used routinely for

loading and ballasting calculations: adding or removing a cargo weight w (in tonnes) changes the mean draught by approximately w/TPC centimetres, provided the change is small enough that the waterplane area does not change significantly.

3.3.5 Coefficients of Form

The hull form of a vessel is characterised by coefficients that relate the actual hull volume to idealised geometric shapes. Bejan et al. (2020) modelled the hull as a rectangular prism with dimensions $D_x \times D_y \times L$, which corresponds to a block coefficient $C_B = 1$ in the simplified analysis. Real vessels have $C_B < 1$ due to the curvature and taper of the hull form.

The block coefficient is defined as the ratio of the actual displaced volume to the volume of the circumscribing rectangular prism:

$$C_B = \frac{\nabla}{L \times B \times T}$$

where ∇ is the displaced volume, L the length between perpendiculars, B the beam, and T the draught. The Katsoulis empirical formula has been employed to estimate the block coefficient during the pre-design stage (Guedes Soares & Santos, 2015):

$$C_B = k \cdot f \cdot L^{\,a} \cdot B^{\,b} \cdot T^{\,c} \cdot V^{d}$$

where V is the service speed and k, f, a, b, c, d are regression coefficients determined from systematic series data (Guedes Soares & Santos, 2015). For the three bulk carriers analysed (35,364–66,533 DWT), the resulting block coefficients ranged from 0.76 to 0.82, values typical of full hull forms of cargo vessels. The block coefficient directly determines the displaced volume for given principal dimensions and hence, through Archimedes' principle (Equation 3.6), the displacement tonnage of the vessel.

The simplified rectangular model nonetheless captures the essential physics: the displaced volume $D_x\, D_y\, L$ determines the buoyancy, while the frontal area $D_x\, D_y$ and wetted surface $(D_x + 2D_y)L$ determine the drag components. The optimal ratios derived from this simplified model ($D_x/D_y \sim 2$, $L/D_x \gg 1$) are confirmed by data from real hulls with varying C_B values (Bejan et al., 2020).

Additional hull form coefficients further characterise the hull geometry (Attwood, 1899). The *midship section coefficient* C_M is the ratio of the immersed midship section area to the circumscribing rectangle:

$$C_M = \frac{A_M}{B \times T}$$

with typical values ranging from 0.85 (fine forms) to 0.99 (full forms) (Attwood, 1899). The *prismatic coefficient* C_P (also called the longitudinal coefficient)

relates the displacement volume to the product of the midship section area and the waterline length:

$$C_P = \frac{\nabla}{A_M \times L}$$

Since $C_B = C_M \times C_P$, the block coefficient can be decomposed into contributions from the fullness of the midship section and the longitudinal distribution of volume. Representative values from early naval architecture: fast steam yachts have $C_B \approx 0.35$–0.45, while full cargo steamers reach $C_B \approx 0.65$–0.80 (Attwood, 1899).

The *waterplane area coefficient* C_W measures the fullness of the waterplane:

$$C_W = \frac{A_W}{L \times B}$$

where A_W is the waterplane area, L the waterline length, and B the beam (Ridley & Patterson, 2014). Typical values range from 0.67 for fine-lined vessels to 0.92 for full-form bulk carriers. The waterplane area coefficient directly governs the tonnes per centimetre immersion (Equation 3.8) and the transverse metacentric radius $BM = I_T/\nabla$, since for most vessel forms the second moment of area of the waterplane I_T increases with C_W (Ridley & Patterson, 2014). The coefficient C_W therefore governs both loading calculations and initial stability assessment.

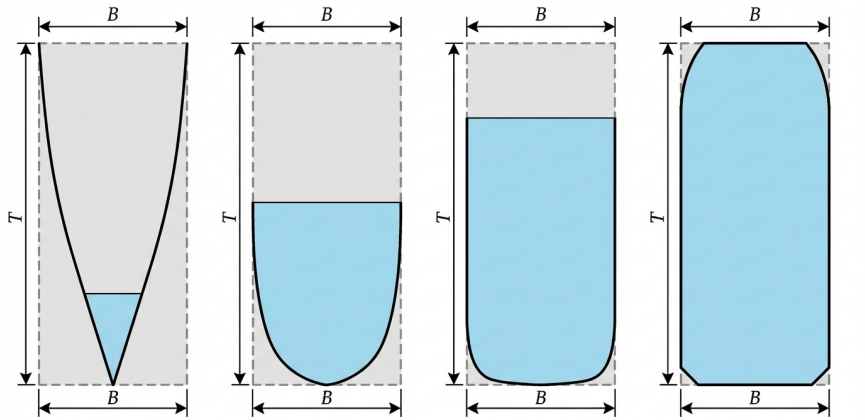

Figure 3.3: Midship cross-sections for four vessel types overlaid on their circumscribing rectangles ($B \times T$): (a) fine-form yacht ($C_B \approx 0.40$), (b) container ship ($C_B \approx 0.60$), (c) general cargo vessel ($C_B \approx 0.72$), and (d) bulk carrier ($C_B \approx 0.82$). The shaded area represents the actual immersed section.

3.4 Applications in Maritime Systems

3.4.1 Fresh Water Allowance and Dock Water

When a vessel moves from salt water ($\rho_{sw} = 1.025\,\mathrm{t/m^3}$) to fresh water ($\rho_{fw} = 1.000\,\mathrm{t/m^3}$), the hull must displace a larger volume to support the same weight, causing the vessel to sink deeper. The *fresh water allowance* (FWA)—the additional sinkage in centimetres—is (Attwood, 1899):

Equation 3.9 — Fresh water allowance:

$$\mathrm{FWA} = \frac{W}{\mathrm{TPC}_{sw}} \times \frac{\rho_{sw} - \rho_{fw}}{\rho_{fw}} \approx \frac{W}{\mathrm{TPC}_{sw}} \times 0.025 \tag{3.9}$$

where W is the displacement in tonnes and TPC_{sw} is the tonnes per centimetre in salt water (Attwood, 1899). The result is in centimetres; the equivalent form $\mathrm{FWA}_{\mathrm{mm}} = W/(4 \times \mathrm{TPC}_{sw})$ is sometimes encountered and gives the sinkage directly in millimetres. For intermediate dock water densities, the allowance is proportioned linearly between zero (at salt water density) and the full FWA (at fresh water density). This correction is essential for safe loading: a vessel loaded to her summer mark in a river port must have sufficient freeboard to prevent overloading when she reaches the open sea.

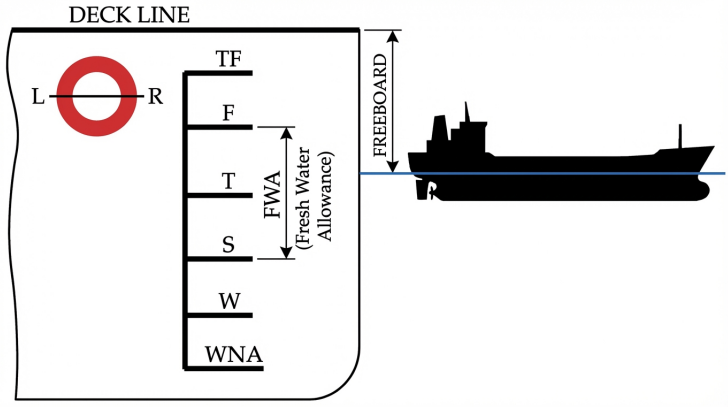

Figure 3.4: International load line marks (Plimsoll mark) on a ship's hull amidships. The vertical series of draught marks—TF (tropical fresh), F (fresh water), T (tropical), S (summer), W (winter), WNA (winter North Atlantic)—is referenced to the deck line. The fresh water allowance (FWA) is the vertical distance between the S and F marks.

Worked Example. A general-cargo vessel has the following particulars at her summer load draught: waterplane area $A_w = 3120\,\mathrm{m^2}$, displacement $W = 14\,500\,\mathrm{t}$. Compute (a) the TPC in salt water at $\rho_{sw} = 1.025\,\mathrm{t/m^3}$, (b) the sinkage when an additional $120\,\mathrm{t}$ of cargo is loaded, and (c) the fresh-water allowance.

1. TPC $= \rho_{sw}\, A_w/100 = 1.025 \times 3120/100 = 31.98\,\text{t/cm}$.
2. Sinkage $= 120/31.98 = 3.75\,\text{cm}$.
3. FWA $= (W/\text{TPC}_{sw}) \times 0.025 = (14\,500/31.98) \times 0.025 = 11.33\,\text{cm}$.

The vessel therefore sinks approximately $11.3\,\text{cm}$ deeper when transiting from salt water to fresh water—nearly an order of magnitude larger than the sinkage caused by 120 tonnes of additional cargo.

3.4.2 Numerical Integration of Hull Forms

The practical computation of displacement, centre of buoyancy, and waterplane properties from the hull lines drawing relies on systematic numerical integration. The standard working method is the displacement sheet—a tabular calculation using Simpson's first rule (Equation 3.7) (Attwood, 1899). The procedure involves:

1. Tabulating half-breadths at each waterline and station from the body plan.
2. Applying Simpson's multipliers vertically (across waterlines) to obtain each station's immersed cross-sectional area.
3. Applying Simpson's multipliers horizontally (along the length) to obtain the total displacement volume.

Simpson's second rule (the three-eighths rule) applies when the number of intervals is a multiple of three (Attwood, 1899):

$$A = \frac{3h}{8}\left(y_1 + 3y_2 + 3y_3 + 2y_4 + 3y_5 + 3y_6 + \cdots + y_n\right)$$

and the *five-eight rule* for estimating the area of an end strip when only three ordinates are available:

$$A_{\text{strip}} = \frac{h}{12}\left(5y_1 + 8y_2 - y_3\right)$$

These rules enable the naval architect to compute all hydrostatic properties—displacement, TPC, centre of buoyancy, second moments of area—directly from the measured hull offsets (Attwood, 1899).

A complementary representation of the hull geometry is the *Bonjean curve*, which plots the immersed cross-sectional area of each station as a function of draught. The construction and use of Bonjean curves is described in the USNA EN400 course notes (United States Naval Academy, 2021): for each of the ship's stations, the half-breadths are integrated vertically (using Simpson's rule) from the keel to each waterline, producing a curve of sectional area versus draught. The complete set of Bonjean curves allows the

displacement and longitudinal centre of buoyancy to be computed for *any* waterline—including trimmed and non-level waterlines—by reading off each station's sectional area at the local draught and integrating longitudinally. This capability is essential for trim calculations and for the evaluation of longitudinal stability at arbitrary loading conditions.

3.4.3 Bilging and the Lost Buoyancy Method

When a compartment is breached and open to the sea (*bilged*), it loses its capacity to provide buoyancy. The standard approach is the *lost buoyancy method*: the flooded compartment is treated as if it were no longer part of the hull, and the vessel must sink to a deeper draught until the remaining intact waterplane area provides sufficient buoyancy to support the unchanged displacement (Attwood, 1899).

For a box-shaped vessel of length L, beam B, and original draught T with a central compartment of length l bilged, the new draught T' is found from (Attwood, 1899):

$$T' = \frac{L \times B \times T}{(L - l) \times B} = \frac{L \times T}{L - l}$$

If the flooded compartment contains watertight structure occupying a fraction μ of its volume (the *permeability*), then only the fraction $(1 - \mu)$ is lost to flooding, and the sinkage is correspondingly reduced (Attwood, 1899). The lost buoyancy method also reveals the change in the position of the centre of buoyancy, which determines the residual stability of the damaged vessel (see Chapter 4, Section 4.4.1). The probabilistic damage stability framework that builds upon this deterministic method is discussed in the *Maritime Safety and Risk Physics* chapter of the companion volume.

3.5 Discussion

The buoyancy constraint $D_x\, D_y\, L = \text{const}$ plays a dual role in vessel design: it ensures floatation, and it constrains the optimisation of hull shape for minimum drag. Bejan et al. (2020) showed that this single constraint, combined with the physics of form drag and skin friction, is sufficient to predict the three fundamental aspect ratios of sailing vessels. This result demonstrates that buoyancy physics alone, as the starting point of ship design, already constrains the major hull proportions.

The vertical stability of the water column surrounding a vessel also depends on buoyancy physics. When a fluid parcel is displaced vertically in a density-stratified ocean, the restoring force produces oscillations at the Brunt–Väisälä frequency (see the *Physical Oceanography* chapter of the companion volume): $N^2 = -(g/\rho)\,\mathrm{d}\rho/\mathrm{d}z$ (Dera, 1992). When $N^2 > 0$, the stratification is stable and vertical mixing is suppressed; this has practical

implications for the dispersion of pollutants and the behaviour of underwater plumes from ship discharges.

The density of seawater itself varies with location and season (Chapter 7), and this variation directly affects the draft of a ship. The fresh water allowance and dock water allowance are operational corrections derived from the buoyancy equation (Equation 3.6) with density values computed from the UNESCO equation of state (Dera, 1992).

The form coefficients have direct practical significance for marine engineering (Ridley & Patterson, 2014): the block coefficient C_B determines the vessel's deadweight capacity for given principal dimensions, the prismatic coefficient C_P governs the longitudinal distribution of displacement volume and hence the wave-making resistance (Chapter 5), and the waterplane area coefficient C_W controls the waterplane inertia that governs both TPC and the initial metacentric radius BM.

The analytical approximations for KB—including the Morrish and Normand formulae—provide rapid preliminary estimates that are accurate to within a few percent for conventional hull forms (Biran, 2003). The Bonjean curve method (United States Naval Academy, 2021) extends the numerical integration framework to arbitrary waterlines, enabling trim and longitudinal stability calculations that the standard displacement sheet (which assumes a level waterline) cannot directly address.

3.6 Conclusion

Fluid statics is the starting point for every other branch of naval architecture. The hydrostatic pressure distribution (Equation 3.1) and Archimedes' principle (Equation 3.5) together determine the buoyant force on any floating body, while the buoyancy equilibrium relation $W = \rho_w \, g \, B \, T \, L$ (Equation 3.6) constrains the three principal hull dimensions for a given displacement. The present chapter has shown that these elementary relations, combined with Simpson's numerical integration rules and the hull form coefficients C_B, C_M, C_P, and C_W, suffice to compute displacement, draft, centre of buoyancy, and tonnes per centimetre immersion for any conventional hull form.

Two results deserve emphasis. First, the buoyancy constraint is not merely a floatation condition: it determines which combinations of beam, draft, and length are physically accessible and therefore sets the stage for the drag-minimisation problem treated in Chapter 5. Second, the operational corrections that arise from density variation—fresh water allowance, dock water allowance, and seasonal draft changes—are direct quantitative consequences of the same constraint applied with the UNESCO equation of state.

Several questions remain open for subsequent chapters. The vertical position of the centre of buoyancy relative to the centre of gravity determines whether a vessel is initially stable, a topic developed in detail in Chapter 4. Damage stability—the residual buoyancy and righting moment after com-

partment flooding—extends the lost buoyancy method introduced here into the probabilistic framework presented in the *Maritime Safety and Risk Physics* chapter of the companion volume. Finally, the Bonjean-curve technique introduced for static conditions provides the starting point for evaluating hull girder loads in waves (see the *Structural Mechanics of Ships* chapter of the companion volume), where the instantaneous waterline varies along the ship's length.

References

Attwood, E. L. (1899). *A text-book of theoretical naval architecture*. Longmans, Green; Co.

Bejan, A., Ferber, L., & Lorente, S. (2020). Convergent evolution of boats with sails. *Scientific Reports*, *10*, Article 2703. https://doi.org/10.1038/s41598-020-58940-5

Biran, A. B. (2003). *Ship hydrostatics and stability*. Butterworth-Heinemann.

Campbell, C. (2025). *Physics: A focused introduction*. CRC Press. https://doi.org/10.1201/9781003571568

Çengel, Y. A., & Boles, M. A. (2019). *Thermodynamics: An engineering approach* (9th ed.). McGraw-Hill Education.

Dera, J. (1992). *Marine physics* (P. Senn, Trans.) [Translated from Polish. Original: *Fizyka morza*, 1983]. Elsevier.

Fischer-Cripps, A. C. (2014). *The physics companion* (2nd ed.). CRC Press. https://doi.org/10.1201/b17356

Guedes Soares, C., & Santos, T. A. (Eds.). (2015). *Maritime technology and engineering: Proceedings of MARTECH 2014*. CRC Press.

Hewitt, P. G., Suchocki, J. A., & Hewitt, L. A. (2012). *Conceptual physical science* (5th ed.). Pearson.

Lewis, E. V. (Ed.). (1988). *Principles of naval architecture* (2nd ed.) [Three volumes]. The Society of Naval Architects; Marine Engineers.

Newman, J. N. (1977). *Marine hydrodynamics*. The MIT Press.

Ridley, J. D., & Patterson, C. J. (2014). *Ship stability, powering and resistance* (Vol. 13). Adlard Coles Nautical.

Tupper, E. C. (2013). *Introduction to naval architecture* (5th ed.). Butterworth-Heinemann.

United States Naval Academy. (2021). En400: Principles of ship performance [Course notes, Fall AY2021].

Chapter 4

Ship Stability and Hydrostatics

4.1 Introduction

Stability is arguably the most critical safety characteristic of any floating vessel. A vessel that cannot right itself when disturbed by external forces—waves, wind, cargo shift—will capsize. The physics of stability is therefore the physics of survival at sea.

The importance of hull geometry for stability manifests as a striking empirical regularity. Bejan et al. (2020) analysed 96 sailboat models and found that the ratio of maximum beam to draft is approximately:

Equation 4.1 — Beam-to-draft ratio:

$$\frac{D_x}{D_y} \approx 2 \tag{4.1}$$

where $D_x \equiv B$ (beam) is the maximum waterline beam and $D_y \equiv T$ (draft) is the mean draft. This ratio holds across four orders of magnitude in boat mass—from small dinghies to large ocean-going yachts—suggesting that it is not an arbitrary design choice but a consequence of physical optimisation.

From a stability perspective, the beam-to-draft ratio is significant because it determines the waterplane area moment of inertia relative to the displaced volume. A wider beam (larger D_x) increases the metacentric radius BM and hence the transverse metacentric height GM, improving initial stability. A deeper draft (larger D_y) lowers the centre of buoyancy and increases form stability. The near-constant ratio $D_x/D_y \approx 2$ thus represents a balance between these competing stability factors (Bejan et al., 2020).

4.2 Scientific Background

4.2.1 Equilibrium Conditions for Floating Bodies

A floating body is in stable equilibrium when a small angular displacement generates a restoring moment that returns the body to its upright position.

From an evolutionary optimisation perspective, among all possible hull cross-sections, natural selection in design converges on the proportions that best satisfy the equilibrium requirements (Bejan et al., 2020).

The beam-to-draft ratio $D_x/D_y \approx 2$ is scale-independent (Bejan et al., 2020). This geometric similarity means that the hydrostatic stability characteristics of the hull cross-section are preserved regardless of vessel size.

The physics of stability is fundamentally the physics of rotational equilibrium. The *torque*—the rotational analogue of force—is defined as the product of the applied force and the perpendicular distance (lever arm) from the axis of rotation (Campbell, 2025):

Equation 4.2 — Torque:

$$\tau = r\, F\, \sin\theta \tag{4.2}$$

where r is the distance from the rotation axis to the point of force application, F is the force magnitude, and θ is the angle between the force vector and the lever arm (Campbell, 2025). The corresponding equation of motion for rotation is Newton's second law in angular form: $\tau_{\text{NET}} = I\alpha$, where I is the moment of inertia and α is the angular acceleration (Campbell, 2025).

For a floating vessel, a small heel angle θ displaces the centre of buoyancy B laterally, creating a restoring torque about the centre of gravity G. Rotational equilibrium ($\tau_{\text{NET}} = 0, \alpha = 0$) requires that no net moment acts on the vessel—the condition of the upright position. Stability demands that any departure from this equilibrium produces a restoring (opposite-sign) torque that drives the vessel back.

Attwood (1899) provides the classical derivation of the metacentric height. When a vessel inclines through a small angle θ from the upright, the underwater volume remains constant but its shape changes: an "emerged wedge" on the rising side is replaced by an "immersed wedge" on the descending side. The centre of buoyancy shifts laterally from B to B', and the vertical through B' intersects the centreline at a point M—the *transverse metacentre*. The three conditions of equilibrium are (Attwood, 1899):

1. If G is below M, the vessel is in *stable* equilibrium (the buoyancy couple restores the upright).

2. If G is above M, the vessel is in *unstable* equilibrium (the couple drives the vessel farther from the upright).

3. If G coincides with M, the vessel is in *neutral* equilibrium (no restoring couple exists).

The distance BM is obtained by considering the moment of transference of the wedges. For a small heel angle θ, the half-breadth of the waterplane at any section is y, and the moment of the elemental wedge transfer is $\frac{2}{3}y^3\,\theta\,dx$. Integrating over the vessel length and dividing by the displaced volume ∇ gives (Attwood, 1899):

Equation 4.3 — Transverse metacentric radius:

$$BM = \frac{I_T}{\nabla} \tag{4.3}$$

where $I_T = \frac{2}{3}\int y^3\,dx$ is the second moment of area (moment of inertia) of the waterplane about its longitudinal centreline, and ∇ is the volume of displacement (Attwood, 1899). This fundamental result links hull geometry directly to initial stability: a wider waterplane (larger I_T) or a smaller displacement volume raises BM and hence increases the metacentric height.

4.2.2 Metacentre and Metacentric Height (GM)

The *metacentric height* GM is the vertical distance from the centre of gravity G to the transverse metacentre M. It is computed from three measurable quantities (Attwood, 1899):

Equation 4.4 — Metacentric height:

$$GM = KB + BM - KG \tag{4.4}$$

where K is the keel (baseline), KB is the vertical distance from the keel to the centre of buoyancy, and KG is the vertical distance from the keel to the centre of gravity (Figure 4.1). Since $BM = I_T/\nabla$ (Equation 4.3), the metacentric height is fully determined by the hull geometry and the vertical weight distribution; for a concise treatment of equilibrium and centre-of-mass concepts, see (Fischer-Cripps, 2014).

The metacentric height is positive when M is above G (stable equilibrium) and negative when M is below G (unstable equilibrium). For conventional merchant vessels, typical values of GM range from approximately $0.15\,\text{m}$ (large passenger vessels, for comfort) to $2.0\,\text{m}$ or more (heavily loaded cargo vessels). Sailing vessels typically have GM values of $0.6\,\text{m}$ to $1.2\,\text{m}$ (Attwood, 1899; Tupper, 2013).

4.2.3 Righting Lever (GZ) and Righting Moment

When a vessel heels through a small angle θ, the arm of the restoring couple is the perpendicular distance GZ from the centre of gravity to the vertical through the displaced centre of buoyancy. For small angles—up to approximately 10–15° (Attwood, 1899)—where the metacentre remains effectively stationary:

Equation 4.5 — Small-angle righting lever:

$$GZ = GM \sin\theta \tag{4.5}$$

The *moment of statical stability*—the restoring couple acting on the vessel—is therefore (Attwood, 1899):

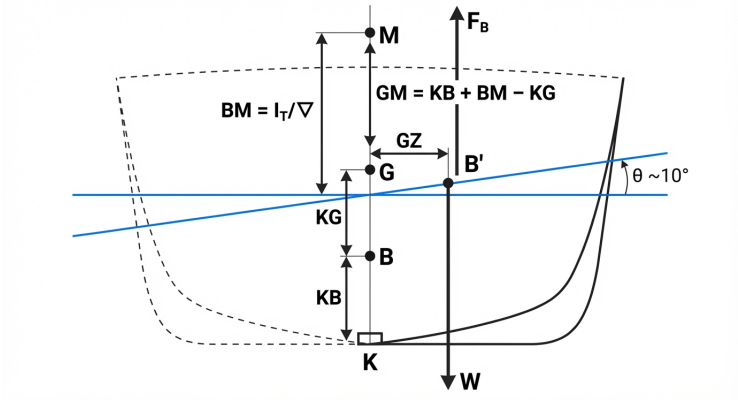

Figure 4.1: Midship cross-section of a vessel heeled through a small angle θ. The keel K, centre of buoyancy B, centre of gravity G, and transverse metacentre M are marked along the vessel centreline. The distances KB, $BM = I_T/\nabla$, KG, and the metacentric height $GM = KB + BM - KG$ are indicated. When M lies above G ($GM > 0$), the buoyancy force B' and weight W form a restoring couple; when M lies below G ($GM < 0$), the couple is capsizing.

Equation 4.6 — Righting moment (small angle):

$$M_{\text{right}} = W \times GM \sin\theta \tag{4.6}$$

where W is the displacement weight. This is termed the *metacentric method* and is the foundation of initial stability calculations. The righting moment is directly proportional to GM: a vessel with a larger metacentric height produces a stronger restoring couple for any given heel angle (Attwood, 1899).

4.3 Theoretical Framework

4.3.1 Initial Stability (Small-Angle)

Initial stability describes the vessel's response to small angular disturbances from the upright equilibrium. The restoring capacity is quantified by the righting moment, which must exceed the heeling moment imposed by external forces for the vessel to remain stable.

Huchet (2021) presented this equilibrium condition in the context of a foiling catamaran (NACRA 17), where the heeling moment arises from the aerodynamic side force on the sails and the righting moment is provided by a combination of hull buoyancy distribution and crew weight placement. The static transverse equilibrium requires:

Equation 4.7 — Heeling moment equilibrium:

$$RM \geq HM \tag{4.7}$$

where RM is the righting moment and HM is the heeling moment (Huchet, 2021). The righting moment has two principal contributions:

1. **Hydrostatic righting moment:** The transverse separation of the centres of buoyancy of the two demihulls generates a restoring couple when the vessel heels. For a catamaran, this component is large because the hulls are widely spaced.

2. **Crew righting moment:** The crew positions themselves on the windward side—on a trapeze in the case of the NACRA 17—to create an additional righting moment through the gravitational force acting at a lateral distance from the centreline.

The crew righting moment is:
Equation 4.8 — Crew righting moment:

$$RM_{\text{crew}} = m_{\text{crew}} \cdot g \cdot d_{\text{crew}} \tag{4.8}$$

where m_{crew} is the crew mass, g is gravitational acceleration, and d_{crew} is the lateral distance of the crew's centre of gravity from the vessel centreline (Huchet, 2021). On the NACRA 17, the crew uses a trapeze system to maximise d_{crew}, extending their body outboard of the hull to increase the moment arm.

The heeling moment is generated by the aerodynamic side force on the sails acting at a height above the water:
Equation 4.9 — Heeling moment from sail force:

$$HM = F_y \cdot h_{CE} \tag{4.9}$$

where F_y is the total aerodynamic side force (see Chapter 8, Equation 8.19) and h_{CE} is the height of the centre of effort of the sail plan above the waterline (Huchet, 2021).

When HM exceeds RM, the vessel heels progressively and may capsize. For the NACRA 17, Huchet (2021) showed that different crew weight combinations (e.g., $130\,\text{kg}$ vs $150\,\text{kg}$ total crew mass) significantly affect the available righting moment and hence the range of wind conditions in which the boat can sail without excessive heel. Heavier crews produce a larger RM_{crew}, permitting sailing in stronger winds before the stability limit is reached.

The metacentric method (Equation 4.6) provides the quantitative link between the Huchet equilibrium condition ($RM \geq HM$) and hull geometry. For a conventional displacement vessel (as opposed to the foiling catamaran), the hydrostatic righting moment at small angles is $W \times GM \sin\theta$ (Attwood, 1899). Since $GM = KB + BM - KG$ (Equation 4.4) and $BM = I_T/\nabla$ (Equation 4.3), a designer can increase initial stability by widening the beam (which raises I_T) or by lowering the centre of gravity (which reduces KG).

This is demonstrated with a simple example (Attwood, 1899): a box-shaped lighter $36.6\,\text{m}$ long, $9.1\,\text{m}$ in beam, floating at $3.05\,\text{m}$ draught has $I_T = \frac{1}{12} \times 36.6 \times 9.1^3 = 2299\,\text{m}^4$ and $\nabla = 36.6 \times 9.1 \times 3.05 = 1015\,\text{m}^3$,

giving $BM = 2299/1015 = 2.27\,\text{m}$. A trapezoidal cross-section of the same waterplane breadth but narrower base has a smaller displacement volume, producing a larger BM and hence a higher metacentre position—illustrating how cross-sectional shape directly governs stability.

4.3.2 Large-Angle Stability and GZ Curves

Beyond approximately 10–15° of heel, the metacentre is no longer stationary and the small-angle approximation $GZ = GM\sin\theta$ breaks down. The general expression for the righting lever at any angle of heel θ is derived using the moment of transference of the immersed and emerged wedges (Attwood, 1899):

Equation 4.10 — Atwood's formula for righting lever:

$$GZ = \frac{v \times hh'}{\nabla} - BG\sin\theta \tag{4.10}$$

where v is the volume of either wedge, hh' is the horizontal distance between the centres of gravity of the emerged and immersed wedges (measured parallel to the inclined waterline), ∇ is the total displacement volume, and BG is the vertical distance between the centre of buoyancy and the centre of gravity in the upright condition (Attwood, 1899). This result—known historically as *Atwood's formula*—requires no assumption of small angles and is the basis of all large-angle stability calculations.

The *curve of statical stability* (or *GZ curve*) is constructed by computing GZ from Equation 4.10 at a series of heel angles (Figure 4.2). Attwood (1899) illustrates this with the case of HMS *Captain*, for which the calculated righting lever reached a maximum of approximately $0.27\,\text{m}$ at 21° and vanished at 54°—an alarmingly small range of positive stability. In comparison, HMS *Monarch*, a contemporary vessel, had a maximum GZ of $0.97\,\text{m}$ at 40° with a vanishing angle of 70° (Attwood, 1899).

The key features of the GZ curve are:

- **Initial slope:** Equals GM (in radians), confirming that the metacentric height governs the initial stiffness.
- **Maximum GZ:** The largest righting lever the vessel can develop; occurs typically between 30° and 70°.
- **Range of positive stability:** The angle at which GZ returns to zero. Beyond this angle, the restoring couple vanishes and the vessel will capsize if heeled further.
- **Area under the curve:** Proportional to the dynamical stability (Section 4.3.3).

For vessels with vertical (or nearly vertical) sides in the neighbourhood of the waterplane—the *wall-sided* condition—an intermediate formula bridges

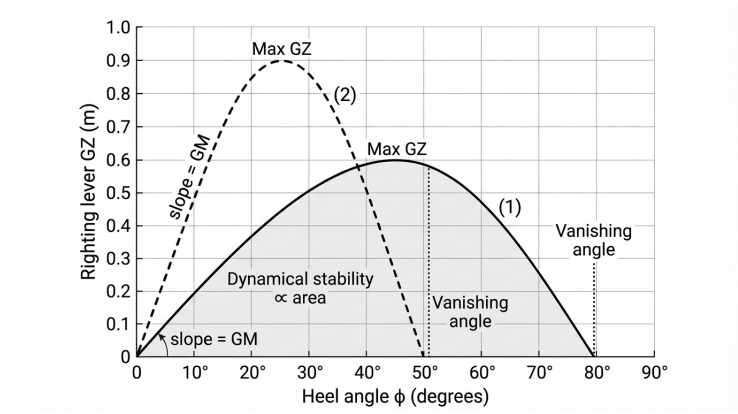

Figure 4.2: Curve of statical stability (GZ curve) for two vessels with different stability characteristics. The initial slope equals GM, the peak locates the maximum righting lever, and the vanishing angle marks the limit of positive stability. The shaded area under each curve is proportional to the dynamical stability (Equation 4.14). A vessel with moderate peak GZ but wide range (solid line) may be safer than one with a high peak but narrow range (dashed line).

the gap between the small-angle metacentric method and the fully general Atwood calculation. Rawson and Tupper (2001) present the *wall-sided formula* (also known as Scribanti's formula), which accounts for the vertical shift of the centre of buoyancy that becomes significant at moderate heel angles:

Equation 4.11 — Wall-sided formula (Scribanti):

$$GZ = \sin\varphi \left[GM + \tfrac{1}{2}\, BM \, \tan^2\varphi \right] \tag{4.11}$$

where φ is the heel angle (denoted θ in Sections 4.2.1–4.2.3; the symbol φ follows the convention of Rawson and Tupper (2001)), GM is the metacentric height, and BM is the metacentric radius (Rawson & Tupper, 2001). Lee (2019) derives this result by decomposing the shift of the centre of buoyancy into horizontal and vertical components: the horizontal shift $\nabla \cdot X = I_T \tan\varphi$ and the vertical shift $\nabla \cdot Y = \tfrac{1}{2} I_T \tan^2\varphi$. The additional $\tfrac{1}{2} BM \tan^2\varphi$ term captures the vertical rise of B that the small-angle approximation neglects (Lee, 2019).

When free surfaces are present, the wall-sided formula incorporates the free surface correction directly (Lewis, 1988; Rawson & Tupper, 2001):

$$GZ_F = \sin\varphi \left[\left(GM - \frac{\rho_\ell \, i_t}{\nabla_s} \right) + \frac{1}{2} \left(BM - \frac{\rho_\ell \, i_t}{\nabla_s} \right) \tan^2\varphi \right]$$

where ρ_ℓ is the liquid density, i_t is the second moment of area of the free surface, and ∇_s is the displacement volume (Rawson & Tupper, 2001).

An important consequence of the wall-sided formula arises when GM is negative. Setting $GZ = 0$ in Equation 4.11 (excluding the trivial solution $\varphi =$

0) yields the *angle of loll*—the equilibrium heel angle at which the vessel settles when initially unstable (Rawson & Tupper, 2001):

Equation 4.12 — Angle of loll:

$$\tan^2 \varphi_{\text{loll}} = \frac{-2\,GM}{BM} \tag{4.12}$$

This result is valid only when $GM < 0$ (since $BM > 0$ always). At the angle of loll, the vessel reaches a new stable equilibrium where the positive curvature of the $\frac{1}{2}\,BM\,\tan^2\varphi$ term compensates for the negative GM. The vessel will loll to either port or starboard with equal probability, and any attempt to correct the loll by loading weight on the high side will worsen the condition—the correct response is to lower the centre of gravity (Rawson & Tupper, 2001).

Ridley and Patterson (2014) emphasise that the practical response to a vessel at her angle of loll is to fill double-bottom tanks (lowering KG), never to add weight on the high side or to transfer cargo—actions that would increase KG and worsen the instability. For box-shaped vessels, the metacentric height can be rapidly estimated from principal dimensions as $GM_0 \approx B^2/(12T) - KG + T/2$, where B is beam and T is draught (Ridley & Patterson, 2014). This approximation, derived from the exact expression for the second moment of area of a rectangular waterplane ($I_T = LB^3/12$), enables immediate assessment of whether a loading condition is likely to produce negative GM and hence a loll condition.

For practical stability assessment across all loading conditions, the *cross curves of stability* (or KN curves) provide a geometry-only representation of the hull's righting capacity. Lee (2019) defines the lever KN such that:

Equation 4.13 — Cross curves of stability:

$$GZ = KN - KG\sin\varphi \tag{4.13}$$

where KN depends only on hull form and displacement, while $KG\sin\varphi$ depends on the loading condition (Lee, 2019). Cross curves plot KN against displacement for fixed heel angles (typically 10°, 20°, 30°, 40°, 60°, and 75°), allowing rapid determination of the complete GZ curve for any loading condition once the hull geometry is known. Lee (2019) describes cross curves as "the most important single set of hydrostatic data for stability assessment," since they separate the hull geometry contribution from the weight distribution, enabling the naval architect to evaluate stability for any combination of cargo, fuel, and ballast.

4.3.3 Dynamic Stability

Dynamical stability is the work done in heeling a vessel from the upright to a given angle θ. Since the righting moment at any intermediate angle ϕ is $W \times GZ(\phi)$, the total work is the integral of this moment over the angular displacement (Attwood, 1899):

Equation 4.14 — Dynamical stability:

$$E_{\text{dyn}} = W \int_0^{\theta} GZ(\phi)\, d\phi \tag{4.14}$$

Graphically, the dynamical stability at any angle equals the displacement multiplied by the area under the GZ curve up to that angle. A heeling agent (such as wind or a wave) must supply energy at least equal to E_{dyn} at the angle of vanishing stability in order to capsize the vessel (Attwood, 1899). This energy criterion is more physically meaningful than the static GZ value alone, because a vessel with a moderate maximum GZ but a wide range of positive stability may be safer than one with a large peak GZ over a narrow range.

The natural roll period of a vessel is directly related to its metacentric height (Lee, 2019):

Equation 4.15 — Roll natural period:

$$T_n = \frac{2\pi\, k}{\sqrt{g\, GM}} \tag{4.15}$$

where k is the radius of gyration about the longitudinal (roll) axis, g is gravitational acceleration, and GM is the metacentric height (Lee, 2019). This result follows from treating the vessel as a conservative system with the GZ curve providing the restoring force: for small oscillations, the restoring moment is $\Delta \cdot g \cdot GM \cdot \varphi$ and the rotational inertia is $\Delta \cdot k^2$, giving a simple harmonic oscillator with period T_n. A vessel with a large GM ("stiff" vessel) rolls quickly with a short period, while a vessel with a small GM ("tender" vessel) rolls slowly with a long period (Lee, 2019). Typical roll periods range from 8 s to 15 s for merchant vessels and 15 s to 25 s for large passenger ships.

The IMO *weather criterion* combines the concepts of dynamical stability and roll period into a practical safety standard. Lee (2019) presents the criterion as an energy balance: the vessel, initially heeled to a steady wind angle φ_0, is subjected to a gust that rolls it to windward by an angle φ_1; as it rolls back through the wind-heel angle, it must not exceed the angle φ_2 (limited by the vanishing angle or 50°, or the angle of downflooding). The criterion requires that the righting energy (area A_1 under the GZ curve from φ_1 to φ_2) must exceed the heeling energy (area A_2 under the wind heeling lever curve over the same range) (Lee, 2019):

$$A_1 \geq A_2$$

This energy-area comparison captures both the magnitude and the range of the righting lever, providing a more comprehensive stability assessment than any single-point criterion based on GM or maximum GZ alone (Lee, 2019).

4.3.4 Free Surface Effect

When a tank aboard a vessel is partially filled with liquid, the liquid's free surface shifts as the vessel heels, causing the liquid's centre of gravity to move

laterally. This produces the same effect as raising the vessel's centre of gravity and constitutes a reduction in metacentric height (Figure 4.3). Attwood (1899) derives this *free surface correction* by treating the liquid surface as a miniature waterplane: when the vessel heels through a small angle θ, the liquid transfers from one side of the tank to the other in the same wedge geometry as the external waterplane problem.

By direct analogy with the derivation of BM (Equation 4.3), the virtual rise of the vessel's centre of gravity due to a free surface is (Attwood, 1899):

Equation 4.16 — Free surface correction:

$$GG_1 = \frac{i}{\nabla} \tag{4.16}$$

where i is the second moment of area of the liquid free surface about its own longitudinal centreline, and ∇ is the total volume of displacement. The effective metacentric height is therefore reduced to:

$$GM_{\text{eff}} = GM - \frac{i}{\nabla}$$

A crucial feature of this result is that the *quantity* of liquid in the tank does not affect the correction—only the *geometry* of the free surface matters. A small amount of liquid with a large free surface area reduces stability more than a large amount with a smaller free surface (Attwood, 1899). If the liquid has a specific gravity ρ_ℓ different from the surrounding water (ρ_w), the correction becomes (Attwood, 1899):

$$GG_1 = \frac{\rho_\ell}{\rho_w} \cdot \frac{i}{\nabla}$$

This result provides the physical justification for standard shipboard practices: keeping slack tanks to a minimum, pressing up or emptying tanks rather than leaving them partially filled, and subdividing wide tanks with longitudinal baffles (which reduces i dramatically, since the second moment of area scales as the cube of tank breadth).

A detailed derivation of this cubic dependence follows (Biran, 2003). For a rectangular tank of breadth b and length l, the second moment of area of the free surface about its centreline is $i = l\,b^3/12$. If a longitudinal centre-line bulkhead divides the tank into two equal halves, each half has breadth $b/2$ and moment of inertia $l(b/2)^3/12 = l\,b^3/96$; the total for both halves is $l\,b^3/48$—only one quarter of the undivided value (Biran, 2003). This dramatic reduction explains why IMO regulations require longitudinal subdivision of large ballast and cargo tanks: a single centre-line bulkhead reduces the free surface correction by 75%, and two longitudinal bulkheads reduce it by approximately 89%. Biran (2003) further shows that the free surface effect is independent of the vertical position of the tank and of the quantity of liquid, reinforcing the counterintuitive result first noted by Attwood (1899).

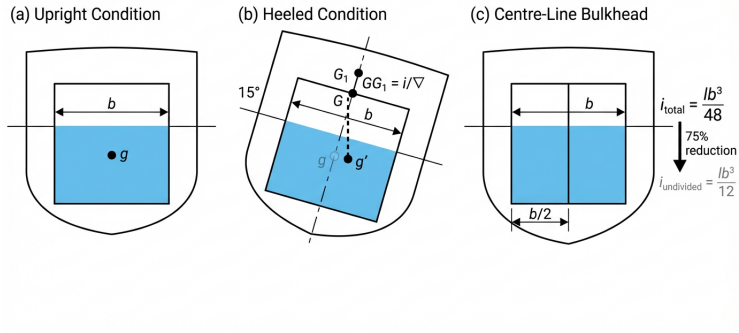

Figure 4.3: Free surface effect in a partially filled tank. (a) Upright condition: the liquid surface is level and the tank's centre of gravity is at g. (b) Heeled condition: the liquid transfers to the low side, shifting the tank's centre of gravity to g' and producing a virtual rise $GG_1 = i/\nabla$ in the vessel's effective centre of gravity. (c) Longitudinal centreline bulkhead: each half-tank has breadth $b/2$, reducing the total free surface moment from $lb^3/12$ to $lb^3/48$—a 75% reduction.

4.3.5 Effect of Suspended Weights and Shifting Cargo

When cargo shifts laterally aboard a vessel, the centre of gravity moves, altering the stability. The position of the centre of mass of a system of discrete masses is (Campbell, 2025):

Equation 4.17 — Centre of mass:

$$x_{\text{COM}} = \frac{\sum m_i \, x_i}{\sum m_i} \tag{4.17}$$

where m_i and x_i are the mass and position of each component (Campbell, 2025). This result generalises straightforwardly to two and three dimensions by computing the centre independently along each Cartesian axis.

For a vessel of displacement Δ with a cargo item of mass w shifted transversely by a distance d, the lateral shift in the overall centre of gravity is:

$$\delta\,\overline{\text{KG}}_y = \frac{w \cdot d}{\Delta}$$

This shift reduces the effective righting lever by $\delta\,\overline{\text{KG}}_y \cos\phi$ at any heel angle ϕ, potentially converting a stable equilibrium into an unstable one if the shift is large enough. Cargo securing therefore has a direct physical basis in the centre-of-mass equation.

When a weight is suspended from a point (such as a crane or a derrick), it behaves as though its entire mass were concentrated at the point of suspension rather than at the weight's actual position. This produces a *virtual rise*

of the centre of gravity from the weight's physical location to the suspension point. Attwood (1899) explains that if a weight w is raised by a distance d above its original position, the overall centre of gravity of the vessel rises by $w \cdot d/W$ (from Equation 4.17). If the weight is then suspended, any subsequent heel causes the weight to swing to the low side of the vessel, effectively acting as though G had risen to the suspension point. The practical consequence is a reduction in GM equal to $w \cdot d_{\text{susp}}/W$, where d_{susp} is the vertical distance from the weight's stowed position to the suspension point (Attwood, 1899).

4.3.6 Trim and Longitudinal Stability

Longitudinal stability governs the vessel's resistance to changes in pitch (rotation about the transverse axis). For conventional displacement vessels, longitudinal stability is generally much larger than transverse stability because the waterplane area moment of inertia about the transverse axis is far greater than about the longitudinal axis. However, for high-speed and foiling vessels, maintaining correct pitch trim is critical for performance and safety.

Huchet (2021) analysed the longitudinal equilibrium of the NACRA 17 foiling catamaran, where pitch stability is a primary design and operational concern. The longitudinal moment balance about the transom (or any reference point) requires that the sum of all moments in the vertical–longitudinal plane equals zero for steady-state sailing:

Equation 4.18 — Longitudinal moment equilibrium:

$$\sum M_{\text{pitch}} = 0 \tag{4.18}$$

The contributing moments include (Huchet, 2021):

1. **Weight moment:** The total weight of the vessel (hull, rig, appendages, crew) acting at the longitudinal centre of gravity (LCG).
2. **Buoyancy/foil lift moment:** The vertical forces from the demihulls (buoyancy) and from the hydrofoils (lift), each acting at their respective longitudinal positions.
3. **Aerodynamic moment:** The sail driving force and side force create a pitching moment about the LCG through their point of application at the centre of effort.
4. **Crew position moment:** The crew can shift their weight fore or aft to adjust the longitudinal trim.

For the foiling NACRA 17, the crew position is a primary means of pitch control. Moving the crew aft shifts the LCG aft, which raises the bows and reduces the risk of pitch-poling (nose-diving). Moving the crew forward lowers the bows, which may be desirable in light winds to reduce the wetted surface area and resistance (Huchet, 2021).

The surface-piercing Z-foils of the NACRA 17 provide a passive pitch stabilisation mechanism: as the bow drops (pitch down), the forward foil submerges deeper, increasing its wetted area and hence its lift force. This increased lift at the bow acts as a restoring moment, resisting further pitch-down motion. Conversely, if the bow rises excessively, the forward foil emerges from the water, reducing its lift and allowing the bow to drop back. This depth-dependent lift characteristic provides inherent heave and pitch stability without active control (Huchet, 2021).

For conventional displacement vessels, the *longitudinal metacentric radius* BM_L is derived by the same wedge-transfer method used for the transverse case, but applied to fore-and-aft inclinations (Attwood, 1899):

Equation 4.19 — Longitudinal metacentric radius:

$$BM_L = \frac{I_L}{\nabla} \tag{4.19}$$

where I_L is the second moment of area of the waterplane about a transverse axis through the centre of flotation F, and ∇ is the displacement volume (Attwood, 1899). The longitudinal metacentric height is then $GM_L = KB + BM_L - KG$. Because the waterplane is much longer than it is wide, $I_L \gg I_T$, and consequently GM_L is typically one to two orders of magnitude larger than GM—explaining why ships are far more resistant to trim changes than to heel.

The change of trim t (in metres) produced by shifting a weight w through a longitudinal distance d is (Attwood, 1899):

Equation 4.20 — Change of trim:

$$t = \frac{w \times d}{W \times GM_L} \times L \tag{4.20}$$

where W is the total displacement and L is the length between perpendiculars. The *moment to change trim one centimetre* (MCT1cm) is the moment required to produce a total trim change of 1 cm (Attwood, 1899):

Equation 4.21 — Moment to change trim 1 cm:

$$\text{MCT1cm} = \frac{W \times GM_L}{100\,L} \tag{4.21}$$

The trim change is distributed between the forward and after perpendiculars in inverse proportion to their distances from the centre of flotation. If the centre of flotation is at distance l_a aft of amidships and l_f forward:

$$\Delta d_{\text{aft}} = \frac{l_{\text{aft}}}{L}\,t, \qquad \Delta d_{\text{fwd}} = \frac{l_{\text{fwd}}}{L}\,t$$

where l_{aft} and l_{fwd} are the distances from the centre of flotation to the after and forward perpendiculars respectively (Attwood, 1899).

4.4 Applications in Maritime Systems

4.4.1 Damage Stability and Subdivision

Modern damage stability assessment employs a probabilistic framework mandated by SOLAS Chapter II-1, which replaced earlier deterministic rules. The probabilistic approach accepts that the location, extent, and penetration of hull damage are random variables and evaluates the vessel's ability to survive over the entire spectrum of feasible damage scenarios.

Guedes Soares and Santos (2015) describe the framework in which the vessel must achieve an attained subdivision index A exceeding a required index R (Papanikolaou, 2014). The attained index aggregates results from three loading draughts:

Equation 4.22 — Attained subdivision index:

$$A = 0.4\,A_s + 0.4\,A_p + 0.2\,A_l \tag{4.22}$$

where A_s, A_p, and A_l are the partial indices at the deepest subdivision draught, partial draught, and light service draught, respectively (Guedes Soares & Santos, 2015). Each partial index sums the products of the probability of each damage case p_i and the corresponding survival factor s_i:

Equation 4.23 — Partial subdivision index:

$$A_i = \sum_j p_{i,j} \times s_{i,j} \tag{4.23}$$

The probability factor $p_{i,j}$ is derived from the statistical distribution of collision damage extent (longitudinal position, length, and transverse penetration depth), compiled from historical casualty data. The survival factor $s_{i,j} \in [0,\,1]$ quantifies the probability that the vessel will not capsize or sink after flooding, based on the residual GZ curve—specifically the maximum righting lever, the range of positive stability, and the equilibrium heel angle in the damaged condition (Guedes Soares & Santos, 2015).

This framework represents a significant advance over deterministic damage stability rules, which evaluated only a prescribed set of damage extents (typically one- or two-compartment flooding). The probabilistic method captures the full range of possible damage scenarios and their relative likelihoods, providing a more realistic measure of the vessel's survivability (Figure 4.4) (Guedes Soares & Santos, 2015).

Sutulo and Guedes Soares (2023) report a complementary data-driven approach to damage consequence assessment. Using random-forest machine-learning classifiers trained on thousands of damage stability calculations, Sutulo and Guedes Soares (2023) showed that the residual GZ curve parameters (maximum GZ, range of positive stability, equilibrium heel angle) after flooding can be predicted with high accuracy from the damage location, extent, and initial loading condition—without repeating the full

hydrostatic calculation for each new scenario. This approach enables rapid screening of damage cases in the early design stage and provides a statistical complement to the physics-based probabilistic framework of Equations (4.22)–(4.23) (Sutulo & Guedes Soares, 2023).

Before the probabilistic framework, deterministic damage stability calculations used two classical methods. Attwood (1899) presents the *lost buoyancy method*: when a compartment is bilged (opened to the sea), the buoyancy it contributed is lost, and the vessel must sink to a deeper draught until the remaining intact waterplane provides sufficient buoyancy to support the unchanged displacement. The new draught is found by equating the original displacement to the volume of the intact hull below the new waterline, excluding the flooded compartment (Attwood, 1899).

The alternative *added weight method* treats the floodwater as an added weight rather than a loss of buoyancy: the ingressed water increases the total displacement and shifts the centre of gravity, and the vessel settles to a new equilibrium accordingly. Both methods yield the same final draught and trim, but the lost buoyancy method is computationally simpler for compartments that are fully open to the sea, since it does not require calculating the mass of floodwater at each iteration (Attwood, 1899).

A detailed comparison of these two approaches is available in the literature (Ridley & Patterson, 2014). In practice, the added weight method becomes essential when the flooded compartment is above the waterline (e.g. a damaged superstructure space), since the lost buoyancy method applies only to compartments below the waterline that contribute to the displacement volume. For a symmetrically flooded midships compartment, both methods yield identical final draughts and residual GM; the difference lies in the calculation procedure and in the physical insight each provides. The lost buoyancy method treats the ship as unchanged in weight and recalculates the waterplane, while the added weight method tracks the progressive increase in displacement and shift in the centre of gravity as floodwater accumulates (Ridley & Patterson, 2014).

4.4.2 Inclining Experiment

The *inclining experiment* is the standard procedure for determining a vessel's metacentric height by direct measurement. Attwood (1899) describes the method: a known weight w is moved transversely through a measured distance d on the vessel's deck, and the resulting heel angle θ is measured (typically with a plumb line or pendulum of length l, for which $\tan\theta = a/l$ where a is the lateral deflection). From the small-angle stability relation (Equation 4.6):

Equation 4.24 — Inclining experiment:

$$GM = \frac{w \times d}{W \times \tan\theta} \tag{4.24}$$

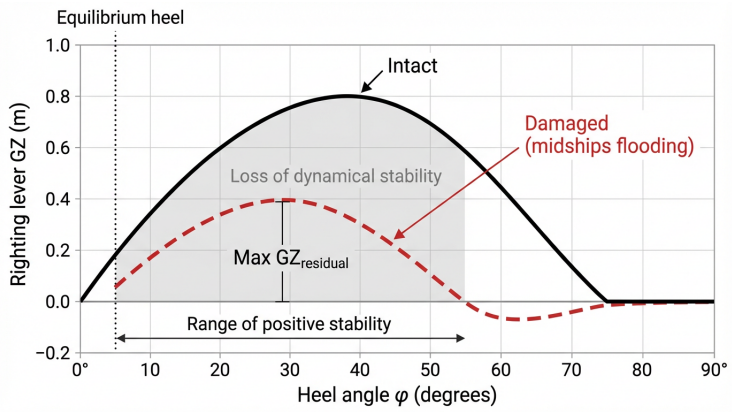

Figure 4.4: Comparison of intact and damaged GZ curves. The intact vessel (solid line) has a larger maximum righting lever and wider range of positive stability. After midships flooding (dashed line), the equilibrium heel angle shifts, the maximum GZ is reduced, and the vanishing angle decreases. The shaded region between the curves represents the loss of dynamical stability due to damage. The survival factor $s_{i,j}$ in the probabilistic framework (Equation 4.23) is determined from the residual curve parameters: maximum GZ, range, and equilibrium heel angle.

where W is the displacement at the time of the experiment (Attwood, 1899). Attwood (1899) emphasises several precautions: the vessel should be in still water, mooring lines should be slack, free surfaces must be minimised (or their corrections applied), and the weights must be moved simultaneously to avoid transient effects. The experiment is typically carried out twice—moving the weight to port and then to starboard—and the results are averaged to eliminate systematic errors.

The United States Naval Academy integrates the inclining experiment into its engineering curriculum. United States Naval Academy (2021) describe laboratory exercises in which midshipmen conduct inclining experiments on model hulls (including FFG-7 frigate and DDG-51 destroyer hull forms), measuring pendulum deflections at multiple weight positions to construct a data set from which GM is obtained by linear regression. The hands-on experience reinforces the physics: the measured GM from the inclining experiment is compared with the calculated value from hydrostatic tables ($KB + BM - KG$), and the agreement—or discrepancy—provides direct insight into the sources of uncertainty (free surface corrections, weight inventory accuracy, and environmental disturbances) (United States Naval Academy, 2021).

4.4.3 Second Generation IMO Intact Stability Criteria

The weather criterion discussed in Section 4.3.3 and the Rahola-based empirical criteria together constitute the *first generation* of intact stability requirements. Both are anchored in historical casualty data—the Rahola criterion in GZ curve statistics from vessels under 100 m, the weather criterion in wind observations up to the 1950s—and their applicability to contemporary ship types (large container ships, cruise vessels, car carriers) cannot be straightforwardly guaranteed. Spyrou et al. (2023) describe the *Second Generation Intact Stability Criteria* (SGISC) developed at IMO over two decades (2001–2020) and published as Interim Guidelines MSC.1/Circ.1627, which adopt a fundamentally different, physics-based approach.

The SGISC identify five distinct failure modes that can cause intact stability loss (Kristiansen, 2005; Spyrou et al., 2023):

1. **Pure loss of stability.** When a wave crest is near amidships, the waterplane area—particularly at the transom stern and bow flare—changes, reducing the instantaneous GZ. At high speed in following seas the vessel remains on the crest longer, prolonging the period of diminished restoring moment.

2. **Parametric roll.** Periodic variation of the waterplane as successive waves pass along the hull modulates the restoring term, exciting a Mathieu-type instability in roll (cf. Equation 6.38 in Chapter 6).

3. **Surf-riding and broaching-to.** In steep following seas a vessel may be captured and accelerated by a wave (surf-riding), losing directional control and yawing violently (broaching), which can produce capsizing heel moments.

4. **Dead ship condition.** A disabled vessel drifting beam-to in wind and waves is subjected to a combined steady wind heeling lever and wave-induced roll excitation—the scenario addressed in less detail by the first-generation weather criterion.

5. **Excessive acceleration.** On vessels with very large GM (“stiff” ships), the resulting short roll period produces lateral accelerations at elevated decks that endanger crew safety and cargo securing.

For each failure mode, the SGISC employ a multi-layered assessment framework comprising three levels of escalating complexity (Spyrou et al., 2023): *Level 1* requires only simple algebraic checks that can be performed by hand; *Level 2* uses spreadsheet-level vulnerability calculations with probabilistic inputs, including wave spectra and operational profiles; and *Level 3* (direct stability assessment) demands time-domain numerical simulations or model experiments conducted in accordance with a detailed specification. A vessel that passes at any level need not proceed to a higher one. For vessels

that fail all three levels, *operational measures*—restricted routes, speed limitations, or real-time stability monitoring—may be prescribed in lieu of design modifications (Spyrou et al., 2023).

The physics-based multi-layered structure has two important consequences for the practice of stability assessment. First, the criteria are applicable to novel hull forms without reliance on historical casualty statistics, since each level is derived from hydrodynamic principles rather than empirical correlations. Second, the escalating cost of assessment is incurred only by vessels whose simplified checks indicate potential vulnerability, avoiding unnecessary computational burden on conventional designs (Spyrou et al., 2023).

4.5 Discussion

The empirical finding that $D_x/D_y \approx 2$ is remarkably constant across four orders of magnitude in displacement (Bejan et al., 2020) has a direct implication for stability science: the stability requirements of a vessel do not change qualitatively with scale. This geometric similarity is consistent with the physical expectation that stability parameters—GM/B, GZ/B—are dimensionless quantities that depend on shape rather than absolute size.

The near-universal beam-to-draft ratio also suggests that stability optimisation is not in conflict with other performance objectives (speed, seakeeping, cargo capacity) but rather represents a zone of compromise that has been independently discovered by designers across centuries and vessel sizes.

The analysis of the NACRA 17 foiling catamaran by Huchet (2021) extends the stability discussion into a regime where hydrostatic stability alone is insufficient. For foiling vessels, the crew's body weight becomes a critical stability element: the righting moment provided by the crew on a trapeze ($RM_{\text{crew}} = m_{\text{crew}} \cdot g \cdot d_{\text{crew}}$) is not a marginal correction but a primary contributor to the total righting moment. Stability physics therefore extends beyond hull geometry and buoyancy distribution to include the dynamic positioning of mass.

The pitch stability mechanism of the surface-piercing Z-foils—where foil lift varies with immersion depth—illustrates a passive feedback control loop governed by Archimedes-like principles applied to hydrodynamic lift rather than hydrostatic buoyancy. This represents a modern extension of classical stability theory to high-speed craft.

Attwood (1899) provides historical context for the relationship between metacentric height and operational behaviour: vessels with excessively large GM roll quickly and uncomfortably ("stiff" vessels), while those with small GM roll slowly but risk insufficient reserve stability ("tender" vessels). The design challenge is to achieve a metacentric height that balances comfort, safety, and operational capability across all loading conditions. This qualitative observation is quantified by the roll natural period $T_n = 2\pi k/\sqrt{g\,GM}$ (Equation 4.15): large GM shortens the period and produces accelerations

that degrade crew performance and passenger comfort, while small GM lengthens the period but reduces reserve stability (Lee, 2019).

The wall-sided formula $GZ = \sin\varphi[GM + \frac{1}{2}BM\ \tan^2\varphi]$ (Equation 4.11) provides a practical bridge between the small-angle metacentric approximation and the fully general Atwood calculation (Rawson & Tupper, 2001). Its prediction of the angle of loll (Equation 4.12) for initially unstable vessels has direct operational significance: a vessel that develops negative GM through improper loading will heel to a loll angle that the wall-sided formula predicts accurately for moderate heel. The cross curves of stability (Equation 4.13) separate hull geometry from loading condition, enabling systematic evaluation of GZ for any combination of cargo, fuel, and ballast (Lee, 2019).

The probabilistic damage stability framework (Equations 4.22–4.23) introduced by Guedes Soares and Santos (2015) marks a departure from deterministic stability assessment. Rather than verifying survivability against a small set of prescribed damage scenarios, the attained subdivision index A integrates over all feasible damage cases, weighted by their probability of occurrence. This approach aligns stability regulations with the quantitative risk assessment philosophy now adopted across the maritime safety framework (see also the *Maritime Safety and Risk Physics* chapter of the companion volume). The machine-learning extension by Sutulo and Guedes Soares (2023), which uses random-forest classifiers to predict residual GZ curve parameters from damage descriptors, demonstrates that the probabilistic framework can be accelerated by data-driven surrogates while retaining physical accuracy.

The detailed free surface treatment of Biran (2003)—showing the cubic dependence of moment of inertia on tank breadth and the consequent 75% reduction from a single longitudinal centre-line bulkhead—provides the quantitative physics behind the IMO's subdivision requirements for tanks. The inclining experiment exercises described by United States Naval Academy (2021) reinforce this quantitative approach by demonstrating that the theoretical GM can be validated by direct measurement, closing the loop between design calculation and experimental verification.

Ridley and Patterson (2014) connect these analytical methods to marine engineering practice by providing systematic worked examples of both the lost buoyancy and added weight methods for damage stability, and by showing how the box-shaped vessel approximation $GM_0 \approx B^2/(12T) - KG + T/2$ enables rapid assessment of metacentric height from principal dimensions—a calculation that remains essential for preliminary stability evaluation at the design stage.

The Second Generation Intact Stability Criteria described by Spyrou et al. (2023) extend this trend from damage stability to intact stability. Where the first-generation weather criterion (Section 4.3.3) relies on an energy-balance check calibrated against historical casualties, the SGISC derive their threshold values from the hydrodynamic mechanisms of each failure mode. Pure loss of stability and parametric roll, for example, are evaluated through waterplane

variations computed for the actual hull in a realistic seaway, while surf-riding and broaching criteria follow from the nonlinear surge and yaw dynamics in steep following seas. The multi-layered framework (Level 1/2/3) mirrors the proportionality principle already established in probabilistic damage stability: simple checks suffice for conventional designs, and expensive time-domain simulations are reserved for vessels whose geometry or operational profile places them near a vulnerability boundary. As Chapter 6 shows, the parametric roll criterion is directly connected to the Mathieu-type instability of ship roll in longitudinal seas.

4.6 Conclusion

Ship stability rests on the physics of rotational equilibrium: the torque $\tau = rF\sin\theta$ and the condition $\tau_{\text{NET}} = 0$ determine whether a displaced vessel returns to the upright. The metacentric height $GM = KB + BM - KG$, with $BM = I_T/\nabla$, provides the single most important index of initial stability; a positive GM ensures a restoring righting moment $W \times GM \sin\theta$ at small heel angles (Attwood, 1899; Campbell, 2025). The scale-independent beam-to-draft ratio $D_x/D_y \approx 2$ observed across sailboat hulls (Bejan et al., 2020) illustrates how the same geometric relationship governs stability from dinghies to displacement vessels, while the centre-of-mass equation $x_{\text{COM}} = \sum m_i x_i / \sum m_i$ links every cargo movement to a quantifiable shift in KG (Campbell, 2025).

Beyond 10–15° of heel the metacentre migrates and the small-angle approximation breaks down; Atwood's formula (Equation 4.10) then supplies the righting lever from wedge geometry, and the wall-sided formula $GZ = \sin\varphi[GM + \frac{1}{2}\,BM\,\tan^2\varphi]$ bridges the gap between the metacentric approximation and the fully general calculation (Lee, 2019; Rawson & Tupper, 2001). The cross curves of stability ($GZ = KN - KG\sin\varphi$) separate hull geometry from loading condition, enabling systematic evaluation of GZ for any combination of cargo and ballast (Lee, 2019). The roll natural period $T_n = 2\pi k/\sqrt{g\,GM}$ quantifies the trade-off between stability reserve and motion comfort: large GM produces rapid, uncomfortable rolling while small GM produces gentle but potentially hazardous motions (Lee, 2019). The free surface correction $GG_1 = i/\nabla$, which depends only on the geometry of the liquid surface and scales as $l\,b^3/12$ for a rectangular tank, demonstrates why a single centre-line bulkhead reduces the correction by 75% and why IMO regulations mandate longitudinal tank subdivision (Attwood, 1899; Biran, 2003). The longitudinal counterpart $BM_L = I_L/\nabla$ and the associated moment to change trim complete the static stability picture for six-degree-of-freedom loading assessment (Attwood, 1899).

The inclining experiment ($GM = wd/(W\tan\theta)$) closes the loop between design calculation and physical verification; laboratory exercises on model hulls—FFG-7, DDG-51—confirm that the experimentally determined GM agrees with the hydrostatic tables and quantify the sources of measurement

uncertainty (Attwood, 1899; United States Naval Academy, 2021). For the NACRA 17 foiling catamaran, the equilibrium condition $RM \geq HM$ takes a distinctive form: crew righting moment ($RM_{\text{crew}} = m_{\text{crew}} \cdot g \cdot d_{\text{crew}}$) is the primary stability contribution, and the depth-dependent lift of surface-piercing Z-foils provides passive pitch stabilisation (Huchet, 2021). The box-shaped approximation $GM_0 \approx B^2/(12T) - KG + T/2$ enables rapid preliminary assessment from principal dimensions alone, and the correct response to a vessel at her angle of loll—lowering the centre of gravity, never adding weight on the high side—follows directly from the physics of the wall-sided formula (Ridley & Patterson, 2014).

Modern stability regulation has moved from deterministic damage scenarios to physics-based probabilistic frameworks. The attained subdivision index A (Equations 4.22–4.23) integrates survivability over all feasible damage cases weighted by their probability of occurrence (Guedes Soares & Santos, 2015), and random-forest classifiers trained on damage stability calculations can now predict residual GZ curve parameters from damage descriptors, accelerating the probabilistic framework while retaining physical accuracy (Sutulo & Guedes Soares, 2023). The IMO weather criterion ($A_1 \geq A_2$) formalises dynamical stability as an energy balance under combined steady wind and gust conditions (Lee, 2019). The Second Generation Intact Stability Criteria extend this philosophy to five physics-based failure modes—pure loss of stability, parametric roll, surf-riding/broaching, dead ship condition, and excessive acceleration—using a three-level assessment (algebraic, probabilistic vulnerability, direct time-domain simulation) that mirrors the proportionality principle already established for damage stability (Spyrou et al., 2023). Together, these frameworks transform ship stability from a static metacentric calculation into a comprehensive, risk-informed discipline that links hull geometry, loading condition, and the seaway environment within a unified analytical structure.

References

Attwood, E. L. (1899). *A text-book of theoretical naval architecture*. Longmans, Green; Co.

Bejan, A., Ferber, L., & Lorente, S. (2020). Convergent evolution of boats with sails. *Scientific Reports*, *10*, Article 2703. https://doi.org/10.1038/s41598-020-58940-5

Biran, A. B. (2003). *Ship hydrostatics and stability*. Butterworth-Heinemann.

Campbell, C. (2025). *Physics: A focused introduction*. CRC Press. https://doi.org/10.1201/9781003571568

Fischer-Cripps, A. C. (2014). *The physics companion* (2nd ed.). CRC Press. https://doi.org/10.1201/b17356

Guedes Soares, C., & Santos, T. A. (Eds.). (2015). *Maritime technology and engineering: Proceedings of MARTECH 2014*. CRC Press.

Huchet, L. (2021). *Investigation of the influence of crew setup on performances for the Olympic NACRA 17 foiling catamaran* [Individual project]. University of Southampton.

Kristiansen, S. (2005). *Maritime transportation: Safety management and risk analysis*. Elsevier Butterworth-Heinemann.

Lee, B. S. (2019). *Hydrostatics and stability of marine vehicles: Theory and practice* (Vol. 7). Springer. https://doi.org/10.1007/978-981-13-2682-0

Lewis, E. V. (Ed.). (1988). *Principles of naval architecture* (2nd ed.) [Three volumes]. The Society of Naval Architects; Marine Engineers.

Papanikolaou, A. (2014). *Ship design: Methodologies of preliminary design*. Springer. https://doi.org/10.1007/978-94-017-8751-2

Rawson, K. J., & Tupper, E. C. (2001). *Basic ship theory* (5th ed.). Butterworth-Heinemann.

Ridley, J. D., & Patterson, C. J. (2014). *Ship stability, powering and resistance* (Vol. 13). Adlard Coles Nautical.

Spyrou, K. J., Belenky, V. L., Katayama, T., & Bačkalov, I. (2023). *Contemporary ideas on ship stability: From dynamics to criteria*. Springer. https://doi.org/10.1007/978-3-031-16329-6

Sutulo, S., & Guedes Soares, C. (2023). Ship dynamics and hydrodynamics. *Journal of Marine Science and Engineering*, *11*(5), 911. https://doi.org/10.3390/jmse11050911

Tupper, E. C. (2013). *Introduction to naval architecture* (5th ed.). Butterworth-Heinemann.

United States Naval Academy. (2021). En400: Principles of ship performance [Course notes, Fall AY2021].

Chapter 5

Fluid Dynamics and Ship Resistance

5.1 Introduction

The resistance experienced by a vessel moving through water is the fundamental quantity that determines powering requirements, fuel consumption, and ultimately the economic and environmental performance of the ship. Ship resistance arises from the combined action of viscous shear, pressure distribution, and wave generation, each governed by distinct physical mechanisms.

A striking illustration of how resistance physics shapes vessel design is the convergent evolution of sailing boats. Bejan et al. (2020) demonstrated that the geometry of boats with sails—spanning displacements from 10^2 to 10^5 kg and construction years from 1899 to 2011—converges toward specific aspect ratios that minimise the total drag force for a given displacement. This convergence is not imposed by regulation or tradition; it emerges directly from the physics of fluid resistance.

Attwood (1899) decomposed the total resistance of a powered ship into three distinct physical contributions: (i) *frictional resistance*, arising from the viscous shear stress along the wetted surface; (ii) *eddy-making resistance*, caused by flow separation at the stern and around appendages; and (iii) *wave-making resistance*, due to the energy radiated in the ship's wave system. The frictional component typically dominates at low speeds, while wave-making resistance grows rapidly at higher speeds and becomes the primary resistance source near the critical hull speed (Attwood, 1899).

5.2 Scientific Background

5.2.1 Fundamental Equations of Fluid Motion

The dynamics of a fluid are governed by the conservation of mass (continuity equation), the conservation of momentum (Navier–Stokes equations), and the conservation of energy. For the ocean as a rotating fluid, Dera (1992) presented the full equation of motion including Coriolis, pressure gradient, viscous, and gravitational forces:

Equation 5.1 — Navier–Stokes equation for ocean flow:

$$\rho \left[\frac{\partial \mathbf{v}}{\partial t} + (\mathbf{v} \cdot \nabla)\mathbf{v} + 2\,\boldsymbol{\omega} \times \mathbf{v} \right] = -\nabla p + \eta\, \nabla^2 \mathbf{v} + \rho\, \mathbf{g} + \mathbf{F}_i \tag{5.1}$$

where ρ is the fluid density, $\mathbf{v}$ is the velocity vector, $\boldsymbol{\omega}$ is the Earth's angular velocity, p is the pressure, η is the dynamic viscosity, $\mathbf{g}$ is the gravitational acceleration, and $\mathbf{F}_i$ represents additional body forces (Dera, 1992, Eq. 1.2.44).

The left-hand side of Equation 5.1 contains the local acceleration ($\partial \mathbf{v}/\partial t$), the nonlinear advective acceleration ($(\mathbf{v} \cdot \nabla)\mathbf{v}$), and the Coriolis acceleration ($2\boldsymbol{\omega} \times \mathbf{v}$) due to the Earth's rotation. The right-hand side contains the pressure gradient force, viscous friction ($\eta\, \nabla^2 \mathbf{v}$), gravity, and any externally imposed forces; for a rigorous mathematical treatment, see (Burton & Noble, 2024).

The viscous friction term involves the dynamic viscosity η of seawater. The molecular viscosity of water is reported as $\eta_w \approx 1.17 \times 10^{-3}\,\mathrm{N\,s\,m^{-2}}$ at $287\,\mathrm{K}$, with the volume (bulk) viscosity approximately $\eta'_w \approx 2.8\,\eta_w$ (Dera, 1992; Lewis, 1988).

For ship resistance problems, the Coriolis and gravitational body force terms are typically negligible compared with the pressure gradient and viscous forces, and Equation 5.1 reduces to the classical Navier–Stokes equation. However, for large-scale ocean circulation (Chapter 12), the Coriolis and hydrostatic pressure terms become dominant.

5.2.2 Bernoulli's Equation and Applications

The relationship between pressure and velocity in a fluid flow is fundamental to understanding ship resistance. For the derivation and conceptual treatment of Bernoulli's equation, see (Hewitt et al., 2012); the practical consequence is directly relevant: as fluid accelerates around a hull, its pressure decreases, and this pressure variation generates forces on the hull surface.

Bejan et al. (2020) applied this principle implicitly in their analysis of the drag force on a sailing vessel's hull. The frontal (blunt-body) drag experienced by the submerged hull cross-section arises from the pressure difference between the bow and stern, which is a direct consequence of Bernoulli's principle applied to the flow field around the hull.

For an ideal (inviscid, incompressible, irrotational) flow, the conservation of energy along a streamline yields Bernoulli's equation: $p + \frac{1}{2}\rho v^2 + \rho g z =$

const, where p is the static pressure, v is the flow speed, and z is the elevation. Attwood (1899) applies this principle — in the form of the energy balance between pressure head and velocity head — to the flow around a ship hull: as water accelerates around the widest part of the hull, the pressure drops, and at the bow and stern where the flow decelerates, the pressure rises. The pressure difference between the stagnation zones (bow, stern) and the suction zone (hull sides) produces a net fore-and-aft force that constitutes the wave-making and eddy-making resistance components (Attwood, 1899).

5.2.3 Viscous Flow and the Boundary Layer

The origin of all fluid drag is the viscosity of the medium. Campbell (2025) presents the general quadratic drag law for an object moving through a fluid:

Equation 5.2 — Quadratic drag force:

$$F_d = b\, v^2 \tag{5.2}$$

where v is the speed of the object relative to the fluid and b is a constant that depends on the object's shape, frontal area, and the fluid properties (Campbell, 2025); for a concise treatment, see (Fischer-Cripps, 2014). The drag always opposes the direction of motion. When a body falls under gravity through a fluid, the drag increases until it balances the gravitational force, at which point the body reaches its *terminal velocity*:

Equation 5.3 — Terminal velocity:

$$v_t = \sqrt{\frac{m\, g}{b}} \tag{5.3}$$

where m is the object's mass (Campbell, 2025). The terminal velocity concept is directly analogous to the steady-state condition of a vessel: when the propulsive thrust equals the total drag, the acceleration is zero and the vessel cruises at constant speed. The constant b in Equation 5.2 absorbs the same physics that Bejan's naval-architecture formulation separates into C_D, C_f, reference areas, and $\frac{1}{2}\rho$.

Attwood (1899) presents the boundary layer concept in terms of the frictional resistance law derived from William Froude's experiments. Froude towed planks of various lengths and surface roughnesses through water at controlled speeds and found that the frictional resistance per unit area follows the power law:

Equation 5.4 — Froude's frictional resistance:

$$R_f = f \cdot S \cdot V^n \tag{5.4}$$

where f is a friction coefficient that depends on the surface roughness and the length of the surface, S is the wetted surface area, V is the speed, and n ranges from approximately 1.83 (for long, smooth surfaces) to 2.16 (for short, rough

surfaces) (Attwood, 1899). The decrease in f with increasing length reflects the growth of the turbulent boundary layer: as the boundary layer thickens along the hull, the velocity gradient at the wall decreases, reducing the local shear stress (Figure 5.1). This length effect is the physical phenomenon captured more precisely by the Reynolds number dependence in the ITTC-57 correlation (Equation 5.7).

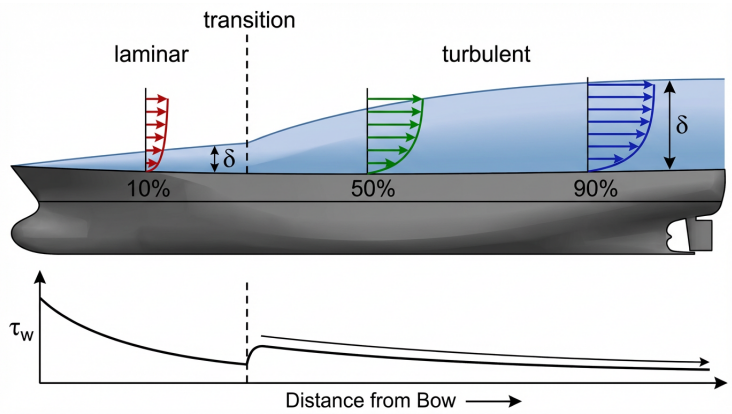

Figure 5.1: Development of the turbulent boundary layer along a ship hull. The boundary layer thickness δ grows from the bow toward the stern; the velocity profile transitions from laminar to turbulent within the first few percent of the waterline length. The wall shear stress τ_w decreases with distance from the bow as the boundary layer thickens, explaining the decrease in frictional resistance coefficient with increasing Reynolds number captured by the ITTC-57 correlation (Equation 5.7).

5.3 Theoretical Framework

5.3.1 Dimensional Analysis and Similarity

Dimensional analysis is the key to decomposing the total resistance of a vessel into its constituent components. Bejan et al. (2020) employed dimensional analysis to derive the optimal hull proportions for sailing vessels. Their approach separated the drag force into two contributions—frontal (pressure) drag and skin friction—each characterised by distinct dimensionless coefficients:

- **Drag coefficient** $C_D \sim 1$: governs the frontal (blunt-body) resistance experienced by the submerged cross-section of the hull.
- **Skin friction coefficient** $C_f \sim 10^{-2}$: governs the tangential shear stress along the wetted surface of the hull in turbulent flow.

The ratio $C_D/C_f \sim 100$ is significant because it determines the optimal

slenderness of the hull. This ratio appears directly in the predicted length-to-beam ratio (Equation 5.23 below).

Attwood (1899) introduces the *Froude number* implicitly through the *law of corresponding speeds*: when comparing geometrically similar ships of different sizes, the speeds must be proportional to the square root of their linear dimensions for the wave patterns to be geometrically similar. This principle, expressed as:

Equation 5.5 — Law of corresponding speeds:

$$\frac{V_1}{V_2} = \sqrt{\frac{L_1}{L_2}} \tag{5.5}$$

is the foundation of the *Froude number* $Fn = V/\sqrt{gL}$, which governs the wave-making resistance (Attwood, 1899; Newman, 1977). The *Reynolds number* $Re = VL/\nu$ governs the frictional resistance. Since it is impossible to match both Fn and Re simultaneously at model scale (unless the model is the same size as the ship), the standard towing tank procedure is:

1. Test the model at the correct Froude number ($Fn_{\text{model}} = Fn_{\text{ship}}$).
2. Measure the total resistance of the model.
3. Subtract the frictional resistance of the model (computed from the ITTC-57 line at the model Reynolds number).
4. The remainder is the *residuary resistance*, which scales geometrically: $R_{R,\text{ship}} = R_{R,\text{model}} \times \lambda^3$, where λ is the scale ratio (Attwood, 1899).
5. Add the frictional resistance of the full-scale ship (computed from the ITTC-57 line at the ship Reynolds number).

This procedure — Froude's *law of comparison* — remains the basis of all model-to-ship resistance extrapolation (Attwood, 1899; Carlton, 2012).

5.3.2 Frictional Resistance

Frictional resistance arises from the viscous shear stress acting along the wetted surface of the hull. Bejan et al. (2020) accounted for this component in their resistance formulation using the skin friction coefficient C_f for turbulent flow, with an order of magnitude of $C_f \sim 10^{-2}$.

In their model, the frictional drag contribution to the total water resistance force is proportional to the wetted surface area of the hull sides and bottom. For a hull of length L, beam $D_x \equiv B$, and submerged depth $D_y \equiv T$ (draft), the frictional component is:

Equation 5.6 — Frictional drag contribution:

$$F_{\text{friction}} \sim C_f \cdot (D_x + 2D_y) \cdot L \cdot \frac{1}{2}\,\rho_w\, V_w^2 \tag{5.6}$$

where ρ_w is the water density and V_w is the boat speed (Bejan et al., 2020).

This formulation shows that frictional resistance scales with wetted area and with the square of speed, as expected for turbulent skin friction.

A widely used engineering correlation for the flat-plate skin friction coefficient in turbulent flow is the ITTC 1957 model–ship correlation line. Huchet (2021) employed this friction line in the resistance prediction of the NACRA 17 catamaran demihulls:

Equation 5.7 — ITTC-57 frictional resistance coefficient:

$$C_f = \frac{0.075}{(\log_{10} Re - 2)^2} \tag{5.7}$$

where $Re = VL/\nu$ is the Reynolds number based on the waterline length L and kinematic viscosity ν of the fluid, and V is the vessel speed (Huchet, 2021). This correlation provides the baseline frictional resistance coefficient for a smooth flat plate in turbulent flow. It is the standard adopted by the International Towing Tank Conference (ITTC) for decomposing model-scale and full-scale resistance.

The ITTC-57 line is not a theoretical derivation from first principles but an empirical correlation that approximates the Schoenherr friction formulation in a computationally convenient closed form. Its widespread adoption ensures consistency in ship resistance prediction across different towing tanks and research groups.

In practical ship design, the wetted surface area S is a critical input for computing frictional resistance. An empirical wetted surface formula used in resistance estimation studies of small displacement vessels:

Equation 5.8 — Wetted surface estimation (displacement vessels):

$$S = 3.223\,\nabla^{2/3} + 0.5402\,L_D\,\nabla^{1/3} \tag{5.8}$$

where ∇ is the displaced volume in m³ and $L_D = 0.5(L_{BP} + L_{WL})$ is the displacement length. This formulation captures the dependence of wetted area on both the volumetric displacement (through $\nabla^{2/3}$) and the hull length (through the $L_D\,\nabla^{1/3}$ term) (Guedes Soares & Santos, 2015).

When extrapolating from model-scale resistance tests to full-scale performance, an allowance ΔC_f is added to the frictional coefficient to account for effects absent in the smooth-model towing tank test. The following trial allowances: hull roughness for all-welded construction ($\Delta C_f = 0.00035$), steering resistance (0.00004), bilge keel resistance (0.00004), and air resistance (0.00008), yielding a total correlation allowance of approximately $\Delta C_f \approx 0.00051$ (Guedes Soares & Santos, 2015). These corrections are added to the ITTC-57 friction coefficient (Equation 5.7) when computing the full-scale frictional resistance.

The most reliable method for determining the hull form factor $(1 + k)$ was proposed by Prohaska (1966, as cited in Birk (2019)) and is recommended by the ITTC. The method exploits the theoretical prediction that at low Froude

numbers ($Fr < 0.2$), wave resistance grows with the fourth power of Fr (Birk, 2019):

Equation 5.9 — Wave resistance at low Froude number:

$$C_W \approx \alpha\, Fr^4 \qquad \text{for } Fr < 0.2 \tag{5.9}$$

where α is a constant. Substituting this approximation into the ITTC form-factor decomposition $C_{TM} = (1 + k)\, C_{FM} + C_W$ and dividing by the ITTC friction coefficient C_{FM} yields (Birk, 2019):

Equation 5.10 — Prohaska's linear relation:

$$\frac{C_{TM}}{C_{FM}} = (1 + k) + \alpha\, \frac{Fr^4}{C_{FM}} \tag{5.10}$$

This has the form of a straight line $y = b + \alpha\, x$, with $y = C_{TM}/C_{FM}$ and $x = Fr^4/C_{FM}$. Data points from low-speed model tests ($Fr \in [0.1,\, 0.2]$) are plotted in these coordinates; the y-intercept of the best-fit line gives the form factor $(1 + k)$ directly (Birk, 2019).

Birk (2019) notes several practical difficulties with the Prohaska method. If the model speed is too low ($Fr < 0.1$), boundary layer relaminarisation or flow separation may corrupt the data; if the speed is too high, wave breaking invalidates the Fr^4 assumption. Vessels with high block coefficient, bulbous bows, or deeply submerged transoms are particularly susceptible to nonlinear effects at the extremes of the data range. Careful observation of flow patterns during towing is essential for selecting the appropriate data subset for the regression (Birk, 2019).

5.3.3 Wave-Making Resistance

When a vessel moves through water, it generates a wave system. The wave-making phenomenon can be addressed through the concept of the transverse bow wave: as the bow of a sailboat moves through the water, it produces a transverse wave. A critical velocity exists at which the wavelength of this transverse wave equals the waterline length of the hull:

Equation 5.11 — Critical (hull) speed:

$$V_c \approx 1.25\, \sqrt{L_{WL}} \tag{5.11}$$

where L_{WL} is the waterline length in metres and V_c is in m/s (Bejan et al., 2020).

At this critical velocity, the vessel becomes "trapped" in the trough of its own wave, and further speed increase requires disproportionately more power. This phenomenon effectively caps the speed of displacement-mode vessels. Exceptions include surfing on external waves or using hydrofoils to lift the hull clear of the water (Bejan et al., 2020).

Attwood (1899) describes the wave system generated by a moving ship: the bow produces a diverging wave pattern that spreads outward and aft, while

the stern generates a similar but weaker pattern. The *effective horsepower* (EHP) required to overcome the total resistance is (Attwood, 1899):

Equation 5.12 — Effective power:

$$P_E = R_T \times V \tag{5.12}$$

where R_T is the total resistance and V is the ship speed. Attwood (1899) notes that at low speeds ($V/\sqrt{L} < 0.5$, in consistent units), the frictional resistance dominates and P_E grows approximately as $V^{2.83}$. At higher speeds, the wave-making component grows rapidly — approximately as V^6 according to Attwood's empirical formulation — making it the dominant resistance source near the hull speed (Figure 5.2).

A complementary approach to resistance estimation is the *Admiralty coefficient*, a classical tool for quick power prediction during preliminary design. Ridley and Patterson (2014) present the Admiralty coefficient C_A as:

Equation 5.13 — Admiralty coefficient:

$$C_A = \frac{\Delta^{2/3} \times V^3}{P_s} \tag{5.13}$$

where Δ is the displacement in tonnes, V is the ship speed in knots, and P_s is the shaft power in kW (Ridley & Patterson, 2014). For geometrically similar vessels operating at similar Froude numbers, C_A is approximately constant, enabling rapid estimation of the power required for a new design from the known performance of a similar vessel. The Admiralty coefficient method is most reliable in the speed range where the resistance–speed relationship follows an approximate cube law; at speeds near the hull speed (Equation 5.11), the rapid increase in wave-making resistance invalidates the constant-C_A assumption (Ridley & Patterson, 2014).

5.3.4 Viscous Pressure Resistance (Form Drag)

The form drag component of resistance arises from the pressure distribution around the submerged hull, modelled as the blunt-body drag experienced by the frontal cross-section of the hull:

Equation 5.14 — Frontal (form) drag contribution:

$$F_{\text{form}} \sim C_D \cdot D_x \cdot D_y \cdot \frac{1}{2}\,\rho_w\, V_w^2 \tag{5.14}$$

where $C_D \sim 1$ is the drag coefficient for the blunt frontal area $D_x \times D_y$ (Bejan et al., 2020).

The distinction between $C_D \sim 1$ (form drag) and $C_f \sim 10^{-2}$ (friction drag) is crucial: it means that the frontal area has approximately 100 times more drag per unit area than the side surfaces. This disparity drives the optimisation toward slender hull forms.

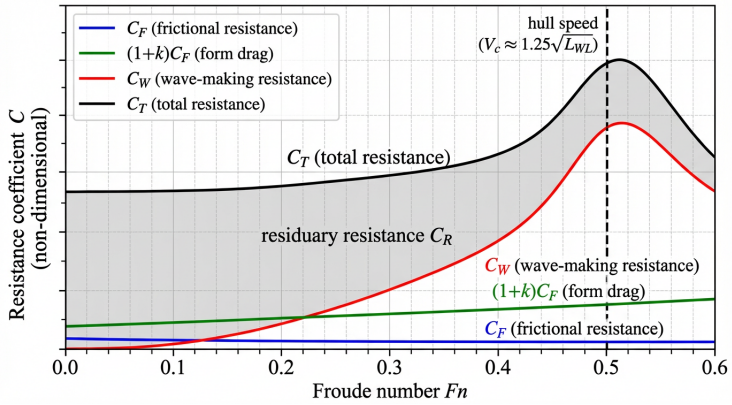

Figure 5.2: Schematic decomposition of total ship resistance into its principal components as a function of Froude number. At low speeds ($Fn < 0.2$), frictional resistance dominates; wave-making resistance grows rapidly at higher speeds and produces a pronounced hump near the critical hull speed $V_c \approx 1.25\sqrt{L_{WL}}$ (Equation 5.11). The residuary resistance C_R is the difference between the total and the viscous component $(1 + k)\, C_F$ (Equation 5.26). At supercritical speeds, wave resistance decreases as the vessel transitions from displacement to planing mode.

For hydrofoil appendages, the drag decomposition takes a more detailed form. Huchet (2021) decomposed the total drag of a hydrofoil section into four distinct physical contributions:

Equation 5.15 — Hydrofoil total drag decomposition:

$$C_{D,\text{total}} = C_{D,P} + C_{D,i} + C_{D,w} + C_{D,\text{spray}} \tag{5.15}$$

where (Huchet, 2021):

- $C_{D,P}$ is the profile (viscous) drag of the foil section, arising from skin friction and flow separation;
- $C_{D,i}$ is the induced drag due to the generation of lift (analogous to the induced drag of a finite wing);
- $C_{D,w}$ is the wave-making drag caused by the foil operating near the free surface;
- $C_{D,\text{spray}}$ is the spray drag generated by water spray at the foil–free-surface junction.

The profile drag is related to the friction coefficient through the form factor. For a hydrofoil section, the form factor accounts for the additional pressure drag caused by the foil's thickness distribution. Huchet (2021) used a Hoerner-type form factor:

Equation 5.16 — Hydrofoil form factor:

$$(1+k) = 1 + 2\left(\frac{t}{c}\right) + 60\left(\frac{t}{c}\right)^4 \tag{5.16}$$

where t/c is the thickness-to-chord ratio of the foil section and $(1+k)$ is the form factor multiplier applied to the friction coefficient to obtain the profile drag coefficient: $C_{D,P} = (1+k) \cdot C_f$ (Huchet, 2021).

The spray drag coefficient for a surface-piercing hydrofoil was expressed as:

Equation 5.17 — Spray drag coefficient:

$$C_{D,\text{spray}} = 0.009 + 0.013\left(\frac{t}{c}\right) \tag{5.17}$$

This formulation shows that thicker foil sections generate more spray drag due to the larger disturbance of the free surface at the foil–water intersection (Huchet, 2021). The spray drag is a significant contributor for surface-piercing foils such as the Z-foils of the NACRA 17 catamaran.

The induced drag coefficient follows from classical lifting-line theory:

$$C_{D,i} = \frac{C_L^2}{\pi \cdot AR \cdot e}$$

where C_L is the lift coefficient, AR is the aspect ratio of the foil, and e is the Oswald efficiency factor. This relationship confirms that higher lift (required for foiling flight) comes at the cost of increased induced drag.

5.3.5 Air Resistance and Wind Forces

The aerodynamic force on a sail, which by extension illustrates the physics of air resistance on maritime vessels, can be formulated as (Bejan et al., 2020):

Equation 5.18 — Aerodynamic force on sail:

$$F_a \sim C_D \cdot \frac{HL}{2} \cdot \frac{1}{2}\,\rho_a\, V_a^2 \tag{5.18}$$

where $C_D \sim 1$, H is the mast height, L is the hull length (so $HL/2$ approximates the sail area), ρ_a is the air density, and V_a is the wind speed.

The same physics applies to the aerodynamic drag on the superstructure of any vessel: the force is proportional to the projected frontal area, the air density, the square of the relative wind speed, and a drag coefficient.

Furthermore, when a sailing vessel moves and the wind blows, the apparent wind angle becomes smaller as boat speed increases. At maximum speed, the sails are pulled to the centreline of the boat as the apparent wind angle approaches its minimum (Bejan et al., 2020).

For powered merchant vessels, the wind resistance on the superstructure is quantified using the projected area method with wind tunnel–derived coefficients (Rawson & Tupper, 2001):

Equation 5.19 — Wind resistance on superstructure:

$$R_{\text{wind}} = \frac{1}{2}\,\rho_a\,C_r\,V_{\text{app}}^2\left(A_T\cos^2\alpha + A_L\sin^2\alpha\right) \tag{5.19}$$

where ρ_a is the air density ($\approx 1.22\,\text{kg/m}^3$), V_{app} is the apparent wind speed (the vector sum of true wind and ship motion), A_T and A_L are the transverse and lateral projected areas of the above-water hull and superstructure, α is the apparent wind angle relative to the ship heading, and C_r is an empirical resistance coefficient (Rawson & Tupper, 2001). Wind tunnel tests on merchant-ship models give typical values of C_r in the range 0.8–1.0 for cargo vessels, 0.8–0.9 for passenger vessels, and 1.0–1.1 for tankers in ballast (with large freeboard) (Rawson & Tupper, 2001). The wind speed increases with height above the sea surface following the power-law profile $V/V_0 = (z/z_0)^{\alpha_w}$, where $z_0 = 10\,\text{m}$ is the standard reference height and $\alpha_w \approx 0.12$ over the open sea (Molland, 2008).

For beam winds ($\alpha \approx 90°$), the lateral component of wind force becomes the dominant concern, producing a heeling moment that reduces stability (Chapter 4). At headwind angles, the longitudinal wind drag adds directly to the hull resistance and must be accounted for in powering calculations (Rawson & Tupper, 2001).

5.3.6 Added Resistance in Waves

When a vessel advances through a seaway, it experiences a mean resistance increment above the calm-water value. This *added resistance in waves* is a second-order hydrodynamic effect arising from the time-averaged drift forces of the wave–body interaction. Rawson and Tupper (2001) describe the physical mechanism: the ship's heave and pitch motions radiate energy into the surrounding wave field, and the time-averaged momentum flux of these radiated waves produces a net retarding force.

The added resistance is most significant when the encounter wave length is comparable to the ship length ($\lambda/L_{pp} \approx 1$), where the heave and pitch RAOs are largest. At long waves ($\lambda/L_{pp} \gg 1$), the ship follows the wave surface with little relative motion and the added resistance is small; at short waves ($\lambda/L_{pp} \ll 1$), the motions are likewise small and the added resistance is dominated by wave reflection from the bow (Rawson & Tupper, 2001).

The non-dimensional added resistance coefficient is defined as (el Moctar et al., 2021):

Equation 5.20 — Added resistance coefficient:

$$C_{AW} = \frac{R_{AW}}{\rho\,g\,\zeta_A^2\,B^2/L_{pp}} \tag{5.20}$$

where R_{AW} is the mean added resistance force, ζ_A is the wave amplitude, B is the ship breadth, and L_{pp} is the length between perpendiculars (el Moctar et al., 2021). The ITTC 1957 friction line (Equation 5.7) addresses calm-water frictional resistance only; the added resistance must be superimposed to obtain the total resistance in a seaway.

For a fully developed sea state, the mean added resistance in irregular waves is obtained by integrating the regular-wave added resistance coefficient over the wave energy spectrum (Rawson & Tupper, 2001):

$$\overline{R}_{AW} = 2 \int_0^\infty C_{AW}(\omega)\, S_\zeta(\omega)\, \mathrm{d}\omega$$

where $S_\zeta(\omega)$ is the wave spectral density. For a typical merchant vessel in head seas of sea state 6, the added resistance can increase total resistance by 30–40%, causing a corresponding involuntary speed reduction even at full engine power (Faltinsen, 1990; Rawson & Tupper, 2001). This has direct consequences for voyage planning, fuel consumption, and schedule reliability.

5.3.7 Total Resistance and Effective Power

The total water resistance on a hull is the sum of the frontal (form) drag and the skin friction drag (Bejan et al., 2020):

Equation 5.21 — Total water drag force:

$$F_w \sim \left[C_D \cdot D_x\, D_y + C_f\, (D_x + 2D_y)\, L \right] \cdot \frac{1}{2}\, \rho_w\, V_w^2 \tag{5.21}$$

The quantity in the square brackets depends on the two aspect ratios D_x/D_y and D_x/L, subject to the constraint that the displaced volume $D_x\, D_y\, L$ is fixed (equal to the vessel's total weight divided by the water density).

Minimising the drag (i.e., minimising the bracketed quantity subject to the volume constraint) yields the optimal hull proportions:

Equation 5.22 — Optimal beam-to-draft ratio:

$$\frac{D_x}{D_y} \sim 2 \tag{5.22}$$

Equation 5.23 — Optimal length-to-beam ratio:

$$\frac{L}{D_x} \sim \left(\frac{C_D}{2\, C_f} \right)^{1/2} \gg 1 \tag{5.23}$$

With $C_D \sim 1$ and $C_f \sim 10^{-2}$, this gives $L/D_x \sim 7$, meaning the hull should be roughly seven times longer than it is wide (Bejan et al., 2020).

When these optimal ratios are applied, the resistance simplifies to:

Equation 5.24 — Optimised drag force:

$$F_w \sim 3 \left(\frac{2C_f}{C_D} \right)^{1/2} L^2 \cdot \frac{1}{2} \rho_w V_w^2 \tag{5.24}$$

The boat speed V_w is then determined by the balance between this optimised drag and the aerodynamic driving force F_a, yielding the mast-to-length ratio (Bejan et al., 2020):

Equation 5.25 — Height-to-length ratio:

$$\frac{H}{L} \sim \left(\frac{V_w}{V_a} \right)^{1/2} \tag{5.25}$$

This result indicates that as the vessel aims for higher speeds (V_w approaching V_a), the mast height should approach the hull length—a prediction confirmed by empirical data from 96 sailboat models (Bejan et al., 2020).

In standard naval architecture practice, the total resistance of a powered ship is decomposed not in terms of forces directly, but in terms of dimensionless resistance coefficients. Guedes Soares and Santos (2015) employ the ITTC methodology in which the total model resistance coefficient is expressed as:

Equation 5.26 — Total resistance coefficient decomposition:

$$C_{TM} = C_F \, (1 + k) + C_R \tag{5.26}$$

where C_F is the ITTC-57 frictional resistance coefficient (Equation 5.7), $(1 + k)$ is the form factor that accounts for the viscous pressure drag beyond the flat-plate friction, and C_R is the residuary resistance coefficient (Guedes Soares & Santos, 2015). The residuary resistance C_R is dominated by wave-making effects at moderate-to-high Froude numbers but also contains contributions from transom stern effects, eddy formation, and flow separation.

The corresponding total resistance force is then:

$$R_T = C_{TM} \cdot \tfrac{1}{2} \, \rho \, S \, V^2$$

where S is the wetted surface area (Equation 5.8) and V is the vessel speed. The effective power required to overcome this resistance is $P_E = R_T \times V$.

United States Naval Academy (2021) present the full *powering chain* that connects the effective power to the engine output. The effective horsepower (EHP$=\ P_E$) must be augmented through several stages to account for hull–propeller interaction, propeller losses, shaft-line losses, and engine margins. The sequence is: EHP $\rightarrow$ thrust horsepower (THP), accounting for thrust deduction and wake fraction; THP $\rightarrow$ delivered horsepower (DHP), incorporating the propeller open-water efficiency; DHP $\rightarrow$ shaft horsepower (SHP), adding shaft bearing and seal losses; and SHP $\rightarrow$ brake horsepower (BHP), including gearbox and generator loads (United States Naval Academy, 2021). The ratio EHP/SHP—the *propulsive coefficient*—is

typically 0.55–0.70 for conventional merchant vessels, meaning that 30–45% of the engine power is dissipated in the hull–propeller–shaft-line system rather than in overcoming water resistance. This powering chain is developed further in Chapter 8.

This coefficient-based decomposition is the foundation of the towing tank methodology: the model is tested at the correct Froude number, the total resistance is measured, frictional resistance is subtracted using the ITTC-57 line, and the remainder (residuary resistance) is scaled to full size under the assumption that C_R is the same at model and ship scale (Guedes Soares & Santos, 2015).

5.4 Applications in Maritime Systems

5.4.1 Hull Form Optimisation

The analysis of Bejan et al. (2020) provides a physics-based template for hull form optimisation. The three predicted aspect ratios ($D_x/D_y \sim 2$, $L/D_x \gg 1$, $H/L \sim 1$), illustrated in Figure 5.3, were confirmed by empirical data from 96 sailboat models spanning displacements from approximately 500 kg (Ultimate 20) to over $51\,000$ kg (Swan 77). Remarkably, the aspect ratios showed no systematic dependence on displacement, confirming scale-independent geometric similarity.

The data also revealed that hull shape configurations (fin keel, long keel, keel/centreboard, lifting keel) and rig setups (fractional sloop, masthead sloop, cutter, yawl) varied, but the fundamental external proportions remained consistent across all designs (Bejan et al., 2020).

This universality suggests that any hull form optimisation procedure—whether using computational fluid dynamics or towing tank testing—will converge toward the same fundamental proportions dictated by drag minimisation physics.

A complementary approach to hull form optimisation is the systematic series method, in which model tests of parametrically varied hull forms are condensed into regression equations. Guedes Soares and Santos (2015) report the application of the Van Oortmerssen regression for estimating the residuary resistance of small displacement vessels in the length range $15\,\mathrm{m}$ to $75\,\mathrm{m}$. This method, developed from 970 data points covering 93 model tests, expresses the residuary resistance ratio R_R/Δ as a function of Froude number F_n, prismatic coefficient C_P, length-to-beam ratio L_D/B, beam-to-draught ratio B/T, midship coefficient C_M, and waterline entrance angle, using a set of 48 regression coefficients (Guedes Soares & Santos, 2015).

For small craft with round-bilge hull forms, Guedes Soares and Santos (2015) also present the WUMTIA C-factor method, which provides a direct estimate of effective power through a single dimensionless performance parameter:

Equation 5.27 — WUMTIA C-factor for small craft power estimation:

$$C_{\text{FAC}} = \frac{V^3}{30.1266\ \Delta\ L\ P_E} \tag{5.27}$$

where V is the vessel speed in m/s, Δ is the displacement in tonnes, L is the waterline length in m, and P_E is the effective power in kW (Guedes Soares & Santos, 2015). This formulation, derived from regression analysis of over 30 round-bilge hull models tested at the University of Southampton, encapsulates the resistance characteristics of the hull into a single number that typically lies between 50 and 70 at volume Froude numbers above 1.0.

Sutulo and Guedes Soares (2023) extend the hull form optimisation discussion to two specialised operating environments. For vessels operating in shallow or restricted waters, the wave-making resistance increases markedly as the depth Froude number $F_{nh} = V/\sqrt{g\,h}$ approaches unity, because the wave system transitions from subcritical to supercritical propagation; the resulting resistance hump can exceed the deep-water value by a factor of two or more (Sutulo & Guedes Soares, 2023). In polar waters, ice-breaking capability imposes additional geometric constraints: the bow form must be designed to break, lift, and clear ice floes, requiring a hull entrance angle and stem profile that differ fundamentally from the fine waterline entrance angles optimal for open-water resistance. Sutulo and Guedes Soares (2023) present parametric studies of polar transport vessel bow forms, showing how the competing demands of ice resistance and open-water resistance are reconciled through multi-objective optimisation. These specialised environments demonstrate that while the fundamental physics of resistance (drag $\propto V^2$) remains universal, the optimal hull geometry is sensitive to the operating boundary conditions.

5.4.2 Speed--Power Prediction

The critical velocity formula $V_c \approx 1.25\sqrt{L_{WL}}$ (Bejan et al., 2020) provides a first-order estimate of the maximum displacement-mode speed of a vessel. This is directly applicable to speed–power prediction: for a sailboat with a waterline length of 10 m, the critical velocity is approximately 3.95 m/s (7.7 kn). Exceeding this speed requires either surfing, planing, or foiling to escape the bow wave trap.

The Performance Handicap Racing Fleet (PHRF) rating system, referenced in the sailboat data of Bejan et al. (2020), provides empirical validation. The fastest boats in the dataset (e.g., DK 46 with PHRF = -30) achieve corrections approximately 1.75 times faster than the slowest (e.g., Bullseye with PHRF = 360), demonstrating the wide range of performance within the design space while still conforming to the same geometric proportions.

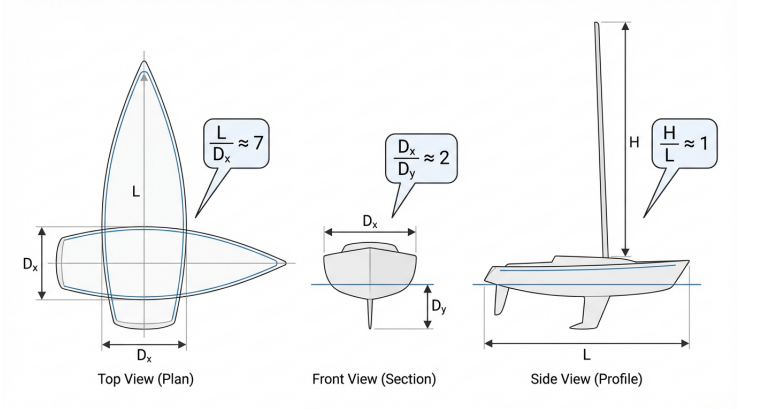

Figure 5.3: Three orthogonal views of a generic sailing-vessel hull illustrating the optimal aspect ratios predicted by drag-minimisation physics. Top view: waterline length L and beam D_x with $L/D_x \approx 7$. Front cross-section: beam D_x and submerged draft D_y with $D_x/D_y \approx 2$. Side profile: hull length L and mast height H with $H/L \approx 1$. These proportions, derived from the balance between form drag ($C_D \sim 1$) and skin friction ($C_f \sim 10^{-2}$), are confirmed across 96 sailboat models spanning four orders of magnitude in displacement (Bejan et al., 2020).

5.4.3 Hull Fouling and Resistance Penalties

Biological fouling of the hull surface—the accumulation of marine organisms including slime, algae, barnacles, and tubeworms—increases the skin friction drag by altering the effective surface roughness. Rawson and Tupper (2001) describe the mechanism: fouling organisms increase the equivalent sand-grain roughness height k_s of the hull surface, which shifts the velocity profile in the turbulent boundary layer and increases the wall shear stress.

The ITTC methodology accounts for hull roughness through the roughness allowance ΔC_F in the full-scale resistance extrapolation (Equation 5.33). For a new vessel with an anti-fouling coating, Birk (2019) recommend $\Delta C_F = 0.00035$–0.0004. As fouling accumulates during service, the effective roughness increases and ΔC_F grows.

Rawson and Tupper (2001) report that heavy fouling can increase the frictional resistance by 25–40% after 12–18 months without cleaning, with a corresponding speed loss of 1–2 knots at constant power or a fuel consumption increase of 10–15% at constant speed. These penalties are equivalent to an increase in the boundary layer momentum thickness, which Equations 5.7 and 5.4 capture through the Reynolds-number dependence of the friction coefficient applied to the fouled surface.

The economic and environmental importance of fouling management—through anti-fouling coatings, hull cleaning schedules, and operational speed profiles—follows directly from this resistance physics: even modest

increases in k_s produce measurable penalties in fuel consumption over an ocean crossing (Rawson & Tupper, 2001).

5.4.4 CFD Verification and Validation for Resistance Prediction

The advent of Reynolds-Averaged Navier–Stokes (RANS) solvers for ship flows has enabled resistance prediction from first principles, but a rigorous framework is needed to quantify the credibility of such predictions. Larsson et al. (2003) reported the results of the Gothenburg 2000 Workshop, an international benchmark exercise in which 20 groups applied 16 different RANS codes to three modern hull forms: the KRISO tanker KVLCC2 (full form, $C_B = 0.81$), the KRISO containership KCS ($C_B = 0.65$), and the US Navy combatant DTMB 5415 ($C_B = 0.506$).

Verification and Validation Framework

The verification and validation (V&V) methodology adopted by the workshop follows the procedures of the 22nd International Towing Tank Conference (ITTC), based on the comprehensive formulation of Stern et al. (2001). The simulation error δ_S is defined as the difference between a simulation result S and the truth T, decomposed into modelling and numerical contributions (Larsson et al., 2003):

Equation 5.28 — Simulation error decomposition:

$$\delta_S = S - T = \delta_{SM} + \delta_{SN} \tag{5.28}$$

where δ_{SM} is the modelling error (turbulence closure, boundary conditions, domain simplifications) and δ_{SN} is the numerical error (discretisation, iteration, time-stepping).

Verification is the process of estimating the simulation numerical uncertainty U_{SN}. The numerical error is decomposed into contributions from iteration convergence, grid spacing, time step, and other parameters (Larsson et al., 2003):

Equation 5.29 — Simulation numerical uncertainty:

$$U_{SN}^2 = U_I^2 + U_G^2 + U_T^2 + U_P^2 \tag{5.29}$$

where U_I, U_G, U_T, and U_P are the uncertainties due to iteration number, grid size, time step, and other parameters, respectively. Of these, the grid uncertainty U_G typically dominates and is estimated through systematic grid-refinement studies using three or more grids.

Validation assesses the modelling uncertainty by comparing numerical results with benchmark experimental data. The comparison error E is (Larsson et al., 2003):

Equation 5.30 — Comparison error:

$$E = D - S = \delta_D - (\delta_{SM} + \delta_{SN}) \tag{5.30}$$

where D is the experimental datum and δ_D its uncertainty. Validation is achieved when $|E|$ is smaller than the validation uncertainty U_V:

Equation 5.31 — Validation uncertainty:

$$U_V^2 = U_D^2 + U_{SN}^2 \tag{5.31}$$

where U_D is the experimental uncertainty. If $|E| < U_V$, the combination of all errors is smaller than the uncertainty level and the simulation is validated at that level. If $U_V \ll |E|$, the sign and magnitude of E can guide modelling improvements (Larsson et al., 2003).

Benchmark Results and Resistance Prediction Accuracy

The Gothenburg 2000 results revealed that the coefficient of variation of the total resistance coefficient C_T across the 20 participating codes was remarkably consistent: 5.2% for KVLCC2, 5.1% for KCS, and 4.6% for DTMB 5415. However, the scatter was much larger for the individual components: the coefficient of variation for the pressure resistance C_P ranged from 18% to 36%, reflecting the greater sensitivity of the pressure-driven flow at the stern to turbulence modelling and grid resolution (Larsson et al., 2003).

Ten of the 20 groups provided quantitative grid-uncertainty estimates. For those following the ITTC procedure, the average numerical uncertainty U_{SN} was 2.9% S for KVLCC2, 2.3% S for KCS, and 3.6% S for DTMB 5415, where S denotes the finest-grid solution. Four submissions achieved validation of C_T at levels ranging from 3% to 15%, determined by comparing $|E|$ against U_V (Equation 5.31) (Larsson et al., 2003).

Turbulence Modelling and the Stern Flow Problem

A central finding of the workshop series—spanning 1980, 1990, 1994, and 2000—was the progressive improvement in predicting the stern viscous flow. The boundary layer methods that dominated the 1980 workshop failed to predict the velocity field near the propeller plane; by 2000, RANS methods with two-equation turbulence models (k–ω, k–ε) or Reynolds stress models routinely captured the hook-shaped axial velocity contours generated by the bilge vortex of the full-form KVLCC2 (Larsson et al., 2003).

The k–ω SST model generally outperformed standard k–ε in stern flow prediction because the SST formulation activates the k–ω model in the near-wall region while blending to k–ε in the free stream, avoiding the sensitivity of pure k–ε to inlet conditions. Reynolds stress models produced the best turbulent kinetic energy profiles, but at greater computational cost and reduced solver robustness. The average grid size grew from 8×10^4 points in 1990 to 7×10^5 in 2000, yet none of the solutions achieved grid independence, and the workshop recommended continued grid refinement (Larsson et al., 2003).

Form Factor Scale Effect

A particularly significant finding concerned the form factor $(1 + k)$. All full-scale RANS predictions for KVLCC2 showed a substantial increase in the form factor compared with the model-scale value: the mean $(1 + k)$ rose from 0.247 (model scale, $Re = 4.6 \times 10^6$) to 0.378 (full scale, $Re = 2.03 \times 10^9$)—an increase of 53% (Larsson et al., 2003). This contradicts the standard ITTC extrapolation procedure (Equation 5.33), which assumes a constant form factor between model and ship scale. The physical explanation lies in the Reynolds-number dependence of the three-dimensional boundary layer development at the stern: at full scale the boundary layer is relatively thinner, the bilge vortex weakens, and the pressure recovery pattern changes, all of which alter the viscous pressure resistance component. This finding has important implications for the accuracy of model-to-ship resistance extrapolation (Larsson et al., 2003). The scatter in computed total resistance coefficients across the participating codes is shown in Figure 5.4.

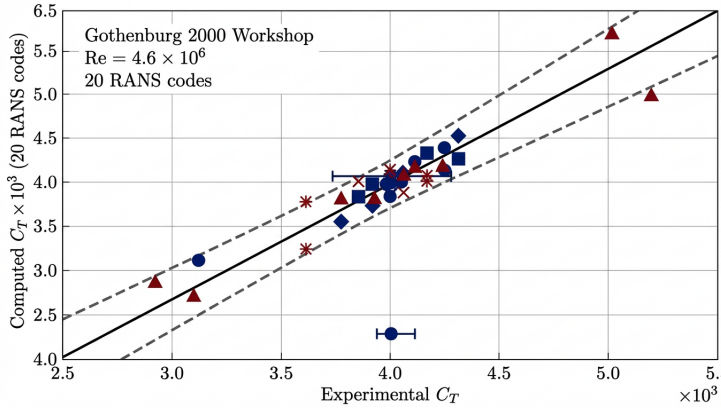

Figure 5.4: Comparison of computed and experimental total resistance coefficient C_T for the KVLCC2 hull form at model scale ($Re = 4.6 \times 10^6$). The scatter across 20 RANS codes in the Gothenburg 2000 benchmark was approximately 5%, with the majority of solutions within 2–3% of the experimental value. The largest discrepancies arise in the pressure resistance component (up to 36% variation), reflecting the sensitivity of stern flow prediction to turbulence modelling and grid resolution (Larsson et al., 2003).

5.5 Discussion

The analysis presented in this chapter, based on Bejan et al. (2020), demonstrates that the physics of ship resistance imposes universal geometric constraints on vessel design. The separation of total resistance into frontal drag (C_D) and frictional resistance (C_f), combined with constrained optimisation,

yields predictions that are confirmed by empirical data spanning over a century of sailboat design.

The ratio $C_D/C_f \sim 100$ is the fundamental driver of hull slenderness. If skin friction were comparable to form drag, the optimal hull would be much less elongated. Conversely, if skin friction were negligible, the optimal hull would be infinitely slender. The actual ratio produces the moderate slenderness ($L/D_x \sim 7$) observed in practice.

The framework also explains why "the boat has been this way since antiquity" (Bejan et al., 2020, p. 2)—the physics of drag has not changed, and so neither has the optimal response to it.

The ITTC-57 friction correlation introduced from Huchet (2021) provides the quantitative bridge between the order-of-magnitude estimates of Bejan et al. (2020) and standard engineering practice. The form $C_f = 0.075/(\log_{10} Re - 2)^2$ gives a numerical value of the friction coefficient as a function of Reynolds number, enabling actual resistance predictions rather than scaling arguments alone.

The hydrofoil drag decomposition (Huchet, 2021) extends the resistance framework to lifting surfaces—a regime not covered by the Bejan et al. (2020) hull-drag model. The four-component decomposition ($C_{D,P} + C_{D,i} + C_{D,w} + C_{D,\text{spray}}$) shows that foiling introduces additional drag mechanisms (induced drag, spray drag) that are absent or negligible for conventional displacement hulls. The form factor $(1+k) = 1 + 2(t/c) + 60(t/c)^4$ quantifies the penalty of foil thickness on viscous drag, while the spray drag coefficient $C_{D,\text{spray}} = 0.009 + 0.013(t/c)$ captures the free-surface interaction unique to surface-piercing foils.

Birk (2019) provides a comprehensive treatment of the resistance test methodology based on the ITTC recommended procedures. A geometrically similar model of the hull is towed at speeds corresponding to a range of Froude numbers. The total model resistance R_{TM} is measured and converted to a non-dimensional coefficient $C_{TM} = 2R_{TM}/(\rho\, S_M\, v_M^2)$, where S_M is the model wetted surface (Birk, 2019).

The ITTC form-factor method decomposes the total resistance coefficient as:

Equation 5.32 — ITTC form-factor decomposition (model scale):

$$C_{TM} = (1+k)\, C_{FM} + C_W \tag{5.32}$$

where C_{FM} is evaluated from the ITTC-57 correlation line (Equation 5.7) at the model Reynolds number $Re_M = v_M\, L_{OS,M}/\nu_M$, and $(1+k)$ is the form factor determined by Prohaska's method (Equation 5.10). The wave resistance coefficient C_W is assumed to be a function of Froude number alone and is the same at model and full scale (Birk, 2019).

Extrapolation to full-scale follows from the principle that C_W is invariant between model and ship at the same Froude number, while the frictional component changes due to the different Reynolds numbers:

Equation 5.33 — Full-scale resistance extrapolation:

$$C_{TS} = (1+k)\,C_{FS} + C_W + \Delta C_F \tag{5.33}$$

where C_{FS} is the ITTC-57 friction coefficient at the ship Reynolds number and ΔC_F is the roughness allowance for surface condition (Birk, 2019). This procedure—Froude's hypothesis combined with the ITTC form-factor method—remains the standard framework for model-to-ship resistance scaling used in towing tanks worldwide.

The systematic series approach (Guedes Soares & Santos, 2015) complements the physics-based drag minimisation of Bejan et al. (2020). While the constructal theory of Bejan et al. (2020) predicts optimal proportions from first principles, the regression methods (Van Oortmerssen, WUMTIA C-factor) provide quantitative resistance predictions for specific hull forms. The resistance decomposition into $C_F(1+k)+C_R$ (Equation 5.26) is the practical implementation of the frictional–pressure drag separation that Bejan et al. (2020) represented by C_f and C_D. Guedes Soares and Santos (2015) also demonstrate the application of Computational Fluid Dynamics (CFD) using Reynolds-Averaged Navier–Stokes (RANS) solvers for resistance prediction, showing discrepancies within a few percent of towing tank results for well-validated cases—an approach increasingly used alongside, and eventually as a complement to, model testing.

The Gothenburg 2000 benchmark results (Larsson et al., 2003) place this claim in quantitative perspective. With C_T scatter of approximately 5% across 20 independent RANS codes and average numerical uncertainties of $U_{SN} \approx 3$–6%, the current generation of CFD methods provides resistance estimates whose accuracy approaches that of towing tank experiments ($U_D \approx 1$–2%). The V&V framework of Equations 5.28–5.31 provides the formal criterion for judging this accuracy: validation is achieved only when the comparison error $|E|$ falls below the combined experimental and numerical uncertainty U_V. The finding that the form factor $(1+k)$ increases by over 50% from model to full scale challenges the constant-form-factor assumption embedded in Equation 5.33 and suggests that RANS-based full-scale simulations may ultimately provide more reliable powering predictions than traditional extrapolation (Larsson et al., 2003).

The Admiralty coefficient method (Ridley & Patterson, 2014) complements the ITTC form-factor decomposition by providing a quick estimation tool that requires only displacement, speed, and shaft power. While it lacks the physical rigour of the $C_T = (1+k)C_F + C_W$ decomposition, its simplicity makes it indispensable for preliminary design and for cross-checking detailed resistance calculations. The Admiralty coefficient is essentially a dimensional-analysis result: since $R_T \sim \rho V^2 L^2$ and $\Delta \sim \rho L^3$, it follows that $P_s = R_T V \sim \rho V^3 L^2 \sim \Delta^{2/3} V^3$, which is the basis of the constant-C_A assumption.

The full powering chain (United States Naval Academy, 2021)—from effective horsepower through thrust, delivered, shaft, and brake horsepower—

quantifies the progressive energy losses between the water resistance and the prime mover. This cascade of efficiencies (hull, propeller, shaft, mechanical) connects the resistance physics developed in this chapter to the propulsion physics of Chapter 8 and provides the engineering framework within which all resistance reduction measures must be evaluated.

The extension to shallow water by Sutulo and Guedes Soares (2023)—where resistance can more than double as the depth Froude number approaches unity—and to polar waters—where ice-breaking constraints fundamentally alter the optimal bow geometry—demonstrates that the universal drag physics ($F \propto V^2$) must be supplemented by environment-specific boundary conditions to obtain practical hull designs.

5.6 Conclusion

Ship resistance is governed by the interplay of three physical mechanisms—viscous friction, pressure drag, and wave-making—whose relative contributions depend on hull geometry and speed. The general quadratic drag law $F_d = bv^2$ establishes the fundamental velocity dependence (Campbell, 2025), and constrained optimisation of total drag under a fixed displacement yields the three aspect ratios that characterise sailing-vessel hulls: $D_x/D_y \sim 2$, $L/D_x \sim (C_D/2C_f)^{1/2} \gg 1$, and $H/L \sim (V_w/V_a)^{1/2}$ (Bejan et al., 2020). These predictions, confirmed across 96 sailboat models spanning four orders of magnitude in displacement, demonstrate that the physics of drag minimisation imposes universal geometric constraints on vessel design. The critical hull speed $V_c \approx 1.25\sqrt{L_{WL}}$ caps the displacement-mode speed of any vessel, and exceeding it requires planing, surfing, or hydrofoil lift (Bejan et al., 2020). The ITTC-57 correlation $C_f = 0.075/(\log_{10} Re - 2)^2$ (Huchet, 2021) provides the quantitative bridge between these scaling arguments and engineering practice, while the hydrofoil drag decomposition into profile, induced, wave, and spray components—with the Hoerner form factor $(1 + k) = 1 + 2(t/c) + 60(t/c)^4$—extends the framework to lifting surfaces (Huchet, 2021).

The model-to-ship extrapolation methodology developed by the ITTC separates the total resistance into a viscous component $(1+k)\,C_F$ and a wave resistance C_W that is assumed invariant between model and ship at the same Froude number (Birk, 2019). The hull form factor $(1 + k)$ is determined by Prohaska's method at low Froude numbers ($Fr < 0.2$), and the full-scale coefficient is obtained as $C_{TS} = (1 + k)\,C_{FS} + C_W + \Delta C_F$, where ΔC_F accounts for hull roughness (Birk, 2019). The Admiralty coefficient $C_A = \Delta^{2/3} V^3/P_s$ provides a complementary rapid estimation tool for preliminary design (Ridley & Patterson, 2014), while the full powering chain (EHP through THP, DHP, SHP, and BHP) quantifies the progressive efficiency losses between water resistance and the prime mover, with propulsive coefficients typically in the range 0.55–0.70 (United States Naval Academy, 2021). The wind resistance

formulation $R_{\text{wind}} \propto C_r V_{\text{app}}^2 (A_T \cos^2\alpha + A_L \sin^2\alpha)$ (Rawson & Tupper, 2001) and the added resistance in waves complete the external force inventory for powering calculations in a seaway.

The Gothenburg 2000 CFD benchmark provides the quantitative standard against which computational resistance predictions are judged. The V&V framework decomposes simulation error into modelling and numerical contributions ($\delta_S = \delta_{SM} + \delta_{SN}$) and defines validation as $|E| < U_V = \sqrt{U_D^2 + U_{SN}^2}$ (Larsson et al., 2003). Across 20 RANS codes and three hull forms, the coefficient of variation in total resistance was approximately 5%, with numerical uncertainties of 2–6%. A particularly significant finding was that the form factor $(1 + k)$ increases by over 50% from model to full scale for a VLCC hull (0.247 $\rightarrow$ 0.378), contradicting the constant-form-factor assumption embedded in the standard ITTC extrapolation and suggesting that RANS-based full-scale simulations may ultimately provide more reliable powering predictions (Larsson et al., 2003). The extension of resistance physics to specialised environments—shallow water, where wave-making resistance doubles as $F_{nh} \rightarrow 1$, and polar waters, where ice-breaking constraints alter the optimal bow geometry—demonstrates that while the fundamental drag physics ($F \propto V^2$) is universal, optimal hull form is sensitive to the operating boundary conditions (Sutulo & Guedes Soares, 2023).

References

Attwood, E. L. (1899). *A text-book of theoretical naval architecture*. Longmans, Green; Co.

Bejan, A., Ferber, L., & Lorente, S. (2020). Convergent evolution of boats with sails. *Scientific Reports*, *10*, Article 2703. https://doi.org/10.1038/s41598-020-58940-5

Birk, L. (2019). *Fundamentals of ship hydrodynamics: Fluid mechanics, ship resistance and propulsion*. John Wiley & Sons. https://doi.org/10.1002/9781119191575

Burton, D. A., & Noble, A. (2024). *A geometrical approach to physics*. Springer. https://doi.org/10.1201/9781003228943

Campbell, C. (2025). *Physics: A focused introduction*. CRC Press. https://doi.org/10.1201/9781003571568

Carlton, J. (2012). *Marine propellers and propulsion* (3rd ed.). Butterworth-Heinemann. https://doi.org/10.1016/C2010-0-68327-1

Dera, J. (1992). *Marine physics* (P. Senn, Trans.) [Translated from Polish. Original: *Fizyka morza*, 1983]. Elsevier.

el Moctar, B. O., Schellin, T. E., & Söding, H. (2021). *Numerical methods for seakeeping problems*. Springer. https://doi.org/10.1007/978-3-030-62561-0

Faltinsen, O. M. (1990). *Sea loads on ships and offshore structures*. Cambridge University Press.

Fischer-Cripps, A. C. (2014). *The physics companion* (2nd ed.). CRC Press. https://doi.org/10.1201/b17356

Guedes Soares, C., & Santos, T. A. (Eds.). (2015). *Maritime technology and engineering: Proceedings of MARTECH 2014*. CRC Press.

Hewitt, P. G., Suchocki, J. A., & Hewitt, L. A. (2012). *Conceptual physical science* (5th ed.). Pearson.

Huchet, L. (2021). *Investigation of the influence of crew setup on performances for the Olympic NACRA 17 foiling catamaran* [Individual project]. University of Southampton.

Larsson, L., Stern, F., & Bertram, V. (2003). Benchmarking of computational fluid dynamics for ship flows: The Gothenburg 2000 workshop. *Journal of Ship Research*, *47*(1), 63–81. https://doi.org/10.5957/jsr.2003.47.1.63

Lewis, E. V. (Ed.). (1988). *Principles of naval architecture* (2nd ed.) [Three volumes]. The Society of Naval Architects; Marine Engineers.

Molland, A. F. (Ed.). (2008). *The maritime engineering reference book: A guide to ship design, construction and operation*. Butterworth-Heinemann. https://doi.org/10.1016/B978-0-7506-8987-8.X0001-7

Newman, J. N. (1977). *Marine hydrodynamics*. The MIT Press.

Rawson, K. J., & Tupper, E. C. (2001). *Basic ship theory* (5th ed.). Butterworth-Heinemann.

Ridley, J. D., & Patterson, C. J. (2014). *Ship stability, powering and resistance* (Vol. 13). Adlard Coles Nautical.

Sutulo, S., & Guedes Soares, C. (2023). Ship dynamics and hydrodynamics. *Journal of Marine Science and Engineering*, *11*(5), 911. https://doi.org/10.3390/jmse11050911

United States Naval Academy. (2021). En400: Principles of ship performance [Course notes, Fall AY2021].

Chapter 6

Ship Motions and Seakeeping

6.1 Introduction

Seakeeping describes a vessel's ability to maintain safe and effective operation in a seaway. The motions of a ship in waves—heave, pitch, roll, surge, sway, and yaw—determine the structural loads on the hull, the comfort and safety of the crew and passengers, the integrity of the cargo, and the operability of onboard equipment. These motions arise from the dynamic interaction between the hull and the incident wave field, a problem that requires the simultaneous treatment of fluid mechanics and rigid-body dynamics.

Hernández-Fontes et al. (2020) demonstrated that the type and severity of wave–structure interaction events, such as green water shipping on deck, depend sensitively on the steepness of the incoming wave (Section 6.3.5). Guedes Soares and Santos (2015) contributed the mathematical framework for computing the wave-induced forces and motions through potential flow theory and boundary element methods (Section 6.2.1).

6.2 Scientific Background

6.2.1 Ship Response as a Dynamic System

The prediction of ship motions in waves requires the solution of a boundary-value problem (BVP) for the velocity potential of the fluid. Guedes Soares and Santos (2015) formulate this problem under the assumption of potential flow of an incompressible fluid about an oscillating floating body in the presence of a free surface.

The velocity potential ϕ satisfies the Laplace equation throughout the fluid domain (Newman, 1977):

Equation 7.1 — Laplace equation in the fluid domain:

$$\nabla^2 \phi = 0 \tag{6.1}$$

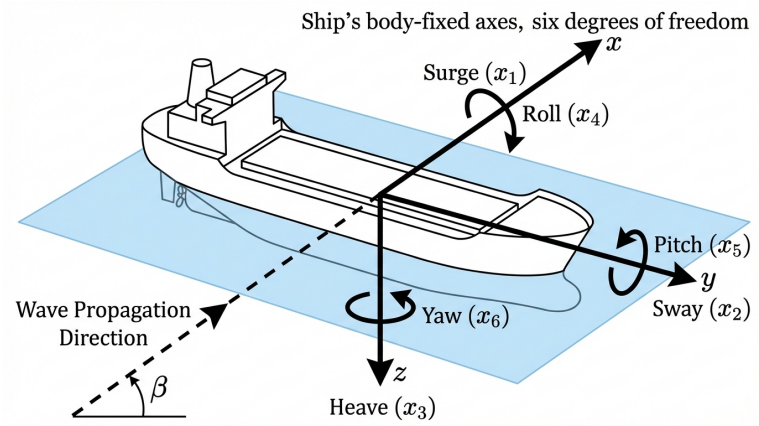

Figure 6.1: The six rigid-body degrees of freedom of a floating vessel. Translational modes—surge (x_1, longitudinal), sway (x_2, lateral), and heave (x_3, vertical)—describe displacements of the centre of gravity, while rotational modes—roll (x_4, about the longitudinal axis), pitch (x_5, about the transverse axis), and yaw (x_6, about the vertical axis)—describe angular orientations relative to the equilibrium waterplane. The coupled interactions among these six modes are governed by the equations of motion developed in Section 6.2.3. Wave propagation direction, heading angle β, and the body-fixed coordinate system are indicated; the origin is located at the intersection of the midship section, centreline plane, and calm waterplane.

On the undisturbed free surface ($z = 0$), the linearised free-surface condition is (Guedes Soares & Santos, 2015):

Equation 7.2 — Linearised free-surface condition:

$$\phi_z - \nu\,\phi = 0 \qquad \text{on } z = 0 \tag{6.2}$$

where $\nu = \omega^2/g$ for infinite water depth, ω is the wave circular frequency, and g is gravitational acceleration. On the body surface S_B, the radiation and scattering boundary conditions require that the normal velocity of the fluid matches the normal velocity of the body or scatters the incident wave, respectively (Guedes Soares & Santos, 2015).

The BVP is solved numerically using a Green function integral equation method. Guedes Soares and Santos (2015) express the radiation potential as:

Equation 7.3 — Green function integral equation:

$$2\pi\,\phi_k(\mathbf{x}) + \iint_{S_B} \phi_k(\boldsymbol{\xi})\,\frac{\partial G(\mathbf{x};\boldsymbol{\xi})}{\partial n}\,\mathrm{d}S = \iint_{S_B} G(\mathbf{x};\boldsymbol{\xi})\,n_k\,\mathrm{d}S \tag{6.3}$$

where ϕ_k is the unit-amplitude radiation potential for motion mode k, $G(\mathbf{x};\boldsymbol{\xi})$ is the free-surface Green function representing the potential at point $\mathbf{x}$ due to a unit source at $\boldsymbol{\xi}$, and n_k is the generalised normal vector on the body boundary (Guedes Soares & Santos, 2015).

The body surface is discretized into quadrilateral panels, each carrying a uniform source distribution. The accuracy of the solution depends on the panel density and distribution, with finer meshes required in regions of strong geometric curvature (bow, stern) and near the waterline (Guedes Soares & Santos, 2015).

6.2.2 Excitation Forces and Moments

The forces exciting a vessel in waves may be decomposed into two distinct components. The *Froude–Krylov force* arises from the pressure field of the undisturbed incident wave acting over the wetted hull surface; it depends only on the wave and the body geometry, not on the body's own radiated wave field. The *diffraction force* accounts for the modification of the incident wave by the presence of the hull. Together, these produce the total wave-exciting force at each oscillation frequency.

For wave lengths long compared with the vessel beam, the incident pressure field varies slowly over the hull cross-section, and the diffraction correction is small. Attwood (1899) exploited this long-wave assumption when analysing the rolling of ships broadside to a regular wave train: the buoyancy varies along the wave profile because the orbital motion of the water particles produces centrifugal acceleration, reducing the *virtual weight* at the crest and increasing it in the trough. The direction of the apparent gravitational acceleration—the *virtual upright*—is everywhere perpendicular to the wave surface, so that a small raft placed on the wave would orient its mast along this virtual upright rather than the true vertical (Attwood, 1899).

The *effective wave slope* θ_1 is the angle between the virtual upright and the true vertical. For a sinusoidal wave profile of height H and length L_w, the maximum wave slope is (Attwood, 1899):

$$\theta_{1,\max} = \frac{\pi H}{L_w}$$

Because the effective wave slope accounts for the reduction due to the ship's finite beam, it is always less steep than the geometric wave profile. This effective slope provides the excitation term in the classical rolling equation (Section 6.3.1).

Quantitative Excitation Force Formulation

Ge et al. (2026) express the total wave excitation load as the sum of the Froude–Krylov force and the diffraction force:

Equation 7.4 — Wave excitation decomposition:

$$F_I = F_K + F_D \tag{6.4}$$

where F_I is the total wave excitation load, F_K the Froude–Krylov force, and F_D the diffraction force. These components are evaluated as surface integrals

of the relevant velocity potentials over the mean wetted body surface S_0 (Ge et al., 2026):

Equation 7.5 — Froude–Krylov and diffraction force integrals:

$$F_K = \rho\, i\omega \iint_{S_0} \phi_0\, n\, \mathrm{d}S, \qquad F_D = \rho\, i\omega \iint_{S_0} \phi_7\, n\, \mathrm{d}S \tag{6.5}$$

where ρ is the seawater density, ω the wave angular frequency, ϕ_0 the incident wave potential, ϕ_7 the diffraction potential, and n the outward unit normal on the body surface (Ge et al., 2026). The Froude–Krylov force represents the pressure that the undisturbed wave field exerts directly on a stationary body, whereas the diffraction force arises from changes in wave direction, shape, and energy distribution caused by the obstruction and scattering effects of the hull (Ge et al., 2026).

Radiation Forces: Added Mass and Damping Coefficients

The motion of the vessel itself generates waves in the surrounding fluid, producing reactive forces termed *radiation forces*. These may be decomposed into a component proportional to the body's acceleration—the *added mass*—and a component proportional to its velocity—the *radiation damping* (Ge et al., 2026). Both quantities are independent of wave direction. The complex radiation coefficient μ_{jk} is obtained from the radiation potential as (Ge et al., 2026):

Equation 7.6 — Radiation coefficient (added mass and damping):

$$\mu_{jk} = \rho \iint_{S_0} \phi_k\, n_j\, \mathrm{d}S = A_{jk} + \frac{i}{\omega}\, B_{jk} \tag{6.6}$$

where A_{jk} is the added mass, B_{jk} the radiation damping, ϕ_k the radiation potential for motion mode k, and the subscripts $j, k = 1, \ldots, 6$ correspond to surge, sway, heave, roll, pitch, and yaw, respectively (Ge et al., 2026). The added mass represents the effective inertia of the fluid displaced by the body's oscillation, while the radiation damping quantifies the energy radiated away as surface waves. For nondimensionalisation, the translational ($j, k = 1, 2, 3$) and rotational ($j, k = 4, 5, 6$) coefficients are scaled as (Ge et al., 2026):

$$A^*_{jk} = \frac{A_{jk}}{m}, \quad B^*_{jk} = \frac{B_{jk}}{m\omega} \quad (j, k = 1, 2, 3)$$

$$A^*_{jk} = \frac{A_{jk}}{mD^2}, \quad B^*_{jk} = \frac{B_{jk}}{mD^2\omega} \quad (j, k = 4, 5, 6)$$

where m is the body mass and D is the characteristic transverse dimension (Ge et al., 2026). Numerical investigations of the DARPA SUBOFF model demonstrate that as submergence depth increases beyond approximately one hull diameter, the added mass coefficients become nearly independent of wave frequency, converging to constant values, while the radiation damping

coefficients approach zero—confirming the vanishing free-surface influence at depth (Ge et al., 2026).

An alternative approach to computing these coefficients, particularly economical for bodies of revolution, is the source distribution method. Ferdinande and Kritis (1980) developed a computation procedure for vertical axisymmetric floating bodies in heaving motion, inspired by the singularity distribution technique of Yeung and the finite-distance radiation condition of Bai. In contrast to the Green function method of Equation (6.3), in which sources are distributed only over the wetted body surface, the source distribution approach places sources over the entire boundary of the fluid region—including the free surface, the radiation boundary at a finite radial distance R' (typically five to six times the body radius), and the seabed. Although this extends the number of boundary elements, the kernels of the resulting integral equations are considerably simpler than those of the free-surface Green function, reducing the per-element computational cost (Ferdinande & Kritis, 1980).

For an axisymmetric body oscillating in heave, the velocity potential depends only on the radial and vertical coordinates, and the three-dimensional boundary can be discretized entirely within a meridional plane. Ferdinande and Kritis (1980) exploit this axial symmetry by subdividing the boundary into co-axial ring elements: horizontal surfaces (free surface, seabed, and any horizontal body surfaces) are divided into plane annular rings, vertical cylindrical surfaces into elementary co-axial cylinders, and non-horizontal body surfaces into elementary conical rings. The potential is taken as constant over each ring, with its value assigned at a mid-element reference point. The resulting set of N linear equations for the N complex potentials $\phi(T_i) = \phi_1 + i\phi_2$ is solved directly, and the real and imaginary parts yield the added mass and damping coefficient, respectively (Ferdinande & Kritis, 1980). The surface integrals P_{ij} and Q_{ij} over each ring admit analytical evaluation in the radial variable and are completed by Gauss–Legendre quadrature in the circumferential direction, providing a combined analytical–numerical scheme that minimises computation time (Ferdinande & Kritis, 1980).

For practical application, the added mass a and damping coefficient b are expressed in nondimensional form scaled by the displacement volume V (Ferdinande & Kritis, 1980):

Equation 7.7 — Nondimensional added mass and damping (volume scaling):

$$a^* = \frac{a}{\rho V}, \qquad b^* = \frac{b}{\rho V \omega} \tag{6.7}$$

where ρ is the fluid density, V the body's volume displacement, and ω the oscillation angular frequency. This volume-based scaling is particularly convenient for comparing bodies of different geometric proportions; for vertical circular cylinders, the single governing parameter is the draft-to-radius ratio D/R, and the nondimensional frequency parameter $\omega^2 R/g$ serves as the abscissa (Ferdinande & Kritis, 1980).

The accuracy of the method was verified against Havelock's classical exact

solution for the heaving hemisphere in deep water, computed numerically by Porter. The nondimensional added mass and damping coefficient obtained from the source distribution method agreed closely with the exact analytical curves across the full frequency range (Ferdinande & Kritis, 1980). Experimental validation was performed in a purpose-built $4\,\mathrm{m} \times 4\,\mathrm{m} \times 1\,\mathrm{m}$ tank using a Scotch-yoke forced-oscillation device. The exciting force was decomposed into its in-phase (inertial) and quadrature (dissipative) components by an electro-mechanical Fourier analyser employing a synchro-resolver and chopper-stabilised integrators, after filtering out higher harmonics and mechanical noise (Ferdinande & Kritis, 1980). For vertical circular cylinders with $D/R = 0.25, 0.50, 0.75, 1.0, 1.5,$ and 2.0, the experimental data confirmed the computed coefficients over the tested frequency range, in both deep water and restricted-depth conditions (water-depth-to-draft ratios h/D from approximately 1.5 to infinity). Interpolation between the tabulated D/R ratios and water-depth ratios enables estimation of the hydrodynamic coefficients for any axisymmetric cylinder of practical interest (Ferdinande & Kritis, 1980).

Added Mass Tensor and Kinetic Energy of the Fluid

The radiation coefficient of Equation (6.6) is a manifestation of a more general concept: the added mass tensor. Korotkin (2009) develops the complete theory by considering a rigid body moving through an ideal, incompressible, infinite fluid. Under these assumptions the flow is irrotational and described by a velocity potential ϕ satisfying the Laplace equation $\Delta\phi = 0$, with the impermeability (water-tightness) condition $\partial\phi/\partial n\big|_{S} = u_n$ on the body surface S and the quiescence condition $\nabla\phi \to 0$ as $r \to \infty$ (Korotkin, 2009).

By decomposing the body velocity into translational components (u_1, u_2, u_3) along the coordinate axes and rotational components (u_4, u_5, u_6) about them, the potential is expressed as a linear superposition of six unit potentials (Korotkin, 2009):

$$\phi = \sum_{i=1}^{6} u_i \, \phi_i$$

where each ϕ_i satisfies the Laplace equation and the boundary condition for unit velocity in the i-th mode. The total kinetic energy of the surrounding fluid is then (Korotkin, 2009):

Equation 7.8 — Kinetic energy of fluid via added mass tensor:

$$2T = \sum_{i=1}^{6} \sum_{k=1}^{6} \lambda_{ik} \, u_i \, u_k \tag{6.8}$$

where the added mass coefficients λ_{ik} are defined by (Korotkin, 2009):

Equation 7.9 — Added mass tensor components:

$$\lambda_{ik} = -\rho \iint_{S} \frac{\partial \phi_i}{\partial n} \, \phi_k \, \mathrm{d}S \tag{6.9}$$

The tensor λ_{ik} is symmetric ($\lambda_{ik} = \lambda_{ki}$), so of the 36 components only 21 are independent. The diagonal terms λ_{ii} are always positive, whereas the off-diagonal (cross-coupling) terms may be positive, negative, or zero (Korotkin, 2009). The dimensions of the tensor components reflect the coupling they represent: λ_{ik} for $i, k = 1, 2, 3$ has dimension of mass, for $i = 1,2,3$ and $k = 4,5,6$ it has dimension of static moment, and for $i, k = 4, 5, 6$ it has dimension of moment of inertia (Korotkin, 2009).

The complete expression for the kinetic energy expands to (Korotkin, 2009):

$$\begin{aligned} 2T = {} & \lambda_{11}u_1^2 + \lambda_{22}u_2^2 + \lambda_{33}u_3^2 + 2\lambda_{12}u_1u_2 + 2\lambda_{13}u_1u_3 + 2\lambda_{23}u_2u_3 \\ & + 2u_1(\lambda_{14}u_4 + \lambda_{15}u_5 + \lambda_{16}u_6) + 2u_2(\lambda_{24}u_4 + \lambda_{25}u_5 + \lambda_{26}u_6) \\ & + 2u_3(\lambda_{34}u_4 + \lambda_{35}u_5 + \lambda_{36}u_6) + \lambda_{44}u_4^2 + \lambda_{55}u_5^2 + \lambda_{66}u_6^2 \\ & + 2\lambda_{45}u_4u_5 + 2\lambda_{46}u_4u_6 + 2\lambda_{56}u_5u_6 \end{aligned}$$

This tensor structure directly underpins the added mass matrix A_{jk} in the six-DOF equation of motion (Equation 6.18). When the body possesses geometric symmetry, many off-diagonal components vanish: a body with one plane of symmetry reduces the 21 independent coefficients to 12; two planes reduce them to 7; and three mutually perpendicular planes of symmetry—the idealised ship hull with port–starboard, fore–aft, and waterplane symmetry—yield only the six diagonal terms (Korotkin, 2009).

Lewis Form Mapping for Ship Sections

For practical computation of the sectional added masses that enter strip-theory seakeeping calculations, the cross-section of each ship station must be conformally mapped to a canonical shape. Korotkin (2009) describes the Lewis form method, in which the ship-frame contour in the physical $\tau = y + iz$ plane is mapped to the exterior of the unit circle in the ζ-plane by the conformal transformation (Korotkin, 2009):

Equation 7.10 — Lewis form conformal mapping:

$$\tau = \frac{T}{1+p+q}\left[(1+p)\,\zeta + q\,\zeta^{-3}\right] \tag{6.10}$$

where T is the half-draft, and p and q are two parameters that encode the shape of the section. These parameters are determined from two geometric properties of the actual ship frame: the fullness coefficient $\beta = S/(BT)$ (the ratio of the section area S to the product of the beam B and draft T), and the draft-to-beam ratio $2T/B$. Specifically (Korotkin, 2009):

$$\frac{1+p+q}{1-p+q} = \frac{2T}{B}, \qquad \beta = \frac{\pi}{4}\,\frac{1-p^2-3q^2}{(1+p+q)^2}\,\frac{2T}{B}$$

Tables of p and q for $0.5 \le \beta \le 1$ and $0.2 \le 2T/B \le 10$ are catalogued in the hydrodynamic literature (Korotkin, 2009). Once p and q are known, the three

characteristic flow functions $w_2(\zeta)$, $w_3(\zeta)$, $w_4(\zeta)$—corresponding to sway, heave, and roll of the section—are obtained in closed form (Korotkin, 2009):

$$w_2 = -\frac{iT}{1+p+q}\left[(1+p)\,\zeta^{-1} + q\,\zeta^{-3}\right]$$

$$w_3 = -\frac{T}{1+p+q}\left[(p-1)\,\zeta^{-1} + q\,\zeta^{-3}\right]$$

$$w_4 = -\frac{iT^2}{(1+p+q)^2}\left[p(1+q)\,\zeta^{-2} + q\,\zeta^{-4}\right]$$

from which the sectional added masses λ_{22}, λ_{33}, λ_{24}, and λ_{44} are evaluated by contour integration of the real and imaginary parts (Korotkin, 2009).

Frequency-Dependent Added Masses on a Free Surface

When a ship oscillates at or near the free surface, the added masses become functions of the oscillation frequency and differ markedly from their infinite-fluid values. The boundary condition on the undisturbed free surface ($z = 0$) for periodic oscillations of circular frequency σ is (Korotkin, 2009):

Equation 7.11 — Free-surface boundary condition:

$$\frac{\partial^2 \phi}{\partial t^2} + g\,\frac{\partial \phi}{\partial z}\bigg|_{z=0} = 0 \tag{6.11}$$

which, for harmonic time dependence, reduces to $\partial\phi_1/\partial z - k_0\,\phi_1 = 0$ on $z = 0$, where $k_0 = \sigma^2/g$ is the wave number (Korotkin, 2009). Two limiting regimes are physically significant: when $k_0 \to \infty$ (high-frequency or short-wave limit), the condition becomes $\phi\big|_{z=0} = 0$, identical to the impact boundary condition; when $k_0 \to 0$ (low-frequency or long-wave limit), it becomes $\partial\phi/\partial z\big|_{z=0} = 0$, the rigid-wall (ultra-heavy fluid) condition (Korotkin, 2009). In the latter case, the added masses equal half those of the *duplicated* hull (the hull reflected about the waterplane) moving in an infinite fluid. The transition between these extremes governs the frequency dependence of the hydrodynamic coefficients used in seakeeping analysis.

The dimensionless sway, heave, sway–roll, and roll added masses (λ_{22}, λ_{33}, λ_{24}, λ_{44}) of Lewis-form ship frames are presented by Korotkin (2009) as functions of the dimensionless frequency parameter $B\sigma^2/(2g) = B\pi/\lambda$, where B is the section beam and λ the wavelength. At low frequencies all four coefficients approach the duplicated-model values, while at high frequencies they converge to the infinite-fluid values. The transition is non-monotonic for some section shapes, with local maxima in the intermediate-frequency range that depend on the fullness coefficient β and the beam-to-draft ratio $B/(2T)$ (Korotkin, 2009).

Approximate Formulas for Hull Added Masses

For preliminary design estimates where Lewis-form computations are not yet warranted, Korotkin (2009) provides simplified engineering formulas for the principal hull added masses of a complete ship. These are derived from the method of an equivalent ellipsoid combined with empirical corrections (Korotkin, 2009):

Equation 7.12 — Approximate hull added mass (heave):

$$\lambda_{33} = \rho\, V \left(1.2 + \frac{B}{3T} \right) \tag{6.12}$$

Equation 7.13 — Approximate hull added mass (sway):

$$\lambda_{22} = \rho\, V \left(0.3 + \frac{0.3\, T}{B} \right) \tag{6.13}$$

where ρ is the fluid density, V the displacement volume, B the maximum beam, and T the mean draft (Korotkin, 2009). These formulas show that the heave added mass exceeds the displacement mass for typical ship proportions ($B/(3T) \approx 1$–2), confirming that the effective inertia in vertical oscillation is several times the ship's own mass. The sway added mass, by contrast, is a smaller fraction of the displaced fluid mass, reflecting the more slender waterplane aspect when viewed from the side. Although these expressions are approximate, they provide a direct design check on the added mass values entering Equations (6.18) and (6.8) before detailed strip-theory computations are undertaken (Korotkin, 2009).

Strip Method Assembly of Sectional Quantities

The sectional added masses computed via the Lewis form mapping (Equation 6.10) or by numerical panel methods are assembled into a global seakeeping prediction by the strip method. el Moctar et al. (2021) describe the procedure: for each transverse section at longitudinal coordinate x, the two-dimensional Rankine source method yields a complex 3×3 added mass matrix whose elements combine the real sectional added mass a_{mn} and the damping d_{mn} into a single complex coefficient (el Moctar et al., 2021):

Equation 7.14 — Complex sectional added mass:

$$\bar{a}_{mn} = a_{mn} + \frac{d_{mn}}{i\,\omega_e}, \qquad m, n \in \{2, 3, 4\} \tag{6.14}$$

where ω_e is the encounter frequency (Equation 6.31) and the indices 2, 3, 4 correspond to sway, heave, and roll, respectively (el Moctar et al., 2021). The sectional force per unit length is then proportional to the section's acceleration: $\hat{\mathbf{f}} = \bar{\mathbf{A}}\, \omega_e^2\, \hat{\mathbf{u}}_x$, where $\hat{\mathbf{u}}_x$ is the local complex motion amplitude (el Moctar et al., 2021).

For a ship advancing at speed U, the variation of section shape along the hull introduces a longitudinal gradient of the added mass matrix. The substantial derivative $D/Dt = \partial/\partial t - U\,\partial/\partial x$ replaces the partial time derivative, and the six-dimensional complex radiation-force matrix is obtained by integrating the sectional contributions over the ship length (el Moctar et al., 2021):

Equation 7.15 — Strip-theory radiation-force matrix:

$$\mathbf{B} = \int_L \mathbf{V}\left(-i\omega_e + U\,\frac{\mathrm{d}}{\mathrm{d}x}\right)\bar{\mathbf{A}}(x)\,\mathbf{W}\,\mathrm{d}x \tag{6.15}$$

where $\mathbf{V}$ is the $6{\times}3$ transformation matrix converting sectional to global forces and moments, $\mathbf{W}$ the 3×6 matrix converting global motions to sectional velocities, and the integration extends over the hull length L (el Moctar et al., 2021). The forward-speed term $U\,\mathrm{d}\bar{\mathbf{A}}/\mathrm{d}x$ captures the rate of change of fluid momentum as different sections pass through the same spatial location. At stations where steady flow separation occurs (e.g. at a dry transom stern), this derivative term must be suppressed to avoid unphysical force spikes (el Moctar et al., 2021).

With the radiation-force matrix $\mathbf{B}$, the restoring matrix $\mathbf{S}$, the mass matrix $\mathbf{M}$, and the wave excitation vector $\hat{\mathbf{F}}_e$, the six-DOF equation of motion in the frequency domain becomes (el Moctar et al., 2021):

$$\left[-\omega_e^2\,\mathbf{M} - \mathbf{B} + \mathbf{S}\right]\begin{pmatrix}\hat{\mathbf{u}}\\ \hat{\boldsymbol{\alpha}}\end{pmatrix} = \hat{\mathbf{F}}_e$$

which is a direct frequency-domain counterpart of the time-domain formulation in Equation (6.18). The surge added mass, which cannot be recovered from transverse-section data, is approximated by (el Moctar et al., 2021):

Equation 7.16 — Surge added mass (ellipsoid approximation):

$$a_{11} = \rho\,\nabla \cdot 0.774\left(\frac{\nabla}{L^3}\right)^{0.675} \tag{6.16}$$

where ∇ is the displacement volume and L the hull length (el Moctar et al., 2021). This empirical formula, derived from added masses of equivalent ellipsoids, is valid for hulls of arbitrary slenderness, from fine naval combatants to full-form tankers (el Moctar et al., 2021). Strip methods remain the workhorse of routine seakeeping analysis because they require far less computational effort than three-dimensional panel codes or viscous CFD while delivering accuracy sufficient for the majority of design decisions, including operability assessments and structural load predictions in the early design spiral (el Moctar et al., 2021).

6.2.3 Coupled Equations of Motion

The most fundamental single degree-of-freedom equation governing ship rolling was derived by Attwood (1899) from the balance of the inertial reaction

and the hydrostatic restoring moment. For a vessel displaced through a small angle θ from the upright, the equation of unresisted rolling in still water is (Attwood, 1899):

Equation 7.17 — Equation of unresisted rolling:

$$\frac{\mathrm{d}^2\theta}{\mathrm{d}t^2} + \frac{g\,\overline{\mathrm{GM}}}{k^2}\,\theta = 0 \tag{6.17}$$

where g is the gravitational acceleration, $\overline{\mathrm{GM}}$ is the transverse metacentric height, and k is the radius of gyration of the vessel about the longitudinal axis through its centre of gravity, defined by $I = Wk^2$, with I the mass moment of inertia and W the displacement (Attwood, 1899). This equation has the same mathematical form as the simple harmonic oscillator (cf. Equation 6.27), confirming that unresisted small-angle rolling is simple harmonic motion; for a concise treatment, see (Fischer-Cripps, 2014).

For the complete problem of rolling among waves with resistance, the single-DOF equation generalises to (Attwood, 1899):

$$\frac{Wk^2}{g}\,\frac{\mathrm{d}^2\theta}{\mathrm{d}t^2} + R\!\left(\frac{\mathrm{d}\theta}{\mathrm{d}t}\right) + W\cdot \mathrm{GZ}(\theta) = W\cdot \mathrm{GZ}_{\mathrm{wave}}(t)$$

where $R(\dot\theta)$ is the moment of the resistances to rolling (Section 6.3.2), $\mathrm{GZ}(\theta)$ is the righting lever, and the right-hand side represents the wave-exciting moment expressed through the effective wave slope (Attwood, 1899).

The single degree-of-freedom treatment generalises to the full six degrees of freedom. Ge et al. (2026) present the coupled six-DOF equation of ship motion as:

Equation 7.18 — Six-DOF coupled equation of motion:

$$\sum_{k=1}^{6}\left[(M_{jk}+A_{jk})\,\ddot{x}_k + (B_{jk}+B^{e}_{jk})\,\dot{x}_k + C_{jk}\,x_k\right] = F_{I_j} \tag{6.18}$$

where M_{jk} is the rigid-body mass matrix, A_{jk} the frequency-dependent added mass matrix (Equation 6.6), B_{jk} the radiation damping matrix, B^{e}_{jk} the viscous damping matrix, C_{jk} the hydrostatic restoring stiffness matrix, x_k the displacement in degree of freedom k, and F_{I_j} the wave excitation load (Equation 6.4) in degree of freedom j (Ge et al., 2026). The subscripts $j,k = 1,\ldots,6$ correspond to surge, sway, heave, roll, pitch, and yaw.

The viscous damping matrix B^{e}_{jk} retains non-zero diagonal entries only for heave, roll, and pitch—the degrees of freedom in which viscous effects contribute appreciably to energy dissipation (Ge et al., 2026):

Equation 7.19 — Viscous damping matrix:

$$B^e_{jk} = \begin{bmatrix} 0 & 0 & 0 & 0 & 0 & 0 \\ 0 & 0 & 0 & 0 & 0 & 0 \\ 0 & 0 & B^e_{33} & 0 & 0 & 0 \\ 0 & 0 & 0 & B^e_{44} & 0 & 0 \\ 0 & 0 & 0 & 0 & B^e_{55} & 0 \\ 0 & 0 & 0 & 0 & 0 & 0 \end{bmatrix} \tag{6.19}$$

The hydrostatic restoring stiffness matrix C_{jk}, which provides the position-dependent restoring forces and moments, takes the form (Ge et al., 2026):

Equation 7.20 — Restoring stiffness matrix:

$$C_{jk} = \begin{bmatrix} 0 & 0 & 0 & 0 & 0 & 0 \\ 0 & 0 & 0 & 0 & 0 & 0 \\ 0 & 0 & \rho g A_W & 0 & -\rho g M_W & 0 \\ 0 & 0 & 0 & \rho g \nabla \overline{\mathrm{GM}}_T & 0 & 0 \\ 0 & 0 & -\rho g M_W & 0 & \rho g \nabla \overline{\mathrm{GM}}_L & 0 \\ 0 & 0 & 0 & 0 & 0 & 0 \end{bmatrix} \tag{6.20}$$

where A_W is the waterplane area, M_W the first moment of the waterplane area, ∇ the volumetric displacement, $\overline{\mathrm{GM}}_T$ the transverse metacentric height, and $\overline{\mathrm{GM}}_L$ the longitudinal metacentric height (Ge et al., 2026). The zero entries in the surge, sway, and yaw rows reflect the absence of hydrostatic restoring forces for horizontal translations and rotation about the vertical axis. The off-diagonal terms $C_{35} = C_{53} = -\rho g M_W$ couple heave and pitch whenever the waterplane is not symmetric about the midship section.

The transverse metacentric height appearing in C_{44} is (Ge et al., 2026):

Equation 7.21 — Transverse metacentric height:

$$\overline{\mathrm{GM}}_T = \overline{\mathrm{BM}}_T - \overline{\mathrm{BG}} \tag{6.21}$$

where $\overline{\mathrm{BM}}_T$ is the transverse metacentric radius and $\overline{\mathrm{BG}}$ the distance between the centre of buoyancy and the centre of gravity (Ge et al., 2026). This expression links the roll restoring stiffness directly to the vessel's hydrostatic geometry.

Cross-Coupling Effects

The six degrees of freedom of a floating body separate into three groups that are uncoupled under linear theory: (i) surge alone; (ii) heave and pitch; and (iii) sway, roll, and yaw (Ge et al., 2026). Within the third group, the coupling between sway and roll is of particular practical importance because lateral wave forces can drive significant roll amplitudes. Ge et al. (2026) quantified this coupling through a parameter:

Equation 7.22 — Coupling effect parameter:

$$\eta = \frac{\mathrm{RAO}_{\mathrm{uncoupled}} - \mathrm{RAO}_{\mathrm{coupled}}}{\mathrm{RAO}_{\mathrm{coupled}}} \tag{6.22}$$

where $\mathrm{RAO}_{\mathrm{coupled}}$ is the roll response amplitude operator with all six degrees of freedom coupled, and $\mathrm{RAO}_{\mathrm{uncoupled}}$ is the roll response with no coupling to other degrees of freedom. Numerical analysis of the SUBOFF model in beam seas yielded $\eta = 2.441$ for on-free-surface conditions and $\eta = 1.466$ for near-free-surface conditions, demonstrating that the sway–roll coupling effect is markedly stronger when the vessel operates on the free surface (Ge et al., 2026). The practical implication is that releasing additional degrees of freedom—particularly sway—helps to mitigate roll motion, because the energy introduced by lateral wave loading is distributed among multiple motion modes rather than concentrated in roll alone (Ge et al., 2026).

Time-Domain Convolution Formulation

The frequency-domain equation of motion (Equation 6.18) assumes simple harmonic motion and employs frequency-dependent added mass $A_{jk}(\omega)$ and radiation damping $B_{jk}(\omega)$. For problems involving transient excitation or nonlinear external forces—such as moored ships subjected to harbour oscillations (discussed in the *Wave Mechanics and Ocean Waves* chapter of the companion volume)—a time-domain formulation is required. Zheng et al. (2022) adopt the convolution-integral form of the six-DOF equation of motion:

Equation 7.23 — Time-domain convolution equation of motion:

$$\sum_{k=1}^{6}\left\{(M_{jk}+a_{jk})\,\ddot{x}_k(t) + \int_0^t \dot{x}_k(\tau)\,K_{jk}(t-\tau)\,\mathrm{d}\tau + C_{jk}\,x_k(t)\right\} = F_j^D(t) + F_j^{\mathrm{nl}}(t), \quad j = 1,\ldots,6 \tag{6.23}$$

where M_{jk} and C_{jk} are the body's inertia and hydrostatic restoring matrices, respectively. The coefficient $a_{jk} = A_{jk}(\omega \to \infty)$ is the added mass at infinite frequency, and $K_{jk}(t)$ is the impulse response (retardation) function obtained by inverse Fourier transformation of the frequency-dependent radiation damping $B_{jk}(\omega)$ (Zheng et al., 2022). The wave exciting force $F_j^D(t)$—comprising both Froude–Krylov and diffraction components (Equations 6.4–6.5)—is computed via the Haskind relation from the incoming wave field, while $F_j^{\mathrm{nl}}(t)$ represents all nonlinear external forces such as those from mooring lines and fenders (Zheng et al., 2022).

The convolution integral captures the *memory effect*: the radiation force at time t depends on the entire history of the body's velocity. This is the time-domain equivalent of the frequency-dependent radiation damping $B_{jk}(\omega)$ in Equation 6.18. The separation of the added mass into the constant infinite-frequency component a_{jk} and the memory kernel $K_{jk}(t)$ enables numerical

integration using standard time-stepping schemes (e.g., fourth-order Runge–Kutta) (Zheng et al., 2022).

Zheng et al. (2022) applied Equation (6.23) to a 6000 TEU container vessel ($L_{OA} = 290$ m, $B = 32.3$ m, draft $= 13$ m, $\nabla = 80\,115$ m^3) moored in Hambantota Port under seismic-induced harbour oscillations. The long-period ship motions ($T = 25$–100 s) consist of two families: (i) *natural modes* of the mooring system, with natural oscillatory periods (NOPs) governed by mooring configuration and stiffness (~ 50 s at 16 t pretension); and (ii) *forced modes* driven by the harbour's natural oscillation modes. When the NOP coincides with a harbour oscillation period—achieved by reducing pretension from 16 t to 4 t, shifting the NOP to ~ 70 s (close to the harbour's third mode at 71 s)—the ship's maximum displacement is amplified by approximately a factor of two (Zheng et al., 2022). The forced ship motions are dominated by high-order harbour modes because the steep spatial gradients across the ship hull in these modes generate the largest wave exciting forces (Zheng et al., 2022).

Impulse Response Functions and Fluid Memory

The computation of the retardation functions in Equation (6.23) proceeds from the frequency-domain radiation damping via the cosine transform (Ölmez & Çakıcı, 2022):

Equation 7.24 — Impulse response function from radiation damping:

$$K_{jk}(t) = \frac{2}{\pi} \int_0^\infty B_{jk}(\omega)\, \cos(\omega t)\, \mathrm{d}\omega \tag{6.24}$$

where $B_{jk}(\omega)$ is the frequency-dependent radiation damping coefficient obtained from the strip-theory or panel-method solution (Ölmez & Çakıcı, 2022). Equation (6.24) confirms that the memory kernel inherits its time-domain behaviour from the frequency structure of the radiation damping: modes with broad-band damping spectra produce rapidly decaying impulse responses, while narrow-band damping spectra yield oscillatory kernels with slow decay.

The infinite-frequency added mass appearing in Equation (6.23) is similarly recovered from the frequency-domain data as (Ölmez & Çakıcı, 2022):

Equation 7.25 — Infinite-frequency added mass from Kramers–Kronig relation:

$$a_{jk} = A_{jk}(\omega) + \frac{1}{\omega} \int_0^\infty K_{jk}(\tau)\, \sin(\omega \tau)\, \mathrm{d}\tau \tag{6.25}$$

where $A_{jk}(\omega)$ is the added mass at any finite frequency (Ölmez & Çakıcı, 2022). Equations (6.24) and (6.25) express the Kramers–Kronig-type relations that link the frequency-dependent added mass and damping to each other and to the time-domain impulse response—a consequence of the causal nature of the hydrodynamic radiation problem.

In practice, the upper limit of the integral in Equation (6.24) is replaced by a finite frequency cut-off beyond which $B_{jk}(\omega)$ is negligible, and the convolution integral in Equation (6.23) is truncated at a fluid memory time t_1 beyond which $K_{jk}(t)$ has decayed to negligible values. McTaggart (1998), as cited by Ölmez and Çakıcı (2022), established practical guidelines for the time-domain integration: the time step and memory cut-off time scale with the vessel length and gravitational acceleration as:

Equation 7.26 — McTaggart fluid memory time-step rules:

$$\Delta t \approx 0.05\sqrt{\frac{L}{g}}, \qquad t_1 \approx 5\sqrt{\frac{L}{g}} \tag{6.26}$$

with the corresponding number of time steps in the memory window $n_1 = t_1/\Delta t \approx 100$ (Ölmez & Çakıcı, 2022). For the typical merchant vessel lengths ($L = 100$–$350\,\mathrm{m}$), Equation (6.26) yields time steps of $\Delta t \approx 0.16$–$0.30\,\mathrm{s}$ and memory times of $t_1 \approx 16$–$30\,\mathrm{s}$, ensuring that the convolution integral in Equation (6.23) is resolved with sufficient temporal resolution while the memory kernel has decayed by at least three orders of magnitude (Ölmez & Çakıcı, 2022).

6.3 Theoretical Framework

6.3.1 Response in Regular Waves

The motions of a vessel in regular waves are characterised by their *natural frequencies*—the frequencies at which the vessel oscillates freely when displaced from equilibrium and released. The foundational treatment of oscillatory motion and pendulum dynamics can be found in (Hewitt et al., 2012). Campbell (2025) derives the natural frequency of a simple pendulum from Newton's second law in angular form ($\tau_{\text{NET}} = I\alpha$), obtaining:

Equation 7.27 — Pendulum natural frequency:

$$\omega_{\text{pendulum}} = \sqrt{\frac{g}{l}} \tag{6.27}$$

where g is gravitational acceleration and l is the pendulum length (Campbell, 2025). This result is independent of mass and amplitude (for small angles), depending only on the gravitational restoring force and the effective length.

A vessel rolling in calm water after being disturbed behaves as a compound pendulum: the gravitational restoring moment is proportional to the metacentric height $\overline{\text{GM}}$, and the resistance to angular acceleration is given by the mass moment of inertia (including hydrodynamic added mass). By analogy with Equation (6.27), the natural roll frequency takes the form $\omega_\phi \propto \sqrt{\Delta\,\overline{\text{GM}}/(I_{xx} + A_{44})}$, where Δ is the displacement, I_{xx} is the dry roll

inertia, and A_{44} is the added mass in roll. The natural roll period is then $T_\phi = 2\pi/\omega_\phi$.

The general solution of Equation (6.17) yields the natural roll period (Attwood, 1899):

Equation 7.28 — Natural roll period:

$$T_\phi = \pi \sqrt{\frac{k^2}{g\,\overline{\mathrm{GM}}}} \tag{6.28}$$

where T_ϕ is the single-swing period (from port extreme to starboard extreme), k is the transverse radius of gyration, g is the gravitational acceleration, and $\overline{\mathrm{GM}}$ is the metacentric height (Attwood, 1899). The period is independent of the amplitude of oscillation for small angles; this property is termed *isochronous rolling* and holds experimentally up to approximately 10°–15° each side of the vertical (Attwood, 1899).

Equation (6.28) reveals two design levers for controlling the roll period: (i) increasing the radius of gyration k, for instance by distributing weight towards the ship's sides, lengthens the period; (ii) decreasing the metacentric height $\overline{\mathrm{GM}}$ also lengthens the period. A long roll period is desirable for seakeeping because it reduces the likelihood of synchronism with the encountered wave period. Attwood (1899) noted that heavily armoured battleships (e.g. HMS *Majestic*, $\overline{\mathrm{GM}} \approx 1.07$ m, $T_\phi \approx 8$ s) had long periods due to their large moments of inertia from side armour, whereas small gunboats with relatively large $\overline{\mathrm{GM}}$ experienced rapid rolling with periods of only 2 s–4 s (Attwood, 1899).

Rolling Among Waves: Froude's Equation

When a ship lies broadside to a regular wave train whose half-period is T_1, the effective wave slope varies sinusoidally with time. Attwood (1899) presents Froude's general equation for unresisted rolling among waves:

Equation 7.29 — Froude's equation for rolling among waves:

$$\frac{\mathrm{d}^2\theta}{\mathrm{d}t^2} + \frac{\pi^2}{T_\phi^2}\,\theta = \frac{\pi^2}{T_\phi^2}\,\theta_{1,\max}\sin\frac{\pi\,t}{T_1} \tag{6.29}$$

where θ is the ship's inclination from the true vertical, $\theta_{1,\max}$ is the maximum effective wave slope, T_ϕ is the still-water roll period, and T_1 is the half-period of the wave (Attwood, 1899).

Synchronism

The critical condition occurs when $T_\phi = T_1$, i.e. the still-water roll period equals the half-period of the encountered wave. In this state of *synchronism*,

the solution of Equation (6.29) shows that the roll amplitude increases by (Attwood, 1899):

$$\Delta\theta = \frac{\pi}{2}\,\theta_{1,\max}$$

for every half-wave that passes, so that an unresisted ship in perfect synchronism must inevitably capsize. Attwood (1899) illustrated this with the example of HMS *Devastation* ($T_\phi = 6.75$ s): in synchronism with waves of 8° maximum slope, the roll would increase by approximately 12.6° every half-wave, reaching dangerous angles within one minute (Attwood, 1899).

Three limiting cases emerge from the general solution (Attwood, 1899):

1. **Synchronism** ($T_\phi = T_1$): unbounded roll growth at a rate of $\frac{\pi}{2}\,\theta_{1,\max}$ per half-wave.
2. **Quick ship** ($T_\phi \ll T_1$): the vessel follows the wave slope like a raft, with maximum heel equal to $\theta_{1,\max}$.
3. **Slow ship** ($T_\phi \gg T_1$): the vessel remains nearly upright regardless of wave steepness.

Case 3 explains the classical design recommendation to make the still-water period as long as possible (small $\overline{\mathrm{GM}}$) for seakeeping, even though such a ship is "crank" (easily inclined by external forces) (Attwood, 1899).

Response Amplitude Operator

The *Response Amplitude Operator* (RAO) quantifies the linear transfer function between wave input and vessel motion output. It is defined as the ratio of the motion amplitude x_k in degree of freedom k to the wave amplitude H, and is obtained directly from the six-DOF equation of motion (Equation 6.18). For the particular case of roll in the uncoupled single-DOF form, the RAO takes the explicit form (Ge et al., 2026):

Equation 7.30 — Roll response amplitude operator:

$$\mathrm{RAO}_\phi = \frac{|F_I^4|}{\sqrt{\left[-(M_{44}+A_{44})\,\omega^2 + C_{44}\right]^2 + \left[(B_{44}+B_{44}^e)\,\omega\right]^2}} \tag{6.30}$$

where M_{44} is the roll moment of inertia, A_{44} the roll added mass, B_{44} the roll radiation damping, B_{44}^e the roll viscous damping, C_{44} the roll restoring stiffness ($C_{44} = \rho g \nabla \overline{\mathrm{GM}}_T$, Equation 6.20), ω the wave angular frequency, and F_I^4 the roll wave excitation load (Ge et al., 2026).

Equation (6.30) reveals a non-monotonic relationship between roll RAO and restoring stiffness: the denominator reaches its minimum—and hence the RAO its maximum—when $C_{44} = (M_{44}+A_{44})\,\omega^2$. Ge et al. (2026) term this condition the *critical restoring stiffness*. When the actual restoring stiffness exceeds this critical value, increasing the restoring stiffness further (for example, by reducing $\overline{\mathrm{BG}}$ to increase $\overline{\mathrm{GM}}_T$, Equation 6.21) reduces the roll RAO. In the wave

frequency range most commonly encountered by ships and submarines ($\omega \approx 0.3$ rad s^{-1} to 1.3 rad s^{-1}), increasing the roll restoring stiffness was found to reduce roll RAO for both on-free-surface and near-free-surface conditions (Ge et al., 2026).

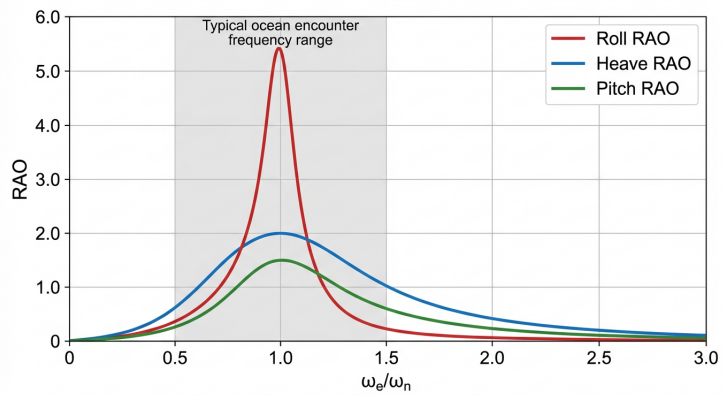

Figure 6.2: Typical Response Amplitude Operator (RAO) curves for heave, pitch, and roll as functions of the non-dimensional encounter frequency ω_e/ω_n. Each curve exhibits a resonance peak near the natural frequency of the respective mode; the roll RAO peak is the sharpest because roll radiation damping is small and viscous damping (not captured by potential-flow theory) governs the peak amplitude. Increasing the restoring stiffness shifts the resonance to higher frequencies and, for roll in the typical wave-frequency band, reduces the peak amplitude (Equation 6.30). The shaded region indicates the encounter-frequency range corresponding to common ocean wave periods at a representative forward speed.

Encounter Frequency and Forward Speed Effects

When a vessel advances at speed U through a wave field, the frequency at which it encounters successive wave crests differs from the absolute wave frequency. The *encounter frequency* is (Ge et al., 2026):

Equation 7.31 — Encounter frequency:

$$\omega_e = \omega - \frac{\omega^2 \, |U|}{g} \cos\beta \tag{6.31}$$

where ω is the wave angular frequency, U the forward speed, g the gravitational acceleration, and β the heading angle between the vessel's advance direction and the wave propagation direction (Ge et al., 2026). In head seas ($\beta = 180°$), $\cos\beta = -1$ and the encounter frequency increases; in following seas ($\beta = 0°$), it decreases. In beam seas ($\beta = 90°$), $\omega_e = \omega$ and forward speed has no effect on the encounter frequency.

Forward speed modifies the hydrodynamic behaviour in two principal ways (Ge et al., 2026): (i) it shifts the peak frequencies of the added mass and radiation damping coefficients, because these are evaluated at the encounter frequency rather than the absolute wave frequency; and (ii) it alters the RAO magnitudes and frequency distributions. Numerical analysis of the SUBOFF model showed that surge and sway RAOs increase with forward speed, while heave and pitch RAOs decrease—a trend that contrasts with conventional surface ships due to the streamlined hull form of the submarine, which generates minimal wave-making resistance and dynamic lift (Ge et al., 2026).

Spectral Response Analysis in Irregular Waves

The RAO framework developed above for regular waves extends naturally to irregular seas through the spectral analysis method. When a vessel advances through long-crested irregular waves characterised by a wave energy spectrum $S_\zeta(\omega_e)$, the response spectrum of any linear output quantity is obtained by (Jiao et al., 2019):

Equation 7.32 — Response spectrum in long-crested irregular waves:

$$S_R(\omega_e) = \left|H(\omega_e)\right|^2 S_\zeta(\omega_e) \tag{6.32}$$

where $H(\omega_e)$ is the RAO evaluated at the encounter frequency and $S_\zeta(\omega_e)$ is the wave energy spectrum expressed in encounter-frequency coordinates (Jiao et al., 2019). Equation (6.32) relates the frequency content of the wave input to the frequency content of the ship response through a simple multiplicative filter—the squared modulus of the transfer function.

The transformation of the wave spectrum from absolute frequency ω to encounter frequency ω_e involves the Jacobian of the frequency mapping (Equation 6.31). Ölmez and Çakıcı (2022) give the encounter spectrum as:

Equation 7.33 — Encounter wave spectrum transformation:

$$S_\zeta(\omega_e) = \frac{S_\zeta(\omega)}{\left|1 - 2\omega\, U \cos\beta \,/\, g\right|} \tag{6.33}$$

where $S_\zeta(\omega)$ is the wave spectrum in absolute frequency and the denominator is the absolute value of $\mathrm{d}\omega_e/\mathrm{d}\omega$ (Ölmez & Çakıcı, 2022). In head seas ($\cos\beta < 0$), the denominator exceeds unity and the spectral energy density is reduced—the spectrum is stretched over a wider encounter-frequency band. In following seas ($\cos\beta > 0$), the denominator can approach zero when $\omega \to g/(2U)$, producing a singularity that reflects the physical accumulation of wave energy as the vessel speed approaches the group velocity of the incident waves. This singularity has direct practical consequences: in following seas at moderate speed, narrow-band swells can produce encounter spectra with very high energy density at the corresponding encounter frequency, significantly amplifying the motion response predicted by Equation (6.32) (Ölmez & Çakıcı, 2022).

Realistic ocean waves, however, are short-crested: their energy is distributed over both frequency and propagation direction. The directional wave spectrum is expressed as the product of a frequency spectrum and a directional spreading function (Jiao et al., 2019):

Equation 7.34 — Directional wave spectrum:

$$S_{\zeta\zeta}(\omega,\theta) = S_{\zeta}(\omega)\, D(\omega,\theta) \tag{6.34}$$

where θ is the angle between a component wave direction and the dominant wave direction, and $D(\omega,\theta)$ is the directional spreading function satisfying $\int_{-\pi/2}^{\pi/2} D(\omega,\theta)\,\mathrm{d}\theta = 1$ (Jiao et al., 2019). A widely used parametric form is the cosine-power model (Jiao et al., 2019):

Equation 7.35 — Cosine-power directional spreading function:

$$D(\omega,\theta) = \frac{\Gamma(n/2+1)}{\sqrt{\pi}\,\Gamma(n/2+1/2)}\,\cos^{n}\theta, \qquad -\frac{\pi}{2} \le \theta \le \frac{\pi}{2} \tag{6.35}$$

where $\Gamma(\cdot)$ denotes the Gamma function and n is a positive integer controlling the degree of directional concentration (Jiao et al., 2019). Large values of n produce a narrow directional distribution approaching the long-crested limit ($n \to \infty$), while small values (e.g. $n = 1$–2) represent broadly spread seas typical of open-ocean swell.

The ship response spectrum in short-crested irregular waves is obtained by a two-dimensional spectral analysis that integrates the directional contributions (Jiao et al., 2019):

Equation 7.36 — Response spectrum in short-crested irregular waves:

$$S_R(\omega_e,\beta_0+\theta) = \left|H(\omega_e,\beta_0+\theta)\right|^2 S_{\zeta\zeta}(\omega_e,\theta) \tag{6.36}$$

where β_0 is the heading angle of the ship with respect to the dominant wave direction (Jiao et al., 2019). The variance (zeroth spectral moment) of the response is then:

Equation 7.37 — Variance from directional spectrum:

$$m_0(\beta_0) = \int_{-\pi}^{\pi}\int_{0}^{\infty} S_R(\omega_e,\beta_0+\theta)\,\mathrm{d}\omega_e\,\mathrm{d}\theta \tag{6.37}$$

and the single significant amplitude (SSA) follows from the Rayleigh distribution as (Jiao et al., 2019):

Equation 7.38 — Significant single amplitude:

$$A_{1/3} = 2\sqrt{m_0} \tag{6.38}$$

Equations (6.32)–(6.38) constitute the complete framework for predicting ship motion and load statistics in irregular seas. Equation (6.32) is the long-crested special case recovered when the spreading function degenerates to a Dirac delta, and Equations (6.36)–(6.38) represent the general short-crested formulation.

Quantitative Effects of Directional Spreading

Comparative model tests and numerical predictions by Jiao et al. (2019) on a 72,000-tonne vessel (313 m overall length) quantified the systematic differences between ship responses in long-crested and short-crested waves. Two complementary experiments were conducted: a 1/50-scale model in a laboratory wave basin generating two-dimensional long-crested waves, and a 1/25 large-scale model in realistic three-dimensional short-crested sea waves at Bohai Bay, China (Jiao et al., 2019).

For head-sea conditions, the ratio of the response SSA in short-crested waves to that in long-crested waves under equivalent sea states was found to lie between 0.714 and 0.906 for pitch, vertical bending moment (VBM) amidships, and vertical shearing force (VSF), indicating that long-crested waves systematically over-estimate these responses (Jiao et al., 2019). In contrast, the same ratio for heave and vertical acceleration lay much closer to unity (0.987–1.092), demonstrating that vertical translatory motions are relatively insensitive to directional spreading (Jiao et al., 2019).

A systematic numerical investigation of the spreading exponent $n = 1$–8 in the directional function (Equation 6.35) revealed three distinct behavioural groups (Jiao et al., 2019):

1. **Roll motion** is most sensitive to directional spreading. In head and following seas, roll decreases rapidly with increasing n (narrower spreading), vanishing in the long-crested limit. Conversely, in beam seas, roll *increases* with n because the wave energy concentrates in the direction of maximum roll excitation.

2. **Vertical motions** (pitch, heave, vertical acceleration) show only mild sensitivity to n for all wave headings. The variation is typically less than 10% across the full range $n = 1$–8.

3. **Sectional loads** (VBM, VSF) increase with n in head and following seas, with the long-crested assumption ($n \to \infty$) yielding conservative structural design loads. In beam seas, however, short-crested waves produce *larger* sectional loads than long-crested waves because oblique wave components—absent in the long-crested idealisation—generate significant bending and shear.

For the commonly adopted spreading parameter $n = 2$, Jiao et al. (2019) compiled comprehensive influence coefficients—the ratio of short-crested to long-crested response SSA—across 13 heading angles from 0° (following seas) to 180° (head seas). In head seas, these coefficients were approximately 0.84 for VBM, 0.96 for pitch, and 1.10 for heave. The most extreme deviations occurred in beam seas (90°), where the VBM ratio reached 2.85–2.96 and the pitch ratio exceeded 7, reflecting the strong excitation of motions that would be zero in long-crested beam waves by symmetry. These quantitative influence coefficients provide a practical tool for estimating short-crested wave responses from long-crested calculations (Jiao et al., 2019).

6.3.2 Roll Dynamics and Damping

Campbell (2025) establishes the general equation of rotational dynamics as Newton's second law in angular form:

Equation 7.39 — Newton's second law for rotation:

$$\tau_{\text{NET}} = I\,\alpha \tag{6.39}$$

where $I = \sum m_i\, r_i^2$ is the moment of inertia of the system about the rotation axis and α is the angular acceleration (Campbell, 2025). The corresponding *rotational kinetic energy* is:

Equation 7.40 — Rotational kinetic energy:

$$K_{\text{rot}} = \frac{1}{2}\, I\, \omega^2 \tag{6.40}$$

where ω is the angular velocity (Campbell, 2025).

Applying Equation (6.39) to vessel roll, the net torque comprises: (i) the hydrostatic restoring moment, proportional to $\overline{\text{GM}} \sin\phi$; (ii) the wave-exciting moment; and (iii) a damping moment that opposes the angular velocity. In the simplest linearised form this yields a driven, damped harmonic oscillator—the same mathematical structure as the mass–spring–dashpot system treated by Campbell (2025) in the context of SHM.

The roll energy budget illustrates why damping is critical: at resonance, the energy input from the wave excitation is balanced solely by the energy dissipated per cycle. From Equation (6.40), the peak roll kinetic energy scales as $K \propto I\,\dot{\phi}_{\text{max}}^2$; damping devices (bilge keels, anti-roll tanks, stabiliser fins) increase the energy dissipation rate, thereby reducing $\dot{\phi}_{\text{max}}$ and the roll amplitude.

Attwood (1899) described an empirical approach developed by William Froude for quantifying roll damping. By deliberately rolling ships in still water and recording the successive angles reached on each swing—the *curve of declining angles*—the rate at which roll energy is dissipated can be measured. From these experiments, the angle lost per swing (the *decrement*) was found to follow a two-term law (Attwood, 1899):

Equation 7.41 — Decremental equation for resisted rolling:

$$-\frac{\mathrm{d}\Phi}{\mathrm{d}n} = a\,\Phi + b\,\Phi^2 \tag{6.41}$$

where Φ is the roll angle in degrees, n is the swing number, and a and b are coefficients determined experimentally for each vessel (Attwood, 1899). The first term ($a\Phi$) arises from resistances whose moment is proportional to the angular velocity—principally wave-making by the rolling hull—while the second term ($b\Phi^2$) arises from resistances whose moment is proportional to the square of the angular velocity—principally the passage of bilge keels and sharp hull features through the water (Attwood, 1899).

Representative coefficients from rolling experiments on Royal Navy vessels include (Attwood, 1899):

Vessel	T_ϕ (s)	a	b	Condition
HMS *Inconstant*	8.0	0.035	0.0051	—
HMS *Revenge*	—	0.014	0.0028	without bilge keels
HMS *Revenge*	—	0.064	0.0028	with bilge keels

The dramatic increase in the a coefficient for HMS *Revenge* upon fitting bilge keels (from 0.014 to 0.064) demonstrates their effectiveness. In rolling experiments starting from 6°, without bilge keels 45–50 swings were required to decay to 2°, whereas with bilge keels only 8 swings were needed (Attwood, 1899).

When synchronism is combined with damping, the roll amplitude does not grow without bound but reaches a steady state. The angle of steady rolling Φ_s satisfies (Attwood, 1899):

$$\frac{\pi}{2}\,\theta_{1,\max} = a\,\Phi_s + b\,\Phi_s^2$$

where the left-hand side is the synchronism increment per half-wave and the right-hand side is the decrement due to resistance. Physical factors that prevent capsizing in practice include: (a) departure from isochronous rolling at large angles, (b) resistance increasing with amplitude, and (c) the improbability of a long succession of waves of precisely equal period (Attwood, 1899).

Frequency-Dependent Coefficients from Panel Methods

The Hess–Smith constant panel method (Ge et al., 2026) provides a systematic procedure for computing the frequency-dependent added mass and radiation damping coefficients from the boundary integral equation (Equation 6.3). The mean wetted surface of the hull is divided into N_P quadrilateral panels, and both the velocity potential and the source strength are assumed constant within each panel. The source distribution over the wetted surface yields the velocity potential at any field point as (Ge et al., 2026):

Equation 7.42 — Panel method source distribution:

$$\phi(\mathbf{x}) = \frac{1}{4\pi}\sum_{\alpha=1}^{N_P} \sigma_\alpha\, G(\mathbf{x}, \mathbf{x}_\alpha, \omega)\,\Delta S_\alpha \tag{6.42}$$

where σ_α is the source strength, $G(\mathbf{x}, \mathbf{x}_\alpha, \omega)$ the free-surface Green function, $\mathbf{x}_\alpha$ the geometric centre of the αth panel, and ΔS_α its area (Ge et al., 2026). The unknown source strengths are determined by applying the body surface boundary condition at each panel collocation point, yielding a dense linear system of dimension N_P. Once the velocity potentials are obtained for each degree of freedom and wave frequency, the added mass and radiation damping follow from Equation (6.6).

Numerical convergence studies on the DARPA SUBOFF model showed that the hydrodynamic coefficients are insensitive to further mesh refinement once the panel count exceeds approximately 2560 elements; finer meshes (up

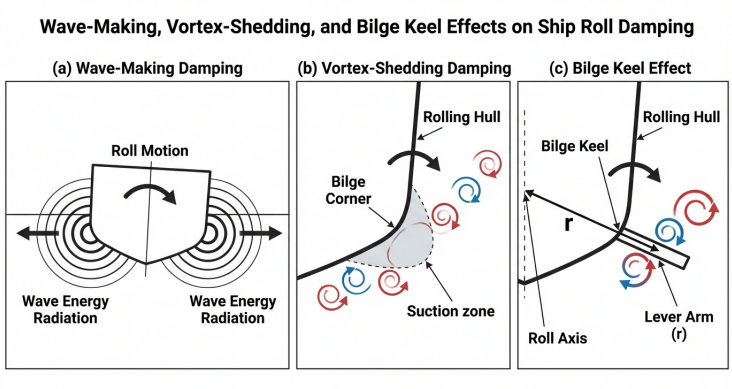

Figure 6.3: Physical mechanisms of roll damping for a ship cross-section oscillating about the longitudinal axis. (a) Wave-making damping: the rolling hull radiates surface waves that carry energy away from the vessel, producing the radiation damping B_{44} captured by potential-flow theory (Equation 6.6). (b) Vortex-shedding damping: alternating vortices detach from sharp bilge corners during each half-cycle of roll, creating low-pressure (suction) zones that oppose the angular velocity; this viscous mechanism corresponds to the quadratic term $b\,\Phi^2$ in Froude's decremental equation (Equation 6.41). (c) Bilge keel effect: flat plates projecting from the turn of the bilge amplify the vortex-shedding mechanism and increase the effective lever arm r, producing a decrement proportional to r^3 (Equation 6.60). The Ikeda decomposition (Equation 6.43) combines these contributions with frictional and hull-lift components into a total equivalent linearised roll damping coefficient.

to 9360 elements) produced virtually identical results (Ge et al., 2026). The computed frequency-dependent behaviour reveals distinct physical trends: at near-free-surface conditions, as the submergence depth increases, both the added mass and radiation damping in all six degrees of freedom decrease. At large submergence depths, the added mass becomes nearly constant (frequency-independent) while the radiation damping approaches zero—the body no longer radiates appreciable surface waves (Ge et al., 2026). Among the six degrees of freedom, surge and roll exhibit the smallest added mass and radiation damping coefficients, because these motions involve the smallest fluid-volume perturbations, whereas sway, heave, pitch, and yaw produce larger values owing to greater fluid displacement (Ge et al., 2026).

Viscous Roll Damping from Vortex Shedding

The panel methods discussed above operate within the assumption of potential flow—inviscid, irrotational fluid—and therefore capture only the *wave-making* component of roll damping (the radiation damping B_{44} in Equation 6.6). However, roll motion is unique among the six degrees of freedom in that viscous effects—flow separation at bilge corners, vortex generation, and eddy formation—contribute a substantial fraction of the total damping. Potential flow theories can introduce large errors for roll prediction because they fail to account for these viscous mechanisms (Jung et al., 2013).

To capture viscous roll damping directly, Jung et al. (2013) employed the Reynolds-averaged Navier–Stokes (RANS) equations with the standard k–ε turbulence model in a two-dimensional numerical wave tank. The free surface was tracked using the volume of fluid (VOF) method, and a sliding mesh technique coupled the fluid solution with the rigid-body equations of motion of a rectangular floating structure ($B = 0.3\,\text{m}$, $H = 0.1\,\text{m}$). The piston-type wave generator produced regular waves at three periods: $T_s = 0.93\,\text{s}$ (equal to the roll natural period T_n), $T_s = 0.8\,\text{s}$ ($T_s < T_n$), and $T_s = 1.2\,\text{s}$ ($T_s > T_n$) (Jung et al., 2013).

The time histories of wave elevation and roll angle agreed well with the experimental results for all three wave periods. The largest roll amplitude occurred at $T_s = T_n = 0.93\,\text{s}$ due to *resonance*, consistent with the synchronism condition described by Equation (6.29). The computed RAO—defined as $\phi/(A_\zeta k)$, the ratio of roll angle to wave slope—was in excellent agreement with both the experimental data and linear potential theory at frequencies away from resonance. At the natural frequency, however, the RAO predicted by linear potential theory was significantly magnified compared to the CFD and experimental values, because the potential theory includes only wave-making damping and omits the viscous contribution (Jung et al., 2013).

The physical mechanism of viscous roll damping was elucidated through detailed analysis of the velocity field and vorticity contours around the structure. At each bottom corner of the rectangular hull, the oscillatory roll motion generated alternating positive (counterclockwise) and negat-

ive (clockwise) vortices that detached from the sharp edges and evolved over successive phases of the roll cycle (Jung et al., 2013). When the wave period equalled or was shorter than the natural period ($T_s \leq T_n$), these corner vortices created regions of low pressure (suction) on the body surface that *opposed* the roll motion—the suction at the leeward bottom corner resisted the counterclockwise roll in one half-cycle, and the corresponding suction at the seaward corner resisted the clockwise roll in the other. This viscous damping mechanism reduced the steady-state roll amplitude below the undamped prediction, and it corresponds physically to the $b\,\Phi^2$ term in Froude's decremental equation (Equation 6.41), which arises from resistances proportional to the square of the angular velocity (Attwood, 1899; Jung et al., 2013).

At the longer wave period ($T_s = 1.2\,\text{s} > T_n$), a qualitatively different vortex evolution mechanism was observed. On the seaward side, the vortex development was governed primarily by the water level variation—the free surface descended faster than the structure corner rotated—rather than by the roll motion itself (Jung et al., 2013). The resulting pressure distribution *boosted* rather than damped the roll motion at this wave period. On the leeward side, the vortex evolution remained governed by the roll motion, as in the shorter-period cases. This asymmetry between seaward and leeward vortex mechanisms at longer wave periods highlights the importance of resolving the full viscous flow field when assessing roll behaviour outside the resonance region (Jung et al., 2013).

The forces acting on the structure exhibited clear physical trends. The horizontal force F_x was governed by the difference in wave elevations on the seaward and leeward sides—effectively the hydrostatic pressure imbalance—while the vertical force F_z followed the ascent and descent of the wave. Both force components increased rapidly as the wave period exceeded the natural period, because the longer waves carried greater energy and produced larger free-surface excursions around the structure (Jung et al., 2013).

Ikeda's Semi-Empirical Roll Damping Decomposition

The viscous flow computations of Jung et al. (2013) resolve individual vortex structures but require considerable computational effort. For routine seakeeping prediction, the semi-empirical method of Ikeda et al. (1978), as described by Ölmez and Çakıcı (2022), decomposes the total equivalent linearised roll damping coefficient into five physically distinct components:

Equation 7.43 — Ikeda roll damping decomposition:

$$B_{44} = B_F + B_W + B_E + B_{BK} + B_L \tag{6.43}$$

where B_F is the frictional component arising from the tangential shear stress on the hull surface, B_W is the wave-making component due to radiative energy loss (equivalent to the potential-flow radiation damping in Equation 6.6), B_E is the eddy-making component generated by flow separation at bilge corners and other sharp hull features, B_{BK} is the bilge keel component

attributable to the drag and vortex shedding from bilge keels, and B_L is the hull lift component produced by the hydrodynamic lift force on the hull at forward speed (Ölmez & Çakıcı, 2022).

Equation (6.43) provides the engineering framework that links the empirical two-term decrement law (Equation 6.41) to the first-principles vortex-shedding mechanism identified by Jung et al. (2013): the frictional and wave-making terms correspond to the linear decrement coefficient a, while the eddy-making and bilge keel terms—both governed by vortex shedding at sharp hull features and proportional to the square of the angular velocity—produce the quadratic decrement coefficient b. The lift component, which vanishes at zero speed, is significant only for vessels underway and increases with the square of forward speed (Ölmez & Çakıcı, 2022). Validation of the YTU DEEP strip-theory code against experimental data from seven AME CRC hull forms at Froude numbers $F_n = 0.285$ and 0.57 confirmed that the Ikeda decomposition, combined with the Salvesen strip theory, reproduces the measured roll, heave, and pitch RAOs with accuracy sufficient for preliminary design (Ölmez & Çakıcı, 2022). This five-component decomposition remains the standard in strip-theory seakeeping codes, where each component is evaluated from the vessel's principal dimensions and bilge geometry using empirical formulas calibrated against forced-roll model tests (Ölmez & Çakıcı, 2022).

Single-Degree-of-Freedom Roll Model with Active Fin Stabilisation

When the principal interest is roll dynamics and active control, the six-DOF coupled equation of motion (Equation 6.18) is often reduced to a single-DOF representation. Jimoh et al. (2021) adopt a 1DOF nonlinear roll model in which the state vector $\mathbf{x} = [\phi \ \dot{\phi}]^\top$ comprises the roll angle ϕ and roll rate $p = \dot{\phi}$:

Equation 7.44 — Single-DOF nonlinear roll dynamics:

$$\ddot{\phi} = a_1\,\phi + a_2\,\phi^3 + a_3\,\dot{\phi} + a_4\,\dot{\phi}\,|\dot{\phi}| + b\,\alpha + M_W \tag{6.44}$$

where α [rad] is the fin stabiliser steering angle (the control input), M_W is the wave-induced moment per unit inertia, and the coefficients encode the vessel's roll dynamics (Jimoh et al., 2021). The first two terms represent the nonlinear restoring moment: $a_1 = -Th/(I_{XX} + J_{XX})$ provides the linear restoring stiffness (proportional to the metacentric height h), and $a_2 = Th/[\phi_v^2(I_{XX} + J_{XX})]$ introduces the cubic nonlinearity governed by the flooding angle ϕ_v. The next two terms model roll damping: $a_3\,\dot{\phi}$ is the linear damping (with contributions from wave-making and added resistance from the fins), and $a_4\,\dot{\phi}|\dot{\phi}|$ is the nonlinear quadratic damping arising from viscous effects at sharp hull features (Jimoh et al., 2021).

The roll moment of inertia including the hydrodynamic added mass is estimated from the vessel's principal dimensions as (Jimoh et al., 2021):

Equation 7.45 — Roll inertia estimation:

$$I_{XX} + J_{XX} = \frac{T\,B_s^2}{g}\left(0.3085 + 0.0227\,\frac{B_s}{d_s} - 0.00043\,\frac{L}{100}\right)^2 \tag{6.45}$$

where T [t] is the vessel displacement, B_s [m] the beam, d_s [m] the draught, L [m] the length between perpendiculars, and g [m s^{-2}] the gravitational acceleration (Jimoh et al., 2021). This empirical formula enables roll dynamics analysis when detailed mass distribution data are unavailable.

The linear damping coefficient D_N and the nonlinear damping coefficient D_W are related to experimental coefficients n_1 and n_2 by (Jimoh et al., 2021):

$$D_N = \frac{2\,n_1}{\pi}\,\sqrt{Th\,(I_{XX} + J_{XX})}, \qquad D_W = \frac{3\,n_2\,(I_{XX} + J_{XX})}{4}$$

These correspond directly to the two-term damping law of Equation (6.41): D_N produces the linear decrement (a coefficient) and D_W yields the quadratic decrement (b coefficient) (Attwood, 1899; Jimoh et al., 2021).

The fin stabiliser generates a control moment per unit inertia through the hydrodynamic lift force acting on the fin surface (Jimoh et al., 2021):

Equation 7.46 — Fin stabiliser control moment:

$$M_C = -\frac{\rho\,U^2\,A_f\,l_f\,C_L^{\alpha}}{I_{XX} + J_{XX}}\,\alpha \tag{6.46}$$

where ρ [kg m^{-3}] is the water density, U [m s^{-1}] the forward speed, A_f [m^2] the fin planform area, l_f [m] the moment arm from the roll axis to the fin, and C_L^{α} the rate of change of the lift coefficient with respect to the fin angle (Jimoh et al., 2021). Equation (6.46) reveals the fundamental physics of fin stabilisation: (i) the control moment is proportional to U^2, making fin stabilisers most effective at high speed and poorly effective at low speed; (ii) the moment scales linearly with fin area A_f and moment arm l_f, favouring large fins placed far from the roll axis; and (iii) the moment is inversely proportional to the total roll inertia, so heavier vessels require larger fins for equivalent roll reduction (Jimoh et al., 2021).

The wave-induced disturbance M_W is modelled as a stochastic process characterised by the Pierson–Moskowitz spectrum (presented in the *Wave Mechanics and Ocean Waves* chapter of the companion volume). Jimoh et al. (2021) approximate the wave excitation by a second-order transfer function in state-space form:

Equation 7.47 — Wave disturbance state-space model:

$$\begin{bmatrix} \dot{d} \\ \dot{d}_w \end{bmatrix} = \begin{bmatrix} 0 & 1 \\ -\omega_0^2 & -2\zeta_w\omega_0 \end{bmatrix} \begin{bmatrix} d \\ d_w \end{bmatrix} + \begin{bmatrix} 0 \\ k_w \end{bmatrix} w_n \tag{6.47}$$

where ω_0 [rad s^{-1}] is the modal (peak) frequency of the wave spectrum, ζ_w is a damping coefficient (typically $\zeta_w = 0.1$), w_n is zero-mean Gaussian white

noise, and $k_w = 2\zeta_w\omega_0\sigma_w$ with $\sigma_w = \sqrt{S(\omega_0)}$ (Jimoh et al., 2021). The wave-induced disturbance entering Equation (6.44) is then $M_W = d_w$. When the vessel moves at forward speed U, the modal frequency is shifted to the encounter frequency $\omega_e = \omega_0 - (\omega_0^2/g)\,U\cos\beta$ (cf. Equation 6.31), where β is the angle between the vessel heading and wave propagation direction (Jimoh et al., 2021).

6.3.3 Response in Irregular Seas

When a vessel navigates in an irregular sea characterised by the short-crested wave spectrum $S(\omega,\mu) = S(\omega)\,D(\mu)$ (as defined in the *Wave Mechanics and Ocean Waves* chapter of the companion volume), the wave-induced perturbation forces vary randomly in time, and the vessel's motion response becomes a stochastic process. The theoretical framework for predicting these responses must connect the spectral description of the wave field to the dynamic equations of the vessel.

State-Space Formulation for Time-Domain Response

Zhang et al. (2025) developed a three-degree-of-freedom (heave, roll, pitch) perturbation model for a vessel in constant-velocity straight-line navigation. By combining the coupled equation of motion (Equation 6.18), the hydrodynamic forces (inertial and viscous), and the restoring forces (Equation 6.20) with the nonlinear Froude–Krylov forces computed over the instantaneous wetted surface, the second-order perturbation equation is reduced to a first-order state-space form (Zhang et al., 2025):

Equation 7.48 — State-space perturbation equation:

$$\dot{\mathbf{X}}_v = \mathbf{A}_v(\mathbf{X}_v)\,\mathbf{X}_v + \mathbf{E}_v\,\mathbf{W}_v(\mathbf{X}_v,t) \tag{6.48}$$

where $\mathbf{X}_v = (\boldsymbol{\xi}_3,\,\dot{\boldsymbol{\xi}}_3)^\top \in \mathbb{R}^6$ is the perturbation state vector comprising the three-DOF displacements $\boldsymbol{\xi}_3 = (\xi_3,\,\xi_4,\,\xi_5)^\top$ and their time derivatives (Zhang et al., 2025). The system matrix is (Zhang et al., 2025):

Equation 7.49 — Perturbation system matrix:

$$\mathbf{A}_v(\mathbf{X}_v) = \begin{pmatrix} \mathbf{0}_{3\times3} & \mathbf{I}_3 \\ (\mathbf{M}_{v3} - \mathbf{M}_{hdI3})^{-1}\,\mathbf{M}_{re3} & (\mathbf{M}_{v3} - \mathbf{M}_{hdI3})^{-1}\,(\mathbf{M}_{hdD3} - \mathbf{M}_{ci3}) \end{pmatrix} \tag{6.49}$$

where $\mathbf{M}_{v3}$ is the vessel inertia matrix, $\mathbf{M}_{hdI3}$ the inertial hydrodynamic (added mass) matrix, $\mathbf{M}_{hdD3}$ the viscous hydrodynamic matrix, $\mathbf{M}_{ci3}$ the Coriolis–centrifugal matrix, and $\mathbf{M}_{re3}$ the restoring force matrix, all reduced to the three active degrees of freedom (heave, roll, pitch) (Zhang et al., 2025). The wave disturbance matrix $\mathbf{E}_v$ and the wave disturbance vector $\mathbf{W}_v(\mathbf{X}_v,t)$ transmit the Froude–Krylov forces into the perturbation dynamics (Zhang et al., 2025):

Equation 7.50 — Wave disturbance matrix and vector:

$$\mathbf{E}_v = \begin{pmatrix} \mathbf{0}_{3\times 3} \\ (\mathbf{M}_{v3} - \mathbf{M}_{hdI3})^{-1} \end{pmatrix}, \qquad \mathbf{W}_v(\mathbf{X}_v, t) = \mathbf{M}_{MNA3}\, \mathbf{M}_{MD}^{\top}(\boldsymbol{\xi}_3, t) \quad (6.50)$$

where $\mathbf{M}_{MNA3}$ encodes the normal vectors and areas of the hull surface mesh elements, and $\mathbf{M}_{MD}(\boldsymbol{\xi}_3, t)$ is the mesh dynamic pressure matrix that depends nonlinearly on both the vessel's instantaneous perturbation state and time (Zhang et al., 2025). Because $\mathbf{A}_v$ depends on $\mathbf{X}_v$ through the restoring force matrix (which varies with vessel attitude), and $\mathbf{W}_v$ depends on both $\mathbf{X}_v$ and t, Equation (6.48) is a *nonlinear, non-stationary* ordinary differential equation that must be solved numerically (Zhang et al., 2025).

Statistical Characterisation of Vessel Response

The time-domain solution of Equation (6.48) produces time histories of the heave displacement $\xi_3(t)$, roll angle $\xi_4(t)$, and pitch angle $\xi_5(t)$. The statistical properties of these responses are characterised by two families of measures (Zhang et al., 2025):

- **Significant values** ($\xi_{3,1/3}$, $\xi_{4,1/3}$, $\xi_{5,1/3}$): the average of the absolute values of the largest maxima and minima in the top one-third of the perturbation time series. These are the motion analogue of the significant wave height $H_{1/3}$ and provide a single-number indicator of motion severity.

- **Dominant angular frequencies** ($\omega_{d\xi_3}$, $\omega_{d\xi_4}$, $\omega_{d\xi_5}$): determined by performing a Fast Fourier Transform on the time series, computing the single-sided amplitude spectrum, and identifying the angular frequency at which the spectral amplitude is maximum (Zhang et al., 2025). The dominant frequency indicates the prevailing period of the vessel's oscillation, which depends on both the wave encounter spectrum and the vessel's natural frequencies.

Sensitivity of Response to Sea-State Parameters

Zhang et al. (2025) conducted a global sensitivity analysis using the Sobol variance-decomposition method, performing 4800 time-domain simulations of the KVLCC2 vessel ($L_{pp} = 320\,\text{m}$, $C_B = 0.81$, Froude number $F_n = 0.142$) across the full range of North Atlantic sea states 2–8, with four input parameters: significant wave height $H_{1/3} \in [0.3\,\text{m},\ 11.5\,\text{m}]$, modal wave period $T_m \in [7.5\,\text{s},\ 16.4\,\text{s}]$, principal wave encounter angle $\mu_e \in [0°,\ 180°]$, and mean vessel speed $V_{va} \in [0,\ 7.97\,\text{m s}^{-1}]$ (≤ 15.5 knot).

The first-order Sobol sensitivity indices revealed a clear hierarchy of influence on the perturbation significant values (Zhang et al., 2025):

1. **Significant wave height** $H_{1/3}$: dominant influence on perturbation amplitude (first-order index $S_1 \approx 0.38$–0.48 for heave, roll, and pitch significant values).
2. **Modal period** T_m: second-largest influence ($S_1 \approx 0.30$–0.36).
3. **Encounter angle** μ_e: moderate influence ($S_1 \approx 0.11$–0.13).
4. **Mean velocity** V_{va}: negligible influence ($S_1 < 0.01$).

For the dominant frequencies of the response, the hierarchy differs: the modal period T_m becomes the most influential parameter ($S_1 \approx 0.28$–0.58), followed by the encounter angle μ_e, while $H_{1/3}$ and V_{va} have negligible effects (Zhang et al., 2025). The total sensitivity indices confirm significant interaction effects among the parameters: the sum of all total indices exceeds unity, indicating that combined (higher-order) effects—particularly between $H_{1/3}$ and T_m—contribute substantially to the variance of the vessel response (Zhang et al., 2025).

Comparative analysis under sea state 4 conditions further revealed non-monotonic directional effects (Zhang et al., 2025): (i) heave amplitude is greatest under beam seas, followed by following seas, and lowest under head seas; (ii) the dominant frequencies of the three-DOF perturbations are highest under head seas and lowest under following seas, consistent with the encounter frequency relation (Equation 6.31). These trends arise because the KVLCC2's waterline length exceeds the wavelengths of most wave components at sea state 4, while the beam is smaller, making transverse wave components more effective at exciting vertical motions (Zhang et al., 2025).

6.3.4 Parametric Rolling

Parametric rolling is a dynamic instability in which roll motion is excited not by a direct wave-induced heeling moment but by the periodic variation of the vessel's restoring arm as it passes through successive wave crests and troughs. The physical mechanism is as follows: in longitudinal seas (head or following), the encounter with successive wave crests and troughs causes the waterplane area and its second moment to change cyclically, thereby modulating the metacentric height GM and the restoring coefficient C_{44} at the encounter frequency (Rawson & Tupper, 2001).

The equation governing roll in the presence of time-varying restoring stiffness takes the form of a damped Mathieu equation (Rawson & Tupper, 2001):

Equation 7.51 — Damped Mathieu equation for parametric roll:

$$\ddot{\phi} + 2\mu\,\dot{\phi} + \omega_0^2\left[1 - 2h\cos(\omega_E\, t)\right]\phi = 0 \tag{6.51}$$

where ϕ is the roll angle, μ is the linear damping coefficient, $\omega_0 = \sqrt{g\,\overline{\mathrm{GM}}/k_{xx}^2}$ is the natural roll frequency in calm water (cf. Equation 6.17), ω_E is the encounter frequency (Equation 6.31), and h is the modulation depth—the ratio

of the amplitude of the GM variation to the mean value $\overline{\mathrm{GM}}$ (el Moctar et al., 2021; Rawson & Tupper, 2001).

The most dangerous condition for parametric excitation occurs when the encounter frequency is approximately twice the natural roll frequency (Rawson & Tupper, 2001):

Equation 7.52 — Principal parametric resonance condition:

$$\omega_E \approx 2\,\omega_0 \tag{6.52}$$

Under this condition, the wave encounter period is half the natural roll period, so the ship experiences a restoring arm increase on each roll through the upright and a restoring arm decrease at each extreme of roll—precisely the phasing that pumps energy into the roll motion. Even modest GM variations ($h \approx 0.1$–0.2) can trigger large roll amplitudes if the damping μ is insufficient (Rawson & Tupper, 2001).

The stability boundaries of Equation (6.51) are given by the Ince–Strutt diagram: the roll is stable (bounded) for most combinations of $(\omega_E/\omega_0,\, h)$ but becomes unbounded in wedge-shaped instability regions emanating from $\omega_E/\omega_0 = 2, 1, 2/3, \ldots$ The width of each instability region increases with the modulation depth h and narrows with increasing damping μ. For practical purposes, only the principal region near $\omega_E \approx 2\omega_0$ is of concern, because the higher-order regions are narrow and easily suppressed by ship damping (el Moctar et al., 2021; Rawson & Tupper, 2001).

Vessels with large bow flare and stern overhang—particularly modern container ships and car carriers—are especially susceptible to parametric rolling because the waterplane shape changes strongly between the crest and trough conditions, producing large values of h. The encounter frequency condition (Equation 6.52) is typically met in head seas at moderate forward speed or in following seas at low speed (Rawson & Tupper, 2001).

Vulnerability Assessment and Operational Mitigation

The Second Generation Intact Stability Criteria (SGISC) described in Chapter 4 (Section 4.4.3) provide a quantitative framework for evaluating susceptibility to parametric rolling. In the Level 2 vulnerability check, a long-term stability failure index C_2 is computed by summing the wave-weighted probability of roll amplitudes exceeding a critical value (typically $25°$) across all combinations of Froude number and heading angle. A vessel is not vulnerable if $C_2 \leq 0.025$ (Spyrou et al., 2023).

The roll amplitude in each representative sea state is estimated using Grim's effective wave concept (Spyrou et al., 2023). The effective wave spectrum is obtained from the incident directional spectrum $S(\omega, \alpha)$ by the transfer function:

Equation 7.53 — Grim's effective wave spectrum for parametric roll assess-

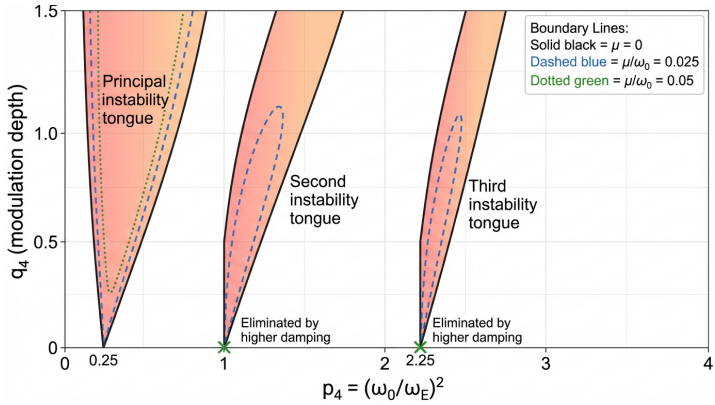

Figure 6.4: Ince–Strutt stability diagram for the Mathieu equation governing parametric roll (Equation 6.54). The horizontal axis is the frequency-ratio parameter $p_4 \approx (\omega_0/\omega_E)^2$; the vertical axis is the modulation depth q_4 proportional to the amplitude of metacentric height variation. Shaded wedge-shaped tongues emanating from $p_4 = 0.25,\ 1,\ 2.25, \ldots$ denote regions of unbounded roll growth (instability). The principal tongue near $p_4 = 0.25$ ($\omega_E \approx 2\omega_0$, Equation 6.52) is the widest and most dangerous. Dashed curves show how increasing linear damping μ/ω_0 contracts the tongue boundaries, with moderate damping ($\mu/\omega_0 \approx 0.05$) eliminating higher-order instability regions entirely (Biran, 2003). The operating point of a specific vessel in a given sea state is determined by the Grim effective-wave spectrum (Equation 6.53).

ment:

$$S_{\eta_{\text{eff}}}(\omega, L_{pp}, \alpha) = \left[\frac{\omega^2}{g\, L_{pp} \cos\chi'} \, \frac{\sin\!\left(\frac{\omega^2}{2g} L_{pp} \cos\chi'\right)}{\pi^2 - \left(\frac{\omega^2}{2g} L_{pp} \cos\chi'\right)^2} \right]^2 S(\omega, \alpha) \qquad (6.53)$$

where $\chi' = \chi - \alpha$, χ is the ship heading, α is the propagating direction of each spectral component, and L_{pp} is the length between perpendiculars. The significant effective wave height $H_{\text{eff}} = 4.0\sqrt{m_0}$ with $m_0 = \iint S_{\eta_{\text{eff}}}\, \mathrm{d}\omega\, \mathrm{d}\alpha$ characterises the amplitude of the waterplane modulation experienced by the hull. The roll response is then computed from an uncoupled nonlinear roll equation with time-varying restoring moment in equivalent regular waves determined from this spectrum (Spyrou et al., 2023).

Case studies reported by Spyrou et al. (2023) illustrate the practical consequences. A C11 class container ship ($L_{pp} = 262\,\text{m}$, $B = 40\,\text{m}$, $GM = 1.965\,\text{m}$) failed both Level 2 checks ($C_1 = 0.437 > 0.06$; $C_2 = 0.026 > 0.025$)—consistent with the historical record, as the actual vessel experienced $40°$ parametric roll in the North Pacific in 1998. For such vessels, *operational measures* offer an alternative to redesign: voyage simulation demonstrated that optimal fuel-consumption routes naturally avoided the low-Froude-number conditions ($Fn < 0.1$) where parametric rolling was predicted, reducing the risk without significant delay (Spyrou

et al., 2023).

A complementary approach uses X-band wave radar to measure the directional wave spectrum in real time and feed it into the Grim effective-wave calculation on board (Spyrou et al., 2023). Validation on a RoPax vessel showed that the simplified method, driven by radar-measured spectra, reproduced the observed maximum roll angle with reasonable accuracy and correctly identified that a 15° heading change would substantially reduce the parametric roll response. This wave-radar-assisted operational guidance connects the physics-based SGISC framework to real-time shipboard decision-making (Spyrou et al., 2023).

Nonlinear Coupling Effects in Parametric Rolling

The Mathieu equation (Equation 6.51) assumes that the roll restoring moment oscillates sinusoidally with the encounter frequency. To connect this physical model to the classical stability analysis, the damped Mathieu equation is reduced to its standard form by the substitution $\phi_a = \xi_4 \exp(\mu\tau)$, where $\tau = \omega_E t$ is the non-dimensional time (Shi et al., 2024):

Equation 7.54 — Standard Mathieu equation for parametric roll stability:

$$\frac{\mathrm{d}^2\phi_a}{\mathrm{d}\tau^2} + \left(p_4 + q_4 \cos\tau\right)\phi_a = 0 \tag{6.54}$$

where $p_4 = \Delta\,\overline{\mathrm{GM}}_0 \,/\, (\omega_E^2\, I'_{xx}) - \mu^2$ is the ratio of the natural roll frequency squared to the encounter frequency squared (diminished by the damping), and $q_4 = \Delta\,\mathrm{GM}_a \,/\, (\omega_E^2\, I'_{xx})$ measures the amplitude of the restoring-stiffness modulation (Shi et al., 2024). Here Δ is the displacement, $\overline{\mathrm{GM}}_0$ the mean metacentric height, GM_a the amplitude of the metacentric height variation, I'_{xx} the roll moment of inertia, and μ the linear damping coefficient. The Ince–Strutt stability diagram in the (p_4, q_4) plane contains wedge-shaped instability tongues emanating from $p_4 = 0.25, 1, 2.25, \ldots$; the principal tongue near $p_4 \approx 0.25$ ($\omega_E \approx 2\omega_0$, Equation 6.52) is the most dangerous because its width increases rapidly with modulation depth q_4 (Shi et al., 2024).

Shi et al. (2024) applied a fully nonlinear potential flow (FNPF) method to simulate parametric rolling of the KRISO Container Ship (KCS, $L_{pp} = 230\,\mathrm{m}$, $C_b = 0.6505$) in head seas. Unlike the linear or weakly nonlinear potential flow methods discussed in Section 6.2.1, the FNPF approach solves the exact free-surface boundary conditions—the Zakharov kinematic and dynamic equations—on the instantaneous wetted surface in the time domain, capturing the fully nonlinear interaction between large incident waves and hull motions (Shi et al., 2024). The acceleration potential technique decomposes the time derivative of the velocity potential into six modal potentials (one per degree of freedom) and a residual, from which the instantaneous added mass matrix is evaluated by pressure integration. This decomposition decouples the acceleration–fluid-force interdependence, enabling stable 6-DOF time-domain integration (Shi et al., 2024).

For the KCS without bilge keels at wave steepnesses $H/\lambda = 0.02$ and wavelength-to-ship-length ratios of $\lambda/L_{pp} = 1.00$ and 1.15, the FNPF simulation reproduced the experimentally observed parametric roll with amplitudes of 24° and 18.7°, respectively, in close agreement with model-test measurements (Shi et al., 2024). Three physical features emerged from the nonlinear analysis that the linearised Mathieu model (Equation 6.54) cannot capture. First, *cross-DoF coupling*: after the onset of parametric rolling, the heave equilibrium position shifted slightly upward and a small bow trim developed in the pitch equilibrium, demonstrating that large-amplitude roll pumps energy into the heave and pitch modes. Second, the *nonlinear restoring moment* computed from the instantaneous wetted surface exceeded the Mathieu model's sinusoidal approximation, exhibiting pronounced higher-order harmonic components due to hull fore–aft asymmetry—the flared stern of the KCS produces a larger roll restoring coefficient in stern-trim conditions than the tapered bow does in bow-trim conditions. Third, potential flow methods omit viscous roll damping; when supplemented by the empirical two-term damping law (Equation 6.41) with coefficients $a = 0.0336$ and $b = 0.0067$, the FNPF simulation captured both the roll amplitude and phase with accuracy comparable to URANS computations (Shi et al., 2024).

6.3.5 Slamming and Green Water

Water shipping (green water) on the deck of marine structures is a recurring problem in coastal, ocean, and offshore engineering, with direct implications for operations and human safety. Hernández-Fontes et al. (2020) conducted systematic wet dam-break experiments to investigate the patterns and vertical loads of shipping water events on a rectangular fixed structure. Their work provides a detailed classification of green water event types as a function of the steepness of the incoming bore.

Classification of Shipping Water Events

In the experiments of Hernández-Fontes et al. (2020), four wet dam-break ratios ($r_d = h_0/h_1 = 0.7, 0.6, 0.5,$ and 0.4) were combined with two freeboards ($f_b = 0.030\,\text{m}$ and $0.042\,\text{m}$) to generate isolated shipping water events on a fixed structure. The ratio $h_0/h_1 = 0.8$ did not produce significant water shipping for either freeboard. High-speed camera visualisation at $500\,\text{fps}$, synchronised with wave probes and a force balance, allowed detailed characterisation of the shipping water patterns.

Three types of shipping water events were identified, defined principally by the size of the air cavity formed at the bow edge and the angle of the flow crest during the initial stages of water invasion (Hernández-Fontes et al., 2020):

1. **Dam-break type (DB):** Obtained with the lowest bore steepness ($\varepsilon \approx 0.12$, $r_d \approx 0.7$). After the water level reached the deck, a small jet in-

vaded the deck followed by the bulk of the water. No air cavity formed at the bow. The crest angles were obtuse ($125° < \theta < 165°$) during the initial shipping stages. This event produced the lowest vertical loads.

2. **Plunging-dam-break with small cavity (PDBSC):** Obtained with moderate bore steepness ($\varepsilon \approx 0.21$–0.33, $r_d \approx 0.6$–0.5). A small plunging wave reached the deck and encapsulated a small amount of air, forming a cavity at the bow edge. The cavity was initially almost circular but underwent anisotropic compression as the shipped water weight increased, until it was trapped by the flow and collapsed. Forward and backward jets formed during cavity closure. The crest angles were sharper than in the DB type ($106° < \theta < 158°$) (Hernández-Fontes et al., 2020).

3. **Plunging-dam-break with large cavity (PDBLC):** Obtained with the highest bore steepness ($\varepsilon \approx 0.55$, $r_d \approx 0.4$). A large air cavity formed at the bow edge, extending horizontally to approximately one-third of the deck length. The maximum water elevation on the deck developed a forward-pointing horn shape. Large upstream and downstream jets formed almost at the end of the deck, and the shipping flow impacted the vertical wall directly. This was the most severe event type (Hernández-Fontes et al., 2020).

This classification extends the earlier work of Greco et al. (2007), as cited in Hernández-Fontes et al. (2020), who identified dam-break (DB), plunging-dam-break (PDB), and hammer-fist (HF) event types using regular waves. The PDBLC event differs from the HF event principally by the formation of a large air cavity that was not reported in the latter.

Cavity Formation and Steepness Dependence

As bore steepness increased from $\varepsilon \approx 0.21$ to $\varepsilon \approx 0.55$, the cavity area (non-dimensionalised as A_{cav}/L^2, where L is the deck length) increased for both freeboards. The cavity aspect ratio $z_{\text{cav}}/x_{\text{cav}}$ decreased with increasing steepness, meaning that steeper bores produced more semi-elliptical cavities with a greater horizontal extent, whereas longer (less steep) bores produced arc-like cavities (Hernández-Fontes et al., 2020). The cavity compression process during PDBSC events was described as analogous to the flip-through cavity evolution on a vertical wall: an initially circular cavity deforms isotropically, then anisotropically as a forward jet propagates along the deck surface, until trapping and collapse (Hernández-Fontes et al., 2020).

Freeboard Exceedance

The non-dimensional maximum freeboard exceedance h^*_{em} at the bow increased with bore height h^*_w, with an approximately linear relationship for low and moderate steepness cases ($\varepsilon \leq 0.33$). For the steepest bore ($\varepsilon \approx 0.55$),

the relationship deviated from linearity, attributed to the steep flow pattern and the formation of the sharp flow crest at nearly right angles when the maximum freeboard exceedance was attained (Hernández-Fontes et al., 2020). For the higher freeboard experiments, bores with a partially broken front were observed for $h_0/h_1 = 0.6$ and 0.5, causing particular features in the initial shipping stages.

Vertical Loads on Deck: Forward and Backflow Loading

Hernández-Fontes et al. (2020) measured the quasi-static vertical loads over the deck of the structure using a force balance of four S-type axial load cells, sampled at 500 Hz with a 100 Hz low-pass filter. They defined two loading phases:

- **Forward loads:** Generated by water propagating from the beginning of the deck to the stage at which it reached maximum displacement on the vertical wall during run-up.
- **Backflow loads:** Generated after the wall run-up maximum, including loads caused by water returning to the reservoir.

The non-dimensional vertical force was defined as:
Equation 7.55 — Non-dimensional vertical force on deck:

$$F^* = \frac{F}{\rho\, g\, h_1\, L^2} \tag{6.55}$$

where F is the measured vertical force, $\rho = 1000\,\mathrm{kg\,m^{-3}}$ is the water density, $g = 9.81\,\mathrm{m\,s^{-2}}$ is gravitational acceleration, h_1 is the upstream water depth, and $L = 0.195\,\mathrm{m}$ is the structure length (Hernández-Fontes et al., 2020).

The mean maximum forward loads increased significantly with bore steepness:

Table 6.1: Mean maximum forward loads by shipping water event type (Hernández-Fontes et al., 2020).

Event type	Bore steepness ε	Mean max. F^* (M_1)
DB	0.12	≈ 0.082
PDBSC ($r_d \approx 0.6$)	0.21	≈ 0.24
PDBSC ($r_d \approx 0.5$)	0.33	≈ 0.424
PDBLC ($r_d \approx 0.4$)	0.55	≈ 0.529

The forward peak load for the PDBLC event was approximately 6.4 times larger than for the DB event. The PDBSC events showed intermediate loading, with the peak load increasing by approximately 176% and 517% relative to the moderate and mild events, respectively, for the $\varepsilon \approx 0.33$ case (Hernández-Fontes et al., 2020).

A key finding was the significance of backflow loading. The ratio of backflow peak (M_2) to forward peak (M_1) was between 0.64 and 0.86 for all cases, indicating that backflow loads are of the same order as forward loads (Hernández-Fontes et al., 2020). For the DB, PDBSC, and moderate PDBSC cases, the load time series showed progressive forward loading, a first peak (M_1), a decay, and then a second peak (M_2) due to backflow. In the PDBLC case, however, the forward loading increased more rapidly, and the subsequent run-down produced an almost constant loading period due to the large water mass over the deck.

The impact pressure generated when the ship's bow re-enters the water after emergence—slamming—is governed by the relative velocity between the hull and the free surface and the local hull geometry (Faltinsen, 1990). Rawson and Tupper (2001) present the slamming pressure as:

Equation 7.56 — Slamming impact pressure:

$$p = \tfrac{1}{2}\,\rho\,\dot{r}^2\,F(\beta) \tag{6.56}$$

where ρ is the water density, $\dot{r}$ is the relative velocity between the hull section and the water surface, and $F(\beta)$ is a function of the local deadrise angle β of the hull section (Rawson & Tupper, 2001). Sections with small deadrise (flat bottom) produce the highest impact pressures because the added mass changes rapidly during water entry. For a wedge-shaped section, $F(\beta) \to \pi/\beta$ as $\beta \to 0$, showing that perfectly flat sections ($\beta = 0$) would experience infinite pressure—the physical reason why all ship sections maintain some minimum deadrise angle in the fore body.

The probability that slamming occurs in a given sea state depends on two simultaneous conditions being satisfied: the bow must emerge from the water, and the relative velocity at re-entry must exceed a threshold value. Rawson and Tupper (2001) express the probability of a slam as:

Equation 7.57 — Slamming probability:

$$\Pr(\text{slam}) = \exp\!\left(-\frac{T_{\text{bow}}^2}{2\,m_{0r}}\right) \tag{6.57}$$

where T_{bow} is the draught at the fore perpendicular and m_{0r} is the variance (zeroth spectral moment) of the relative vertical motion at the bow (Rawson & Tupper, 2001). Similarly, the probability of deck wetness at the bow is (Rawson & Tupper, 2001):

Equation 7.58 — Deck wetness probability:

$$\Pr(\text{wetness}) = \exp\!\left(-\frac{F_b^2}{2\,m_{0r}}\right) \tag{6.58}$$

where F_b is the freeboard at the location of interest. Equations (6.57) and (6.58) follow from the Rayleigh distribution of peak amplitudes in a narrow-band Gaussian process. They show that slamming and wetness become exponentially less probable as draught and freeboard increase relative to the motion variance—a direct design guide for bow geometry.

6.3.6 Added Resistance in Waves

When a vessel advances through a seaway, it experiences a mean resistance increment above its calm-water value. This *added resistance in waves* arises from the second-order (time-averaged) drift forces generated by the interaction of the hull with the wave field. el Moctar et al. (2021) derive the mean drift force by time-averaging the second-order pressure forces over one wave period.

The total drift force is decomposed into two contributions (el Moctar et al., 2021). The first arises from the integration of the first- and second-order pressures over the mean wetted surface:

Equation 7.59 — Drift force from pressure integration:

$$\overline{\mathbf{F}_A} = \sum_{\text{panels}} \left[\overline{p_2}\,\mathbf{n}_0 + \overline{p_1\,\mathbf{n}_1} + \overline{p_0\,\mathbf{n}_2} \right] \tag{6.59}$$

where p_0, p_1, and p_2 are the zeroth-, first-, and second-order pressures, $\mathbf{n}_0$, $\mathbf{n}_1$, and $\mathbf{n}_2$ are the corresponding panel normal vectors, and the overbar denotes the time average (el Moctar et al., 2021). The second contribution arises from the variable waterline: the oscillation of the wave surface relative to the hull adds a line-integral term along the instantaneous waterline intersection (el Moctar et al., 2021).

The mean longitudinal drift force $\overline{F_x}$ is non-dimensionalised as the added resistance coefficient C_{AW} (Equation 5.20 in Chapter 5), which peaks when the wave length is comparable to the ship length ($\lambda/L \approx 1$) and the radiated wave energy is greatest (el Moctar et al., 2021). The practical consequence is involuntary speed reduction: the propulsion system must overcome both calm-water resistance and the time-averaged wave drift force, with the fuel-consumption and schedule implications discussed in Section 5.3.6.

6.4 Applications in Maritime Systems

6.4.1 Seakeeping Criteria and Operability

The seakeeping performance of a vessel is assessed against quantitative limiting criteria that define the boundary between acceptable and unacceptable operating conditions. Rawson and Tupper (2001) present the principal criteria used in naval architecture practice:

1. **Vertical acceleration.** The RMS vertical acceleration at the bridge or cargo spaces must not exceed a threshold (typically $0.2\,g$ for crew comfort, $0.1\,g$ for passenger vessels). The vertical acceleration at any point along the ship is a combination of heave and pitch contributions and increases toward the extremities (Rawson & Tupper, 2001).

2. **Slamming frequency.** From Equation (6.57), the probability of a slam per wave encounter is computed for each sea state and heading. The

limiting criterion is typically 3–5 slams per 100 wave encounters for merchant ships (Rawson & Tupper, 2001).

3. **Deck wetness.** From Equation (6.58), the frequency of green water on deck must remain below a specified limit—usually 5% of wave encounters at the bow (Rawson & Tupper, 2001).

4. **Propeller emergence.** The propeller should not emerge above the free surface by more than one-quarter of its diameter, as this causes racing, load fluctuations, and potential cavitation damage. The criterion is that the depth of the propeller tip $T_0 - D/4$ should not be exceeded (Rawson & Tupper, 2001).

5. **Motion sickness incidence (MSI).** The percentage of unacclimatised persons who become seasick within a given exposure period depends on the vertical acceleration level and its frequency. The MSI increases sharply when the acceleration frequency is near 0.17 Hz (≈ 6 s period), corresponding to the peak of human vestibular sensitivity. Rawson and Tupper (2001) report a subjective motion measure of the form $SM = A(f)\,a^{1.43}$, where $A(f)$ is a frequency-dependent weighting and a is the acceleration amplitude.

For each combination of sea state, heading, and speed, the motion spectrum is computed from the RAO (Equation 6.30) and the wave spectrum. The spectral moments yield the RMS values of each criterion quantity. The set of speed–heading combinations at which all criteria are satisfied defines the *operability index*—the fraction of a given mission profile during which the vessel can perform its intended function (Lewis, 1988; Molland, 2008; Rawson & Tupper, 2001).

6.4.2 Hull Form Design for Seakeeping

The dominant hull form parameters affecting seakeeping performance are the length-to-beam ratio L/B, the block coefficient C_b, the bow flare angle, and the hull section shape at the fore body (Molland, 2008; Rawson & Tupper, 2001).

Rawson and Tupper (2001) identify the following design trends:

- **Length.** Longer ships have lower natural frequencies in heave and pitch (both scale as $1/\sqrt{L}$) and experience reduced motions relative to their length. The ratio of ship length to wave length L/λ directly controls the RAO: when $L/\lambda > 1$, the ship spans more than one wavelength and individual wave effects tend to cancel.

- **Block coefficient.** Finer hull forms (lower C_b) generally exhibit smaller heave and pitch motions because the waterplane area changes more gradually as the ship moves through waves. However, fine forms may

also reduce damping, potentially increasing roll in beam seas (Rawson & Tupper, 2001).

- **Bow flare.** Increased bow flare enlarges the waterplane area as the bow immerses, providing a nonlinear restoring force that limits pitch amplitude. However, large flare also amplifies slamming pressures (Equation 6.56) because it reduces the effective deadrise angle of the impacting section (Rawson & Tupper, 2001).
- **Beam-to-draught ratio.** A larger B/T ratio increases the metacentric height and stiffens the roll response, reducing the natural roll period. While this improves roll stability limits, it may bring the natural roll period closer to common encounter frequencies, increasing roll amplitudes (Molland, 2008; Rawson & Tupper, 2001).

6.4.3 Motion Stabilisation Systems

Bilge Keels

The most common passive roll-damping device is the bilge keel—a flat plate projecting from the hull along the turn of the bilge. Attwood (1899) analysed the physics of bilge keel damping by modelling each keel as a flat surface moving through water, using data from Froude's experiments with an oscillating flat board. The resistance offered by a bilge keel depends on the square of the relative velocity between the keel and the water, and the resulting decrement contribution is (Attwood, 1899):

Equation 7.60 — Bilge keel decrement:

$$\Delta\Phi_{\text{BK}} = \frac{8}{3}\,\frac{c\,A\,r^{3}}{I}\,\Phi^{2} \tag{6.60}$$

where c is the coefficient of normal pressure at unit velocity, A is the area of one side of the bilge keels, r is the mean lever arm from the centre of oscillation to the bilge keel, I is the moment of inertia of the vessel (with $I = Wk^{2}/g$), and Φ is the roll angle (Attwood, 1899).

Equation (6.60) reveals several important design principles: (i) the decrement increases linearly with keel area A; (ii) it increases as the cube of the lever arm r, so that keels placed far from the roll axis (i.e. at the bilge rather than near the keel) are most effective; (iii) the decrement varies inversely with the vessel's moment of inertia, so bilge keels are proportionally less effective on vessels with large I; and (iv) the decrement increases with the square of the roll angle, meaning bilge keels are most effective at large amplitudes—precisely when they are most needed (Attwood, 1899).

The pressure-rise mechanism at the bilge keel was further investigated by Professor Bryan (I.N.A., 1900), as discussed by Attwood (1899): when the hull rotates, the flow at the sharp bilge corner must decelerate and change direction, producing a local pressure rise on both the upstream and downstream

faces of the keel. The resulting forces create a restoring moment that opposes the rolling motion, and the effect is more pronounced for sharper bilge sections than for rounded ones (Attwood, 1899).

Attwood (1899) also noted that bilge keels add slightly to the roll period—approximately 5% in the case of HMS *Revenge*—because the entrained water increases the effective moment of inertia. Forward motion of the vessel into undisturbed water further enhances the resistance to rolling, so bilge keel effectiveness improves when the vessel is underway (Attwood, 1899).

Active Fin Stabilisers

Active fin stabilisers employ controllable hydrofoils mounted at the bilge to generate anti-rolling moments. The control moment produced by each fin (Equation 6.46) is proportional to the square of the forward speed, the fin planform area, and the lift-curve slope, providing a direct physical mechanism to counteract wave-induced roll (Jimoh et al., 2021).

The physical constraints on fin stabiliser operation are set by the maximum mechanical angle $\alpha_{\max}$ (typically $\pm 30°$) and the maximum angular rate of the fin actuator ($\sim 25\,°\,\mathrm{s}^{-1}$). Exceeding the effective angle of attack leads to dynamic stall, sharply reducing lift and potentially amplifying roll rather than reducing it (Jimoh et al., 2021). These actuator limitations have important practical consequences: control strategies that do not account for magnitude and rate saturation may produce roll *amplification* instead of the intended reduction (Jimoh et al., 2021).

Jimoh et al. (2021) quantified fin stabiliser performance under sea state 5 conditions ($H_s = 3.5$ m) for a vessel with design speed of $7.7\,\mathrm{m\,s}^{-1}$ (≈ 15 knot), examining three encounter directions and two forward speeds. Table 6.2 summarises the roll reduction achieved by the constrained fin stabiliser under representative sailing conditions.

Table 6.2: Roll angle reduction by active fin stabiliser under sea state 5 ($H_s = 3.5$ m) with fin angle constraint $\pm 30°$ and rate constraint $25\,°\,\mathrm{s}^{-1}$ (Jimoh et al., 2021).

Sea condition	Speed [$\mathrm{m\,s}^{-1}$] (kn)	Open-loop RMS	Roll reduction
Beam seas ($\beta = 90°$)	7.7 (15)	$2.08°$	63.7%
Beam seas ($\beta = 90°$)	5.1 (10)	$2.12°$	52.2%
Quartering seas ($\beta = 45°$)	7.7 (15)	$3.39°$	74.4%
Quartering seas ($\beta = 45°$)	5.1 (10)	$3.22°$	66.8%
Bow seas ($\beta = 135°$)	7.7 (15)	$1.00°$	53.0%
Bow seas ($\beta = 135°$)	5.1 (10)	$1.46°$	39.0%

Several physical trends emerge from these data (Jimoh et al., 2021). First, fin stabiliser efficacy decreases with forward speed—reducing from $7.7\,\mathrm{m\,s}^{-1}$ to $5.1\,\mathrm{m\,s}^{-1}$ (15 to 10 knot) consistently lowers the roll reduction across all encounter angles—confirming that the U^2 dependence of the fin moment

(Equation 6.46) is the governing factor. Second, the greatest absolute roll reduction occurs in quartering seas ($\beta = 45°$), where the open-loop roll is most severe and the fin has sufficient dynamic range to counteract the disturbances. Third, in bow seas ($\beta = 135°$), the open-loop roll is smallest owing to the high encounter frequency, and the fin provides proportionally less reduction—particularly at reduced speed. Fourth, compensation for the *rate of change* of wave-induced disturbances, in addition to their magnitude, yields significantly improved stabilisation compared to methods that address only disturbance magnitude (Jimoh et al., 2021).

Beyond active fins, two additional categories of roll stabilisation devices address scenarios where fin systems are impractical. Rawson and Tupper (2001) classify these as passive and active tank systems, and gyroscopic stabilisers.

Anti-roll tanks. Passive tank stabilisers exploit the inertia of water sloshing inside athwartship tanks to generate a moment opposing the roll motion. In the *flume* (U-tube) tank configuration, water flows through a duct connecting two wing tanks; internal baffles regulate the flow rate so that the liquid transfer is approximately $90°$ out of phase with the roll motion, producing maximum damping at the tuned frequency (Rawson & Tupper, 2001). The tank natural period is adjusted to match the ship's roll period by varying the duct cross-section and baffle geometry. el Moctar et al. (2021) describe the mathematical treatment: the lowest eigenfrequency of the sloshing motion must be similar to the roll eigenfrequency, and the sloshing force is incorporated as an additional matrix in the coupled motion equations. For shallow-water tanks, el Moctar et al. (2021) solve the two-dimensional momentum conservation on a Cartesian grid using the Glimm method to handle flow speeds exceeding the surge velocity $\sqrt{gh}$, where h is the water depth in the tank.

Free-surface tank systems operate on the same principle but without the connecting duct: the liquid surface in a wide, shallow tank shifts as the vessel rolls, providing a counter-moment. The tuning is achieved by controlling the liquid depth, since the sloshing period depends on the tank breadth and fill level (Rawson & Tupper, 2001). Both flume and free-surface tanks are effective at zero speed—a critical advantage over fin stabilisers—making them suitable for vessels that spend extended periods at anchor or at low speed (Rawson & Tupper, 2001).

Gyroscopic stabilisers. A large flywheel spinning at high angular velocity possesses considerable angular momentum. When the vessel rolls, the precession of the gyroscope generates a torque that opposes the roll motion. Rawson and Tupper (2001) note that gyroscopic stabilisers were common in the early twentieth century, particularly on smaller vessels and yachts, but their high weight-to-effectiveness ratio and the mechanical complexity of the bearing systems led to their displacement by fin stabilisers for most commercial applications. Modern variants employing high-speed flywheels in vacuum enclosures have revived interest in gyroscopic stabilisation for

mega-yachts and patrol vessels, where zero-speed performance is required without the free-surface effects associated with tank systems (Rawson & Tupper, 2001).

6.4.4 Weather Routing and Voyage Optimisation

Seakeeping predictions provide the quantitative basis for weather routing—the selection of an optimal route and speed profile that minimises voyage time, fuel consumption, or structural loading while satisfying seakeeping criteria. Rawson and Tupper (2001) describe the methodology in which the added resistance in waves (Equation 5.20) is computed for each candidate route segment using the forecast wave spectrum and the vessel's RAO. The speed–power relationship in waves is then determined by subtracting the added resistance from the available thrust, yielding the achievable speed on each route leg.

The route optimisation problem is formulated as the minimisation of a cost function (e.g. voyage time or fuel consumption) subject to the constraint that the seakeeping criteria of Section 6.4.1 are not violated along any route segment (Molland, 2008; Rawson & Tupper, 2001). The operability constraints ensure that the vessel does not enter sea-state–heading combinations where slamming frequency, deck wetness, or vertical acceleration exceed their limits. This methodology, combined with numerical weather prediction, provides significant fuel savings—typically 3–5% on trans-oceanic routes—and reduces the risk of heavy-weather damage (Rawson & Tupper, 2001).

6.5 Discussion

The potential flow formulation (Equations 6.1–6.3) provides the foundation for linear seakeeping analysis. Guedes Soares and Santos (2015) demonstrate two complementary approaches built on this foundation.

First, the frequency-domain panel code approach discretizes the hull surface into quadrilateral panels and solves the Green function integral equation (Equation 6.3) for the radiation and diffraction potentials at each wave frequency. A mesh convergence study on a shuttle tanker ($L_{pp} = 264\,\text{m}$) showed that the hydrodynamic coefficients and motion amplitudes are sensitive to panel size, particularly in the bow and stern regions where geometric curvature is greatest. The convergence criterion adopted—panel diagonal length less than 1/6 of the shortest wave length—provides a practical guideline for mesh generation (Guedes Soares & Santos, 2015).

Second, the three-dimensional Numerical Wave Tank (NWT) approach solves the fully nonlinear free-surface boundary-value problem in the time domain using a boundary integral equation method. Guedes Soares and Santos (2015) verified this NWT against second-order Stokes wave theory and against

experimental data for a Wigley hull ($L = 1.025\,\text{m}$, $B = 0.513\,\text{m}$, $T = 0.1\,\text{m}$) in head seas. The heave and pitch motions computed by the nonlinear NWT showed closer agreement with experimental measurements than the linear time-domain solution, particularly for wave-length-to-ship-length ratios of 1.0 and 1.5 (Guedes Soares & Santos, 2015).

A further advance beyond the linear panel code and NWT is the fully nonlinear potential flow (FNPF) method. Shi et al. (2024) developed an FNPF approach based on a spectral coupled boundary element method that solves the Zakharov free-surface boundary conditions on the evolving instantaneous wetted surface in the time domain. By decomposing the time derivative of the velocity potential into six modal acceleration potentials and a residual, the added mass matrix is obtained by pressure integration and the 6-DOF equation of motion is decoupled from the fluid-force calculation—an acceleration-potential technique that generalises the frequency-domain added mass concept (Equation 6.6) to the fully nonlinear regime. The spectral layer reduces the far-field boundary element problem to a high-order spectral solve with $\mathcal{O}(N \log N)$ complexity, enabling FNPF simulations of the KCS container ship ($L_{pp} = 230\,\text{m}$, $F_n = 0.26$) in less than one minute per wave period—two to three orders of magnitude faster than URANS while still capturing the nonlinear effects of large incident waves on the instantaneous wetted surface and motion response. Heave and pitch RAOs predicted by this method agreed well with experimental data and CFD results across a range of wavelength-to-ship-length ratios; for large waves ($H = 4.8\,\text{m}$), the peak heave RAO decreased by approximately 5% compared to the small-amplitude limit ($H = 0.4\,\text{m}$), an effect attributable to the nonlinear changes in wetted surface geometry that are inaccessible to linear theory (Shi et al., 2024).

For bodies of revolution, Ferdinande and Kritis (1980) demonstrated that a source distribution method with co-axial ring discretization provides an economical alternative to the full panel code. By exploiting axial symmetry, the three-dimensional boundary-value problem reduces to a set of integrals in a single meridional plane, yielding the heave added mass and damping coefficient (Equation 6.7) with considerably less computational effort. The method agreed with Havelock's exact analytical solution for the hemisphere and with experimental forced-oscillation data for vertical circular cylinders across a range of draft-to-radius ratios ($D/R = 0.25$–2) and water depths. Where the panel code requires $\mathcal{O}(N^2)$ operations on the full three-dimensional surface mesh, the symmetric ring representation reduces the unknowns to the number of meridional segments, making parametric studies over many geometric variants tractable even on modest computing resources (Ferdinande & Kritis, 1980).

The theoretical foundation for all these numerical methods is the added mass tensor of Korotkin (2009), whose kinetic energy formulation (Equation 6.8) shows that the fluid inertia associated with an arbitrarily moving body is completely characterised by 21 independent coefficients. The diagonal added masses are always positive, so the effective inertia in each mode

always exceeds the rigid-body value. The Lewis form conformal mapping (Equation 6.10) provides an efficient analytical pathway from the geometric parameters of an actual ship frame—fullness coefficient β and draft-to-beam ratio—to the sectional added masses that enter strip-theory calculations. The free-surface boundary condition (Equation 6.11) introduces a frequency dependence absent in infinite-fluid theory: at low frequencies the added masses approach the duplicated-hull values, while at high frequencies they revert to infinite-fluid values, with a non-monotonic transition that depends on section shape. The approximate hull formulas (Equations 6.12–6.13) provide a rapid design check: for typical merchant-ship proportions ($B/T \approx 3$–4), the heave added mass λ_{33} is roughly 2–2.5 times the displaced fluid mass ρV, confirming that vertical oscillation engages substantially more fluid inertia than the static displacement alone (Korotkin, 2009).

These numerical methods extend the analytical framework of the shipping water experiments (Section 6.3.5): while Hernández-Fontes et al. (2020) provided direct physical measurements of wave–structure interaction loads, the panel code and NWT approaches enable prediction of motions and loads for arbitrary hull geometries and sea states.

The time-domain convolution formulation (Equation 6.23) extends these methods to problems where nonlinear external forces preclude frequency-domain treatment. For moored ships, the restoring forces from mooring lines and fenders enter through $F_j^{\mathrm{nl}}(t)$ and may exhibit nonlinear load–displacement characteristics that depend on the instantaneous positions of the attachment points. Zheng et al. (2022) demonstrated that when harbour oscillations generated by seismic ground motion force a moored ship at periods close to the natural oscillatory period of the mooring system, resonant amplification of approximately two times occurs. This finding has direct implications for mooring system design in seismically active regions: the natural periods of the mooring system should be separated from the dominant harbour oscillation periods to avoid resonance (Zheng et al., 2022).

A complementary perspective is provided by viscous CFD methods. While the panel code and NWT approaches are confined to potential flow, Jung et al. (2013) demonstrated that RANS-based simulations with the VOF method and a sliding mesh technique reproduce both the wave elevation and the roll angle of a rectangular floating structure to good accuracy across multiple wave periods. Crucially, the computed RAO matched the experimental values near resonance—where linear potential theory overestimates the response by a large margin because it omits viscous damping (Section 6.3.2). The resolved vorticity field revealed that the viscous damping arises from alternating vortex shedding at the bottom corners of the hull, with the pressure footprint of these vortices directly opposing the roll motion when $T_s \leq T_n$ (Jung et al., 2013). This finding connects the empirical two-term damping law (Equation 6.41) to first-principles fluid mechanics: the $b\,\Phi^2$ decrement corresponds to the vortex-induced suction forces at sharp hull features.

Sutulo and Guedes Soares (2023) extend the RANS-based motion ana-

lysis to full-scale operational scenarios. The contributions in that volume include systematic RANS predictions of wave-induced motions for ships at forward speed, demonstrating that the viscous effects captured by RANS—particularly flow separation around bilge keels and hull appendages—resolve the overprediction of roll amplitude inherent in potential-flow strip theory. Additionally, semi-empirical roll damping models calibrated against free-decay tests and roll derivative databases provide practitioners with computationally tractable alternatives to full RANS simulation for each sea state (Sutulo & Guedes Soares, 2023). These contributions reinforce the finding of Jung et al. (2013) that viscous damping, not wave-radiation damping, governs the peak roll response near resonance.

Biran (2003) provides a rigorous textbook derivation of the Mathieu equation for parametric rolling, starting from the time-dependent metacentric height and arriving at the Ince–Strutt stability diagram through Floquet theory. The textbook treatment explicitly derives the instability boundary as a function of the modulation depth h and the damping ratio μ/ω_0, showing that even moderate damping ($\mu/\omega_0 \approx 0.05$) contracts the principal instability tongue substantially and eliminates the higher-order tongues entirely (Biran, 2003). This analytical result complements the numerical FNPF simulations of Shi et al. (2024) and the operational vulnerability assessments of Spyrou et al. (2023) by providing closed-form expressions for the stability boundaries that can be evaluated without computational resources.

The seakeeping laboratory exercises at the United States Naval Academy (United States Naval Academy, 2021) demonstrate the practical application of the encounter frequency concept (Equation 6.31). Midshipmen observe model hulls in a wave channel and measure the roll, heave, and pitch responses as a function of heading angle and model speed, directly verifying the $\omega_e = \omega - (\omega^2 U/g)\cos\beta$ relationship and identifying the synchronism condition at which roll amplitudes are maximised (United States Naval Academy, 2021). This hands-on verification of the theoretical framework is a powerful pedagogical complement to the mathematical analysis presented in this chapter.

The comparative analysis of the DARPA SUBOFF model reveals that two distinct hydrodynamic mechanisms govern the intensification of motion responses near the free surface (Ge et al., 2026): first, the substantial reduction of wave radiation damping as the body approaches the surface reduces motion stability; second, the amplified Froude–Krylov forces at decreasing submergence depth inject greater excitation energy. The net effect is that all six degrees of freedom exhibit progressively more violent motions as the vehicle moves closer to the free surface, with the added mass coefficients becoming frequency-independent and the radiation damping approaching zero once the submergence depth exceeds approximately one hull diameter ($h^* > 1D$). The practical consequence is an operational imperative: the transition through the near-surface zone during submarine deployment and recovery should be completed as rapidly as possible to minimise exposure to

the amplified motion regime. Furthermore, the forward-speed behaviour of the streamlined SUBOFF hull differs qualitatively from surface ships—heave and pitch RAOs decrease with increasing speed rather than increase—because the submarine generates minimal wave-making resistance and dynamic lift (Ge et al., 2026). This discrepancy demonstrates the need for submarine-specific hydrodynamic models rather than direct application of surface-ship methodologies.

The strip method described by el Moctar et al. (2021) connects the sectional added masses of Korotkin (2009) to the global six-DOF equation of motion (Equation 6.18). By combining the real added mass and damping of each transverse section into a single complex coefficient (Equation 6.14) and integrating these quantities over the hull length via the radiation-force matrix (Equation 6.15), the strip method transforms local two-dimensional hydrodynamic data into a complete frequency-domain seakeeping prediction with forward-speed corrections. The substantial-derivative formulation $D/Dt = \partial/\partial t - U\,\partial/\partial x$ ensures that the longitudinal variation of hull geometry and the convective transport of fluid momentum are properly captured. The surge added mass, inaccessible from transverse-section analysis, is recovered through the ellipsoid approximation of Equation 6.16. Despite its simplifying assumptions—two-dimensional flow, neglect of longitudinal disturbance components, and the ϕ_{xx} error inherent in applying the two-dimensional Laplace equation to a three-dimensional body—the strip method has remained the standard engineering tool for seakeeping assessment since the pioneering work of Korvin-Kroukovski in the 1950s, with typical accuracy sufficient for operability assessments and structural load prediction in the preliminary design spiral (el Moctar et al., 2021).

Ölmez and Çakıcı (2022) provide a comprehensive theoretical manual for a practical implementation of this strip-theory framework—the YTU DEEP ship motion program. Their treatment addresses three aspects absent from the preceding analysis. First, the Ikeda roll damping decomposition (Equation 6.43) provides the standard engineering method for estimating the viscous roll damping that neither potential-flow panel methods nor the strip-theory radiation calculation can capture; each of the five components is evaluated from hull principal dimensions and bilge geometry, avoiding the computational cost of the RANS simulations required by Jung et al. (2013). Second, the impulse response function computation (Equation 6.24) and the McTaggart time-step rules (Equation 6.26) supply the practical link between the frequency-domain hydrodynamic data—produced by Equations (6.14)–(6.15)—and the time-domain convolution equation (Equation 6.23): the memory kernel is obtained via a cosine transform of the radiation damping, and the integration parameters scale with the simple physical quantity $\sqrt{L/g}$. Third, the encounter spectrum transformation (Equation 6.33) supplies the Jacobian that maps the wave spectrum from absolute to encounter frequency, quantifying the spectral energy amplification in following seas that can drive unexpectedly large motions. Validation of the code against the AME CRC

model-test series (seven hull forms at $F_n = 0.285$ and 0.57) confirmed that the combined framework—Salvesen strip theory, Lewis sectional hydrodynamics, and Ikeda roll damping—reproduces measured RAOs with accuracy consistent with the state of the art for strip-theory predictions (Ölmez & Çakıcı, 2022).

The vulnerability assessment framework for parametric rolling introduced by the SGISC (Spyrou et al., 2023) connects the Mathieu-equation description (Equation 6.51) to regulatory practice. The Grim effective-wave spectrum (Equation 6.53) quantifies the actual modulation amplitude that a particular hull experiences in a given sea state, replacing the idealised monochromatic modulation depth h with a spectral measure that accounts for directional spreading and wavelength–hull-length mismatch. The Level 2 indices C_1 and C_2 then translate this into a probabilistic statement about lifetime exposure by weighting across all realistic combinations of significant wave height, zero-crossing period, and heading. Where the Ince–Strutt diagram (Section 6.3.4) predicts instability for a single frequency ratio, the SGISC Level 2 check integrates over the full scatter table to answer the engineering question: *how often* will this vessel encounter conditions inside the instability tongue? The wave-radar-assisted operational guidance adds a real-time dimension—onboard measurement of the directional spectrum and instant evaluation of the simplified roll model—enabling masters to adjust heading by as little as 15° to move the encounter conditions outside the parametric roll zone (Spyrou et al., 2023).

6.6 Conclusion

The prediction of ship motions in waves rests on the potential-flow boundary-value problem for the velocity potential about an oscillating hull (Equations 6.1–6.3), solved numerically by Green function integral equations (Guedes Soares & Santos, 2015) or by the Hess–Smith panel method (Ge et al., 2026). The resulting hydrodynamic forces decompose into Froude–Krylov and diffraction excitation components (Equations 6.4–6.5) and frequency-dependent radiation forces characterised by the added mass tensor and radiation damping (Equations 6.6–6.9). The symmetric 6×6 added mass tensor λ_{ik}, whose 21 independent components encode the kinetic energy of the surrounding fluid (Korotkin, 2009), is evaluated economically for ship sections through the Lewis form conformal mapping (Equation 6.10) and assembled into a global prediction by the strip method (Equations 6.14–6.16) (el Moctar et al., 2021). Approximate hull formulas confirm that the heave added mass exceeds the displaced fluid mass by a factor of roughly 2–2.5 for typical merchant-ship proportions (Korotkin, 2009), and the free-surface boundary condition (Equation 6.11) introduces a non-monotonic frequency dependence absent in infinite-fluid theory.

The six-DOF coupled equation of motion (Equation 6.18), incorporating

the viscous damping and restoring stiffness matrices (Equations 6.19–6.20), provides the complete framework for predicting vessel responses (Ge et al., 2026). The natural roll period (Equation 6.28) depends on metacentric height and radius of gyration (Attwood, 1899), and synchronism between this period and the wave half-period drives unbounded roll growth in the absence of damping—a critical condition quantified by Froude's classical equation (Equation 6.29). Roll damping is governed by both wave-making and viscous mechanisms: the empirical two-term decremental law (Equation 6.41) captures the combined linear and quadratic damping (Attwood, 1899), the Ikeda decomposition (Equation 6.43) separates the five physical sources for strip-theory codes (Ölmez & Çakıcı, 2022), and RANS-based CFD resolves the individual vortex-shedding events at sharp hull corners that produce the viscous contribution potential flow methods cannot capture (Jung et al., 2013). Active fin stabilisers (Equation 6.46) achieve 39–74% roll reduction at sea state 5 with efficacy scaling as the square of forward speed (Jimoh et al., 2021), while passive bilge keels reduce the number of decay swings from 45–50 to only 8 (Attwood, 1899).

Extension to irregular seas proceeds through the spectral response framework (Equations 6.32–6.38): the response spectrum is the product of the squared RAO and the wave energy spectrum, with directional spreading quantified by the cosine-power model (Jiao et al., 2019). Comparative experiments show that long-crested waves overestimate head-sea vertical bending moments by 10–29% relative to short-crested seas, while the encounter spectrum transformation (Equation 6.33) reveals a singularity in following seas that can amplify motion responses when the vessel speed approaches the group velocity (Ölmez & Çakıcı, 2022). For transient or nonlinear problems, the time-domain convolution formulation (Equation 6.23) replaces frequency-dependent radiation damping with a memory-effect integral whose kernel is obtained by cosine transform of the damping (Equation 6.24), with practical time-step and memory cut-off rules scaling as $\sqrt{L/g}$ (Ölmez & Çakıcı, 2022; Zheng et al., 2022). Global sensitivity analysis of KVLCC2 simulations confirms that perturbation amplitude is dominated by significant wave height ($S_1 \approx 0.38$–0.48) and modal period ($S_1 \approx 0.30$–0.36), while mean vessel speed has negligible influence (Zhang et al., 2025).

Parametric rolling, driven by periodic variation of the metacentric height in longitudinal seas, is governed by the damped Mathieu equation (Equation 6.51) with the principal resonance condition $\omega_E \approx 2\omega_0$ (Equation 6.52). Fully nonlinear potential flow simulations of the KCS container ship capture cross-DoF coupling, nonlinear restoring moments, and roll amplitudes matching model-test measurements (Shi et al., 2024), while the SGISC Level 2 vulnerability framework quantifies lifetime exposure through the Grim effective-wave spectrum (Equation 6.53) (Spyrou et al., 2023). For green water and slamming, the classification of shipping water events into dam-break, small-cavity, and large-cavity types shows that vertical deck loads increase by up to a factor of 6.4 with bore steepness, and backflow loads are of the same

order as forward loads (Hernández-Fontes et al., 2020). These theoretical and computational tools—from Froude's nineteenth-century rolling experiments through strip theory and fully nonlinear potential flow to RANS-based viscous simulations—collectively provide the quantitative basis for operability assessment, hull form optimisation, and weather routing in contemporary naval architecture (Molland, 2008; Rawson & Tupper, 2001).

References

Attwood, E. L. (1899). *A text-book of theoretical naval architecture*. Longmans, Green; Co.

Biran, A. B. (2003). *Ship hydrostatics and stability*. Butterworth-Heinemann.

Campbell, C. (2025). *Physics: A focused introduction*. CRC Press. https://doi.org/10.1201/9781003571568

el Moctar, B. O., Schellin, T. E., & Söding, H. (2021). *Numerical methods for seakeeping problems*. Springer. https://doi.org/10.1007/978-3-030-62561-0

Faltinsen, O. M. (1990). *Sea loads on ships and offshore structures*. Cambridge University Press.

Ferdinande, V., & Kritis, B. G. (1980). An economical method of determining added mass and damping coefficients of axisymmetric floating bodies in oscillatory heaving motion. *International Shipbuilding Progress*, *30*, 231–238. https://doi.org/10.3233/ISP-1980-2731303

Fischer-Cripps, A. C. (2014). *The physics companion* (2nd ed.). CRC Press. https://doi.org/10.1201/b17356

Ge, D., Chen, Y., Wang, G., Ge, J., You, Y., & Feng, A. (2026). Comparison investigation of hydrodynamic responses for SUBOFF travelling on and near free surface. *Ocean Engineering*, *343*, 123138. https://doi.org/10.1016/j.oceaneng.2025.123138

Guedes Soares, C., & Santos, T. A. (Eds.). (2015). *Maritime technology and engineering: Proceedings of MARTECH 2014*. CRC Press.

Hernández-Fontes, J. V., Vitola, M. A., Esperança, P. T. T., Sphaier, S. H., & Silva, R. (2020). Patterns and vertical loads in water shipping in systematic wet dam-break experiments. *Ocean Engineering*, *197*, 106891. https://doi.org/10.1016/j.oceaneng.2019.106891

Hewitt, P. G., Suchocki, J. A., & Hewitt, L. A. (2012). *Conceptual physical science* (5th ed.). Pearson.

Jiao, J., Chen, C., & Ren, H. (2019). A comprehensive study on ship motion and load responses in short-crested irregular waves. *International Journal of Naval Architecture and Ocean Engineering*, *11*, 364–379. https://doi.org/10.1016/j.ijnaoe.2018.07.003

Jimoh, I. A., Küçükdemiral, I. B., & Bevan, G. (2021). Fin control for ship roll motion stabilisation based on observer enhanced MPC with disturbance rate compensation. *Ocean Engineering*, *224*, 108706. https://doi.org/10.1016/j.oceaneng.2021.108706

Jung, J. H., Yoon, H. S., Chun, H. H., Lee, I., & Park, H. (2013). Numerical simulation of wave interacting with a free rolling body. *International Journal of Naval Architecture and Ocean Engineering*, *5*, 333–347. https://doi.org/10.2478/IJNAOE-2013-0137

Korotkin, A. I. (2009). *Added masses of ship structures*. Springer. https://doi.org/10.1007/978-1-4020-9432-3

Lewis, E. V. (Ed.). (1988). *Principles of naval architecture* (2nd ed.) [Three volumes]. The Society of Naval Architects; Marine Engineers.

Molland, A. F. (Ed.). (2008). *The maritime engineering reference book: A guide to ship design, construction and operation*. Butterworth-Heinemann. https://doi.org/10.1016/B978-0-7506-8987-8.X0001-7

Newman, J. N. (1977). *Marine hydrodynamics*. The MIT Press.

Ölmez, A., & Çakıcı, F. (2022). Theoretical manual of 'YTU DEEP' SHIP motion program. *Ocean Engineering*, *266*, 112451. https://doi.org/10.1016/j.oceaneng.2022.112451

Rawson, K. J., & Tupper, E. C. (2001). *Basic ship theory* (5th ed.). Butterworth-Heinemann.

Shi, K., Zhu, R., Zheng, M., & Li, C. (2024). Simulation of ship motion response in head seas using a fully nonlinear potential flow method. *Ocean Engineering*, *309*, 118309. https://doi.org/10.1016/j.oceaneng.2024.118309

Spyrou, K. J., Belenky, V. L., Katayama, T., & Bačkalov, I. (2023). *Contemporary ideas on ship stability: From dynamics to criteria*. Springer. https://doi.org/10.1007/978-3-031-16329-6

Sutulo, S., & Guedes Soares, C. (2023). Ship dynamics and hydrodynamics. *Journal of Marine Science and Engineering*, *11*(5), 911. https://doi.org/10.3390/jmse11050911

United States Naval Academy. (2021). En400: Principles of ship performance [Course notes, Fall AY2021].

Zhang, J., Qu, L., Du, L., & Hong, G. (2025). Numerical modeling of vessel's wave-induced responses based on fast surface pressure method. *Ocean Engineering*, *337*, 121887. https://doi.org/10.1016/j.oceaneng.2025.121887

Zheng, Z., Ma, X., Yan, M., Ma, Y., & Dong, G. (2022). Hydrodynamic response of moored ships to seismic-induced harbor oscillations. *Coastal Engineering*, *176*, 104147. https://doi.org/10.1016/j.coastaleng.2022.104147

Chapter 7

Thermodynamics in Marine Engineering

7.1 Introduction

Thermodynamics pervades every aspect of marine science and engineering. Beyond powering ship propulsion systems through heat engine cycles, thermodynamic principles govern the physical properties of seawater itself—its density, compressibility, and thermal behaviour—which in turn determine ocean circulation, acoustic propagation, and the vertical stability of the water column. As Dera (1992) emphasised, seawater is a complex thermodynamic system whose state is fully described by three independent variables: temperature T, salinity S, and pressure p.

The equation of state—the functional relationship $\rho = \rho(S, T, p)$ linking density to these three state variables—is the central thermodynamic tool in marine physics. Its accurate formulation is essential for computing hydrostatic pressure, buoyancy forces, sound speed, and geostrophic currents. This chapter establishes the thermodynamic foundations, beginning with the classical laws and proceeding to the equation of state for seawater.

The historical evolution of marine propulsion is fundamentally a story of steadily improving thermodynamic conversion. The transition from sail to steam in the early nineteenth century represented the first application of heat engine technology to shipping: reciprocating steam engines burning coal drove paddle wheels and, later, screw propellers through increasingly sophisticated compound and triple-expansion cycles (Molland, 2008). Each successive engine generation exploited higher boiler pressures and additional expansion stages to extract more work from the same fuel input, a direct application of the Carnot principle (Section 7.3.2). The introduction of the compression-ignition diesel engine to marine service in the early twentieth century marked a fundamental thermodynamic shift: by eliminating the external boiler and achieving higher compression ratios, the diesel cycle offered superior thermal efficiency (Woodyard, 2009). Modern low-speed

two-stroke crosshead diesel engines, achieving brake thermal efficiencies approaching 55%, represent the culmination of over a century of incremental optimisation of this cycle (Molland, 2008). Parallel developments in gas turbine propulsion (the open Brayton cycle) have found application in naval combatants and fast ferries, while hybrid arrangements—combining diesel and gas turbine drives—seek to optimise cycle efficiency across the full operational envelope (Molland, 2008).

7.2 Scientific Background

7.2.1 Zeroth and First Law of Thermodynamics

The zeroth law of thermodynamics establishes the concept of thermal equilibrium: if two systems are each in thermal equilibrium with a third, they are in equilibrium with each other. This seemingly elementary principle provides the physical basis for temperature measurement—a prerequisite for all oceanographic observations.

The first law of thermodynamics expresses conservation of energy (Çengel & Boles, 2019; Hewitt et al., 2012). For a parcel of seawater, the internal energy changes through heat exchange and pressure–volume work. The thermodynamic state of seawater is more complex than that of an ideal gas because it depends on three independent variables: temperature T, salinity S, and hydrostatic pressure p (Dera, 1992).

Dera (1992) presented the general differential equation of state for seawater in terms of the specific volume $\alpha = 1/\rho$:

Equation 8.1 — General differential equation of state:

$$\frac{\mathrm{d}\alpha}{\alpha_0} = k_T \,\mathrm{d}T - k_S \,\mathrm{d}S - k_p \,\mathrm{d}p \tag{7.1}$$

where α is the specific volume, α_0 is a reference specific volume, and k_T, k_S, and k_p are dimensionless coefficients that characterise the response of seawater to changes in each state variable (Dera, 1992, Eq. 3.1.4).

The three coefficients in Equation 7.1 are defined as follows.

Equation 8.2 — Thermal expansion coefficient:

$$k_T = \frac{1}{\alpha}\left(\frac{\partial \alpha}{\partial T}\right)_{S,p} \tag{7.2}$$

The thermal expansion coefficient k_T quantifies the fractional increase in specific volume per unit rise in temperature at constant salinity and pressure. For typical oceanic conditions, k_T ranges from approximately 50×10^{-6} K^{-1} near the freezing point to 300×10^{-6} K^{-1} in warm surface waters (Dera, 1992, Eq. 3.1.6).

Equation 8.3 — Saline contraction coefficient:

$$k_S = -\frac{1}{\alpha}\left(\frac{\partial \alpha}{\partial S}\right)_{T,p} \tag{7.3}$$

The saline contraction coefficient k_S describes the fractional decrease in specific volume (increase in density) per unit increase in salinity. The negative sign in the definition ensures that k_S is positive, since increasing salinity always increases density (Dera, 1992, Eq. 3.1.7).

Equation 8.4 — Isothermal compressibility:

$$k_p = -\frac{1}{\alpha}\left(\frac{\partial \alpha}{\partial p}\right)_{T,S} \tag{7.4}$$

The isothermal compressibility k_p measures the fractional decrease in specific volume per unit increase in pressure at constant temperature and salinity. For seawater, k_p is of order 4×10^{-10} Pa^{-1}, reflecting the low compressibility of liquid water (Dera, 1992, Eq. 3.1.8).

Together, these three coefficients completely characterise the linearised thermodynamic response of seawater to infinitesimal changes in its state variables. The nonlinear dependence of k_T, k_S, and k_p on T, S, and p—and, critically, their cross-dependencies—necessitates the polynomial empirical equations of state discussed below.

7.2.2 Second Law of Thermodynamics

The second law of thermodynamics introduces the concept of entropy and establishes the directionality of natural processes: heat flows spontaneously from higher to lower temperature. For seawater, the second law has a particularly important consequence in the form of adiabatic processes.

In its most general form, the first law may be written as (Campbell, 2025)

Equation 8.12 — First law of thermodynamics (general form):

$$\Delta E_{\text{th}} = Q + W \tag{7.5}$$

where ΔE_{th} is the change in thermal (internal) energy of the system, Q is the heat added to the system (positive if energy enters, negative if it leaves), and W is the work done on the system with the same sign convention (Campbell, 2025, Eq. 5.11). This compact statement—that the change in a system's internal energy equals the sum of heat and work inputs—underlies all thermodynamic analysis in marine engineering, from seawater properties to propulsion cycles.

When a water parcel sinks in the ocean, the increasing hydrostatic pressure compresses it adiabatically (without heat exchange with the surroundings). This compression raises the temperature of the parcel even though no heat has been added. Dera (1992) derived the adiabatic temperature change using the Kelvin formula:

Equation 8.5 — Adiabatic lapse rate in seawater (Kelvin formula):

$$\left(\frac{\partial T}{\partial p}\right)_{\sigma} = \frac{k_T \cdot T}{C_{p,S}} \tag{7.6}$$

where the subscript σ denotes an isentropic (adiabatic) process, k_T is the thermal expansion coefficient (Equation 7.2), T is the absolute temperature, and $C_{p,S}$ is the specific heat capacity at constant pressure and salinity (Dera, 1992, Eq. 3.3.3).

In the open ocean, this adiabatic gradient is approximately $0.11\,\mathrm{K}$ per $1000\,\mathrm{m}$ depth (Dera, 1992, Eq. 3.3.6). Although seemingly small, this systematic warming must be removed before water temperatures at different depths can be meaningfully compared. This motivates the concept of potential temperature:

Equation 8.6 — Potential temperature:

$$\theta = T - \delta T \tag{7.7}$$

where θ is the potential temperature, T is the in situ temperature, and δT is the cumulative adiabatic warming that would occur if the water parcel were brought from its in situ pressure to the surface reference pressure (Dera, 1992, Eq. 3.3.7). The correction δT is obtained by integrating Equation 7.6 from the in situ pressure to atmospheric pressure.

Potential temperature is the standard variable used to identify and trace water masses in the ocean. Two water parcels with the same potential temperature and salinity but at different depths belong to the same water mass, having been modified only by adiabatic compression during their descent.

The statistical interpretation of entropy provides the most fundamental formulation of the second law. Campbell (2025) showed that an isolated system of M particles, each assignable to one of two states, has 2^M microstates grouped into macrostates whose multiplicities follow the binomial coefficient. The macrostate corresponding to the most probable configuration—the one with the greatest number of microstates—is the equilibrium state. As the number of particles $M \to \infty$, the probability of observing a significant departure from this most probable macrostate becomes vanishingly small (Campbell, 2025, Sec. 5.8). This is the microscopic origin of the macroscopic irreversibility observed in all marine thermodynamic systems.

7.2.3 Third Law and Absolute Temperature

The third law of thermodynamics states that the entropy of a perfect crystalline substance approaches zero as the absolute temperature approaches zero (Çengel & Boles, 2019). While no marine system operates at absolute zero, the third law provides the reference point for the absolute entropy scale and is essential for evaluating entropy changes in thermodynamic cycles. The absolute temperature scale (kelvin) that follows from the third law is

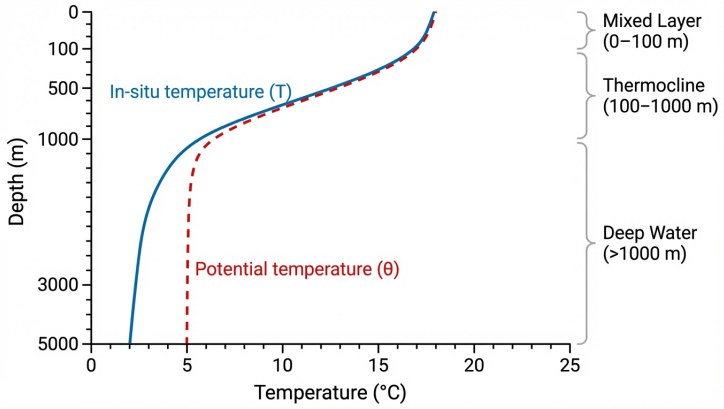

Figure 7.1: Vertical temperature profile in a typical mid-latitude open ocean. The in-situ temperature T (solid blue) decreases rapidly through the thermocline (100–1000 m) and then increases slightly at depth due to adiabatic compression (≈ 0.11 K per 1000 m). The potential temperature θ (dashed red) removes this adiabatic warming (Equation 7.6), revealing the true thermal identity of deep water masses (Dera, 1992).

the scale used in all efficiency calculations, including the Carnot expression (Equation 7.16).

The practical relevance of low-temperature thermodynamics to maritime operations centres on the transport of cryogenic cargoes, most notably liquefied natural gas (LNG). LNG is stored at approximately $-162\,^{\circ}\mathrm{C}$ (111 K) at near-atmospheric pressure. At these temperatures, the thermodynamic properties of methane differ markedly from ideal-gas behaviour, and the enthalpy of vaporisation ($\approx 510\,\mathrm{kJ\,kg^{-1}}$) governs the boil-off rate that must be managed by the cargo containment and re-liquefaction systems (Molland, 2008). The design of cargo tank insulation is a heat transfer problem (Section 7.3.5) in which the steady-state heat leak $\dot{Q}$ from the ambient hull structure at $T_H \approx 300$ K to the cargo at $T_C \approx 111$ K drives the continuous generation of boil-off gas (BOG). The second law requires that any re-liquefaction plant must supply at least

$$W_{\min} = Q_C \left(\frac{T_H}{T_C} - 1 \right) \tag{7.8}$$

of work to reject the absorbed heat, with actual re-liquefaction systems consuming several times this minimum due to compressor irreversibilities and heat exchanger approach temperatures (Çengel & Boles, 2019).

7.3 Theoretical Framework

7.3.1 Equation of State for Seawater

The practical application of the thermodynamic principles described in Section 7.2 requires an accurate empirical equation of state. Dera (1992) presented the UNESCO International Equation of State for Seawater (EOS-80), which represents the culmination of decades of laboratory measurements:

Equation 8.7 — UNESCO International Equation of State (EOS-80):

$$\rho(S,T,p) = \frac{\rho(S,T,0)}{1 - p \,/\, K(S,T,p)} \tag{7.9}$$

where $\rho(S,T,0)$ is the density at atmospheric pressure and $K(S,T,p)$ is the secant bulk modulus (Dera, 1992, Eq. 3.5.23).

The density at atmospheric pressure is itself a polynomial in S and T, referenced to the density of Standard Mean Ocean Water (SMOW):

Equation 8.8 — Density of Standard Mean Ocean Water:

$$\rho_{\text{SMOW}} = a_0 + a_1 T + a_2 T^2 + a_3 T^3 + a_4 T^4 + a_5 T^5 \tag{7.10}$$

with coefficients $a_0 = 999.842\,594$, $a_1 = 6.793\,952 \times 10^{-2}$, $a_2 = -9.095\,290 \times 10^{-3}$, $a_3 = 1.001\,685 \times 10^{-4}$, $a_4 = -1.120\,083 \times 10^{-6}$, $a_5 = 6.536\,332 \times 10^{-9}$, valid for 0–$40\,^{\circ}\text{C}$ at $101\,325$ Pa, yielding density in kg m^{-3} (Dera, 1992, Eq. 3.5.22).

The density at atmospheric pressure incorporating salinity is (Dera, 1992, Eq. 3.5.25):

$$\rho(S,T,0) = \rho_{\text{SMOW}} + B(T)\,S + C(T)\,S^{3/2} + d_0\,S^2 \tag{7.11}$$

where $B(T)$ and $C(T)$ are polynomials in temperature and $d_0 = 4.8314 \times 10^{-4}$.

The secant bulk modulus $K(S,T,p)$ in Equation 7.9 is expressed as a second-order polynomial in pressure:

$$K(S,T,p) = K(S,T,0) + A(S,T)\,p + B(S,T)\,p^2 \tag{7.12}$$

with $K(S,T,0)$, A, and B each being polynomials in S and T whose full coefficients are tabulated by Dera (1992, Eqs. 3.5.26–3.5.29). The EOS-80 system has a stated accuracy of approximately $\pm 0.009\ \text{kg m}^{-3}$ over the full oceanic range of temperature, salinity, and pressure.

For convenience and compact notation, oceanographers use the *abbreviated density* (sigma-T):

$$\sigma_T = \left(\frac{\rho(S,T,0)}{\rho_w(4\,^{\circ}\text{C},0)} - 1 \right) \times 1000 \tag{7.13}$$

where typical ocean values fall in the range $\sigma_T \approx 24$–28 (Dera, 1992, Eq. 3.5.16). This notation avoids quoting cumbersome density values near $1025\ \text{kg m}^{-3}$.

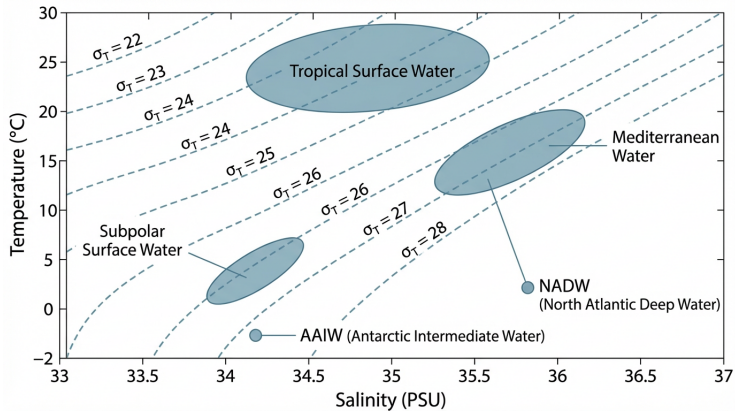

Figure 7.2: Temperature–salinity diagram with σ_T density contours computed from the UNESCO EOS-80 (Equation 7.9). Characteristic water mass positions are marked: Antarctic Intermediate Water (AAIW), North Atlantic Deep Water (NADW), Mediterranean Water, tropical surface water, and subpolar surface water. The nonlinear curvature of the density contours reflects the temperature-dependent thermal expansion coefficient k_T (Equation 7.2) (Dera, 1992).

7.3.2 Thermodynamic Cycles for Marine Propulsion

All marine heat engines—whether diesel, gas turbine, or steam—operate by cycling a working fluid through a sequence of thermodynamic processes. Campbell (2025) classified the four fundamental processes that compose every practical cycle (see also Çengel & Boles, 2019):

- **Isobaric** ($\Delta P = 0$): pressure is held constant; work $W = -P\,\Delta V$ and heat $Q = nC_P\,\Delta T$.
- **Isochoric** ($\Delta V = 0$): volume is held constant; work $W = 0$ and heat $Q = nC_V\,\Delta T$.
- **Isothermal** ($\Delta T = 0$): temperature is held constant; work $W = -nRT\ln(V_f/V_i)$ and the first law requires $Q = -W$.
- **Adiabatic** ($Q = 0$): no heat transfer; the pressure and volume are related by

Equation 8.13 — Adiabatic relation for an ideal gas:

$$P_1 V_1^{\gamma} = P_2 V_2^{\gamma} \tag{7.14}$$

where $\gamma = C_P/C_V$ is the adiabatic exponent ($\gamma = 7/5 = 1.4$ for diatomic gases such as air) (Campbell, 2025, Eq. 5.21). The corresponding temperature–volume relation is $T_1 V_1^{\gamma-1} = T_2 V_2^{\gamma-1}$ (Campbell, 2025, Eq. 5.22).

In any complete thermodynamic cycle the working fluid returns to its initial state, so the net change in internal energy is zero ($\Delta E_{\text{th,cycle}} = 0$). The first law then requires that the net work produced equals the net heat absorbed. A heat engine operating between a hot reservoir at temperature T_H and a cold reservoir at T_C takes in heat Q_H, rejects heat Q_C, and produces net work $W = Q_H - Q_C$ (Campbell, 2025, Ex. 5.4). The thermal efficiency is

Equation 8.14 — Thermal efficiency of a heat engine:

$$\eta = \frac{W}{Q_H} = 1 - \frac{Q_C}{Q_H} \tag{7.15}$$

The second law of thermodynamics places an upper bound on this efficiency. Campbell (2025) derived the Carnot limit:

Equation 8.15 — Carnot efficiency limit:

$$\eta \leq 1 - \frac{T_C}{T_H} \tag{7.16}$$

where T_C and T_H are the absolute temperatures of the cold and hot reservoirs, respectively, and equality holds only in the idealised, reversible (and therefore unattainable) limit (Campbell, 2025, Eq. 5.38). For a marine diesel engine with combustion gases at $T_H \approx 2000$ K rejecting heat to seawater cooling at $T_C \approx 300$ K, the Carnot limit gives $\eta_{\max} = 1 - 300/2000 = 0.85$. Actual two-stroke marine diesel engines achieve thermal efficiencies of approximately 0.50–0.55, reflecting irreversibilities due to friction, finite-rate heat transfer, and incomplete combustion.

For heat pump applications—relevant to on-board refrigeration, HVAC, and cargo cooling—the coefficient of performance (COP) replaces efficiency as the figure of merit:

Equation 8.16 — Maximum COP for cooling:

$$\text{COP}_{\text{cooling}} = \frac{Q_C}{W} \leq \frac{T_C}{T_H - T_C} \tag{7.17}$$

and the corresponding limit for heating is $\text{COP}_{\text{heating}} \leq T_H/(T_H - T_C)$ (Campbell, 2025, Eqs. 5.41, 5.44).

7.3.3 Marine Diesel Engine Thermodynamics

The marine diesel engine is the dominant prime mover for commercial shipping, and its thermodynamics is governed by the compression–ignition cycle (Harrington, 1992; Heywood, 1988). Molland (2008) provides a comprehensive treatment of modern marine diesel engine technology.

Low-speed two-stroke engines operate at 55–250 rpm with bore diameters of 260–1080 mm and stroke-to-bore ratios up to 4.4:1, directly coupled to

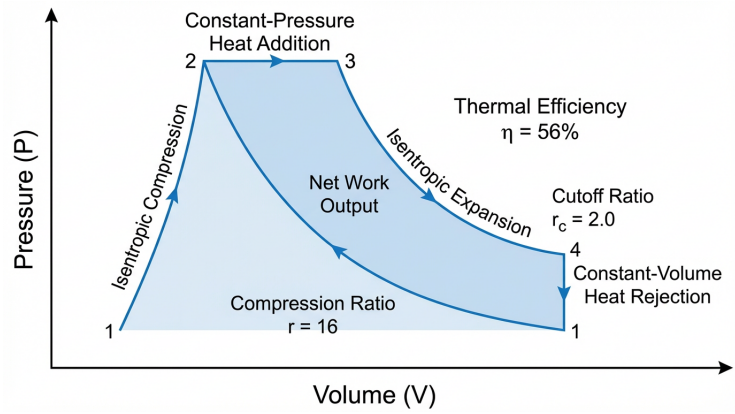

Figure 7.3: Pressure–volume diagram of the ideal Diesel (compression-ignition) cycle with compression ratio $r = 16$ and cutoff ratio $r_c = 2.0$. The cycle consists of isentropic compression ($1 \to 2$), constant-pressure heat addition ($2 \to 3$), isentropic expansion ($3 \to 4$), and constant-volume heat rejection ($4 \to 1$). The ideal thermal efficiency of 56% compares with the Carnot limit of 85% and actual marine diesel efficiencies of 50–55% (Campbell, 2025; Çengel & Boles, 2019).

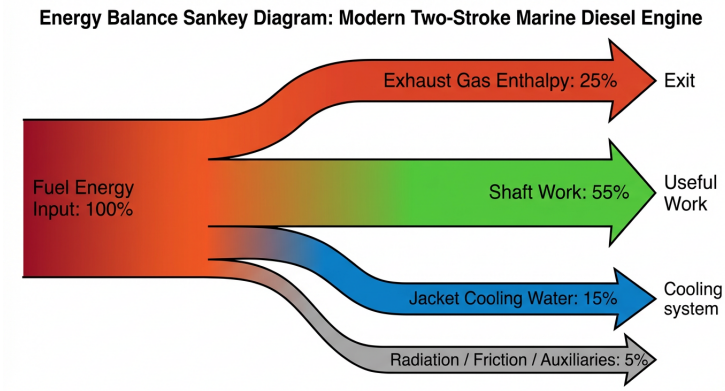

Figure 7.4: Approximate energy balance of a modern large-bore two-stroke marine diesel engine. Of the total fuel energy input, approximately 50–55% is converted to shaft work, 25% is rejected as exhaust gas enthalpy, 15% is removed by jacket cooling water, and the remainder is lost to radiation, friction, and auxiliary loads (Molland, 2008). The exhaust and cooling losses represent the thermodynamic irreversibilities that prevent the engine from reaching the Carnot limit (Equation 7.16).

the propeller without a reduction gearbox. Molland (2008) reports that modern low-speed two-stroke engines achieve a mean effective pressure (MEP) exceeding 20 bar and maximum cylinder pressures up to 180 bar on research engines. The brake specific fuel consumption (BSFC) of the most efficient large-bore models has been reduced to as low as $154\,\mathrm{g/kWh}$—a thermal efficiency of approximately 54%, the highest of any reciprocating heat engine (Molland, 2008).

Medium-speed four-stroke engines (400–1000 rpm, bore 200–640 mm) are used either via a reduction gearbox for propulsion or as genset drives for diesel-electric propulsion. They offer greater power density and installation flexibility than low-speed engines, at the cost of somewhat higher specific fuel consumption (Molland, 2008).

All modern marine diesel engines employ *constant-pressure turbocharging*: exhaust gas drives a turbocharger that compresses the scavenging air to 2.5–4.5 bar, significantly increasing the mass of air available for combustion in each cycle (Woodyard, 2009). In two-stroke engines, the standard scavenging arrangement is *uniflow scavenging* via a single exhaust valve in the cylinder head, which produces the most efficient gas exchange with minimal short-circuiting (Molland, 2008). When the turbocharger produces surplus energy beyond what is needed for scavenging air compression, the excess can drive a *power gas turbine* (Turbo Compound System), recovering additional mechanical energy that would otherwise be wasted in the exhaust (Molland, 2008).

Electronic engine control has enabled *variable injection timing* (VIT) and *variable exhaust valve closing*, which maintain a constant maximum firing pressure across the load range. This allows the engine to operate at optimum thermal efficiency at partial loads, rather than only at the design point (Molland, 2008). The exhaust temperature serves as a practical performance limit: Molland (2008) notes that "the economical limit is reached shortly after the exhaust temperature begins to curve upwards," indicating that further increases in MEP or turbocharger pressure ratio yield diminishing returns in efficiency.

For NO_x emission reduction, the primary methods include delayed injection timing, water injection into the combustion chamber, exhaust gas recirculation (EGR), and selective catalytic reduction (SCR) in the exhaust stream (Molland, 2008). These measures involve direct thermodynamic trade-offs: delayed injection reduces peak combustion temperature (lowering NO_x) but also reduces cycle efficiency, while SCR recovers the efficiency penalty by treating emissions after the cylinder rather than during combustion.

7.3.4 Gas Turbine Marine Propulsion

Gas turbines operate on the open Brayton cycle and are employed in naval vessels and fast ferries where high power-to-weight ratio is essential. Molland (2008) describes combined arrangements—CODAG (combined diesel and gas),

CODLAG (combined diesel-electric and gas), and CODEG (combined diesel-electric and gas-electric)—in which the gas turbine provides boost power for high-speed operation while diesel engines handle cruise-speed propulsion. This hybrid approach exploits the high specific power of gas turbines at full load while avoiding their poor part-load fuel economy (Molland, 2008).

7.3.5 Heat Transfer Mechanisms

The rate at which heat is exchanged between a marine system and its surroundings depends on the temperature difference and the material properties involved. Campbell (2025) defined the specific heat capacity of a material as

Equation 8.17 — Specific heat and heat transfer:

$$Q = m\,c\,\Delta T \tag{7.18}$$

where m is the mass, c is the specific heat capacity in J kg^{-1} K^{-1}, and ΔT is the temperature change (Campbell, 2025, Eq. 5.32); for a concise treatment, see (Fischer-Cripps, 2014). The rate of heat transfer through a solid material is governed by Fourier's law, $\dot{Q} = -kA\,dT/dx$, while convective heat transfer from a surface to a fluid obeys Newton's law of cooling, $\dot{Q} = hA\,(T_s - T_\infty)$; both mechanisms are essential to the design of marine heat exchangers, engine cooling jackets, and cargo tank insulation (Incropera et al., 2007). For liquid water, $c = 4.19 \times 10^3$ J kg^{-1} K^{-1}—the highest specific heat of any common substance, which makes seawater an exceptionally effective thermal reservoir and coolant (Campbell, 2025, Table 5.3). This property is exploited in every marine heat exchanger: seawater circulated through engine cooling jackets absorbs large quantities of waste heat with only modest temperature rises.

In a closed system where no mechanical work is done, conservation of energy requires $\sum Q = 0$, meaning the heat lost by one component must equal the heat gained by another (Campbell, 2025, Eq. 5.33). This calorimetric principle underlies the thermal balance calculations for marine cooling circuits, cargo tank heating systems, and ballast water thermal management.

The three fundamental modes of heat transfer—conduction, convection, and radiation—each play distinct roles in marine thermal systems (Incropera et al., 2007).

Conduction is governed by Fourier's law, which states that the heat flux through a solid is proportional to the negative temperature gradient:

$$\dot{Q}_{\text{cond}} = -k\,A\,\frac{\mathrm{d}T}{\mathrm{d}x} \tag{7.19}$$

where k is the thermal conductivity of the material (W m^{-1} K^{-1}), A is the cross-sectional area normal to the heat flow, and $\mathrm{d}T/\mathrm{d}x$ is the temperature gradient (Incropera et al., 2007). In marine applications, conduction determines the heat loss through hull plating, the thermal resistance of cargo tank insulation, and the temperature distribution within engine cylinder walls.

Convection describes heat transfer between a solid surface and an adjacent moving fluid. Newton's law of cooling expresses the convective heat flux as

$$\dot{Q}_{\text{conv}} = h\,A\,(T_s - T_\infty) \tag{7.20}$$

where h is the convection heat transfer coefficient (W m^{-2} K^{-1}), T_s is the surface temperature, and T_∞ is the bulk fluid temperature (Incropera et al., 2007). The value of h depends on the flow regime: for forced convection in seawater cooling circuits, typical values range from 500 to $10\,000$ W m^{-2} K^{-1}, while natural convection in air yields $h \approx 5$–25 W m^{-2} K^{-1} (Incropera et al., 2007). The high convection coefficients achievable with seawater make it an exceptionally effective coolant for marine diesel engines.

Radiation transfers energy through electromagnetic waves and requires no intervening medium. The maximum rate at which a surface can emit thermal radiation is given by the Stefan–Boltzmann law:

$$\dot{Q}_{\text{rad}} = \varepsilon\,\sigma\,A\,T_s^4 \tag{7.21}$$

where ε is the surface emissivity ($0 \le \varepsilon \le 1$), $\sigma = 5.670 \times 10^{-8}$ W m^{-2} K^{-4} is the Stefan–Boltzmann constant, and T_s is the absolute surface temperature (Incropera et al., 2007). The net radiative exchange between two surfaces at temperatures T_1 and T_2 is proportional to $(T_1^4 - T_2^4)$. Radiation is the dominant heat transfer mode in combustion chambers at peak flame temperatures, where it accounts for a substantial fraction of total in-cylinder heat transfer in marine diesel engines (Heywood, 1988).

In practice, marine heat exchangers—used for engine cooling, lubricating oil cooling, and freshwater generation—combine conduction through metal tube walls with forced convection on both the seawater and service-fluid sides. The overall heat transfer coefficient U for a flat-walled exchanger is

$$\frac{1}{U} = \frac{1}{h_i} + \frac{t_w}{k_w} + \frac{1}{h_o} \tag{7.22}$$

where h_i and h_o are the inner and outer convection coefficients, and t_w and k_w are the wall thickness and thermal conductivity, respectively (Incropera et al., 2007). Fouling of the seawater-side surface by biological growth or mineral deposits increases the thermal resistance and can significantly reduce heat exchanger effectiveness, necessitating periodic cleaning or the use of anti-fouling coatings (Molland, 2008).

7.3.6 Refrigeration and HVAC Systems

Refrigeration and air conditioning are essential auxiliary systems aboard virtually all commercial and naval vessels. Cargo refrigeration maintains perishable goods at controlled temperatures during transit, while HVAC (heating, ventilation, and air conditioning) ensures habitable conditions for crew in all climatic zones.

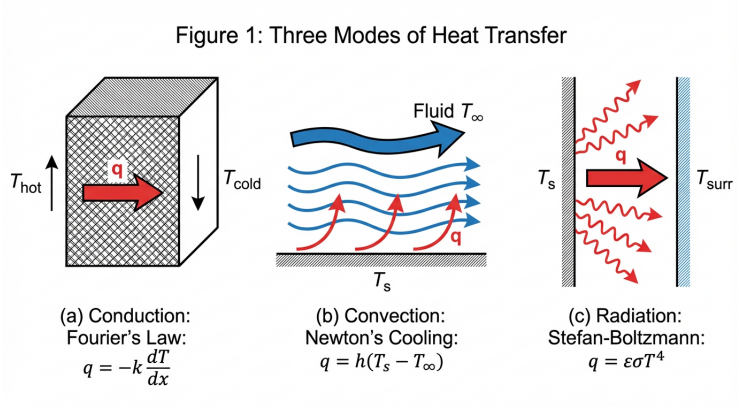

Figure 7.5: The three fundamental modes of heat transfer and their governing laws. Conduction (Fourier's law, Equation 7.19) transfers heat through solid materials; convection (Newton's law of cooling, Equation 7.20) transfers heat between a surface and a moving fluid; radiation (Stefan–Boltzmann law, Equation 7.21) transfers heat via electromagnetic emission. In a marine diesel engine, all three modes act simultaneously: conduction through the cylinder liner, forced convection from coolant circuits, and radiation from combustion gases (Heywood, 1988; Incropera et al., 2007).

The vapour-compression refrigeration cycle is the thermodynamic basis of nearly all marine refrigeration and air conditioning plant. The cycle operates by circulating a refrigerant through four processes (Çengel & Boles, 2019):

1. **Compression** ($1 \rightarrow 2$): the compressor raises the low-pressure refrigerant vapour to a high-pressure superheated state, requiring work input W_{in}.

2. **Condensation** ($2 \rightarrow 3$): the high-pressure vapour rejects heat Q_H to the seawater cooling circuit and condenses to a high-pressure liquid.

3. **Expansion** ($3 \rightarrow 4$): the liquid passes through an expansion valve, undergoing an irreversible throttling process that reduces its pressure and temperature.

4. **Evaporation** ($4 \rightarrow 1$): the low-pressure liquid–vapour mixture absorbs heat Q_L from the refrigerated space (cargo hold or air handling unit), evaporating completely before returning to the compressor.

The performance of the cycle is measured by the coefficient of performance for cooling, $\text{COP} = Q_L / W_{\text{in}}$ (cf. Equation 7.17). Practical marine refrigeration systems achieve COP values of 2–4, depending on the evaporating and condensing temperatures (Çengel & Boles, 2019).

For cargo refrigeration on container ships and reefer vessels, the refrigerant circuit must maintain evaporator temperatures as low as $-30\,^{\circ}\text{C}$ for

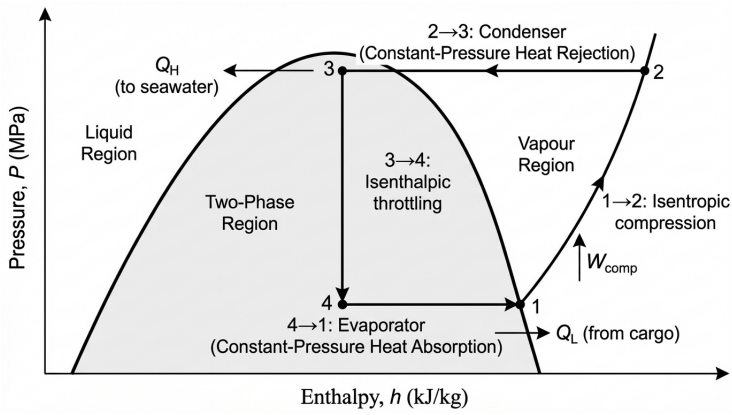

Figure 7.6: Pressure–enthalpy (P–h) diagram of the ideal vapour-compression refrigeration cycle. The four processes are: isentropic compression ($1 \to 2$), constant-pressure heat rejection ($2 \to 3$), isenthalpic throttling ($3 \to 4$), and constant-pressure heat absorption ($4 \to 1$). The shaded area under the saturation dome represents the two-phase liquid–vapour region. Marine systems reject heat Q_H to seawater at the condenser and absorb heat Q_L from the cargo hold or air handling unit at the evaporator (Çengel & Boles, 2019).

frozen cargo, while the condenser rejects heat to seawater that may be as warm as $32\,^{\circ}\text{C}$ in tropical waters (Molland, 2008). This wide temperature lift reduces the COP (Equation 7.17) and increases the compressor power required per unit of cooling capacity. Two-stage compression with intercooling is often employed for deep-frozen cargo to improve cycle efficiency at large pressure ratios (Çengel & Boles, 2019).

For accommodation HVAC, the thermodynamic loads include sensible heating or cooling and dehumidification. In warm, humid climates the air conditioning system must remove both sensible heat (temperature reduction) and latent heat (moisture condensation). The energy required to condense moisture from air is determined by the latent heat of vaporisation of water ($\approx 2450\,\text{kJ kg}^{-1}$ at $20\,^{\circ}\text{C}$) (Çengel & Boles, 2019).

7.4 Applications in Maritime Systems

7.4.1 Waste Heat Recovery Systems

The energy balance of a modern marine diesel engine (Figure 7.4) shows that approximately 45–50% of the fuel energy is rejected as waste heat: roughly 25% in the exhaust gas stream and 15% to the jacket cooling water, with the remainder lost to radiation, charge air cooling, and lubricating oil (Molland, 2008). Waste heat recovery (WHR) systems aim to convert a portion of these thermal losses back into useful work or heating duty.

The most widespread WHR device is the *exhaust gas economiser*, a heat exchanger fitted in the exhaust duct that generates steam from the enthalpy of the flue gas. The steam produced (typically at 7–10 bar) can supply the ship's steam services—fuel oil heating, cargo tank heating, freshwater generation—or drive a steam turbine for additional electrical power (Woodyard, 2009). The thermodynamic limit on this recovery is set by the minimum stack temperature: the exhaust gas must not be cooled below the acid dew point ($\approx 120\,^{\circ}\mathrm{C}$ for heavy fuel oil combustion products) to prevent corrosive condensation of sulphuric acid on the heat exchanger surfaces (Woodyard, 2009).

When the turbocharger produces more shaft work than needed to compress the scavenging air, the surplus energy can drive a *power turbine* connected to the ship's electrical generator through a gearbox. This *turbo compound system* extracts mechanical energy from the exhaust stream before it enters the economiser, thereby cascading the heat recovery in order of decreasing temperature and increasing entropy—consistent with the second-law principle that work should be extracted at the highest available temperature (Molland, 2008).

For lower-temperature heat sources, the *organic Rankine cycle* (ORC) replaces water with an organic working fluid whose lower boiling point allows it to generate vapour from heat sources at moderate temperatures. An ORC system recovering heat from the jacket cooling water and the charge air cooler can improve the overall plant efficiency by several percentage points (Molland, 2008).

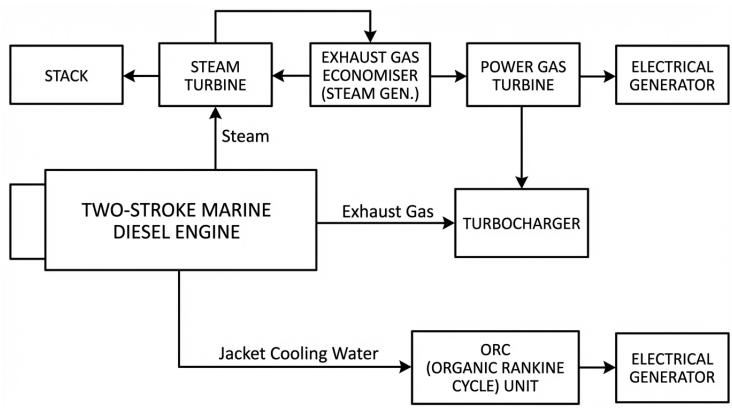

Figure 7.7: Schematic of a combined waste heat recovery system for a large two-stroke marine diesel engine. Exhaust gas first drives the turbocharger and (if surplus energy is available) a power gas turbine, then passes through an exhaust gas economiser that generates steam. A separate organic Rankine cycle (ORC) recovers low-grade heat from the jacket cooling water. The recovered energy supplements the ship's electrical generation (Molland, 2008; Woodyard, 2009).

7.4.2 LNG and Cryogenic Cargo Thermodynamics

The transport of liquefied natural gas (LNG) presents the most demanding cryogenic engineering challenge in commercial shipping. Natural gas, composed primarily of methane (CH_4), liquefies at approximately $-162\,^{\circ}\mathrm{C}$ ($111\,\mathrm{K}$) at atmospheric pressure, reducing its volume by a factor of roughly 600 relative to the gaseous state (Molland, 2008). The thermodynamic implications of maintaining cargo at this temperature aboard a vessel operating in ambient conditions of $300\,\mathrm{K}$ are governed by the heat transfer and second-law principles developed in Sections 7.3.5 and 7.2.2.

Despite extensive thermal insulation, a continuous heat leak $\dot{Q}$ from the environment to the cargo is inevitable. This heat input supplies the latent heat of vaporisation and generates *boil-off gas* (BOG) at a rate

$$\dot{m}_{\mathrm{BOG}} = \frac{\dot{Q}}{h_{fg}} \tag{7.23}$$

where $h_{fg} \approx 510\,\mathrm{kJ\,kg^{-1}}$ is the latent heat of vaporisation of LNG at its boiling point (Çengel & Boles, 2019).

The BOG must be managed to control tank pressure. Two thermodynamically distinct strategies are employed (Molland, 2008):

- **BOG as fuel:** The boil-off gas is routed to the main boilers (in steam turbine LNG carriers) or to dual-fuel diesel engines, converting the thermal loss into propulsive energy.
- **Re-liquefaction:** A refrigeration plant re-condenses the BOG and returns it to the cargo tanks. The minimum work required for re-liquefaction is bounded by Equation 7.8; actual systems consume several times this thermodynamic minimum due to compressor and heat exchanger irreversibilities (Çengel & Boles, 2019).

The cargo containment system must simultaneously provide thermal insulation (to limit $\dot{Q}$), structural integrity against sloshing loads, and gas-tightness. The two principal designs—the membrane system (using thin corrugated metal sheets backed by rigid insulation) and the independent spherical tank (Moss-type)—reflect different engineering compromises between thermal performance and structural design (Molland, 2008).

7.4.3 Exergy Analysis and Thermodynamic Efficiency

The first-law efficiency (Equation 7.15) measures the fraction of heat input converted to work, but it does not distinguish between high-quality and low-quality energy. *Exergy analysis* (also called *availability analysis*) provides a more discriminating measure by accounting for the quality—or "work potential"—of each energy stream relative to the environment (Çengel & Boles, 2019).

The exergy of a thermodynamic stream is defined as the maximum useful work obtainable when the system is brought to equilibrium with the surrounding environment (the "dead state" at T_0, P_0). For a steady-flow stream, the specific flow exergy is (Çengel & Boles, 2019)

$$\psi = (h - h_0) - T_0(s - s_0) + \tfrac{1}{2}V^2 + gz \tag{7.24}$$

where h and s are the specific enthalpy and entropy of the stream, h_0 and s_0 are the corresponding dead-state values, V is the velocity, and z is the elevation.

The exergy destruction in any irreversible process is directly proportional to the entropy generated:

$$\dot{X}_{\text{dest}} = T_0\, \dot{S}_{\text{gen}} \tag{7.25}$$

which is known as the Gouy–Stodola theorem (Çengel & Boles, 2019). This expression quantifies the thermodynamic cost of every irreversibility in the marine power plant: friction in bearings, temperature differences in heat exchangers, mixing of streams at different temperatures, and throttling across valves each generate entropy and destroy exergy.

Applying exergy analysis to the marine diesel engine reveals that the largest single source of exergy destruction is the combustion process itself, which accounts for a substantial fraction of the fuel exergy input due to the irreversible mixing and chemical reaction at finite temperature differences (Heywood, 1988). The jacket cooling water, by contrast, carries heat at only 80–$90\,^{\circ}$C—close to the dead-state temperature—and therefore has low specific exergy despite its substantial first-law energy content (Çengel & Boles, 2019).

The *second-law efficiency* (or *exergetic efficiency*) of a marine power plant is defined as the ratio of useful work output to the exergy of the fuel input:

$$\eta_{\text{II}} = \frac{\dot{W}_{\text{net}}}{\dot{X}_{\text{fuel}}} \tag{7.26}$$

The thermodynamic reasoning behind energy efficiency regulations for shipping—which aim to reduce the exergy destruction per unit of transport work—is developed from these principles; the regulatory framework itself (EEDI, EEXI, CII) and compliance pathways are treated in the *Environmental Physics in Maritime Operations* chapter of the companion volume.

7.4.4 Fire Thermodynamics on Ships

Fire aboard a vessel is a thermodynamic event: it involves the rapid, exothermic oxidation of fuel in which chemical energy is converted to thermal energy. The *fire triangle*—fuel, oxidiser (oxygen), and heat (ignition energy)—defines the three necessary conditions; removing any one extinguishes the fire.

The energy released by combustion is quantified by the *enthalpy of reaction* ΔH_r. For a hydrocarbon fuel of composition C_xH_y undergoing complete combustion:

$$C_xH_y + \left(x + \tfrac{y}{4}\right) O_2 \longrightarrow x\,CO_2 + \tfrac{y}{2}\,H_2O + |\Delta H_r| \tag{7.27}$$

The *heat release rate* (HRR), $\dot{Q}_{\text{fire}} = \dot{m}_f \times \Delta H_c \times \chi$, where $\dot{m}_f$ is the fuel mass loss rate, ΔH_c is the effective heat of combustion, and χ is the combustion efficiency, governs the thermal severity of a fire (Çengel & Boles, 2019).

The *adiabatic flame temperature* is the maximum temperature achievable when all combustion enthalpy heats the products without heat loss. For stoichiometric combustion of a hydrocarbon in air this temperature reaches approximately 2200–2500 K (Çengel & Boles, 2019). Actual flame temperatures aboard ship are lower due to radiative heat loss (Equation 7.21) and excess air dilution.

Fire suppression exploits the same thermodynamic principles in reverse:

- **Water mist and sprinkler systems** remove heat from the fire plume by evaporating water droplets. The latent heat of vaporisation of water ($\approx 2260\,\text{kJ kg}^{-1}$ at $100\,^\circ\text{C}$) makes water an exceptionally effective heat-extraction agent (Campbell, 2025).

- **CO_2 and inert gas systems** suppress combustion by displacing oxygen below the limiting concentration required to sustain the reaction.

The fundamental thermodynamics of fire—heat release, flame temperature, and heat extraction—are developed from these principles; fire safety engineering (detection systems, CFD zone models, and structural fire response) is treated in the *Maritime Safety and Risk Physics* chapter of the companion volume.

7.5 Discussion

The thermodynamic framework established in this chapter—particularly the equation of state (Equations 7.9–7.12) and the concept of potential temperature (Equation 7.7)—underpins the analysis in several subsequent chapters. The density of seawater, determined by the EOS-80 polynomial system, directly governs hydrostatic pressure (Chapter 3), drives thermohaline circulation, and governs acoustic propagation speed. The adiabatic lapse rate (Equation 7.6) is required for interpreting deep-ocean temperature data.

The thermodynamic cycle analysis of Section 7.3.2 demonstrates that every marine power plant is ultimately bounded by the Carnot limit (Equation 7.16). The gap between actual marine diesel efficiency (≈ 0.50–0.55) and the theoretical maximum (≈ 0.85) represents the combined effect of mechanical friction, finite-rate heat transfer across cylinder walls, incomplete combustion,

and auxiliary power consumption. Understanding where in the thermodynamic cycle these irreversibilities arise is the first step toward the waste heat recovery systems discussed in Section 7.4.1, which seek to extract useful work from the energy rejected in Q_C (Campbell, 2025).

The fundamental challenge for future marine propulsion lies in the thermodynamic conversion step itself. A conventional heat engine must always reject waste heat at T_C (the seawater temperature), and thus its efficiency is bounded by the Carnot limit (Equation 7.16). Electrochemical conversion—specifically fuel cells—offers an alternative pathway that bypasses the Carnot constraint: by converting chemical energy directly to electrical energy without combustion, fuel cells can in principle achieve higher efficiencies than any heat engine operating between the same temperature limits (Çengel & Boles, 2019). The thermodynamic analysis of these emerging energy conversion pathways, and their integration with marine propulsion and auxiliary systems, represents an active area of development whose outcomes will shape the next generation of marine power plants.

7.6 Conclusion

This chapter has demonstrated that thermodynamics provides the quantitative framework for both the physical oceanography of seawater and the full spectrum of marine engineering thermal systems. The thermodynamic state of seawater is fully described by three independent variables—temperature T, salinity S, and pressure p (Dera, 1992)—and the general differential equation of state (Equation 7.1) introduces the three fundamental response coefficients: thermal expansion k_T, saline contraction k_S, and isothermal compressibility k_p. The UNESCO EOS-80 (Equation 7.9) provides the operational polynomial equation of state with an accuracy of $\pm 0.009\,\mathrm{kg\,m^{-3}}$ over the full oceanic range, while the concept of potential temperature θ (Equation 7.7)—necessitated by the adiabatic warming of approximately 0.11 K per 1000 m depth—enables meaningful comparison of water masses at different pressures.

On the engineering side, every marine power plant is bounded by the Carnot efficiency limit (Equation 7.16). Modern low-speed two-stroke marine diesel engines achieve brake specific fuel consumption as low as 154 g/kWh—a thermal efficiency of approximately 54%—through constant-pressure turbocharging, uniflow scavenging, and electronic control of injection timing and exhaust valve closing (Molland, 2008). The exergy analysis (Section 7.4.3) reveals that the dominant source of thermodynamic loss is combustion irreversibility rather than mechanical friction, directing future efficiency efforts toward waste heat recovery systems (Section 7.4.1) and alternative energy conversion pathways. The three modes of heat transfer—conduction, convection, and radiation (Section 7.3.5)—govern the design of heat exchangers, engine cooling systems, cargo tank insulation, and fire suppression, while

the vapour-compression cycle (Section 7.3.6) underpins refrigeration and HVAC systems essential to cargo integrity and crew habitability. The thermodynamic principles established here connect directly to the *Environmental Physics in Maritime Operations* chapter of the companion volume, where the efficiency of thermodynamic conversion determines the carbon intensity of shipping operations.

References

Campbell, C. (2025). *Physics: A focused introduction*. CRC Press. https://doi.org/10.1201/9781003571568

Çengel, Y. A., & Boles, M. A. (2019). *Thermodynamics: An engineering approach* (9th ed.). McGraw-Hill Education.

Dera, J. (1992). *Marine physics* (P. Senn, Trans.) [Translated from Polish. Original: *Fizyka morza*, 1983]. Elsevier.

Fischer-Cripps, A. C. (2014). *The physics companion* (2nd ed.). CRC Press. https://doi.org/10.1201/b17356

Harrington, R. L. (Ed.). (1992). *Marine engineering*. The Society of Naval Architects; Marine Engineers.

Hewitt, P. G., Suchocki, J. A., & Hewitt, L. A. (2012). *Conceptual physical science* (5th ed.). Pearson.

Heywood, J. B. (1988). *Internal combustion engine fundamentals*. McGraw-Hill.

Incropera, F. P., DeWitt, D. P., Bergman, T. L., & Lavine, A. S. (2007). *Fundamentals of heat and mass transfer* (6th ed.). John Wiley & Sons.

Molland, A. F. (Ed.). (2008). *The maritime engineering reference book: A guide to ship design, construction and operation*. Butterworth-Heinemann. https://doi.org/10.1016/B978-0-7506-8987-8.X0001-7

Woodyard, D. (2009). *Pounder's marine diesel engines and gas turbines* (9th ed.). Butterworth-Heinemann.

Chapter 8

Marine Propulsion Physics

8.1 Introduction

Marine propulsion is the process of generating thrust to move a vessel through water (Harrington, 1992). Whether the energy source is wind, fossil fuel, nuclear power, or battery electricity, the fundamental physics is the same: momentum must be transferred to the vessel to overcome hydrodynamic resistance.

The oldest form of marine propulsion—the sail—remains one of the most instructive for understanding propulsion physics. Bejan et al. (2020) showed that the force balance between sail thrust and hull drag governs vessel speed, and that the optimal sail-to-hull proportions are predictable from first principles. This analysis introduces the principles underlying all forms of marine propulsion.

8.2 Scientific Background

8.2.1 Fundamentals of Thrust Generation

Thrust is generated by changing the momentum of a working fluid. For a sailing vessel, the working fluid is air; for a propeller-driven vessel, it is water. In both cases, the thrust force equals the rate of momentum change imparted to the fluid (Carlton, 2012).

Bejan et al. (2020) formulated the thrust force on a sail as:

Equation 9.1 — Aerodynamic thrust from sail:

$$F_a \sim C_D \cdot \frac{HL}{2} \cdot \frac{1}{2}\,\rho_a\, V_a^2 \tag{8.1}$$

where $C_D \sim 1$ is the drag coefficient, H is the mast height, L is the hull length (so $HL/2$ is the sail area), ρ_a is the air density, and V_a is the wind speed.

This equation embodies the momentum-transfer principle: the sail intercepts a stream of air, deflects it, and thereby extracts momentum. The force

is proportional to the sail area (the cross-section of the intercepted air stream) and to the dynamic pressure $\frac{1}{2}\rho_a V_a^2$ (the momentum flux per unit area).

The same principle applies to modern propulsors—propellers, water jets, and thrusters—where the working fluid is water rather than air, and the momentum change is generated by rotating blades or accelerating a water jet.

8.2.2 Propeller Geometry and Terminology

A marine propeller converts the rotational motion of the engine shaft into thrust. The fundamental quantity in this conversion is *torque*—the rotational analogue of force. Campbell (2025) defines torque as:

Equation 9.11 — Torque:

$$\tau = r\,F\,\sin\theta \tag{8.2}$$

where r is the radial distance from the rotation axis (shaft centreline), F is the applied force, and θ is the angle between the force vector and the radial direction (Campbell, 2025). Each blade element at radius r exerts a tangential hydrodynamic force on the water; by Newton's third law, the water exerts an equal and opposite tangential force on the blade, and the integral of $r\,\mathrm{d}F$ over the blade span yields the total propeller torque Q.

The rate at which the shaft delivers energy to the propeller is the *rotational power* (Campbell, 2025):

Equation 9.12 — Shaft power:

$$P_{\text{shaft}} = \tau\,\omega = 2\pi\,n\,Q \tag{8.3}$$

where ω is the angular velocity and $n = \omega/(2\pi)$ is the rotational speed in revolutions per second (Campbell, 2025); for a concise treatment, see (Fischer-Cripps, 2014). This expression links the engine output (torque at a given rotational speed) to the hydrodynamic load (propeller torque Q) and is the fundamental energy-transfer equation for all shaft-driven propulsion systems.

The fundamental geometric parameter of a screw propeller is the *pitch* P—the distance the driving face would advance in one revolution if working in a solid nut. The *pitch ratio* $p = P/D$, where D is the propeller diameter, characterises the helical form of the blade. The *speed of screw* is defined as $N \cdot P$ where N is the rotational speed in revolutions per minute, representing the theoretical advance per unit time in the absence of slip (Attwood, 1899).

The *projected blade area* A_p is the area of all blades projected onto a plane perpendicular to the shaft axis. For the Admiralty pattern blade (whose developed outline is an ellipse with semi-major axis equal to the propeller radius), the relationship between developed and projected area is (Attwood, 1899):

$$A_{\text{dev}} = A_p\,\sqrt{1 + 0.425\,p^2}$$

Typical values of the projected-area-to-disc-area ratio range from 0.33 for large naval vessels with reciprocating machinery to 0.4–0.56 for turbine-driven vessels, the larger values being necessary to avoid cavitation at high rotational speeds (Attwood, 1899).

The most widely used systematic propeller series is the *Wageningen B-series*, developed at MARIN (Maritime Research Institute Netherlands). Birk (2019) describes the B-series as a family of fixed-pitch propellers characterised by blade number Z (2–7), expanded area ratio A_E/A_0 (0.30–1.05), and pitch–diameter ratio P/D. Their open-water performance—thrust coefficient K_T, torque coefficient K_Q, and efficiency η_O—has been condensed into polynomial expressions by Oosterveld and van Oossanen (1975, as cited in Birk (2019)), enabling rapid computation for any combination of design parameters.

For propeller design, Birk (2019) employs the Bu_2-chart method. A shortened thrust loading coefficient $C_S = K_T/J^2$ is computed from the required thrust, advance speed, and propeller diameter. The fourth root $\sqrt[4]{C_S}$ is entered into the Bu_2-chart, where its intersection with the optimum-efficiency curve yields the pitch–diameter ratio, advance coefficient J, and maximum achievable open-water efficiency η_O (Birk, 2019).

To ensure that the propeller does not suffer excessive cavitation, the minimum required blade area is estimated using Keller's formula (Birk, 2019):

Equation 9.25 — Keller's expanded area ratio:

$$\left(\frac{A_E}{A_0}\right)_{\text{req}} = \frac{(1.3 + 0.3\,Z)\,T_{\text{req}}}{(p_0 - p_v)\,D^2} + K \tag{8.4}$$

where Z is the blade number, T_{req} is the required thrust, $p_0 = p_A + \rho g h_0$ is the total static pressure at the shaft centreline, p_v is the vapour pressure, D is the propeller diameter, and K is a constant depending on the vessel type ($K = 0.2$ for single-screw merchant ships) (Birk, 2019). If the Keller check indicates that a larger blade area is needed, the designer selects a higher A_E/A_0 chart and repeats the optimisation (Birk, 2019).

8.2.3 Flow Field Around a Propeller

The flow field around a marine propeller is governed by the same potential flow theory used for seakeeping (Chapter 6). Guedes Soares and Santos (2015) describe the Boundary Element Method (BEM) for propeller analysis, in which the blade surfaces and hub are discretized into quadrilateral panels, each carrying a distribution of sources and dipoles. The velocity potential satisfies the Laplace equation ($\nabla^2 \phi = 0$) throughout the fluid domain, with boundary conditions imposed on the blade surfaces (kinematic condition) and at infinity (radiation/decay condition).

For a propeller operating in open water (uniform inflow), the BEM solves for the pressure distribution on the blade surfaces at each advance ratio. The

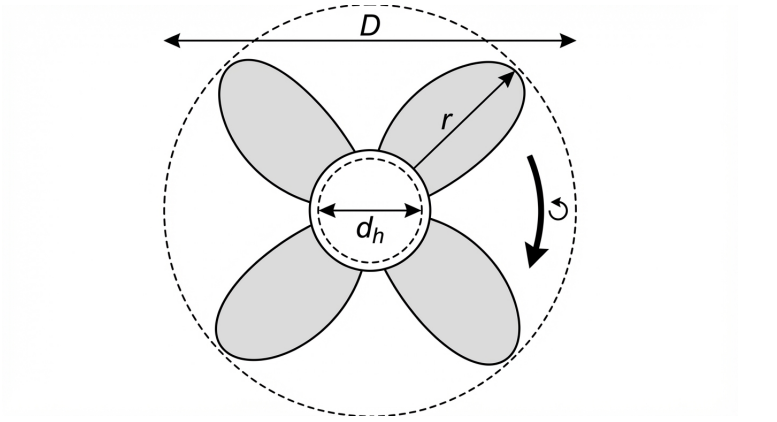

Figure 8.1: Face view of a four-bladed marine propeller showing the key geometric parameters: overall diameter D, hub diameter d_h, radial coordinate r, and direction of rotation. The blade outline illustrates the expanded area with moderate skew characteristic of Wageningen B-series propellers.

method captures the three-dimensional flow features—including radial flow, tip vortex roll-up, and blade loading distribution—that govern propulsive performance (Guedes Soares & Santos, 2015). However, as a potential flow method, the BEM cannot capture viscous phenomena such as leading-edge vortex effects, which become significant for highly skewed propellers (Guedes Soares & Santos, 2015).

RANS Formulation for Viscous Propeller Flows

The limitations of potential-flow methods motivate the use of the Reynolds-Averaged Navier–Stokes (RANS) equations for propeller wake analysis. Pêgo (2007) applied RANS-based computational fluid dynamics to the study of ship propulsion systems, demonstrating that viscous effects—particularly in the swirling wake downstream of the propeller—require turbulence modelling beyond the Boussinesq approximation.

For an incompressible, isothermal flow (appropriate for ship and propeller flows), the instantaneous velocity field U_i is decomposed into a time-averaged (mean) component $\overline{U}_i$ and a fluctuating component u_i' via the Reynolds decomposition $U_i = \overline{U}_i + u_i'$ (Pêgo, 2007). Substituting this decomposition into the continuity and Navier–Stokes equations and time-averaging yields the RANS continuity equation:

Equation 9.39 — RANS continuity:

$$\frac{\partial \overline{U}_i}{\partial x_i} = 0 \tag{8.5}$$

and the RANS momentum equations:

Equation 9.40 — RANS momentum:

$$\overline{U}_j \frac{\partial \overline{U}_i}{\partial x_j} = -\frac{1}{\rho}\frac{\partial \overline{P}}{\partial x_i} + \nu \frac{\partial^2 \overline{U}_i}{\partial x_j \partial x_j} - \frac{\partial \overline{u_i' u_j'}}{\partial x_j} \tag{8.6}$$

where $\overline{P}$ is the mean pressure, ν is the kinematic viscosity, and $-\rho\,\overline{u_i' u_j'}$ is the Reynolds stress tensor (Pêgo, 2007). This symmetric tensor introduces six additional unknowns to the four equations (one continuity, three momentum), creating the *closure problem* of turbulence modelling: there are ten unknowns but only four governing equations (Pêgo, 2007).

Eddy-viscosity models (e.g. the k–ε model) close the system by assuming that the Reynolds stress tensor is proportional to the mean strain rate through a scalar eddy viscosity:

Equation 9.41 — Boussinesq hypothesis:

$$-\overline{u_i' u_j'} = \nu_t \left(\frac{\partial \overline{U}_i}{\partial x_j} + \frac{\partial \overline{U}_j}{\partial x_i} \right) - \frac{2}{3} k\, \delta_{ij} \tag{8.7}$$

where ν_t is the eddy viscosity, $k = \frac{1}{2}\overline{u_i' u_i'}$ is the turbulent kinetic energy, and δ_{ij} is the Kronecker delta (Pêgo, 2007). While these models are robust and computationally economical, Pêgo (2007) demonstrated through comparison with laser Doppler anemometry (LDA) measurements that they fail to predict the highly anisotropic turbulence in propeller wakes—particularly the swirl-dominated flow downstream of rotating blades. The implicit assumption of local isotropy inherent in the Boussinesq approximation is inadequate for this class of flows (Pêgo, 2007).

To address this deficiency, Pêgo (2007) employed full Reynolds stress transport models—the SSG model (Speziale, Sarkar and Gatski) and the Anisotropy-Invariant Reynolds Stress Model (AIRSM)—which solve a differential transport equation for each component of $\overline{u_i' u_j'}$ individually. Both models correctly captured the spreading rate and mean velocity profiles of propeller-like swirling flows, with no significant difference in accuracy between them. The AIRSM, based on the invariant map theory of Lumley and Newman and requiring less empirical input, represents a more physically grounded approach to turbulence closure for marine propulsion applications (Pêgo, 2007).

8.2.4 Momentum Theory (Actuator Disk)

The momentum theory of propulsion treats the propulsor as an idealised device that imparts a change in momentum to the working fluid. For a sail, Bejan et al. (2020) showed that the aerodynamic force (Equation 8.1) must be balanced against the hydrodynamic drag (the hull resistance), yielding the steady-state speed ratio:

Equation 9.2 — Speed ratio:

$$\frac{H}{L} \sim \left(\frac{V_w}{V_a}\right)^{1/2} \tag{8.8}$$

This result has a clear physical interpretation: to achieve a boat speed (V_w) comparable to the wind speed (V_a), the mast height H must approach the hull length L. In the language of propulsion efficiency, this means the "propulsor" (sail) must be appropriately sized relative to the "hull" (resistance source).

When the optimal hull proportions are imposed (Section 5.3.7), the driving force and resistance force can be balanced to yield the complete performance relationship. The formula governing performance evolution is (Bejan et al., 2020):

Equation 9.3 — Mast slenderness (structural–propulsive coupling):

$$\frac{d}{H} \sim \left(\frac{\rho_a V_a^2}{\sigma}\right)^{1/3} \left(\frac{V_a}{V_w}\right)^{2/3} \tag{8.9}$$

where d is the mast diameter, σ is the allowable stress of the mast material, ρ_a is air density, and V_a, V_w are wind and boat speeds respectively (Bejan et al., 2020).

This equation reveals an important propulsion–structure coupling: a stronger mast material (larger σ) permits a thinner mast (smaller d/H), which reduces dead weight, decreases the submerged hull volume, reduces drag, and ultimately increases boat speed. Thus, material science advances directly improve propulsive performance (Bejan et al., 2020).

The momentum theory can be formalised for a screw propeller through the *actuator disk* concept, first developed by Rankine and extended by R. E. Froude. Birk (2019) presents the complete derivation, in which the propeller is replaced by an infinitesimally thin disk of area $A_0 = \pi D^2/4$ that imparts a uniform pressure jump Δp to the fluid passing through it, producing a thrust:

Equation 9.18 — Actuator disk thrust:

$$T = A_0 \, \Delta p \tag{8.10}$$

A fixed control volume is drawn around the disk. Fluid enters at the advance velocity v_A and exits the slipstream at a higher velocity $v_3 = v_A(1 + b)$, where $b > 0$ is the fractional velocity increase (Birk, 2019). The fluid is assumed inviscid, incompressible, and in steady flow, and the race boundary is treated as a stream surface.

Applying conservation of momentum and mass to the control volume, Birk (2019) showed that the thrust equals the rate of change of axial momentum:

Equation 9.19 — Thrust from momentum:

$$T = b \, Q_2 \, v_A \tag{8.11}$$

where $Q_2 = \rho\, v_A(1+a)\, A_0$ is the mass flow rate through the disk and a is the axial induction factor at the disk plane (Birk, 2019). Applying Bernoulli's equation between the inlet and the disk (upstream side), and between the disk (downstream side) and the outlet, Birk (2019) derived the fundamental result:

Equation 9.20 — Axial induction relation:

$$a = \frac{b}{2} \tag{8.12}$$

This means that half of the total velocity increase in the slipstream occurs upstream of the disk. The thrust and mass flow may then be expressed entirely in terms of v_A, b, and A_0 (Birk, 2019):

$$T = \tfrac{1}{2}\,\rho\, v_A^2\,(2b + b^2)\, A_0 \tag{8.13}$$

The *ideal* (or *jet*) *efficiency* of the actuator disk is defined as the ratio of useful thrust power $P_T = T\, v_A$ to the total kinetic energy added to the flow per unit time (Birk, 2019):

Equation 9.22 — Ideal propulsive efficiency:

$$\eta_{TJ} = \frac{T\, v_A}{T\, v_A\big(1 + \frac{b}{2}\big)} = \frac{2}{2+b} \tag{8.14}$$

Maximum efficiency is approached as $b \to 0$, but thrust also vanishes, so a compromise is required. For a given thrust, increasing the disk area A_0 (larger propeller diameter) permits a smaller b, yielding higher efficiency (Birk, 2019). This is the theoretical basis for the naval architect's rule that the largest propeller that can be fitted should be selected.

The relationship between efficiency and loading is expressed through the *thrust loading coefficient* (Birk, 2019):

Equation 9.23 — Thrust loading coefficient:

$$C_{Th} = \frac{T}{\frac{1}{2}\,\rho\, v_A^2\, A_0} = 2b + b^2 \tag{8.15}$$

Solving the quadratic $b^2 + 2b - C_{Th} = 0$ for the physically meaningful root ($b > 0$) and substituting into Equation 8.14 yields the classical result (Birk, 2019):

Equation 9.24 — Efficiency vs. thrust loading:

$$\eta_{TJ} = \frac{2}{1 + \sqrt{1 + C_{Th}}} \tag{8.16}$$

Equation 8.16 establishes that a lightly loaded propeller ($C_{Th} \ll 1$) approaches unity efficiency, while a heavily loaded propeller ($C_{Th} \gg 1$, as in bollard pull conditions) has markedly reduced efficiency. Most ship propellers operate with $C_{Th} \sim 1$ (Birk, 2019).

The sail force model can be developed further by resolving the aerodynamic forces into components aligned with the vessel's course. Huchet (2021) presented a complete sail force model for the NACRA 17 catamaran, building on the fundamental principle that a sail generates both lift (perpendicular to the apparent wind) and drag (parallel to the apparent wind).

The relationship between the true wind and the apparent wind is fundamental to all sail propulsion analysis. The **wind triangle** defines the apparent wind angle (AWA) and apparent wind speed (AWS) from the vector sum of the true wind and the vessel's velocity vector:

Equation 9.4 — Apparent wind angle:

$$\beta_{AW} = \arctan\left(\frac{V_{TW}\sin\beta_{TW}}{V_{TW}\cos\beta_{TW} + V_b}\right) \tag{8.17}$$

where β_{TW} is the true wind angle (relative to the vessel heading), V_{TW} is the true wind speed, and V_b is the boat speed (Huchet, 2021). The apparent wind speed is:

$$V_{AW} = \sqrt{(V_{TW}\sin\beta_{TW})^2 + (V_{TW}\cos\beta_{TW} + V_b)^2}$$

As the boat speed increases, the apparent wind shifts forward (smaller β_{AW}) and increases in magnitude ($V_{AW} > V_{TW}$ when sailing downwind). This is consistent with the observation of Bejan et al. (2020) that at maximum speed, the sails are trimmed close to the centreline.

The sail generates aerodynamic lift L and drag D relative to the apparent wind direction. These forces are resolved into components parallel and perpendicular to the vessel's course (Huchet, 2021):

Equation 9.5 — Driving force (along course):

$$F_x = L\sin\beta_{AW} - D\cos\beta_{AW} \tag{8.18}$$

Equation 9.6 — Side force (perpendicular to course):

$$F_y = L\cos\beta_{AW} + D\sin\beta_{AW} \tag{8.19}$$

where $L = \frac{1}{2}\rho_a V_{AW}^2 A_{\text{sail}} C_L$ and $D = \frac{1}{2}\rho_a V_{AW}^2 A_{\text{sail}} C_D$, with C_L and C_D being the sail lift and drag coefficients as functions of the apparent wind angle, obtained from ORC (Offshore Racing Congress) sail aerodynamic data (Huchet, 2021).

The driving force F_x is the component that accelerates the vessel; the side force F_y is the component that causes heeling and leeway. The balance $F_x = R_{\text{total}}$ (total hydrodynamic resistance) determines the equilibrium speed, while the balance of F_y against the lateral hydrodynamic force on the hull and appendages determines the leeway angle.

For the NACRA 17, the heeling moment generated by F_y must be balanced by the righting moment (see Chapter 4, Equation 4.7), which establishes the coupling between the propulsion system (sails) and the stability system (hull geometry and crew weight) (Huchet, 2021).

8.2.5 Blade Element Theory

Blade element theory (BET) treats each radial section of a propeller blade as a two-dimensional aerofoil operating in a local flow field determined by the advance velocity and the rotational velocity at that radius. Rawson and Tupper (2001) derive the elemental forces on a blade strip of width $\mathrm{d}r$ at radius r:

Equation 9.31 — Elemental thrust from blade element:

$$\mathrm{d}T = \mathrm{d}L\,\cos\beta_i - \mathrm{d}D\,\sin\beta_i \tag{8.20}$$

Equation 9.32 — Elemental torque from blade element:

$$\mathrm{d}Q = \left(\mathrm{d}L\,\sin\beta_i + \mathrm{d}D\,\cos\beta_i\right) r \tag{8.21}$$

where $\mathrm{d}L$ and $\mathrm{d}D$ are the lift and drag forces on the element, and β_i is the hydrodynamic pitch angle—the angle between the resultant inflow velocity and the plane of rotation (Rawson & Tupper, 2001). The resultant inflow velocity at each element is $V_R = \sqrt{V_a^2 + (2\pi n r)^2}$, where V_a is the advance velocity and n is the rotational speed. The lift and drag are:

$$\mathrm{d}L = \tfrac{1}{2}\,\rho\,V_R^2\,c\,C_L\,\mathrm{d}r, \qquad \mathrm{d}D = \tfrac{1}{2}\,\rho\,V_R^2\,c\,C_D\,\mathrm{d}r$$

where c is the local chord length and C_L, C_D are the section lift and drag coefficients, which depend on the local angle of attack $\alpha = \theta_g - \beta_i$ (the difference between the geometric pitch angle and the hydrodynamic pitch angle) (Rawson & Tupper, 2001).

The total thrust and torque are obtained by integrating Equations (8.20) and (8.21) over the blade span from the hub radius r_h to the tip radius R, and multiplying by the number of blades z (Rawson & Tupper, 2001).

8.2.6 Combined Blade Element Momentum Theory (BEMT)

Blade element momentum theory combines the momentum theory of Section 8.2.1 with the blade element theory of Section 8.2.5 by equating the thrust and torque from the two approaches at each radial station. Rawson and Tupper (2001) show that the momentum balance for an annular stream tube of width $\mathrm{d}r$ at radius r yields:

Equation 9.33 — Axial momentum balance:

$$\mathrm{d}T = 4\pi\,\rho\,r\,V_a^2\,(1+a)\,a\,\mathrm{d}r \tag{8.22}$$

where a is the axial inflow factor at radius r (Rawson & Tupper, 2001). Equating this with the blade element thrust (Equation 8.20) for z blades gives an implicit equation for a at each radius. Similarly, the tangential momentum balance yields an equation for the tangential inflow factor a'. The coupled system is solved iteratively: an initial guess for a and a' determines β_i, from which C_L and C_D are obtained; the blade element forces are then computed and used to update the inflow factors until convergence (Rawson & Tupper, 2001).

BEMT provides the radial distribution of loading along the blade, which is essential for structural design and cavitation assessment. The optimum loading distribution—that which maximises efficiency for a given total thrust—is the Goldstein distribution, in which each blade section operates at a constant ratio of lift to drag (Rawson & Tupper, 2001).

8.2.7 Propeller Open Water Characteristics

The performance of a marine propeller is characterised by three non-dimensional coefficients as functions of the advance coefficient J. Guedes Soares and Santos (2015) define the relative differences between rigid and flexible propeller performance as:

Equation 9.8 — Relative thrust coefficient difference:

$$\Delta K_T = \frac{K_{T,\text{rigid}} - K_{T,\text{flexible}}}{K_{T,\text{rigid}}} \times 100\% \tag{8.23}$$

Equation 9.9 — Relative torque coefficient difference:

$$\Delta K_Q = \frac{K_{Q,\text{rigid}} - K_{Q,\text{flexible}}}{K_{Q,\text{rigid}}} \times 100\% \tag{8.24}$$

where K_T and K_Q are the thrust and torque coefficients, respectively, and the subscripts "rigid" and "flexible" denote the rigid-blade and deformed-blade performance (Guedes Soares & Santos, 2015).

The open water efficiency is $\eta_0 = (J/2\pi)\times(K_T/K_Q)$, where $J = V_a/(n\,D)$ is the advance coefficient, V_a the advance speed, n the rotational speed, and D the propeller diameter.

A BEM–FEM coupled analysis of the four NSRDC propellers (4381–4384), which differ only in skew angle, showed that the hydro-elastic response is strongly influenced by skew. The structural equilibrium for the flexible blade is (Guedes Soares & Santos, 2015):

Equation 9.10 — Hydro-elastic equilibrium:

$$\mathbf{K}\cdot\mathbf{u} = \mathbf{f}_h(\mathbf{u}) + \mathbf{f}_{ce} \tag{8.25}$$

where $\mathbf{K}$ is the structural stiffness matrix, $\mathbf{u}$ the displacement vector, $\mathbf{f}_h(\mathbf{u})$ the hydrodynamic force vector (which depends on the deformed geometry), and $\mathbf{f}_{ce}$ the centrifugal force vector (Guedes Soares & Santos, 2015). The coupling is solved iteratively: the BEM computes hydrodynamic pressures on the current blade geometry, the FEM computes the resulting deformations, and the blade geometry is updated until convergence.

Highly skewed propellers showed the largest relative change in thrust coefficient ΔK_T due to flexibility, because the movement of the hydrodynamic load centre toward the trailing edge at high advance ratios creates a large de-pitching moment on the skewed blade (Guedes Soares & Santos, 2015).

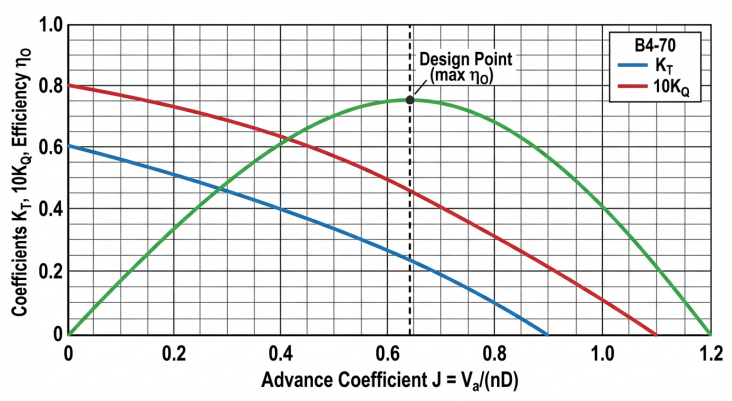

Figure 8.2: Open-water propeller characteristics for a Wageningen B4-70 type propeller: thrust coefficient K_T, torque coefficient $10K_Q$, and open-water efficiency η_O as functions of the advance coefficient $J = V_a/(nD)$. The design point at $J = 0.65$ corresponds to the maximum efficiency operating condition.

8.2.8 Behind-Hull Performance

A propeller working behind a hull operates in a flow field that differs fundamentally from uniform open-water conditions. Attwood (1899) identified three key phenomena that govern behind-hull performance: the wake, the augmentation of resistance, and the resulting hull efficiency.

Wake Fraction

The friction of the water on the hull creates a boundary layer that is carried aft, so that at the stern there exists a belt of water with a forward velocity. This body of water is the *frictional wake*. Attwood (1899) expressed the wake speed as a fraction w of the ship speed V, so that the speed of advance of the propeller through the water is:

Equation 9.13 — Speed of advance (wake fraction):

$$V_a = (1 - w)\, V \tag{8.26}$$

where w is the wake fraction and V is the ship speed (Attwood, 1899). A single-screw vessel benefits more from the wake than a twin-screw vessel, because the wake velocity is greater near the centreline of the hull (Attwood, 1899). Representative wake fractions based on Luke's investigations (I.N.A., 1910), as cited by Attwood (1899), are:

$$w_{\text{twin}} \approx 0.20 + 0.55\, C_B, \qquad w_{\text{single}} \approx 0.05 + 0.50\, C_B$$

where C_B is the block coefficient.

Thrust Deduction

The action of the propeller at the stern interferes with the natural closing-in of the stream lines, causing an augmentation of the hull resistance. Rather than treating this as an increased resistance, Attwood (1899) expressed it as a reduction in the effective thrust:

Equation 9.14 — Thrust deduction:

$$R = T\,(1 - t) \tag{8.27}$$

where T is the total propeller thrust, R is the hull resistance (without propeller), and t is the thrust deduction fraction (Attwood, 1899). For a single-screw ship, the thrust deduction is greater than for a twin-screw ship because the propeller is closer to the hull centreline where the stream-line disturbance is strongest (Attwood, 1899).

Hull Efficiency

The useful work done by the ship is $R \times V$; the work done by the propeller is $T \times V_a$. The ratio of these is the *hull efficiency* (Attwood, 1899):

Equation 9.15 — Hull efficiency:

$$\eta_H = \frac{R \times V}{T \times V_a} = \frac{1 - t}{1 - w} \tag{8.28}$$

The usual value assumed for hull efficiency is approximately unity, the gain due to the wake being roughly balanced by the loss due to thrust deduction (Attwood, 1899).

Ridley and Patterson (2014) provide representative numerical values that illustrate the magnitudes involved. For a typical single-screw cargo vessel: $w \approx 0.30$, $t \approx 0.20$, giving $\eta_H = (1 - 0.20)/(1 - 0.30) = 1.14$—a hull efficiency greater than unity, meaning the hull–propeller interaction is beneficial overall. For a twin-screw vessel: $w \approx 0.10$, $t \approx 0.12$, giving $\eta_H = (1 - 0.12)/(1 - 0.10) = 0.98$—slightly below unity, reflecting the weaker wake and relatively greater thrust deduction of the twin-screw arrangement (Ridley & Patterson, 2014).

Propulsive Coefficient

The overall efficiency of the propulsion system—the ratio of effective horse-power (EHP) to indicated horse-power (IHP)—is the *propulsive coefficient*. Attwood (1899) decomposed it as:

Equation 9.16 — Propulsive coefficient:

$$\frac{\text{EHP}}{\text{IHP}} = \frac{1 - t}{1 - w} \times e_p \times e_m \tag{8.29}$$

where e_p is the propeller efficiency (ratio of propeller useful work to shaft work) and e_m is the mechanical efficiency of the engine (ratio of shaft horse-power to indicated horse-power) (Attwood, 1899). For typical values of $e_m = 0.85$, $e_p = 0.65$, $w = 0.15$, and $t = 0.15$, the propulsive coefficient is approximately 55% (Attwood, 1899). In Froude's towing experiments on HMS *Greyhound*, the best propulsive coefficient measured was only 42%, meaning that 58% of the engine power was lost to wake effects, propeller inefficiency, and mechanical friction (Attwood, 1899).

Slip

The difference between the theoretical screw speed and its actual speed of advance through the water is the *slip*. The true slip ratio is (Attwood, 1899):

Equation 9.17 — Slip ratio:

$$s = \frac{N P - V_a \times \frac{6080}{60}}{N P} \tag{8.30}$$

where N is revolutions per minute, P is the pitch in feet, and V_a is the speed of advance in knots (Attwood, 1899). In SI-consistent units (P in metres, V_a in m s^{-1}, n in revolutions per second), the slip ratio simplifies to $s = 1 - V_a / (n\,P)$. Since the wake speed is not generally known in practice, the *apparent slip* is commonly used instead, with the ship speed V substituted for V_a. Because $V_a < V$, the true slip is always greater than the apparent slip. Negative apparent slip has been recorded when the sternward velocity of the water from the propeller is less than the forward speed of the wake; however, negative true slip is physically impossible, as it would imply thrust without sternward momentum transfer (Attwood, 1899).

The vibration and noise characteristics arising from propeller operation in a non-uniform wake are treated in Section 8.2.10.

8.2.9 Cavitation Physics

Cavitation occurs when the local pressure on the suction (forward) face of a propeller blade falls below the vapour pressure of seawater, causing the water to separate from the blade surface and leave a vapour-filled cavity (Carlton, 2012; Newman, 1977). Attwood (1899) described the mechanism: "The water will not follow up at the back of the blades of the propeller if the thrust is too great and if the velocity of the blades is sufficiently high. This causes a loss of thrust-producing power, and is termed cavitation."

To avoid cavitation, Attwood (1899) reported two practical criteria from contemporary investigators:

- The limit of thrust pressure should be approximately 6.9 kPa (1 lb/in^2) for every 5.08 m s^{-1} (1000 ft/min) of circumferential blade-tip velocity (Speakman, Scottish Inst. E. & S., 1905, as cited in Attwood (1899)).

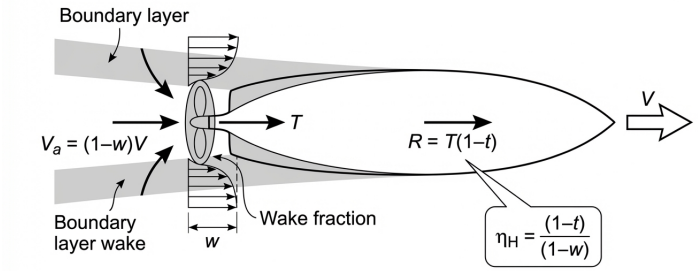

Figure 8.3: Schematic of hull–propeller interaction showing the wake fraction w and thrust deduction factor t. The ship moves at speed V, but due to the boundary-layer wake the propeller advance velocity is $V_a = (1-w)V$ (Equation 8.26). The propeller thrust T is partially absorbed by augmented hull resistance, so that $R = T(1-t)$ (Equation 8.27). The hull efficiency $\eta_H = (1-t)/(1-w)$ quantifies the net benefit of this interaction.

- The maximum average thrust should not exceed 77.6 kPa (11.25 lb/in^2) of projected blade area at 0.305 m (12 in) tip immersion, with an additional 5.2 kPa (0.75 lb/in^2) for each additional 0.305 m (foot) of immersion (Barnaby, as cited in Attwood (1899)).

These criteria explain why turbine-driven vessels, which operate at much higher rotational speeds than reciprocating-engine ships, require propellers with larger projected blade area ratios (0.4–0.56 versus 0.33 for reciprocating machinery) and smaller diameters to keep the blade-tip velocity within acceptable limits (Attwood, 1899).

A quantitative criterion for cavitation assessment is provided by the Burrill cavitation chart (Birk, 2019). The propeller cavitation number is defined as:

Equation 9.26 — Burrill cavitation number:

$$\sigma_b = \frac{p_0 - p_v}{\frac{1}{2}\,\rho\, v_1^2} \tag{8.31}$$

where $p_0 = p_A + \rho g h_0$ is the total static pressure at the shaft centreline, p_v is the vapour pressure of seawater (approximately 1671 Pa at $15\,^\circ$C), and $v_1 = \sqrt{v_A^2 + (0.7\,\pi\, n\, D)^2}$ is a simplified velocity at the $0.7R$ blade section, combining the advance speed and circumferential velocity (Birk, 2019).

The Burrill chart plots the maximum permissible thrust loading coefficient τ_c against σ_b for specified percentages of back cavitation. For the 5% back cavitation limit commonly adopted for merchant vessels, Birk (2019) provides the regression:

Equation 9.27 — Burrill 5% cavitation limit:

$$\tau_c = 0.715\,\sigma_b^{0.184} - 0.437 \tag{8.32}$$

The required projected blade area is then (Birk, 2019):

$$A_{P,\text{req}} = \frac{T_{\text{prop}}}{\frac{1}{2}\,\rho\,v_1^2\,\tau_c} \tag{8.33}$$

Projected area is converted to expanded area via Taylor's formula $A_P = (1.067 - 0.229\,P/D)\,A_D$, with $A_E \approx A_D$ for propellers with moderate rake (Birk, 2019). If the required expanded area ratio exceeds the initial design value, the designer must iterate using a B-series chart with higher A_E/A_0, accepting a small reduction in open-water efficiency (Birk, 2019).

Beyond sheet and tip vortex cavitation, the hub vortex constitutes a third cavitation mechanism that is particularly challenging to predict. The concentrated vorticity shed from the blade roots coalesces into a single vortex filament along the hub axis, and the attendant pressure depression can sustain a continuous tubular cavity that extends well downstream of the propeller. Sutulo and Guedes Soares (2023) present a computational study using a coupled RANS–BEM approach in which the boundary element method provides the blade loading while the viscous solver resolves the hub vortex structure. The results show that hub vortex cavitation inception correlates primarily with blade root circulation and hub diameter ratio rather than with the back-cavitation parameters captured by the Burrill criterion (Equation 8.31), highlighting the need for dedicated inception checks at the hub in addition to the blade-section analysis.

8.2.10 Propeller-Induced Vibration and Noise

A marine propeller operating in the non-uniform wake behind a ship hull produces periodically varying forces that constitute the primary source of hull vibration and underwater radiated noise. The physics of this excitation involves both mechanical and hydrodynamic mechanisms (*CFD 2003: Computational Fluid Dynamics Technology in Ship Hydrodynamics*, 2003).

Blade-Rate Excitation

The wake field behind a hull is non-axisymmetric: the axial inflow velocity varies with angular position due to the boundary layer, shaft brackets, and other appendages. As each blade sweeps through this non-uniform inflow, the angle of attack—and hence the hydrodynamic loading—changes cyclically. For a propeller with z blades rotating at n revolutions per second, the fundamental excitation frequency is the blade-rate frequency:

Equation 9.29 — Blade-rate frequency:

$$f_z = z \cdot n \tag{8.34}$$

where f_z is in hertz (*CFD 2003: Computational Fluid Dynamics Technology in Ship Hydrodynamics*, 2003). The resulting hull excitation contains harmonics at f_z, $2f_z$, $3f_z$, etc. The amplitude of each harmonic depends on the wake harmonic content: if the spatial Fourier decomposition of the wake contains a strong zth-order component, the blade-rate force harmonic will be dominant.

For the typical case of a four-bladed propeller rotating at $n = 2\,\mathrm{s}^{-1}$ (120 rpm), the blade-rate frequency is $f_z = 4 \times 2 = 8$ Hz. This low-frequency excitation falls within the range that can excite structural resonances in the hull, superstructure, and machinery foundations.

Hull Surface Pressure Fluctuations

The fluctuating blade loading radiates pressure fluctuations to the hull surface above the propeller. These are characterised by the non-dimensional pressure coefficient:

Equation 9.30 — Propeller-induced pressure coefficient:

$$K_p = \frac{\Delta p}{\rho\, n^2\, D^2} \tag{8.35}$$

where Δp is the peak-to-peak pressure fluctuation amplitude at the hull surface, ρ is the water density, n is the rotational speed, and D is the propeller diameter (*CFD 2003: Computational Fluid Dynamics Technology in Ship Hydrodynamics*, 2003). The magnitude of K_p decreases rapidly with increasing tip clearance (the distance between the blade tip and the hull), making the propeller–hull clearance a critical design parameter for vibration control.

CFD 2003: Computational Fluid Dynamics Technology in Ship Hydrodynamics (2003) demonstrated that boundary element methods can predict the unsteady propeller blade loading—including thrust coefficient K_T and torque coefficient K_Q harmonics—by solving Green's identity on the blade surface with the effective wake as inflow. The computational approach decomposes the total flow into a potential (irrotational) part treated by the boundary element method and a rotational part treated by a finite-volume Euler or RANS solver.

Cavitation-Induced Vibration and Noise

When the propeller operates above the cavitation inception threshold (Section 8.2.9), the unsteady growth and collapse of vapour cavities on the blade surface produce pressure fluctuations that can be an order of magnitude larger than those from non-cavitating blade loading. The cavity volume changes cyclically at the blade-rate frequency, and the rapid collapse of cavitation bubbles generates broadband noise extending to high frequencies.

CFD 2003: Computational Fluid Dynamics Technology in Ship Hydrodynamics (2003) modelled the cavity dynamics by imposing the condition that the pressure on the cavity surface equals the vapour pressure p_v, while the cavity thickness evolves according to a kinematic boundary condition that couples the

rate of change of cavity thickness to the local flow velocity components on the blade surface. The predicted cavity extents—including sheet cavitation, tip vortex cavitation, and developed cavitation on ducted propellers and rudders—determine the amplitude of the cavitation-induced pressure pulses.

The practical consequence is that even a small amount of cavitation can transform the vibration signature from the discrete blade-rate tonal excitation of a non-cavitating propeller to a combination of intense tonal and broadband excitation. This is why the Burrill cavitation check (Equation 8.31) is an essential step in propeller design: maintaining σ_b above the inception threshold not only preserves blade material but also controls vibration and noise (Birk, 2019; *CFD 2003: Computational Fluid Dynamics Technology in Ship Hydrodynamics*, 2003).

8.3 Applications in Maritime Systems

8.3.1 Propeller Selection and Design

The systematic propeller selection procedure combines the B-series charts of Section 8.2.2 with the behind-hull interaction coefficients of Section 8.2.8. Rawson and Tupper (2001) describe the complete design sequence:

1. From the effective power P_E and the hull–propeller interaction factors (w, t, η_R), compute the required propeller thrust $T_{\text{req}} = R_T/(1-t)$ and the advance speed $V_a = (1-w)V$.
2. Enter the thrust coefficient $K_T = T_{\text{req}}/(\rho\, n^2\, D^4)$ or the shortened thrust loading coefficient $C_S = K_T/J^2$ into the appropriate B-series chart for the selected blade number and area ratio (Birk, 2019).
3. Read off the optimum pitch–diameter ratio P/D, the advance coefficient J, and the open-water efficiency η_O.
4. Verify cavitation using the Burrill criterion (Equation 8.31); if insufficient blade area, increase A_E/A_0 and repeat (Birk, 2019).
5. Check the propulsive coefficient $\text{PC} = \eta_H \times \eta_O \times \eta_R$ (Equation 8.29) and determine the required brake power (Rawson & Tupper, 2001).

This iterative procedure—chart selection, optimisation, cavitation check, area adjustment—converges within two to three iterations to a final propeller specification that balances efficiency against cavitation risk (Birk, 2019; Rawson & Tupper, 2001).

8.3.2 Controllable Pitch Propellers (CPP)

A controllable pitch propeller allows the blade pitch angle to be varied during operation, enabling thrust reversal and optimal loading at different vessel speeds without changing the shaft rotational speed. Rawson and Tupper

(2001) explain the physics: by rotating each blade about its spindle axis, the geometric pitch angle θ_g is changed, which alters the angle of attack α at every radial station and hence the thrust and torque produced.

The principal advantage of CPP is operational flexibility: the engine can run at constant speed (optimal for fuel efficiency and auxiliary power generation), while the pitch is adjusted to match the required thrust at each operating condition—manoeuvring, free running, towing, or crash stop (Molland, 2008; Rawson & Tupper, 2001). The disadvantage is mechanical complexity: the hub must accommodate the blade-turning mechanism, which increases the hub diameter ratio and reduces the effective blade area near the root, marginally reducing peak efficiency compared with a fixed-pitch propeller of the same diameter and blade number (Rawson & Tupper, 2001).

8.3.3 Azimuth Thrusters and Podded Propulsion

Azimuth thrusters and podded propulsion systems mount the propeller on a unit that can rotate through 360° about a vertical axis, providing thrust in any horizontal direction without the need for a rudder. Molland (2008) describe the physics: the propeller is driven by an electric motor housed in a streamlined pod beneath the hull, with power delivered through a vertical shaft or, in modern designs, directly by an electric motor within the pod.

The hydrodynamic advantage of podded propulsion is the elimination of the rudder and its associated drag, together with the ability to direct the propeller slipstream in any direction for manoeuvring. The wake field entering a podded propeller is more uniform than that of a conventional stern arrangement because the pod is located in relatively undisturbed flow (Molland, 2008). This uniform inflow reduces unsteady blade loading and hence propeller-induced vibration (cf. Equation 8.34).

The principal applications are cruise ships, icebreakers, and offshore vessels where manoeuvrability is paramount. For dynamic positioning operations, azimuth thrusters provide the thrust vectors required to maintain station against wind, waves, and current without forward motion (Molland, 2008).

Contra-Rotating Propellers and Wake Efficiency

Pod drives can be further enhanced by employing contra-rotating propellers—a tandem arrangement in which the front and rear propellers rotate in opposite directions on a common axis. Pêgo (2007) conducted a systematic experimental investigation of twenty-four pod drive models in the water tunnel facility at LSTM-Erlangen, varying the distance between propeller planes and the ratio of rotational frequencies n_2/n_1 between the rear and front propellers. Co-rotating and contra-rotating pairs (three-bladed, $D = 250$ mm) were compared using a dedicated three-component water tunnel balance to measure thrust and torque independently for each propeller (Pêgo, 2007).

The key finding was that contra-rotating propellers achieved an overall increase of approximately 8% in system efficiency compared with co-rotating configurations (Pêgo, 2007). The physical mechanism was confirmed through two-component laser Doppler anemometry (LDA) measurements at three axial stations downstream of the rear propeller plane ($x/D_1 = 1$, 5, and 10): the contra-rotating arrangement produced substantially less residual swirl in the wake, with the counter-rotation of the rear propeller recovering most of the tangential momentum imparted by the front propeller (Pêgo, 2007). In the co-rotating case, by contrast, the maximum tangential velocity component reached half of the axial velocity component, representing significant energy lost to swirl (Pêgo, 2007).

The LDA measurements further revealed that the torque loading was unequally distributed between the front and rear propellers. For co-rotating pods, the rear propeller torque varied little with advance ratio J, while the front propeller experienced accentuated variations. For contra-rotating pods, the frequency ratio n_2/n_1 strongly influenced the rear propeller loading (increasing with n_2/n_1) while affecting the front propeller only marginally (Pêgo, 2007). The wake of contra-rotating propellers was also found to be more homogeneous, with the cyclic flow variations decaying over a shorter distance than in the co-rotating case (Pêgo, 2007).

Analysis of the Reynolds stress distributions (three normal stresses and five of the six Reynolds stress components) confirmed that the flow in both propeller wakes was highly anisotropic. Plotting the scalar invariants II_a and III_a of the anisotropy tensor a_{ij} on the Lumley–Newman invariant map showed that the turbulence state lay close to the axisymmetric limiting state, supporting the use of full Reynolds stress models (Section 8.2.3) rather than isotropic eddy-viscosity closures for computational prediction of propeller wake flows (Pêgo, 2007).

8.3.4 Alternative Propulsion Systems

Sail propulsion, the oldest form of marine propulsion, remains a subject of engineering interest both historically and for modern wind-assisted propulsion concepts. Bejan et al. (2020) showed that the physics of sail propulsion is governed by the aerodynamic force on the sail area ($HL/2$), the ratio $\rho_w/\rho_a \sim 10^3$ (water-to-air density), and the balance between form drag ($C_D \sim 1$) and skin friction ($C_f \sim 10^{-2}$).

The fastest monohull sailboats achieve maximum speeds with a single mast and 2–3 sails. The velocity is limited by the transverse bow wave (critical speed $V_c \approx 1.25\sqrt{L_{WL}}$), unless the vessel can surf external waves or use hydrofoils (Bejan et al., 2020).

The apparent wind phenomenon has direct implications for sail design: as boat speed increases, the apparent wind angle decreases, and the sails must be trimmed closer to the centreline. At the limit, the sail operates as an aerofoil generating lift rather than simply capturing drag (Bejan et al., 2020).

Huchet (2021) extended the sail propulsion analysis with two additional components that affect the total aerodynamic force budget:

Windage: The hull, rig, and crew above the waterline experience aerodynamic drag that opposes forward motion. This windage force is modelled as:

Equation 9.7 — Windage drag:

$$F_{\text{windage}} = \frac{1}{2}\,\rho_a\,V_{AW}^2\,A_{\text{ref}}\,C_{D,\text{windage}} \tag{8.36}$$

where A_{ref} is the projected frontal area of the hull, rig, and crew exposed to the apparent wind, and $C_{D,\text{windage}}$ is the windage drag coefficient (Huchet, 2021). Unlike the sail force, windage always opposes motion; it is a parasitic drag that reduces the net driving force available for propulsion.

Flat depowering: When the sail force exceeds the vessel's stability limit (i.e., when $HM > RM$), the crew must depower the sails. Huchet (2021) modelled this through a flat depowering parameter f_{flat} ($0 < f_{\text{flat}} \leq 1$), which reduces the effective sail lift:

$$C_{L,\text{eff}} = f_{\text{flat}} \cdot C_L$$

Setting $f_{\text{flat}} < 1$ reduces the driving force and, more importantly, the heeling moment, allowing the vessel to sail in conditions that would otherwise cause capsize. This parameter represents the physical actions of easing the mainsheet, twisting the sail, or reefing (Huchet, 2021).

Velocity Prediction Program (VPP): The overall methodology used by Huchet (2021) to predict NACRA 17 performance is a VPP: an iterative solver that finds the equilibrium boat speed and heel angle by simultaneously satisfying the force balance in the longitudinal direction ($F_x = R_{\text{total}} + F_{\text{windage}}$) and the moment balance in the transverse direction ($RM \geq HM$). The VPP approach is the standard tool for performance prediction of sailing vessels and provides the quantitative link between aerodynamic models (Chapter 8), resistance models (Chapter 5), and stability models (Chapter 4).

Flettner rotors exploit the Magnus effect to generate a propulsive force from wind. When a vertical cylinder of radius R is spun at angular velocity ω in a crossflow of velocity V_∞, the asymmetric velocity field produces a pressure difference that results in a net lift force perpendicular to the wind direction. In the potential-flow idealisation, the lift per unit span of the rotating cylinder is given by the Kutta–Joukowski theorem:

$$L' = \rho_a\,V_\infty\,\Gamma, \qquad \Gamma = 2\pi\,R^2\,\omega \tag{8.37}$$

where Γ is the circulation induced by the spinning surface, ρ_a is the air density, and L' is the lift per unit length (Carlton, 2012). In practice, viscous effects and three-dimensional end losses reduce the achievable lift below the ideal prediction, but the lift coefficients remain several times higher than those achievable by conventional sails or aerofoils, making Flettner rotors

attractive as wind-assisted propulsion devices for merchant vessels on routes with favourable beam or quartering winds (Carlton, 2012; Molland, 2008).

Oar propulsion is among the oldest forms of marine propulsion, yet the complex, unsteady hydrodynamics of a rowing oar blade were not systematically investigated until recently. Grift et al. (2021) presented the first time-resolved flow field measurements around a realistic rowing oar blade moving along a realistic path through water, obtained through particle image velocimetry (PIV) at the Delft University of Technology. The oar blade kinematics were captured during actual on-water rowing (a men's coxless four at standard pace) and then reproduced at 1:2 scale using a four-degree-of-freedom robot arm in a laboratory tank, enabling simultaneous PIV and force measurements.

The oar blade path results from the superposition of the boat's forward motion and the pivoting rotation of the oar. During the drive phase (from "catch" to "release"), the oar angle sweeps from $\theta \approx -50^\circ$ to $\theta \approx +30^\circ$, and the blade tip traces a looping path spanning approximately $1\,\mathrm{m}^2$, with a typical "slip" (the distance the blade travels against the boat's direction) of about one blade width (Grift et al., 2021). The resulting accelerations and decelerations reach up to $10\,\mathrm{m\,s^{-2}}$, producing Reynolds numbers $Re = \rho\, L_{\mathrm{ref}}\, V_{\mathrm{ref}}/\mu$ in the range $O(10^5)$–$O(10^6)$, where $L_{\mathrm{ref}} = \sqrt{l_a \cdot l_b}$ is derived from the blade width l_a and height l_b, and V_{ref} is the mean blade tip velocity during the drive (Grift et al., 2021).

The hydrodynamic force on the oar blade can be decomposed in two ways (Grift et al., 2021): (i) into a propulsive component F_x (in the direction of boat motion) and a non-propulsive component F_y (perpendicular), or (ii) into lift F_L and drag F_D relative to the blade's instantaneous direction of motion:

$$F_x = F_n \cos\theta - F_t \sin\theta, \qquad F_y = F_n \sin\theta + F_t \cos\theta, \tag{8.38}$$

$$F_L = F_n \cos\alpha - F_t \sin\alpha, \qquad F_D = F_n \sin\alpha + F_t \cos\alpha, \tag{8.39}$$

where F_n and F_t are the measured normal and tangential force components on the blade, θ is the oar angle, and α is the angle of attack (Grift et al., 2021).

The total propulsive impulse generated during a single drive is the time integral of the propulsive force: $J_x = \int_{t_{\mathrm{catch}}}^{t_{\mathrm{release}}} F_x(t)\,\mathrm{d}t$. Grift et al. (2021) defined two performance metrics. The *impulse efficiency* η_J quantifies the alignment of the generated impulse with the propulsive direction:

Equation 9.37 — Impulse efficiency of rowing propulsion:

$$\eta_J = \frac{J_x}{|\mathbf{J}|}, \qquad 0 < \eta_J \leq 1, \tag{8.40}$$

where $|\mathbf{J}|$ is the magnitude of the total impulse vector. An impulse efficiency of $\eta_J = 1$ indicates that all generated impulse is directed along the boat's direction of travel (Grift et al., 2021). The *energetic efficiency* η_E is the ratio of propulsive impulse to total energy (work) expended during the drive:

Equation 9.38 — Energetic efficiency of rowing propulsion:

$$\eta_E = \frac{J_x}{E}, \qquad E = \int_{t_{\text{catch}}}^{t_{\text{release}}} P(t)\,\mathrm{d}t, \tag{8.41}$$

where $P(t) = \mathbf{F}(t) \cdot \mathbf{V}(t) + M(t)\,\dot{\theta}(t)$ is the instantaneous power, including both translational and rotational contributions (Grift et al., 2021). This metric has dimensions of s m^{-1} (reciprocal velocity).

The PIV measurements revealed three distinct flow phases during the drive (Grift et al., 2021). (1) In the first phase ($t^* < 0.33$, where t^* is a dimensionless time normalised by the drive duration), a leading-edge vortex (LEV) forms at the blade tip and a vortex sheet develops at the trailing edge, generating lift that contributes to propulsion—analogous to LEV-based lift enhancement observed in insect and bird flight. (2) In the middle phase ($t^* \approx 0.60$), the blade moves approximately normal to its surface; drag dominates propulsion and is enhanced by the low-pressure zone of the trailing vortical structure (the evolved LEV). (3) Near the release ($t^* \approx 0.89$), the blade decelerates and a second large vortex forms, creating—together with the earlier LEV—a counter-rotating vortex pair that produces a jet-like structure whose orientation corresponds to the direction of the generated impulse. For the standard oar configuration, lift contributed 40% and drag 60% of the total propulsive impulse, independent of the velocity scaling factor κ (Grift et al., 2021).

A key practical finding was that the standard oar blade attachment ($\beta = 0°$, where β is the blade angle relative to the oar shaft) yields a suboptimal impulse efficiency of $\eta_J = 0.84$, meaning that 16% of the impulse is directed perpendicular to the boat's motion. By rotating the blade to $\beta = 15°$, the impulse efficiency increased to $\eta_J \approx 1.0$ (a 19% improvement) and the energetic efficiency increased by approximately 20% (Grift et al., 2021). The authors estimated that this blade angle change could increase on-water propulsion by 5–9.5%, a substantial margin in competitive rowing where finish-time differences are typically less than one second over a six-minute race. Importantly, the force measurements scaled with $V_{\text{ref}}^2 \sim \kappa^2$ and the general flow pattern was independent of velocity scaling for $\kappa \geq 0.50$ (corresponding to $Re \geq 0.82 \times 10^5$), confirming Reynolds-independent scaling in the turbulent regime (Grift et al., 2021).

Wave energy conversion represents an alternative approach to marine energy: rather than propelling a vessel, a Wave Energy Converter (WEC) extracts power from the ocean wave field for electricity generation at offshore or island sites. Pozzi et al. (2018) describe the Pendulum Wave Energy Converter (PeWEC), a floating device in which a pendulum enclosed within a sealed hull oscillates in response to the hull's wave-induced pitch motion. The relative rotation of the pendulum drives an electrical generator acting as a Power Take Off (PTO). The PTO torque is modelled as a linear damper with coefficient c, and the coupled dynamics of the hull (surge, heave, pitch) and

the internal pendulum are formulated via the Lagrangian of the system (Pozzi et al., 2018).

A key design principle for WECs is *resonance tuning*: maximum power extraction occurs when the undamped natural frequency of the device matches the dominant frequency of the incoming wave (Pozzi et al., 2018). For the PeWEC prototype ($L = 3\,\text{m}$, $R = 1.5\,\text{m}$, $m_b = 3176\,\text{kg}$, $m_p = 410\,\text{kg}$), the design wave period was $2.2\,\text{s}$, corresponding to the most energetic sea state at the Pantelleria Island site in the Mediterranean Sea (Pozzi et al., 2018). The coupling between the hull and the internal pendulum introduces two resonance peaks, broadening the band of wave periods over which efficient energy extraction is possible.

The overall efficiency of a WEC is quantified by the *Relative Capture Width* (RCW):

Equation 9.36 — Relative Capture Width:

$$\text{RCW} = \frac{\bar{P}_e}{P_w \cdot W} \tag{8.42}$$

where $\bar{P}_e$ is the time-averaged extracted power, P_w is the wave power density (power per unit crest width, in W m^{-1}), and W is the device width (Pozzi et al., 2018). Experimental tank testing of a 1:12 scale PeWEC prototype at the INSEAN wave basin achieved RCW $\approx 50\%$ in regular waves and RCW $\approx 47\%$ in irregular waves representative of the Pantelleria site (Pozzi et al., 2018). The PTO damping coefficient governs the power extraction: at the design wave period, increasing the PTO damping coefficient from $40\,\text{N m s rad}^{-1}$ to $600\,\text{N m s rad}^{-1}$ monotonically increased the extracted power (Pozzi et al., 2018).

The hydrodynamic model of the floating hull is based on Cummins' time-domain equation (Equation 6.23), with the convolution integral representing the radiation memory effect. Pozzi et al. (2018) found that a nonlinear viscous damping correction of the form $F_{\text{vis}} = \beta\,\dot{\delta}\,|\dot{\delta}|$ (where β is an empirical coefficient identified from experimental data) was necessary to achieve acceptable agreement between numerical and experimental results near the pitch resonance period. This quadratic damping supplements the linear potential-flow radiation damping, which underestimates energy dissipation at large motion amplitudes (Pozzi et al., 2018). With this correction, the average relative error between model and experiment was within 12% for all primary physical quantities (Pozzi et al., 2018).

Water jet propulsion generates thrust by accelerating a stream of water through a nozzle. Molland (2008) describe the operating principle: water is drawn in through an inlet in the hull bottom, accelerated by an impeller (axial or mixed-flow pump), and expelled through a nozzle at the stern. The thrust is governed by the momentum equation:

Equation 9.34 — Water jet thrust:

$$T = \dot{m}\,(V_j - V_s) \tag{8.43}$$

where $\dot{m}$ is the mass flow rate, V_j is the jet exit velocity, and V_s is the ship speed (Molland, 2008). The jet velocity ratio V_j/V_s determines the propulsive efficiency: higher ratios produce more thrust but lower efficiency, following the same momentum theory trade-off as for conventional propellers (Molland, 2008). Water jets are preferred for high-speed craft ($V > 15.4\,\mathrm{m\,s^{-1}}$, approximately $30\,\mathrm{kn}$) where conventional propellers suffer cavitation, and for vessels operating in shallow water where propeller immersion is insufficient (Molland, 2008).

The Voith–Schneider propeller (VSP) is a cycloidal propulsion system in which vertical blades protrude below the hull and rotate about a vertical axis while simultaneously oscillating about their own axes. Molland (2008) explain that this kinematics produces a thrust vector that can be directed through 360° by adjusting the blade oscillation phase, providing combined propulsion and steering without a rudder. The VSP is used primarily on tugs, ferries, and mine countermeasures vessels where high manoeuvrability at low speed is essential (Molland, 2008).

8.3.5 Propulsive Efficiency and Energy Saving Devices

The overall propulsive efficiency from engine to hull is decomposed as (cf. Equation 8.29) (Rawson & Tupper, 2001):

Equation 9.35 — Overall propulsive efficiency:

$$\eta_D = \eta_H \times \eta_O \times \eta_R \times \eta_S \tag{8.44}$$

where $\eta_H = (1-t)/(1-w)$ is the hull efficiency (Equation 8.28), η_O is the propeller open-water efficiency, η_R is the relative rotative efficiency (the ratio of propeller efficiency behind the hull to that in open water), and η_S is the shaft transmission efficiency (≈ 0.97–0.99) (Rawson & Tupper, 2001).

Typical values for a single-screw merchant vessel are: $\eta_H \approx 1.0$–1.2, $\eta_O \approx 0.55$–0.70, $\eta_R \approx 1.0$–1.05, giving $\eta_D \approx 0.55$–0.75 (Rawson & Tupper, 2001). Energy saving devices—pre-swirl stators, post-swirl fins, boss cap fins, and wake equalising ducts—improve η_D by modifying the wake field or recovering rotational energy from the propeller slipstream, typically providing 3–8% fuel savings under favourable conditions (Molland, 2008).

8.4 Discussion

The sail propulsion analysis of Bejan et al. (2020) demonstrates that the fundamental physics of propulsion—momentum transfer, force balance, and structural constraints—applies universally across all propulsion technologies. The key parameters that govern performance are the ratio of propulsive force to resistance force, the structural capacity of the propulsion system, and the density ratio of the working fluids.

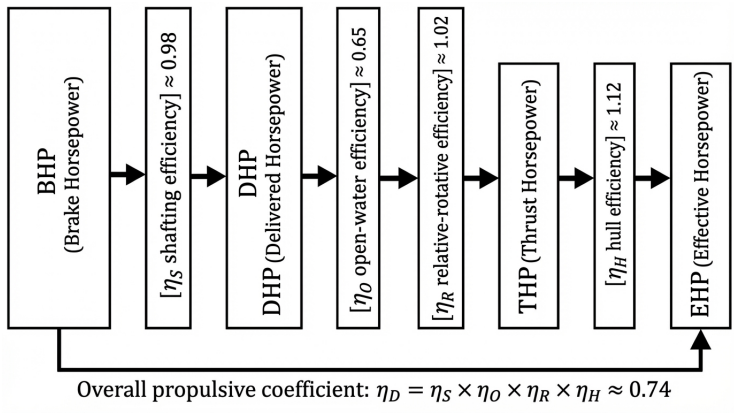

Figure 8.4: Propulsive coefficient breakdown showing the sequential energy conversion stages from engine brake horsepower (BHP) to effective horsepower (EHP). The overall propulsive efficiency $\eta_D = \eta_S \times \eta_O \times \eta_R \times \eta_H \approx 0.74$ represents the fraction of prime-mover power converted to useful thrust power (Equation 8.44).

The historical evolution of sailing vessels (from single-mast Egyptian galleys to multi-mast Napoleonic ships and back to single-mast modern racers) shows that internal complexity changes while the fundamental external proportions—which are dictated by propulsion physics—remain constant (Bejan et al., 2020).

The detailed sail force model of Huchet (2021) complements the scaling analysis of Bejan et al. (2020) by providing the force-resolution framework needed for quantitative performance prediction. The decomposition of the aero force into driving force ($F_x = L\sin\beta_{AW} - D\cos\beta_{AW}$) and side force ($F_y = L\cos\beta_{AW} + D\sin\beta_{AW}$) establishes the direct link between sail aerodynamics and vessel dynamics: F_x determines speed while F_y determines heel and leeway.

The wind triangle formulation shows that at small apparent wind angles (close-hauled sailing), the driving force is dominated by the lift component $L\sin\beta_{AW}$, confirming that efficient upwind sailing requires the sail to function as a lifting aerofoil—not a drag device. This is the quantitative basis for the observation by Bejan et al. (2020) that the sails are pulled to the centreline at high speeds.

The windage model and flat depowering parameter (Huchet, 2021) introduce the practical constraints that limit the idealised performance predicted by scaling theory. Windage is an ever-present parasitic loss that grows with boat speed (via the apparent wind), while depowering represents the necessary sacrifice of propulsive force to maintain stability. Together, they define the operational envelope of a sailing vessel.

The propulsive coefficient framework of Attwood (1899) (Equation 8.29) provides a systematic decomposition of the power losses in a ship propulsion

system. Of the total indicated power, a fraction e_m reaches the propeller shaft; of this, a fraction e_p is converted to useful propeller work; and the hull efficiency $(1-t)/(1-w)$ accounts for the interaction between propeller and hull. Froude's *Greyhound* experiments demonstrated that in the best case only 42% of the engine power was usefully employed, and even modern vessels with fine lines achieve only approximately 50% propulsive efficiency (Attwood, 1899). This energy audit—from engine cylinder, through shaft, to propeller, to hull—remains the basis of all propulsive efficiency analyses.

The rowing propulsion study of Grift et al. (2021) extends the propulsion analysis into the domain of unsteady, human-powered hydrodynamics. While the momentum theory for propellers assumes a steady or quasi-steady flow, the oar blade operates in a fundamentally unsteady regime: the blade accelerates rapidly after the catch, sweeps through a complex curved path, and decelerates before the release. The identification by Grift et al. (2021) that leading-edge vortices—a mechanism well characterised in insect and bird flight—contribute 40% of the propulsive impulse in rowing demonstrates that unsteady lift generation is not confined to biological locomotion but also governs human-powered marine propulsion. The impulse efficiency η_J (Equation 8.40) and energetic efficiency η_E (Equation 8.41) provide complementary metrics to the propulsive coefficient η_D (Equation 8.44): η_J captures the directional quality of momentum transfer, while η_E captures the cost per unit propulsion. The finding that a 15° blade angle increases η_J from 0.84 to 1.0 illustrates that even for a propulsion mode as ancient as rowing, physics-based optimisation can yield substantial performance improvements.

The wake fraction and thrust deduction (Equations 8.26–8.27) establish a key design trade-off: a single-screw arrangement benefits from a larger wake (higher w, hence lower approach velocity and higher apparent propeller loading) but suffers greater thrust deduction (higher t) than a twin-screw arrangement. When $(1-t)/(1-w) \approx 1$, the two effects approximately cancel, and the hull efficiency is near unity (Attwood, 1899). The numerical examples from Ridley and Patterson (2014) confirm this trade-off quantitatively: $\eta_H = 1.14$ for a single-screw vessel (where the large wake fraction outweighs the thrust deduction) versus $\eta_H = 0.98$ for a twin-screw vessel, demonstrating that the net benefit of the hull–propeller interaction is configuration-dependent.

The Wageningen B-series design chart methodology provides a systematic, iterative approach to propeller selection. Birk (2019) demonstrates the complete design process through a worked example for a container vessel. The procedure begins by computing the shortened thrust loading coefficient $C_S = K_T/J^2 = T_{\text{req}}/(\rho\, v_A^2\, D^2)$ from the service-condition resistance (with appropriate margin), the thrust deduction factor, and the wake-corrected advance speed (Birk, 2019).

The Bu_2-chart is entered with $\sqrt[4]{C_S}$, and the optimum open-water self-propulsion point is read off at the intersection with the $\eta_{O,\text{opt}}$ curve. However, Birk (2019) notes that the optimum propeller for the behind-hull condition,

where the inflow is non-uniform due to the wake, typically operates at a slightly higher advance coefficient. A reduction of 1–5% in $1/J$ is applied (3% being typical for vessels with normal hull lines), which shifts the operating point above the optimum line and requires a corresponding increase in pitch–diameter ratio to restore the required thrust. The resulting loss in open-water efficiency is small but serves as a safety margin against further efficiency degradation due to hull fouling during service (Birk, 2019).

After the initial design, the Burrill cavitation check (Equations 8.31–8.33) determines whether the blade area is sufficient. If not, the design is repeated with a higher A_E/A_0 chart. This iterative process—chart selection, optimisation, cavitation check, area adjustment—converges within two to three iterations to a final propeller specification (diameter, pitch ratio, blade area ratio, and rotational speed) that balances efficiency against cavitation risk (Birk, 2019).

The analysis of propeller-induced vibration and noise (Section 8.2.10) reveals that propeller design must satisfy not only efficiency and cavitation criteria but also vibration constraints. The blade-rate frequency $f_z = z \cdot n$ (Equation 8.34) determines the fundamental excitation frequency, while the hull surface pressure coefficient K_p (Equation 8.35) quantifies the pressure fluctuation transmitted to the hull. Boundary element and RANS methods, as demonstrated in the RINA CFD 2003 proceedings (*CFD 2003: Computational Fluid Dynamics Technology in Ship Hydrodynamics*, 2003), provide the computational tools to predict unsteady blade loading and cavitation-induced pressure pulses—information that is essential for meeting vibration comfort and underwater noise standards.

The RANS formulation introduced by Pêgo (2007) provides the viscous-flow complement to the potential-flow BEM analysis of Guedes Soares and Santos (2015). While the BEM captures inviscid blade loading and tip vortex roll-up, it cannot model the turbulent wake that governs downstream interactions—particularly the swirl recovery that makes contra-rotating propellers superior to co-rotating arrangements. The RANS momentum equation (Equation 8.6) and its closure through Reynolds stress transport models (rather than the Boussinesq eddy-viscosity approximation of Equation 8.7) are essential for predicting the anisotropic turbulence state observed in propeller wakes, where the flow lies near the axisymmetric limit of the Lumley–Newman invariant map (Pêgo, 2007). The experimental finding that contra-rotating pod drives achieve approximately 8% higher system efficiency than co-rotating configurations—confirmed by LDA-measured reductions in residual swirl at $x/D_1 = 1$, 5, and 10 downstream—quantifies the energy recovery mechanism that underpins modern pod drive design (Pêgo, 2007).

The wave energy conversion results of Pozzi et al. (2018) demonstrate that the same hydrodynamic principles governing ship motions (Chapter 6)—added mass, radiation damping, and Cummins' convolution formulation—also govern the energy extraction capability of floating WECs. The resonance

tuning principle—matching the device's natural frequency to the dominant wave frequency—is the direct analogue of the seakeeping problem in which resonance amplifies motion (and thus must often be avoided for ships but deliberately exploited for energy converters). The Relative Capture Width (Equation 8.42) provides a physics-based efficiency metric analogous to the propulsive efficiency η_D (Equation 8.44): both quantify the fraction of available energy that is usefully converted. The necessity of nonlinear viscous damping corrections near resonance confirms a general finding in marine hydrodynamics: linear potential-flow theory underestimates energy dissipation at large motion amplitudes, regardless of whether the objective is motion prediction or power extraction (Pozzi et al., 2018).

The edited volume of Sutulo and Guedes Soares (2023) extends the propeller design toolkit in three directions. First, systematic parametric studies of propeller cup geometry—a small curvature applied to the trailing edge of each blade—demonstrate that cup increases the effective pitch locally at the blade tip, shifting the open-water efficiency curve and expanding the cavitation-free operating envelope without increasing blade area. Second, a coupled RANS–BEM investigation of hub vortex cavitation shows that the concentrated root vortex can sustain a continuous tubular cavity downstream of the propeller hub, an inception mechanism not captured by the blade-section Burrill criterion (Equation 8.31). Third, a shaft-line vibration study couples the torsional dynamics of the propulsion shafting with the hydrodynamic torque fluctuations at blade-rate frequency (Equation 8.34), revealing that shaft whirl resonances can amplify hull vibration beyond the levels predicted by the propeller pressure-coefficient analysis alone (Sutulo & Guedes Soares, 2023).

The engineering course notes of United States Naval Academy (2021) complement the theoretical propulsive-coefficient derivation (Equation 8.44) with a practical pedagogical framework. The USNA treatment traces each watt of engine brake power through the shaft transmission ($\eta_S \approx 0.97$–0.99), open-water propeller (η_O), relative rotative (η_R), and hull interaction (η_H) stages, reinforcing Froude's observation that over half of the prime-mover energy is dissipated before useful thrust is produced. Laboratory exercises on model propeller testing and propulsive-coefficient measurement provide students with hands-on experience of the behind-hull correction factors (w, t, η_R) that distinguish open-water from self-propulsion performance (United States Naval Academy, 2021).

8.5 Conclusion

All forms of marine propulsion rest on a single principle: thrust requires momentum transfer to a working fluid. For sails, the aerodynamic force scales with sail area and the square of wind speed (Equation 8.1), and the optimal mast-height-to-hull-length ratio $H/L \sim (V_w/V_a)^{1/2}$ couples propulsive

sizing to vessel geometry (Bejan et al., 2020). The wind-triangle formulation (Equation 8.17) and the resolution of sail force into driving and side components (Equations 8.18–8.19) establish the quantitative link between aerodynamics, speed, and heel (Huchet, 2021). These same momentum-transfer fundamentals extend to mechanical propulsors, where torque $\tau = rF \sin\theta$ and rotational power $P = \tau\omega$ (Equations 8.2–8.3) connect engine output to hydrodynamic loading (Campbell, 2025).

The actuator-disk momentum theory (Equations 8.10–8.16) yields the classical ideal efficiency $\eta_{TJ} = 2/(1 + \sqrt{1 + C_{Th}})$, demonstrating that larger, lightly loaded propellers are inherently more efficient (Birk, 2019). Blade element momentum theory refines this by accounting for the radial load distribution, while the Wageningen B-series charts, Keller's expanded-area formula (Equation 8.4), and Burrill's cavitation criterion (Equations 8.31–8.32) provide a systematic iterative design methodology. Behind the hull, the wake fraction reduces the advance speed to $V_a = (1 - w)V$ (Equation 8.26) and the thrust deduction absorbs part of the propeller output as $R = T(1 - t)$ (Equation 8.27); the resulting hull efficiency $\eta_H = (1 - t)/(1 - w)$ is configuration-dependent, with typical values of 1.14 for single-screw and 0.98 for twin-screw arrangements (Attwood, 1899; Ridley & Patterson, 2014). The full propulsive-coefficient chain $\eta_D = \eta_H \times \eta_O \times \eta_R \times \eta_S$ (Equation 8.44) confirms that over half of prime-mover energy is dissipated before producing useful thrust—a finding first quantified by Froude's *Greyhound* experiments at 42% (Attwood, 1899; United States Naval Academy, 2021).

Propeller-induced vibration at blade-rate frequency $f_z = z \cdot n$ (Equation 8.34) and the associated hull-surface pressure fluctuations characterised by K_p (Equation 8.35) impose additional design constraints beyond efficiency and cavitation (*CFD 2003: Computational Fluid Dynamics Technology in Ship Hydrodynamics*, 2003). Cavitation amplifies these pressure pulses by an order of magnitude, which confirms the need for the Burrill check for vibration and noise control as well as blade integrity (Birk, 2019; *CFD 2003: Computational Fluid Dynamics Technology in Ship Hydrodynamics*, 2003). At the computational level, the RANS formulation (Equations 8.5–8.7) reveals that propeller wakes are highly anisotropic, lying near the axisymmetric limit on the Lumley–Newman invariant map; full Reynolds stress transport models (SSG or AIRSM) are therefore required in place of isotropic eddy-viscosity closures (Pêgo, 2007). This viscous-flow framework confirms that contra-rotating pod drives recover tangential wake momentum, achieving approximately 8% higher system efficiency than co-rotating configurations (Pêgo, 2007). Advanced topics—propeller cup geometry, hub-vortex cavitation inception, and shaft-line torsional dynamics—extend the design toolkit beyond classical blade-section analysis (Sutulo & Guedes Soares, 2023).

Alternative propulsion modes obey the same physics. In rowing, the oar blade generates thrust through unsteady lift (40%) and drag (60%), with leading-edge vortices enhancing lift analogously to insect flight; optimising the blade attachment angle from $\beta = 0°$ to $15°$ raises the impulse efficiency η_J

(Equation 8.40) from 0.84 to 1.0 (Grift et al., 2021). Wave energy converters exploit resonance tuning to maximise power extraction, achieving Relative Capture Widths of approximately 47–50% in Mediterranean sea states (Equation 8.42) (Pozzi et al., 2018). Whether the propulsor is a sail, a screw, an oar, or a pendulum oscillator, the governing framework remains consistent: the balance between momentum flux, resistance, and structural constraints determines the achievable efficiency envelope.

References

Attwood, E. L. (1899). *A text-book of theoretical naval architecture*. Longmans, Green; Co.

Bejan, A., Ferber, L., & Lorente, S. (2020). Convergent evolution of boats with sails. *Scientific Reports*, *10*, Article 2703. https://doi.org/10.1038/s41598-020-58940-5

Birk, L. (2019). *Fundamentals of ship hydrodynamics: Fluid mechanics, ship resistance and propulsion*. John Wiley & Sons. https://doi.org/10.1002/9781119191575

Campbell, C. (2025). *Physics: A focused introduction*. CRC Press. https://doi.org/10.1201/9781003571568

Carlton, J. (2012). *Marine propellers and propulsion* (3rd ed.). Butterworth-Heinemann. https://doi.org/10.1016/C2010-0-68327-1

CFD 2003: Computational Fluid Dynamics Technology in Ship Hydrodynamics. (2003). The Royal Institution of Naval Architects.

Fischer-Cripps, A. C. (2014). *The physics companion* (2nd ed.). CRC Press. https://doi.org/10.1201/b17356

Grift, E. J., Tummers, M. J., & Westerweel, J. (2021). Hydrodynamics of rowing propulsion. *Journal of Fluid Mechanics*, *918*, A29. https://doi.org/10.1017/jfm.2021.318

Guedes Soares, C., & Santos, T. A. (Eds.). (2015). *Maritime technology and engineering: Proceedings of MARTECH 2014*. CRC Press.

Harrington, R. L. (Ed.). (1992). *Marine engineering*. The Society of Naval Architects; Marine Engineers.

Huchet, L. (2021). *Investigation of the influence of crew setup on performances for the Olympic NACRA 17 foiling catamaran* [Individual project]. University of Southampton.

Molland, A. F. (Ed.). (2008). *The maritime engineering reference book: A guide to ship design, construction and operation*. Butterworth-Heinemann. https://doi.org/10.1016/B978-0-7506-8987-8.X0001-7

Newman, J. N. (1977). *Marine hydrodynamics*. The MIT Press.

Pêgo, J. P. G. M. (2007). *Advanced fluid mechanics studies of ship propulsion systems* [Doctoral dissertation, Friedrich-Alexander-Universität Erlangen-Nürnberg].

Pozzi, N., Bracco, G., Passione, B., Sirigu, S. A., & Mattiazzo, G. (2018). PeWEC: Experimental validation of wave to PTO numerical model. *Ocean Engineering*, *167*, 114–129. https://doi.org/10.1016/j.oceaneng.2018.08.028

Rawson, K. J., & Tupper, E. C. (2001). *Basic ship theory* (5th ed.). Butterworth-Heinemann.

Ridley, J. D., & Patterson, C. J. (2014). *Ship stability, powering and resistance* (Vol. 13). Adlard Coles Nautical.

Sutulo, S., & Guedes Soares, C. (2023). Ship dynamics and hydrodynamics. *Journal of Marine Science and Engineering*, *11*(5), 911. https://doi.org/10.3390/jmse11050911

United States Naval Academy. (2021). En400: Principles of ship performance [Course notes, Fall AY2021].

List of Abbreviations

Abbreviation	Definition
AWA	Apparent Wind Angle
AWS	Apparent Wind Speed
BEM	Boundary Element Method
BHP	Brake Horsepower
BOG	Boil-Off Gas
BSFC	Brake Specific Fuel Consumption
CFD	Computational Fluid Dynamics
CII	Carbon Intensity Indicator
CODAG	Combined Diesel and Gas
CODEG	Combined Diesel-Electric and Gas-Electric
CODLAG	Combined Diesel-Electric and Gas
COP	Coefficient of Performance
CPP	Controllable Pitch Propeller
DHP	Delivered Horsepower
DOF	Degrees of Freedom
DTMB	David Taylor Model Basin
DWT	Deadweight Tonnage
EEDI	Energy Efficiency Design Index
EEXI	Energy Efficiency Existing Ship Index
EGR	Exhaust Gas Recirculation
EHP	Effective Horsepower
EOS-80	UNESCO International Equation of State of Seawater (1980)
FEM	Finite Element Method
FNPF	Fully Nonlinear Potential Flow
FWA	Fresh Water Allowance
GNSS	Global Navigation Satellite System
HVAC	Heating, Ventilation, and Air Conditioning
IMO	International Maritime Organization
ITTC	International Towing Tank Conference
ITTC-57	ITTC 1957 Model–Ship Correlation Line

Abbreviation	Definition
KCS	KRISO Containership
KRISO	Korea Research Institute of Ships and Ocean Engineering
KVLCC2	KRISO Very Large Crude Carrier 2
LCG	Longitudinal Centre of Gravity
LNG	Liquefied Natural Gas
MCT1cm	Moment to Change Trim One Centimetre
MEP	Mean Effective Pressure
NOP	Natural Oscillatory Period
NWT	Numerical Wave Tank
ORC	Organic Rankine Cycle; also Offshore Racing Congress
PeWEC	Pendulum Wave Energy Converter
PTO	Power Take-Off
RANS	Reynolds-Averaged Navier–Stokes
RAO	Response Amplitude Operator
RCW	Relative Capture Width
SCR	Selective Catalytic Reduction
SGISC	Second Generation Intact Stability Criteria
SHM	Simple Harmonic Motion
SHP	Shaft Horsepower
SMOW	Standard Mean Ocean Water
SNAME	Society of Naval Architects and Marine Engineers
SOFAR	Sound Fixing and Ranging
SOLAS	Safety of Life at Sea
SSA	Single Significant Amplitude
TEOS-10	Thermodynamic Equation of Seawater (2010)
THP	Thrust Horsepower
TPC	Tonnes Per Centimetre Immersion
URANS	Unsteady Reynolds-Averaged Navier–Stokes
USNA	United States Naval Academy
V&V	Verification and Validation
VBM	Vertical Bending Moment
VIT	Variable Injection Timing
VOF	Volume of Fluid
VPP	Velocity Prediction Program
VSF	Vertical Shearing Force
WEC	Wave Energy Converter

Glossary

Added mass
Effective inertia of surrounding fluid that must be accelerated together with a floating body; enters the equations of motion as a frequency-dependent virtual increase in the body's mass matrix.

Admiralty coefficient
Empirical index $C_A = \Delta^{2/3} V^3 / P_s$ relating displacement, speed, and shaft power; used for rapid power estimation in preliminary ship design.

Advance coefficient (J)
Dimensionless ratio of propeller advance speed to tip speed: $J = V_a/(nD)$; the primary independent variable in open-water propeller performance charts.

Angle of loll
Equilibrium heel angle at which an initially unstable vessel ($\mathrm{GM} < 0$) finds a new balance due to second-order righting-moment recovery; $\phi_{\text{loll}} = \sqrt{-2\,\mathrm{GM}/\mathrm{BM}}$ for a wall-sided hull.

Apparent wind
Vector sum of the true wind velocity and the vessel's own velocity; the wind actually experienced on board, governing sail forces and aerodynamic loading.

Archimedes' principle
The buoyant force on a submerged or floating body equals the weight of the fluid it displaces.

Bernoulli's equation
Energy conservation along a streamline in steady, inviscid, incompressible flow: $p + \tfrac{1}{2}\rho v^2 + \rho g z = \text{const}$.

Bilge keel
Flat-plate longitudinal fin fitted at the turn of the bilge to increase roll damping through enhanced vortex shedding.

Blade element theory
Method of computing propeller thrust and torque by treating each radial blade section as a two-dimensional aerofoil in local flow and integrating the sectional forces over the span.

Block coefficient (C_B)
Ratio of the hull's displaced volume to the product of waterline length, beam, and draught: $C_B = \nabla / (L \times B \times T)$; a primary measure of hull fullness.

Bonjean curve
Plot of immersed cross-sectional area versus draught at each transverse station along the hull; enables displacement and centre-of-buoyancy calculations for any waterline.

Boundary layer
Thin region adjacent to the hull surface in which the flow velocity rises from zero at the wall to the free-stream value; its thickness and state (laminar or turbulent) govern frictional resistance.

Brayton cycle
Open gas-turbine thermodynamic cycle consisting of isentropic compression, constant-pressure heat addition, and isentropic expansion; used in naval and fast-ferry propulsion.

Broaching
Loss of directional control in following or quartering seas when wave-induced yaw moments overcome rudder authority, potentially leading to capsize.

Buoyancy
Upward force exerted on a body by the surrounding fluid, equal to the weight of fluid displaced by the body.

Carnot efficiency
Maximum thermodynamic efficiency attainable between two temperature reservoirs: $\eta_{\text{Carnot}} = 1 - T_C / T_H$; an upper bound for all heat engines.

Cavitation
Formation and collapse of vapour-filled cavities on propeller blade surfaces when the local pressure falls below the vapour pressure of seawater.

Centre of buoyancy (B)
Geometric centroid of the underwater hull volume; the point through which the resultant buoyant force acts.

Centre of gravity (G)
Point through which the total weight of the vessel acts; its vertical position relative to the metacentre determines initial stability.

Coefficients of form
Set of dimensionless shape ratios—block (C_B), midship (C_M), prismatic (C_P), and waterplane (C_W)—that characterise hull geometry relative to idealised prismatic shapes.

Cross curves of stability
Family of curves giving the lever KN as a function of displacement at fixed heel angles; they separate hull geometry from the loading condition and enable rapid GZ computation for any KG.

Damping
Energy dissipation opposing oscillatory motion; in ship dynamics it comprises radiation damping (energy lost to radiated waves) and viscous damping (vortex shedding, skin friction, eddy making).

Dead ship condition
Stability failure mode in which the vessel drifts beam-on to wind and waves without propulsion or steering; one of the five Second Generation Intact Stability failure modes.

Design spiral
Iterative ship design process in which hull form, resistance, propulsion, stability, and structural analysis are refined through successive loops of increasing precision.

Diesel cycle
Compression-ignition thermodynamic cycle with constant-pressure combustion; the predominant power cycle in marine propulsion, achieving thermal efficiencies exceeding 50%.

Diffraction force
Component of wave excitation arising from the scattering of incident waves by the hull; supplements the Froude–Krylov force to give the total wave-exciting force.

Displacement
Total weight of water displaced by the hull, equal to the vessel's weight at static equilibrium; equivalently, $\Delta = \rho\, g\, \nabla$.

Drift angle
Angle between the ship's centreline and its velocity vector during a turn or under lateral environmental forces.

Dynamical stability
Work required to heel the vessel from one angle to another; proportional to the area under the GZ curve between those angles.

Encounter frequency
Frequency at which a moving vessel meets successive wave crests: $\omega_e = \omega - (\omega^2\, V \cos\beta)/g$, where β is the heading angle relative to the waves.

Exergy
Maximum useful work extractable from a thermodynamic flow stream relative to the dead-state environment: $E_{\text{flow}} = (h - h_0) - T_0(s - s_0)$.

Flettner rotor
Spinning vertical cylinder that generates aerodynamic lift via the Magnus effect; used as a wind-assisted propulsion device.

Form factor ($1 + k$)
Multiplier applied to the flat-plate friction coefficient to account for three-dimensional viscous-pressure (form) drag on the actual hull shape.

Free surface effect
Reduction of effective metacentric height caused by the lateral shift of liquid in partially filled tanks during heel; the correction $GG_1 = i/\nabla$ depends on tank geometry, not liquid quantity.

Freeboard
Vertical distance from the waterline to the main deck edge; determines the reserve buoyancy available before the deck becomes immersed.

Fresh water allowance
Additional sinkage when a vessel moves from salt water to fresh water; FWA $\approx W/(4 \times \text{TPC}_{sw})$ in millimetres.

Frictional resistance
Component of hull resistance arising from viscous shear stress along the wetted surface; proportional to wetted area, dynamic pressure, and the skin-friction coefficient.

Froude number (Fn)
Dimensionless ratio $V/\sqrt{gL}$ of inertial to gravitational forces; governs the scaling of wave-making resistance between model and full scale.

Froude–Krylov force
Component of wave excitation computed from the undisturbed incident-wave pressure field acting on the hull surface; assumes the hull does not scatter the wave.

Froude's law of comparison
Principle that geometrically similar hulls at the same Froude number produce identical non-dimensional wave resistance; the foundation of towing-tank methodology.

GZ curve
Plot of righting lever versus heel angle; the primary tool for assessing transverse stability, yielding initial slope ($\approx$ GM), peak righting lever, and vanishing angle.

Hull efficiency (η_H)
Ratio $(1-t)/(1-w)$; accounts for the combined effect of wake fraction and thrust deduction on propulsive performance; often exceeds unity for well-designed single-screw vessels.

Hull speed
Critical speed at which the bow and stern wave systems constructively interfere, producing a steep rise in wave-making resistance; approximately $V_c \approx 1.25\sqrt{L}$ (knots, L in feet) or Fn ≈ 0.4.

Hydrostatic pressure
Pressure due to the weight of overlying fluid: $p = p_0 + \rho\, g\, z$ for constant density; the fundamental loading in ship hydrostatics.

ITTC-57 friction line
Standard empirical formula $C_f = 0.075/(\log_{10}\mathrm{Re} - 2)^2$ used to compute the flat-plate frictional resistance and to extrapolate model-test data to ship scale.

Keel (K)
Longitudinal structural backbone at the bottom of the hull; the reference baseline from which vertical stability measurements (KB, KG, KM) are taken.

Lewis form
Conformal-mapping representation of ship cross-sections that enables closed-form computation of sectional added mass and radiation damping for strip-theory seakeeping analysis.

Load line (Plimsoll mark)
Markings on the hull amidships indicating the maximum permissible draught in various water density and seasonal conditions (TF, F, T, S, W, WNA).

Magnus effect
Lateral force generated when a rotating cylinder moves through a fluid; the physical basis of Flettner-rotor wind-assisted propulsion.

Metacentre (M)
Point at which the line of action of the buoyant force intersects the vessel's centreline during a small heel; its position above G determines initial stability.

Metacentric height (GM)
Vertical distance from the centre of gravity to the metacentre: $\mathrm{GM} = KB + BM - KG$; the primary measure of initial transverse stability.

Metacentric radius (BM)
Distance from the centre of buoyancy to the metacentre: $BM = I_T / \nabla$, where I_T is the second moment of the waterplane area about its centreline.

Midship coefficient (C_M)
Ratio of the immersed midship section area to its circumscribing rectangle $B \times T$; indicates fullness of the midship section.

Moment to change trim one centimetre
Longitudinal couple required to alter the total trim by one centimetre: $\mathrm{MCT1cm} = W \times \mathrm{GM}_L / (100\,L)$.

Navier–Stokes equations
Fundamental equations governing viscous fluid motion; combine conservation of mass, momentum, and energy with a constitutive relation for the viscous stress tensor.

Natural roll period
Period of free roll oscillation in still water: $T_\phi = 2\pi\, k_{xx} / \sqrt{g\,\mathrm{GM}}$; a short period indicates a stiff ship with large GM.

Open-water efficiency (η_O)
Propeller efficiency measured in uniform inflow without hull interaction: ratio of thrust power ($T \times V_a$) to shaft power ($2\pi\, n\, Q$).

Parametric roll
Dynamic instability in which periodic variation of the waterplane area (and thus GM) in head or following seas excites large roll amplitudes; the principal resonance condition is $\omega_E \approx 2\omega_0$.

Permeability
Fraction of a flooded compartment volume actually occupied by water, accounting for structure, machinery, and cargo; used in damage stability calculations.

Potential temperature
In-situ temperature corrected for adiabatic compression; obtained by removing the pressure-dependent warming (≈ 0.11 K per 1000 m depth), enabling meaningful comparison of water masses at different depths.

Prismatic coefficient (C_P)
Ratio of displaced volume to the product of midship section area and waterline length; indicates how volume is distributed longitudinally along the hull.

Propulsive coefficient (η_D)
Overall efficiency from engine brake power to effective thrust power, combining shafting, open-water, relative-rotative, and hull efficiencies: typically 0.55–0.70 for merchant vessels.

Residuary resistance
Difference between total resistance and frictional resistance; dominated by wave-making at moderate-to-high Froude numbers and scaled from model to ship via Froude's law.

Resistance decomposition
Partition of total resistance into frictional and residuary (primarily wave-making) components: $C_T = (1+k)\,C_F + C_W$; the foundation of the model-to-ship extrapolation method.

Reynolds number (Re)
Dimensionless ratio VL/ν of inertial to viscous forces; determines whether the boundary layer is laminar or turbulent and governs frictional resistance.

Righting lever (GZ)
Horizontal distance between the lines of action of weight and buoyancy when the vessel is heeled; the moment arm that generates the restoring couple.

Righting moment
Restoring couple tending to return a heeled vessel to the upright: $M_R = W \times \mathrm{GZ}$.

Roll damping
Energy dissipation opposing roll motion; comprises wave-radiation, bilge-keel vortex-shedding, hull skin-friction, eddy-making, and lift components.

Scribanti's formula
Wall-sided approximation for the righting lever at large angles: $\mathrm{GZ} = \sin\phi\,[\mathrm{GM} + \tfrac{1}{2}\,\mathrm{BM}\,\tan^2\phi]$.

Seakeeping
A vessel's ability to operate safely and effectively in a seaway; quantified by motion amplitudes, accelerations, slamming, deck wetness, and added resistance in waves.

Significant wave height (H_s)
Standard statistical measure of sea severity; equals four times the square root of the zeroth spectral moment of the wave energy spectrum: $H_s = 4\sqrt{m_0}$.

Simpson's rule
Numerical integration method using parabolic interpolation between equally spaced ordinates; the standard technique for computing areas, volumes, and moments of ship hull forms.

Skin friction coefficient (C_f)
Dimensionless measure of viscous shear stress on the hull surface; depends on Reynolds number and surface roughness.

Surf-riding
Capture of the vessel by a following wave, accelerating it beyond its self-propelled speed; a precursor to broaching and a recognised intact stability failure mode.

Tactical diameter
Perpendicular distance from the original track to the vessel's position when heading has changed by 180° during a steady turn; a key measure of manoeuvrability.

Thermal efficiency (η_{th})
Ratio of net work output to heat input in a thermodynamic cycle; bounded above by the Carnot efficiency.

Thrust coefficient (K_T)
Non-dimensional propeller thrust: $K_T = T/(\rho\, n^2\, D^4)$; plotted against advance coefficient J in open-water diagrams.

Thrust deduction (t)
Fraction of propeller thrust absorbed by the augmented hull resistance caused by the propeller's suction effect at the stern: $R = T(1 - t)$.

Tonnes per centimetre immersion (TPC)
Displacement weight increase per one-centimetre increase in mean draught: $\text{TPC} = \rho_w\, A_w / 100$; used for loading and ballasting calculations.

Torque coefficient (K_Q)
Non-dimensional propeller torque: $K_Q = Q/(\rho\, n^2\, D^5)$; plotted as $10K_Q$ alongside K_T and η_O in open-water diagrams.

Towing tank
Experimental facility in which scale models are towed at controlled speeds to measure resistance, propulsion characteristics, and seakeeping behaviour.

Trim
Difference between the draughts at the forward and aft perpendiculars; positive trim by the stern indicates deeper draught aft.

Vanishing angle
Heel angle at which the GZ curve crosses zero from positive to negative; beyond this angle the restoring moment reverses and the vessel will capsize if unaided.

Wake fraction (w)
Fraction of ship speed lost at the propeller plane due to the hull boundary layer: $V_a = (1-w)\,V$; typically estimated as $w \approx 0.50\,C_B + 0.05$ for single-screw vessels.

Waterplane area coefficient (C_W)
Ratio of waterplane area to $L \times B$; governs the tonnes-per-centimetre immersion and, through the second moment of waterplane area, the metacentric radius.

Wave-making resistance
Component of hull resistance due to energy radiated in the bow and stern wave systems; dominant at high Froude numbers and scaling as Fn^4 in the low-speed regime.

Wave energy spectrum
Distribution of wave energy across frequency, $S(\omega)$; characterises an irregular sea state and serves as the input to spectral seakeeping analysis.

Weather criterion (IMO)
Intact stability regulation requiring the area under the righting-arm curve (dynamical stability) to equal or exceed the area under the wind heeling-lever curve during a combined steady-wind and gust scenario.

Wetted surface
Total area of the hull in contact with water; the primary geometric input for frictional resistance calculation.